DEVELOPMENT AND EVALUATION OF PASSIVE VARIABLE-PITCH VERTICAL AXIS WIND TURBINES

A thesis submitted for the degree of

Doctor of Philosophy

By

N.C.K. Pawsey

B.E.(Mech)

Supervisor: A.J. Barratt

Co-supervisor: Dr T.J. Barber

School of Mechanical and Manufacturing Engineering,

The University of New South Wales.

November 2002

Abstract

Vertical-axis wind turbines do not need to be oriented to the wind direction and offer direct rotary output to a ground-level load, making them particularly suitable for water pumping, heating, purification and aeration, as well as stand-alone electricity generation. The use of high-efficiency Darrieus turbines for such applications is virtually prohibited by their inherent inability to self-start. The provision of blade-articulation (variable-pitch blades) has been demonstrated by a number of researchers to make Darrieus turbines self-starting. One aim of this thesis is to evaluate the various concepts manifested in the numerous specific passive variable-pitch designs appearing in the literature, often without theoretical analysis. In the present work, two separate mathematical models have been produced to predict the performance of passive variable-pitch Darrieus-type turbines. A blade-element/momentum theory model has been used to investigate the relationships between the key parameter values and turbine steady-state performance. A strategy for parameter selection has been developed on the basis of these results. A free vortex wake model for passive variable-pitch turbines has been developed, allowing the study of unsteady performance. Significant reduction of average efficiency in a turbulent wind is predicted for a Darrieus turbine. The improved low-speed torque of passive variable-pitch turbines is predicted to significantly improve turbulent wind performance.

Two new design concepts for passive variable-pitch turbines are presented that are intended to allow greater control of blade pitch behaviour and improved tur-

bulent wind performance. A prototype turbine featuring these design concepts has been designed, constructed and tested in the wind tunnel. As part of this testing, a technique has been developed for measuring the pitch angle response of one of the turbine blades in operation. This allows comparison of predicted and measured pitch histories and gives insight into the performance of turbines of this type. Results have demonstrated the usefulness of the mathematical models as design tools and have indicated the potential of one of the new design concepts in particular to make a vertical axis wind turbine self-starting.

I hereby declare that this submission is my own work and to the best of my knowledge it contains no materials previously published or written by another person, nor material which to a substantial extent has been accepted for the award of any other degree or diploma at UNSW or any other educational institution, except where due acknowledgement is made in the thesis. Any contribution made to the research by others, with whom I have worked at UNSW or elsewhere, is explicitly acknowledged in the thesis.

I also declare that the intellectual content of this thesis is the product of my own work, except to the extent that assistance from others in the project's design and conception or in style, presentation and linguistic expression is acknowledged.

N.C.K. Pawsey

Acknowledgements

I wish to thank all those who have contributed to my work and supported me during my study. I have been supported by an Australia Postgraduate Award, while the research was supported by an Australian Research Council Small Grant.

Thank you to my supervisor, Tony Barratt, for introducing me to the field of wind energy, keeping me on the right track and for getting his hands dirty with the test rig on numerous occasions.

Thank you to my co-supervisor, Tracie Barber, for her advice, encouragement and unwavering optimism.

Thank you to the workshop staff who manufactured the prototype turbine components and assisted me with the wind tunnel testing, especially Ron Montgomery and Terry Flynn.

Thank you to Dorothy at Meury Enterprises for her generous donation of glue and equipment.

Thank you finally to my friends and family who supported me through three and a half years, and most especially to my beloved Jannet, for whom the struggle was hardly less arduous, but suffered with good humour and unfailing support.

Notation

Symbol	Definition
a	Flow induction factor
A	Turbine swept area; $\equiv R$ x L
AoA	Angle of Attack
C_p	Power coefficient; $\equiv Power/\frac{1}{2}\rho A{U_\infty}^3$
C_q	Torque coefficient; $\equiv Torque/\frac{1}{2}\rho AR{U_\infty}^2$
d	Rolling profile contact point offset from centre of gravity
F_N	Normal component of aerodynamic force on blade
F_T	Tangential component of aerodynamic force on blade
I_{pivot}	Mass moment of inertia of the blade assembly relative to the pivot axis
I_t	Mass moment of inertia of the turbine, including rotor, blades and load
L	Blade length
N_b	Number of blades
R	Turbine radius
R_{ac}	Distance from pitch axis to blade aerodynamic centre
R_{cg}	Distance from pitch axis to centre of gravity of blade assembly
T_{acc}	Torque component accelerating the turbine
T_{load}	Torque component driving the load
TSR	Tip Speed Ratio; $\equiv R\omega/U_\infty$
U	Wind velocity at blade
U_∞	Free wind velocity

y	Rolling profile radial coordinate
y_0	Value of rolling profile radial coordinate y at $\theta = 0$
ϕ	Azimuth angle - the orbital position of the blade relative to the wind direction
ρ	Air density
θ	Blade pitch angle. Positive 'tail out'
ω	Turbine angular velocity

Contents

List of Tables

List of Figures

Chapter 1

Introduction

1.1 Background

The harnessing of the energy of the wind to perform useful work is a practice that has been maintained from at least the sixth century until the beginning of the twenty-first and interest in the field is growing.

Motivation for the increased use of wind-generated power arises from a number of fronts. Primary among these is the recognised need to reduce Greenhouse gas emissions in order to avoid catastrophic climate change. While global fossil fuel supplies remain plentiful, many nations are also wary of reliance on imported energy sources in an international climate of uncertainty. Wind is an ideal alternative to fossil fuels in these regards, as a renewable, non-polluting, local resource. These are the motivations that are prompting developed nations to increase the proportion of their energy needs provided by wind energy.

For developing nations, the motivations are different. While the adoption of large-scale wind electricity generation in the world's most rapidly growing populations would significantly assist the global effort to avert climate change and improve local pollution problems, it is the decentralised nature of wind that offers the greatest hope of improvement to a large number of people's lives. Two billion people throughout the world have no access to electricity (IEA, 1999). Renewable energy including wind is able to provide energy to remote communities and

in developing nations where no electricity grid exists. In many instances, they represent the only economically viable means of providing an energy source to remote areas. The same argument applies to remote communities in countries like Australia, where vast distances make the extension of the grid uneconomic.

Therefore while the utility-scale electricity-generating horizontal axis wind turbines that are proliferating throughout Europe, the US and Australia are the current focus of attention, the development of smaller turbines for stand-alone applications deserves equal effort. It will be argued that vertical axis wind turbines, if they can be made self-starting while retaining simplicity, could play an important part in the provision of energy to people without access to grid power.

1.2 Wind Energy Industry

1.2.1 History and current industry status

Utility scale wind turbines

Wind energy's contribution to global energy supply is currently very small. According to the IEA (2001a), renewable energy sources excluding hydro, combustible renewables and waste contributed just 0.5% of the global total primary energy supplies in 1999. This category includes wind energy, geothermal, solar and others. The contribution of this same category to global electricity production was 1.6% in 1999. Wind energy's contribution to total US electricity generation was 0.12% in 1999, constituting some 1% of the renewables category (EERE, 2001). In Australia, as of 2001, approximately 9% of electricity supply came from renewables, the vast bulk of which came from hydro. Only 0.04% of total electricity generation came from the 41 MW of wind capacity installed in June 2000 (IEA, 2001b).

However global installed wind capacity is increasing rapidly. Figure 1.1 illus-

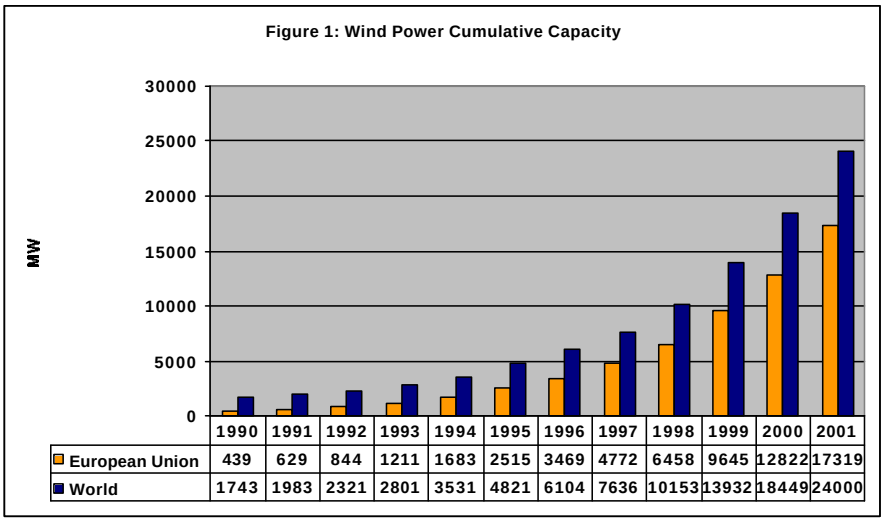

Source: BTM Consult and EWEA

Figure 1.1: Growth of installed wind power capacity in EU and the world to end 2001 (EWEA, 2002)

trates the global and European growth in installed wind generating capacity. At the end of 2001 the European Union had 17,319 MW of installed wind capacity (IEA, 2001a), the US 4,258 MW (AWEA, 2002a) and the world total was 24,000 MW (IEA, 2001a). In Europe 4,500 MW of new capacity was installed in 2001, the most ever in a single year (EIA, 2002). The average annual market growth rate in Europe over the period 1993 - 2000 was 40% (EWEA, 2002). Towards the end of this period, the annual capacity installation rate was increasing at 35% p.a. In the US, 1,700 MW or US$1.7 billion worth of new generating equipment was installed in 16 states in 2001. This is more than twice the previous record for installation in one year (732 MW in 1999) (AWEA, 2002b). The more than 6,000 MW of capacity installed globally in 2001 amounts to annual sales of about US$ 7 billion (AWEA, 2001).

In Australia, the installed capacity at the end of 2001 had risen to 73 MW, up 128% on the previous year. A further 100 MW is expected to be operational by

the end of 2002 (EIA, 2002) and 500 MW of wind projects currently at various stages of planning and development. This trend is expected to continue.

The European Wind Energy Association (EWEA) has set a target that by 2010 Europe will have 60 GW of installed wind capacity, contributing 4.4% of Europe's total electricity generation, up from 1.0% in 2000 (EWEA, 2000). At the start of 2002, 50% of the EU's wind capacity was in Germany providing some 3.5% of that country's electricity. The German government has announced plans to boost that figure to "at least 25% by 2025" (EWEA, 2002).

In the US, according to the AWEA, "Wind is well on its way to providing six percent of our nation's electricity–as much as 25 million households use annually–by the year 2020" (AWEA, 2002b).

The Australian Wind Energy Association (AusWEA) has set a target of 5000 MW of installed capacity in Australia by 2010 (IEA, 2001b).

Small wind turbines

Utility-scale wind turbines have a typical generating capacity of hundreds of kilowatts to more than a megawatt. However, small turbines ranging from 1 kilowatt to a few tens of kilowatts find application in non-grid connected, or stand-alone, roles. Opportunities for wind energy in the field of Remote Area Power Supply are growing. The Australian Greenhouse Office (AGO, 2002) estimates that there are in excess of 10,000 stand-alone and hybrid Remote Area Power Supply systems in Australia. Diesel generators currently provide the bulk of non-grid connected electricity in regional Australia. High transport costs and the need to reduce Greenhouse gas emissions provide a strong motivation to replace diesel with a clean renewable source of energy such as solar or wind or both. The Australian government has launched the Renewable Remote Power Generation Program (RRPGP)

to support the replacement of diesel as fuel for off-grid generation by renewable sources such as wind. RRPGP offers up to 50% rebate of capital cost of new renewable energy RAPS installations.

1.3 Vertical Axis Wind Turbines (VAWTs)

1.3.1 History

The earliest known wind turbines featured a vertical axis. The earliest known design was a panemone used in Persia between 500-900 A.D., which had a shield to block the wind from the half of the rotor moving upwind. It was used to grind grain and to pump water. It is widely believed that vertical axis windmills have existed in China for 2000 years, however the earliest actual documentation of a Chinese windmill was in 1219 A.D. by the Chinese statesman Yehlu Chhu-Tshai (Dodge, 2001).

A patent for the particular design concept being studied here was filed in France by military engineer Georges Jean Marie Darrieus in 1925. His idea received little attention and in the late 1960s the design was independently re-invented by Canadian researchers (South and Rangi, 1973) at the National Research Council in Ottawa. Upon discovering the existing patent, they named the design after the original inventor. Following the 1973 Arab oil embargo, the Canadians shared their information with the US Department of Energy, which began a research program to develop the technology (Sandia National Laboratories, 1987). Promising results from a number of test turbines led to two companies - VAWTPOWER and FloWind - to commence manufacture in the 1980s in California and by the mid 80s, some 500 VAWTs were generating electricity in that state.

Vertical axis wind turbines have fallen out of favour with the wind turbine industry. No new vertical axis wind turbines have been installed in California since 1986 (CEC, 1995). By 1999, of the 11,368 electricity generating turbines reported in operation in that state, none were vertical axis (CEC, 1999). California alone generated approximately 11% of the world's wind generated electricity in 1999 (CEC, 2001).

Horizontal axis wind turbines are similarly dominant in Europe.

1.3.2 Lift and drag VAWTs

A distinction is made between vertical axis turbines that operate using the drag force of the wind on its rotor and those that employ lift forces to generate torque. Drag type devices employ a blade shape that has a higher drag coefficient with the wind incident on one side than on the other. In this way the downwind drag force on the retreating blades is greater than the retarding force on the blades advancing in to the wind on the other side of the rotor. A net torque is thus generated. Examples of drag type turbines are the cup anemometer and the Savonius turbine. Well-designed Savonius turbines generate high torque at low rotational speed. The speed of the rotor is inherently limited because the blades on the retreating side can never travel faster than the wind. In wind turbine parlance, they are said to operate at tip speed ratios (TSRs) of less than one. The TSR is the ratio of the ground speed of the blade tips and the free wind velocity. It is a limitation of drag type turbines that higher speeds and higher peak efficiencies cannot be attained. In addition, relatively large amounts of material are required for a given swept area, however construction is typically simple and inexpensive compared to other types of turbine.

Lift type turbines, such as the Darrieus turbine, employ aerofoil-section blades to generate lift. Such turbines are able to convert this lift into positive torque when

their blades are travelling sufficiently fast relative to the free-stream flow. Such turbines operate at TSRs up to approximately 6 and achieve greater efficiencies than drag turbines. Theoretically achievable peak outputs are comparable to those obtainable by a horizontal axis wind turbine (HAWT) with the same rotor area.

1.3.3 Explanation of Darrieus concept

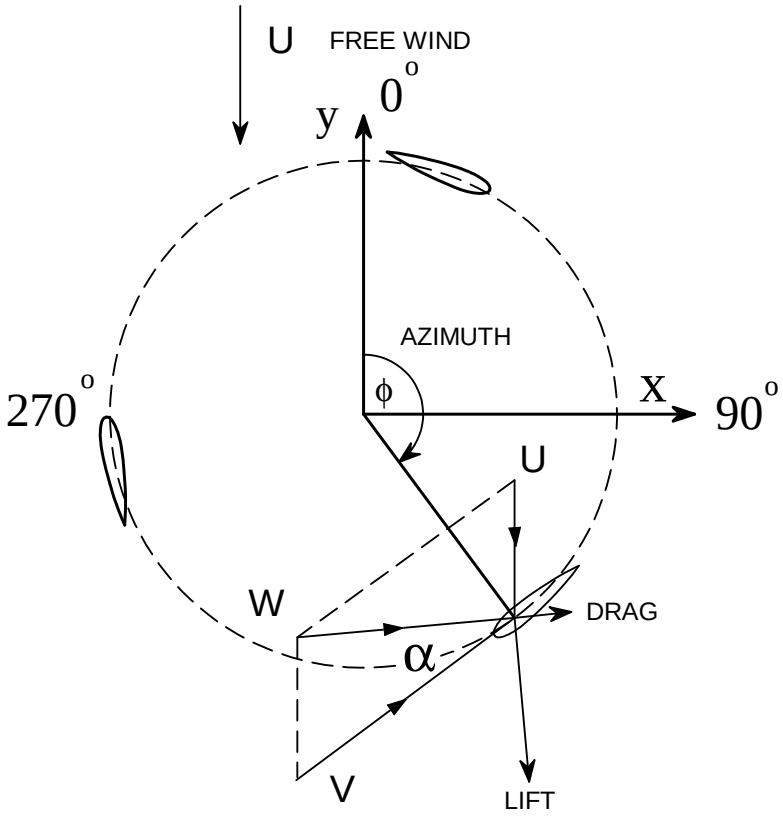

Figure 1.2: Illustration of Darrieus concept

Consider the two-dimensional case of a blade moving in a circular path, as shown in Figure 1.2. As the blade rotates, it experiences a changing relative flow, which is the vector sum of the local wind speed and the blade's own speed. Both the angle of incidence of this relative flow and the magnitude of its velocity vary with the orbital position of the blade, called the azimuth. In general, the relative flow always comes from the upwind side of the blade: that is the outer side of the

blade on the upwind pass and the inner side on the downwind pass. Thus the angle of attack swings through positive and negative values each revolution. At small non-zero angles of attack the lift force generated by the blade has a tangential component in the direction of rotation. Provided that drag is small, the blade then contributes positive torque to the rotor on which it is mounted. This torque is used to drive a load, thus extracting energy from the wind. In the absence of a free wind the angle of attack is at all times zero and no lift is produced.

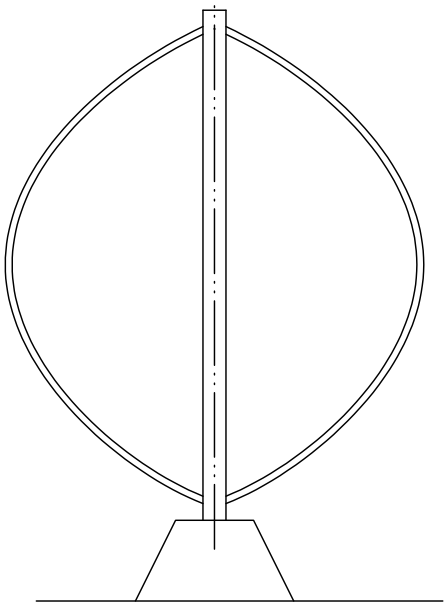

Figure 1.3: Illustration of troposkien Darrieus.

Due to the oscillating angle of attack, unlike a HAWT, the blades of the Darrieus turbine always produce a fluctuating force, even in steady conditions. The original form of the turbine features curved blades that have the shape that a rope takes when its ends are fixed to a vertical axis and spun, called a troposkien (see Figure 1.3). This shape is designed to eliminate bending loads in the blade due to centrifugal force, so that loads are purely tensile. Straight-bladed turbines must withstand greater bending due to centrifugal loads, but have all of the blade length operating at the full tip radius and normal to the plane of rotation.

1.3.4 Advantages of the vertical axis format

Wilson and Lissaman (1974) state that the Darrieus rotor has performance near that of a propeller-type rotor. The principal advantages of the vertical axis format are the ability to accept wind from any direction without yawing and the ability to provide direct rotary drive to a fixed load.

The absence of yaw requirement simplifies the design of the turbine. Hansen et al. (1990) state that failures of yaw drive subsystems have been the second leading cause of horizontal axis turbine downtime in California. They state also that smaller turbines with free-yaw (passive) systems also experience problems, such as overloading due to excessive yaw rates and poor alignment with the wind.

The vertical turbine axis allows rotary loads to be driven directly. For example, a generator may be driven either at the top of the tower or at ground level without the need to mount it within the yawing nacelle. Wiring to the generator may be fixed, rather than having to pass through slip rings and without requiring some periodic 'untwisting' mechanism. A rotary drive pump, such as a helical rotor borehole pump, may be driven directly, or using a step up belt drive at ground level. There is anecdotal evidence of attempts to connect horizontal axis wind turbines to such loads using bevel gearing resulting in the turbine being yawed away from the wind by the shaft reaction torque.

VAWTs are also well suited to other, low speed, vertical axis loads such as the aeration and destratification of ponds and the heating of water or other working fluid by direct mechanical agitation.

A further potential application is the desalination or purification of water by reverse osmosis, for which the pressure head can be maintained by direct mechanical input, bypassing the mechanical-electrical-mechanical conversion step.

The market niche for vertical axis wind turbines is in relatively small-scale applications such as these, and in Remote Area Power Supply uses in general. To realise the potential of the format however, Darrieus turbines must be made reliably self-starting without sacrificing mechanical simplicity.

1.4 Low and Intermediate Tip Speed Ratio Performance

Darrieus turbine blades typically use aerofoil sections designed as aircraft wing profiles. The NACA0012, NACA0015 and NACA0018 profiles are commonly used as blade sections. Typically these are designed to operate at small angles of attack (less than 10°). At angles higher than this the aerofoil undergoes stall: the flow separates from the upper surface of the wing causing a loss of lift and an increase in drag.

As explained in Section 1.3.3, each blade experiences a periodically varying velocity and angle of incidence of apparent flow. The amplitude of this variation is related to the tip speed ratio. This is illustrated in Figure 1.4. This is a simplified representation of the change in angle of attack pattern with TSR. For simplicity the effect of the turbine on the free wind velocity is neglected. In reality, as turbine speed increases, more energy is extracted from the stream and the flow is decelerated. This causes the 'effective TSR' felt by the blade to be greater than is assumed here. However the relationship is qualitatively similar. At start up, the angle of attack varies right through 360°. At TSR 1, the angle of attack ranges from -180° to +180°. For TSR > 1, the cyclical variation in angle of attack approaches a sinusoid of decreasing amplitude. As the blade's velocity becomes much larger than the free wind velocity, the amplitude of the variation approaches zero.

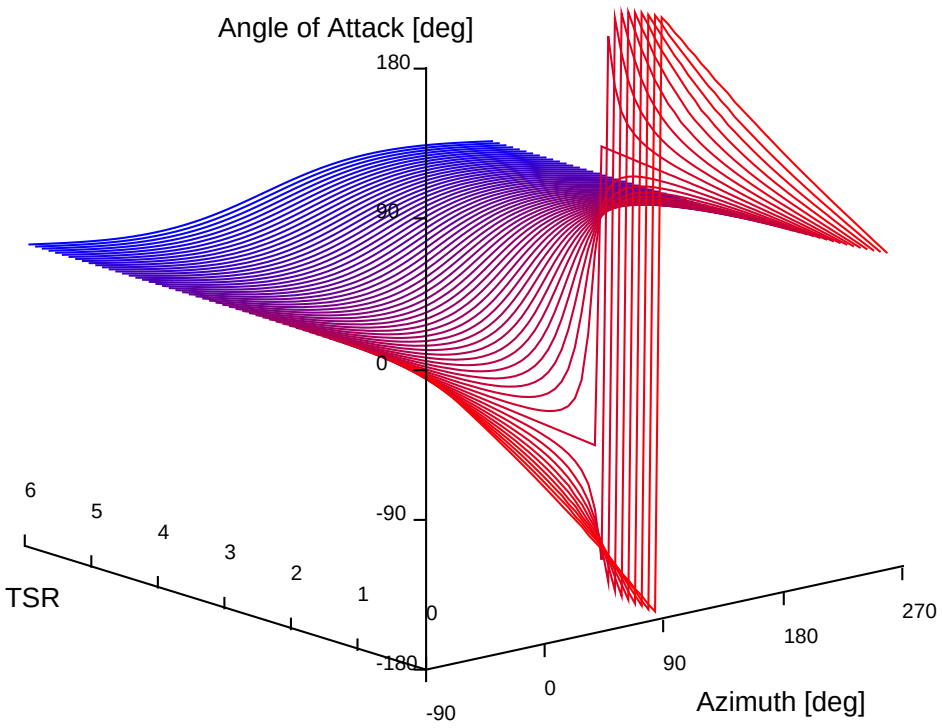

Figure 1.4: Illustration of the change in the pattern of cyclical angle of attack on a blade with increasing TSR. Azimuth angle defines the orbital position of the blade relative to the wind direction. Here the wind velocity is assumed constant and is not affected by the turbine.

This pattern of angle of attack variation produces a variation in the tangential aerodynamic force on a blade of the type shown in Figure 1.5. Again, the deceleration of the flow that would occur in reality has been neglected here to illustrate the principle. Also unsteady aerodynamic effects have been ignored and the static lift and drag coefficients published for the NACA 0018 section have been used.

It can be seen from Figure 1.5 that at low tip speed ratios the blade is stalled at virtually all azimuth angles. Some small positive force is experienced at azimuth angles between 0° and 180°. This is the half of the revolution in which the blade is retreating from the wind and it is purely drag that is producing the small thrust.

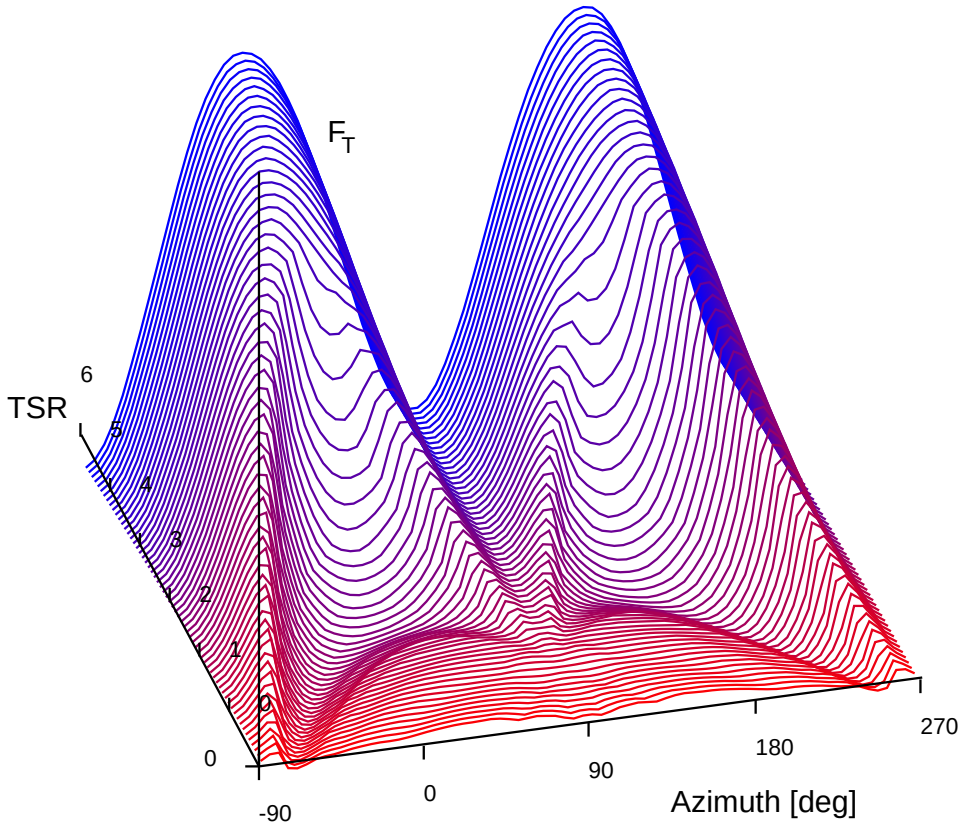

Figure 1.5: Illustration of the change in the pattern of tangential aerodynamic force on a blade F_T. Again the wind velocity is assumed constant, allowing a greater force at high TSR than would really occur. Of interest here is the variation at lower TSR where stall affects the average torque.

On the advancing side of the revolution, the blade enters regions either side of azimuth 270° (pointing straight into the wind) where the angle of attack is below the stall angle and lift thrust is produced. As the TSR increases, the extent of these regions increases. These are visible as the ridges at either side of the F_T surface in Figure 1.5.

Once the TSR exceeds 1, similar regions of lift thrust occur either side of azimuth 90° and it is only where the blade is travelling essentially across the wind that the blade remains stalled. As speed increases further, these stall 'depressions' in the F_T surface shrink until at TSR $\approx$ 4 they disappear and the blade does

not stall at any point in the revolution. There are then two distinct peaks in thrust separated by valleys where tangential force is zero or slightly negative, corresponding to the points when the angle of attack passes through zero.

It should be remembered that in this simplified analysis the deceleration of the flow is neglected and in reality the TSR at which stall is eliminated will in general be lower than is shown here. The trends illustrated however remain valid and explain the low torque produced by fixed bladed Darrieus turbines at low and intermediate TSRs. Figure 1.5 shows the variation in tangential force for a single blade. For a turbine with three blades the total torque is smoother, being the summation of three such curves with 120° phase separation. The average turbine torque for a revolution is found by integration of this tangential load. This is shown in Figure 1.6.

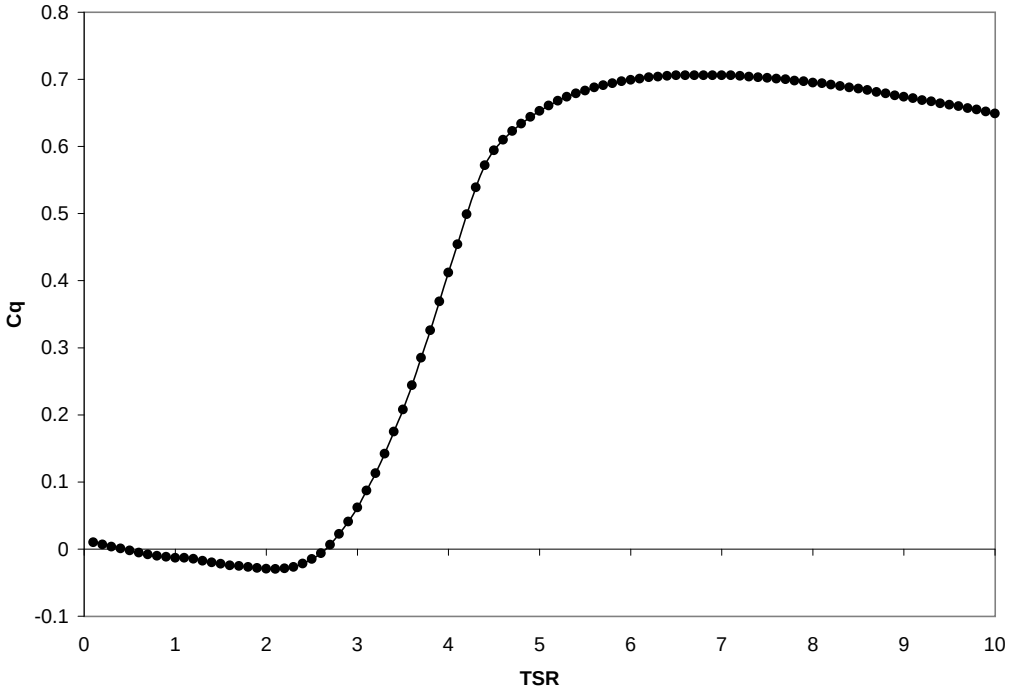

Figure 1.6: Illustration of the variation of non-dimensionalised torque C_q with TSR for the case shown in Figure 1.5. Because deceleration of the wind is neglected the torque rises later, achieves a higher peak and persists to higher TSRs than would occur in reality.

Figure 1.6 illustrates the trough in the torque curve that occurs at intermediate tip speed ratios - between approximately 0.5 and 2.5 here. At TSR < 0.5 torque is slightly positive due to the difference in drag between advancing and retreating halves of the each blade's revolution. Thus the turbine may well begin to move from rest and accelerate up to some equilibrium speed at TSR ≈ 0.5. However the trough where torque is negative prevents the turbine from accelerating of its own accord to the TSR at which torque increases rapidly (and above which useful work can be done).

The addition of flow deceleration, parasitic aerodynamic drag, transmission friction and load torque to this simplified analysis would serve only to exacerbate the inability to self-start. The only real factor neglected here that would improve starting performance is the consideration of unsteady aerodynamic effects. Under dynamic conditions, the flow is able to remain attached and stall is delayed to higher angles of attack than apply under static conditions. These effects are important to the analysis of Darrieus starting performance and are also very difficult to accurately account for. This subject will be discussed in detail in Chapter 5.

The actual location and depth of the torque trough is dependent on a number of factors, including the number and size of the blades, the radius of the turbine and the free wind velocity. In some cases the torque in the trough may actually be small but positive. The most serious consequence of this characteristic is the inability to reliably self-start. While the turbine may be able to begin spinning and accelerate up to a speed where the torque curve reaches zero, it is not able to accelerate beyond the trough to the high TSRs at which torque is high enough for useful work to be done. Even if the ideal torque curve is at all speeds positive,

parasitic aerodynamic drag, drive train friction and load resistance are likely to exceed output torque in the trough.

The inability to self-start is not a major impediment to large grid-connected turbines with control mechanisms that are able to drive the turbines up to speed when sufficient wind is measured. However it is a virtually prohibitive shortcoming for small, stand-alone turbines, which need to operate passively and unattended, to be economically viable.

The negative torque region that prevents self-starting in a steady wind presents a further problem for turbines operating in turbulent wind. In a real wind, velocity fluctuations occur very much faster than inertia allows the turbine speed to respond. Thus the instantaneous tip speed ratio varies significantly. If the torque-speed curve has a deep trough immediately below the running TSR range, there will be frequent periods during which the torque is low or negative. This may significantly affect the total energy captured from the wind. As pointed out by Bayly (1981), this phenomenon is especially significant for turbines driving synchronous generators that are made to operate at a constant speed.

The primary focus of this thesis therefore is the investigation of methods of increasing the torque produced by Darrieus turbines at intermediate tip speed ratios, so that they may be reliably self-starting and more efficient in turbulent wind conditions.

1.5 Variable-Pitch Darrieus Turbines

A number of methods for making a Darrieus turbine self-starting have been proposed by previous researchers. A review of these is given by Kirke (1998). The particular method studied here is the variable-pitch turbine design. It appears to

offer the greatest potential for achieving significantly increased torque at low and intermediate tip speed ratios without compromising peak efficiency.

As discussed in Section 1.4, the inability to self-start is due to the stalling of the blades at low and intermediate tip speed ratios. Stall occurs when the angle of attack becomes too large and the flow separates from the surface of the blade resulting in a loss of lift and an increase in drag. If the angle of attack can be reduced sufficiently, the flow over the blade can remain attached. This reduction in angle of attack requires that the blade orientation be changed to point closer to the apparent wind direction. Figure 1.4 shows that if the blade pitch angle is varied as an approximately sinusoidal function of the azimuth angle, in phase with the variation in angle of attack, the amplitude of the angle of attack oscillation experienced by the blade can be reduced. Any reduction in the proportion of time that the blade spends stalled will increase the average torque for the revolution.

Reduction of stall is the principal mechanism by which variable-pitch increases torque at intermediate TSRs, but the concept may also produce significant improvements at start up and low TSRs. Below TSR = 1, it is not practical for a blade to pitch sufficiently quickly to prevent stall. However even for moderate pitch amplitudes, the blades are able to act as more efficient drag devices, like the mainsail of a yacht running before the wind with the boom swung wide from the keel line. These two separate mechanisms are able to significantly increase the starting and intermediate TSR performance of Darrieus turbines. They are illustrated in Figure 1.7.

1.5.1 Active variable-pitch

The question then is how to produce the required variation in blade pitch. A central cam with pushrods connected to the blades may be used to produce a

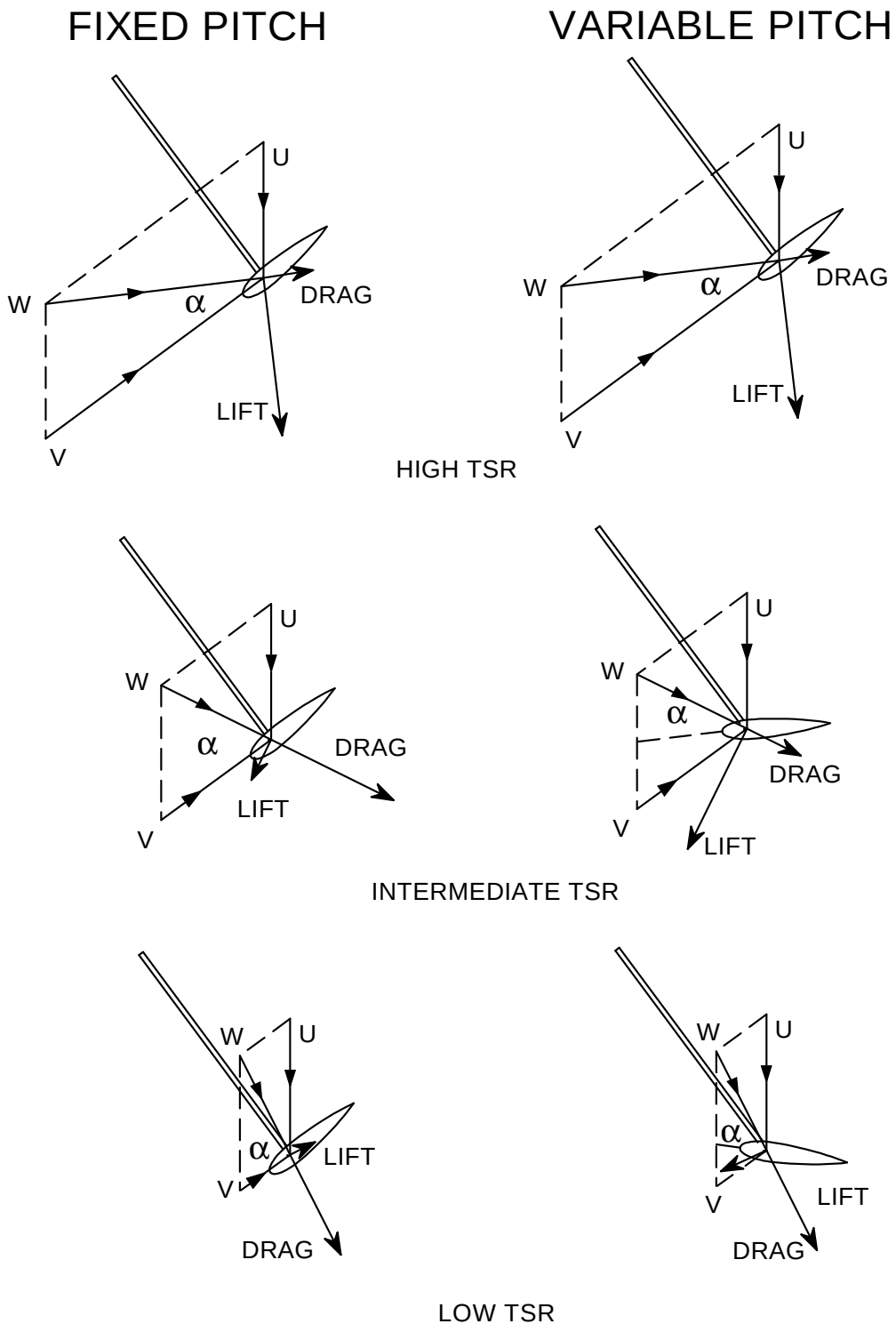

Figure 1.7: Darrieus rotor aerodynamics. Blade pitch variation allows the angle of attack to be reduced. At high TSR, no pitching is required. At intermediate TSR, pitching prevents the blade stalling. At low TSR, pitching produces a more favourable combination of lift and drag.

periodic variation in pitch angle as a function of azimuth angle. Such designs have been tested by a number of researchers, including Drees (1978) and Grylls et al. (1978). It is clear from Figure 1.4 that as the amplitude of the angle of attack variation on a fixed blade decreases with tip speed ratio, so does the amplitude of pitch variation required to prevent or reduce stalling.

This was confirmed experimentally by Grylls et al. (1978), whose results are shown in Figure 1.8. They tested a variable-pitch VAWT whose blades were driven by a central cam. They tested four different amplitudes of pitch variation and found that while a large amplitude offered good starting torque and low TSR performance, the turbine was unable to accelerate to higher TSRs, or to produce a good maximum efficiency. Conversely, a small pitch amplitude was found to produce good high speed efficiency, but the low TSR benefits were lost.

This finding was confirmed by mathematical modelling of a cam-driven turbine by Pawsey and Barratt (1999). To elaborate on these results, a series of simulations was run using the momentum theory mathematical model developed for this project and discussed in Chapter 5. The performance of a turbine with a preset sinusoidal pattern of pitch variation was predicted at a wind speed of 7 m/s for different pitch amplitudes, ranging from $\pm 30^\circ$ to fixed blades. The dimensions and solidity of the turbine are the same as those tested by Grylls et al.

The results for gross power coefficient C_p (parasitic drag not subtracted) are shown in Figure 1.9. The requirement for pitch amplitude to diminish with TSR is confirmed. In this case, the predicted gross power is positive at all TSRs, even for the fixed-blade turbine (0° amplitude). However a significant improvement in low and intermediate TSR performance is indicated given the appropriate pitch amplitude. These results indicate the desirability of having a pitch variation schedule

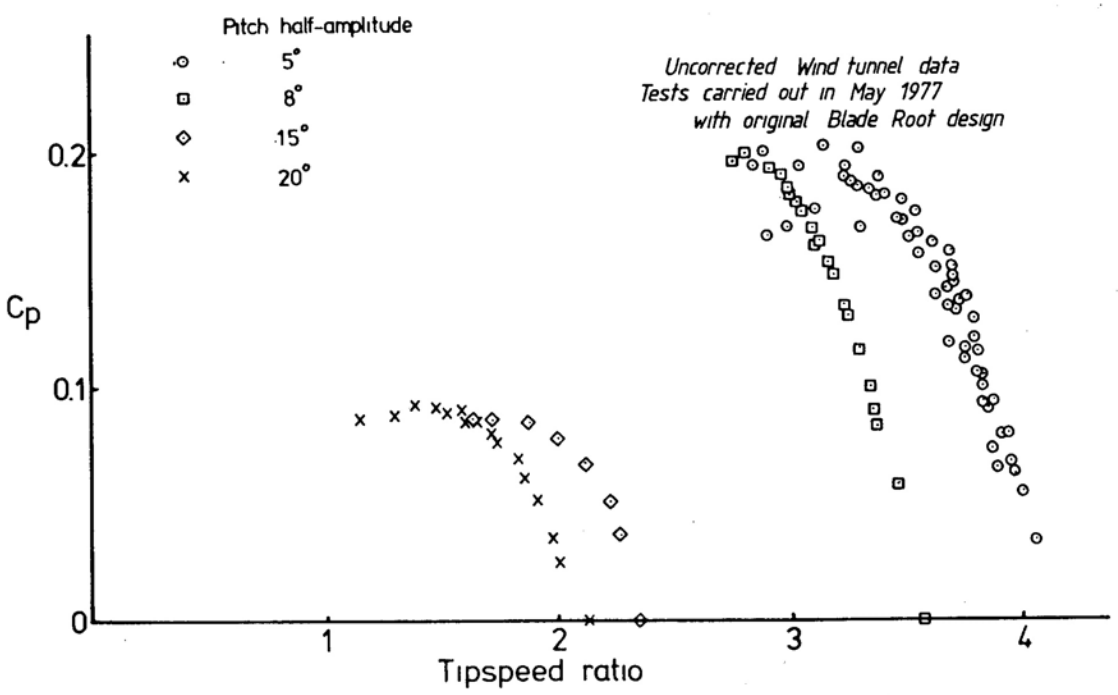

Figure 1.8: Power coefficient wind tunnel test data from Grylls et al. (1978) for a 2.4 metre diameter x 1.6 metre VAWT with a cam-driven blade pitch schedule

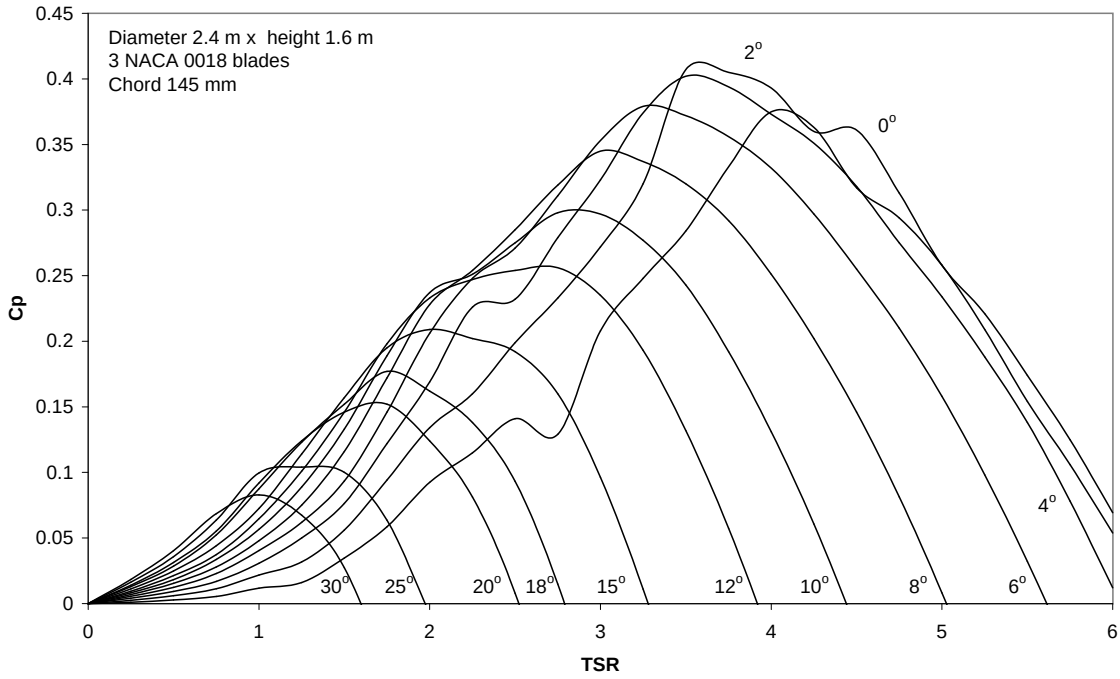

Figure 1.9: Predicted performance of a cam-driven variable pitch VAWT for a range of pitch amplitudes. Gross power coefficient is shown, before parasitic drag and friction are subtracted. Turbine 2.4 metre diameter x 1.6 metre, 3 blades NACA 0018, chord 145 mm.

whose amplitude is variable. The turbine could then 'ride the envelope' of the individual curves in Figure 1.9, producing improved performance at tip speed ratios from 0 to the higher design speeds of the standard Darrieus turbine.

This is difficult to achieve in practice with a cam design. Some measurement and control system would also be required to sense the wind speed relative to the rotor speed.

This is a major reason for opting for a 'passive' variable-pitch system: one in which the pitch of the blades is determined directly by the wind forces on the blades themselves. This removes the need for any sensing or central control and provides the flexibility needed to overcome the limitations inherent in pre-determining the blade pitch schedule.

1.5.2 Passive variable-pitch

The basis for the passive variable-pitch concept is that a blade that is free to pitch about a spanwise (longitudinal) axis near the leading edge will seek to point into the apparent wind.

Work done by Bayly and Kentfield (1981) and Kirke and Lazauskas (1993) has demonstrated the ability of two different passive variable-pitch VAWTs to achieve self-starting. Their work however also demonstrated the sensitivity of the performance of their turbines to variation in the key parameters that affected the blade pitch response. While an approximately sinusoidal pattern of pitch variation is required, the amplitude, phase and higher order deviations from this pattern have a great effect on the torque at any given speed. Under static conditions, the magnitude of the equilibrium angle of attack adopted by a blade depends on the relative strengths of the aerodynamic and restoring moments about the pivot axis. Under dynamic conditions, the inertia of the blade becomes significant and

the combination of these three factors determines the blade pitch response. The magnitudes of all three of these factors may be determined by the specific design of the blade and its connection to the rotor. It is the aim of this thesis to investigate the features of desirable passive blade pitch response and the ways in which such response may be achieved through the design of the blade-rotor connection.

1.6 Structure of Thesis

Mathematical modelling

In order to evaluate different turbine designs and their performance under different operating conditions a mathematical model is required. Bayly and Kentfield (1981) and Kirke and Lazauskas (1993) developed steady-state performance prediction models for their respective designs. To assess the potential of different designs for achieving desirable pitch response, for this thesis a more general mathematical model has been developed for steady-state performance. In addition, a separate model has been developed for investigation of transient turbine behaviour, especially performance in turbulent conditions.

New turbine design

On the basis of insights gained from the results of theoretical analysis, two new design concepts have been conceived and studied. Predicted performance is presented for these designs and explanation of their potential advantages is given.

Experimental procedure

In order to assess the potential of the new design concepts, a prototype turbine has been designed and constructed and tested in a wind tunnel. A new technique for measuring the blade pitch response pattern of the turbine in operation has been

developed. Results of this testing and conclusions on the potential of the designs are presented.

Chapter 2

Review of Passive Pitch Control Systems for Darrieus Turbines

2.1 Review of Existing Variable-Pitch Darrieus Turbines

2.1.1 Active variable-pitch Darrieus turbines

Variable-pitch Darrieus turbines may be divided into active and passive types. Active designs may be defined as those systems that produce blade pitch change through means other than the direct action of the aerodynamic forces acting on them. These may range from systems that measure and calculate appropriate pitch angles continuously and use hydraulic or similar actuators to drive the blades to the desired angle, through to cam-driven designs mentioned in Section 1.5.

Work has been done on this type of turbine by McConnell (1979) and Meikle (1993). The cost and complexity of such systems is not considered justifiable for small stand-alone turbines. A more simple type of active system is one in which the blades are moved by pushrods driven by a central cam, which produces a pre-set schedule of pitch variation. Darrieus (1931) included such a cam-driven design in his original patent for the fixed-pitch turbine (see Figure 2.1). Drees (1978) developed a similar design called a 'Cycloturbine' with the Pinson Energy Corporation. The blade pitch schedule is set using a central cam and pushrods to each blade. The cam is oriented with the wind direction using a small tail vane. Drees

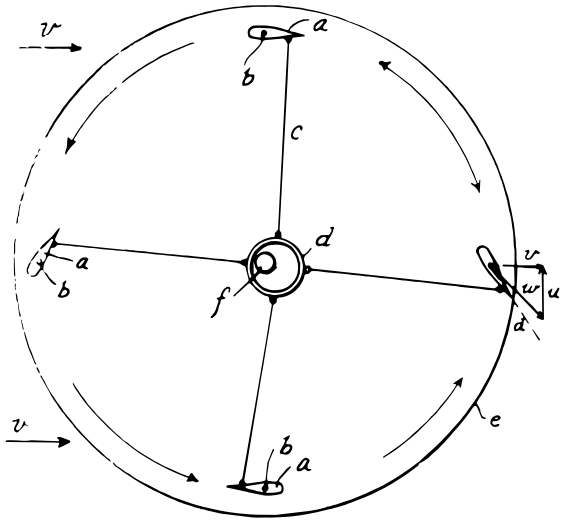

Figure 2.1: Darrieus' cam driven design

reported reliable self-starting and a high maximum power coefficient Cp of 0.45 in field tests. As mentioned in Section 1.4, Grylls et al. (1978) performed theoretical and experimental analysis of a turbine similar to that of Drees. They developed a multiple streamtube type mathematical model that incorporated a preset schedule of pitch variation. Both theoretical and wind tunnel results indicated one of the major problems of such active designs: the amplitude of the pitch variation is fixed by the cam and so cannot vary to suit the tip speed ratio. This limits the efficient performance of the turbine to a narrow band of TSR. Large amplitude ($\pm 20°$) produces good starting torque and performance up to TSR 1.5, which then drops off rapidly with increasing speed. A small amplitude of $\pm 5°$ yields good high speed performance (and much higher efficiency) at the detriment of starting performance. This limitation could be overcome by providing some means of varying the cam profile with turbine speed, however the technical difficulty of accomplishing this would greatly increase the cost.

Grylls et al. also reported problems of high friction associated with the cam and pushrod mechanism. These problems and the increased cost and complexity

of active systems are the reason for the exclusive focus on passive designs in the current work.

2.1.2 Passive variable-pitch Darrieus turbines

Sicard (1977) patented a design in which the blades are free to pivot about an axis in the chord line and are balanced so that their centre of mass lies radially outboard of the pivot axis when the blade is in a 'zero-pitch' position - i.e. with its chord line tangential to the orbit of the pivot axis. This design is shown in Figure 2.2. Under the action of centrifugal 'force' a stabilising or restoring moment is applied to the blade so that it seeks the zero-pitch position. Thus the blade is like a pendulum in an inertial field. No stops are mentioned to limit the pitch angle of the blades and so at rest there is nothing to prevent the blades all turning to point into the wind, thus generating no thrust.

Sicard does mention a variation on the design in which the upper ends of the blades are mounted at a slightly larger radius than the lower ends, thus causing the blades to seek a zero pitch orientation at rest under the influence of gravity. It seems unlikely however that for small tilt angles this would produce enough moment to allow the turbine to self-start using the drag of the blades. No theoretical or experimental analysis of the design by Sicard was found.

Brenneman (1983) designed a turbine that in one form, which he terms an 'inertial' type, is identical to Sicard's design with the addition of stops to limit pitch angle. A second embodiment, which he calls an 'elastic' type, has the blades balanced about the pivot axis, with some elastic device, such as a steel rod or wire spring, to return the blade to its undisturbed position as shown in Figure 2.3. For this design he makes the claim that it is inherently speed limiting, as the natural frequency of the blade oscillation is fixed by the moment of inertia of the

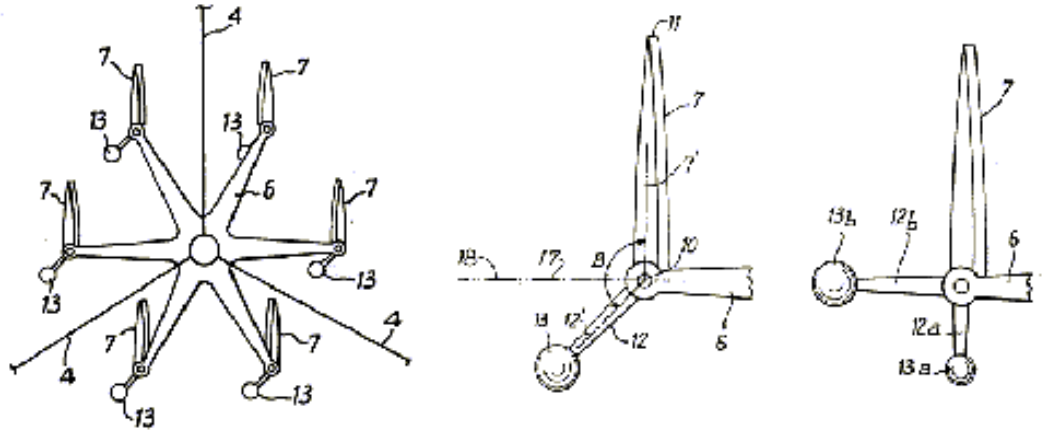

Figure 2.2: The design patented by Sicard (1977)

blade and the stiffness of the spring. This means that when the rotational speed of the turbine, which is equal to the frequency of the driving force, exceeds the natural frequency, the blade motion becomes out of phase with the angle of attack variation, causing the turbine to lose thrust and decelerate rapidly.

He recognises that the inertial type does not have this feature, as the natural frequency varies linearly with the rotational speed of the turbine, so that the ratio of the two is constant. However he does not address the fact that for his elastic design, the variation of the frequency ratio with turbine speed means the amplitude and phase angle of the pitch response of the blades varies accordingly, in a manner that is not likely to be favourable. Specifically at start up the frequency ratio is close to zero, so while the response will be in phase with the driving force, its amplitude is likely to be small. As speed increases and approaches the natural frequency, the amplitude will increase. Coupled with the fact that the magnitude of the driving aerodynamic force increases with the square of relative wind speed,

a pitch amplitude that increases with speed will result. This is the opposite of the trend that is desirable, as discussed in Section 1.5.

No experimental work to test the design concept is mentioned. An essentially identical concept is embodied in the design of Cameron (1978).

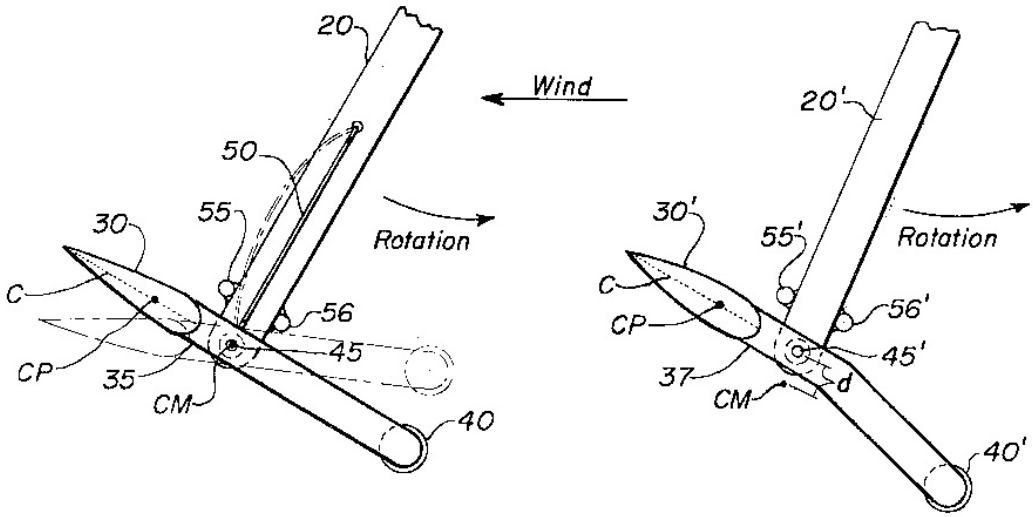

Figure 2.3: The elastic (left) and inertial designs of Brenneman (1983)

Leigh (1980) proposed a design in which each blade is pivoted about a point on the chord forward of the aerodynamic centre. The blade is balanced using a counterweight hidden inside the radial arm (thus reducing parasitic drag) and acting on the blade via a pushrod (see Figure 2.4). Springs produce a restoring moment on the blade, returning it to the neutral position. Like Brenneman's elastic design, the restoring moment is independent of the centrifugal load and the turbine should behave in the same manner as Brenneman's.

Evans (1978) designed a passive variable pitch turbine in which the blades were pivoted about a point at the 1/3 chord location and balanced about this point. The stated aim of the design was to allow the blade to pitch to reduce the angle of attack so that it is just below stall. The concept is based on pitching moment,

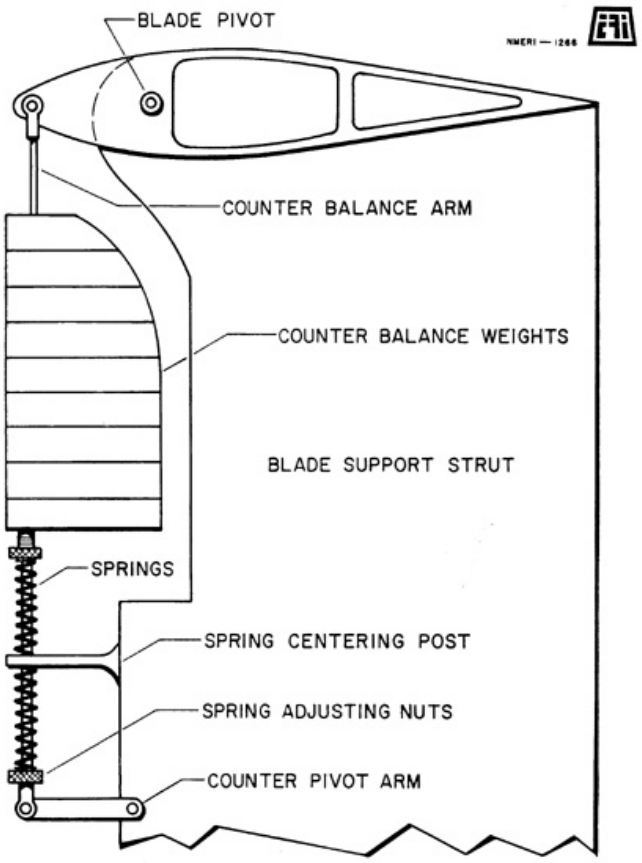

Figure 2.4: Leigh's "automatic blade pitch" design concept (reproduced from Leigh, 1980)

or movement of the centre of pressure. For angles of attack well below stall, the centre of pressure should be forward of the pivot axis (near the quarter chord), while if stalled, the centre of pressure should be aft of the 1/3 chord position. These movements were intended to always move the blade to the angle of attack that was considered ideal, just below stall. The stated role of the spring is to bias the pitch in the direction of decreased angle of attack, though it appears that it would actually reduce the angle of pitch, which would often increase the angle of attack.

As no test data is given for the turbine, it is difficult to say whether this concept could be successful. Evans also proposed a design in which the blades are free to

pivot and are linked to each other by a set of rods or wires. No counterweight is used, but the blades mutually cancel out the tendency to flare outwards under centrifugal force. The blades are hence not free to pitch independently and it is not clear that the angles that they adopt would be optimum or even advantageous.

Liljegren (1984) patented a design in which the blades are pivoted about the centre of mass, which is on the chord (see Figure 2.5). The pitching motion of the blades is regulated by the action of two independent masses, the centrifugal weight of which oppose the inward and outward pitch of the blade. In addition, springs are used to supplement the restoring moment of the masses when rotational speed is low. The design is intended to produce diminishing pitch response amplitude with increasing speed and to finally prevent pitching altogether at running speeds. No quantitative analysis or experimental work on the design could be found in the literature, though Kirke (1998) demonstrated success with a similar design concept.

Sharp (1982) designed a turbine in which the blade lies radially outboard of the pivot axis. The centre of mass on the chord of the balanced blade is connected via a 'rocker arm' to a hinge at the end of the support arm (see Figure 2.6). He claims that this is superior to the Sicard concept because the moment of inertia of the blade assembly is lower, thus allowing the blades to be more responsive and faster moving. While the moment of inertia about the mass centre is lower, the rocker arm arrangement means that the relevant moment of inertia, that about the hinge, is almost the same.

The placement of the pivot axis off the blade chord means that the blade no longer seeks a zero angle of attack under static conditions. When the turbine is generating torque, as it is designed to do, the tangential load will produce

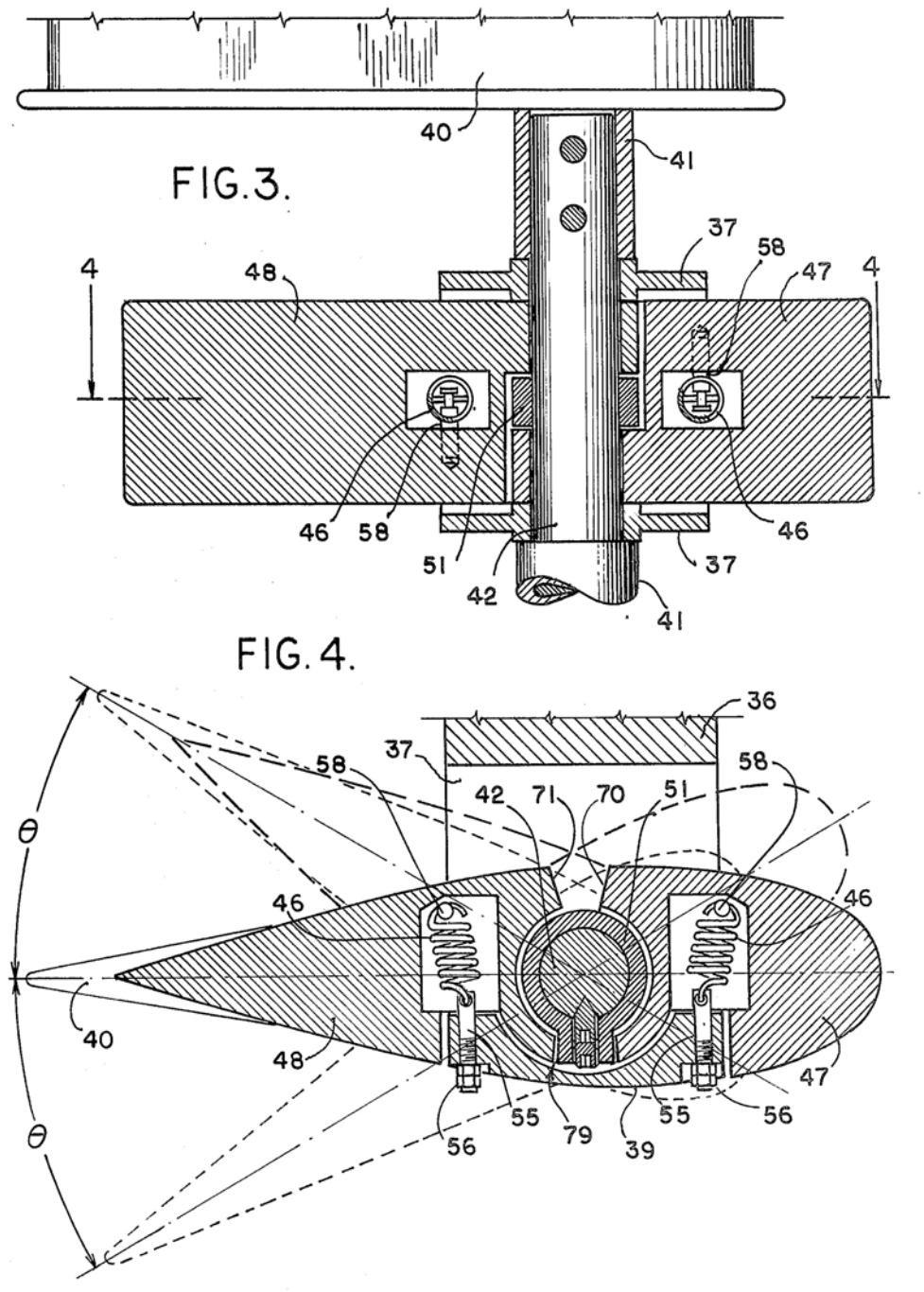

Figure 2.5: Sketch of Liljegren's inertial and spring design (Liljegren, 1984)

a moment about the pivot hinge, which must result in some bias in the blade angle. Apart from this characteristic, the turbine should operate in much the same manner as the Sicard design, though no quantitative analysis was presented.

The design of Marie (1984) is essentially the same with the addition of a spring to supplement the inertial restoring moment.

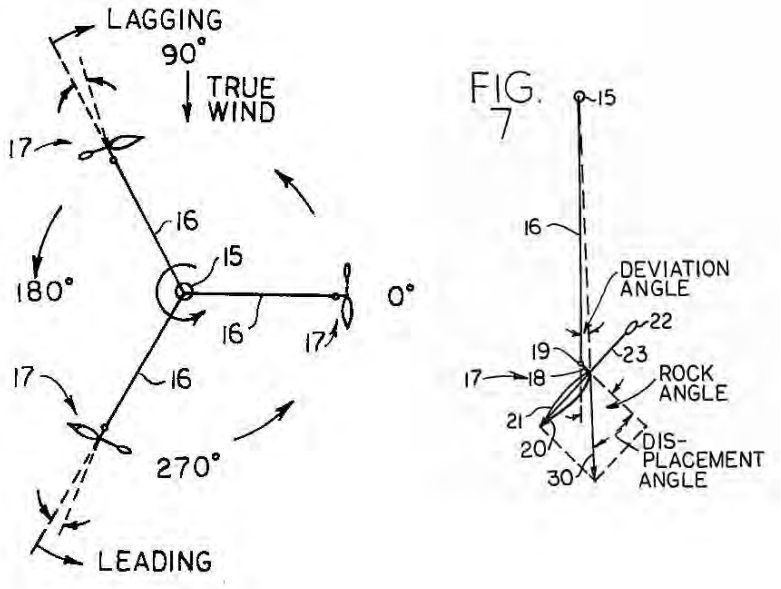

Figure 2.6: Images of Sharp's design included in his patent (1982)

Verastegui (1996) patented a design for a passive variable-pitch turbine in which the response is regulated through the aerodynamic loads acting on the blade and a smaller 'stabiliser' blade just inboard and mechanically linked to it (see Figure 2.7). The relative masses and pivot locations of the blade and stabiliser are set so that there is no tendency to pitch under centrifugal force alone. The stabiliser is pivoted about a point aft of its aerodynamic centre and the main blade is pivoted forward of its aerodynamic centre, so that aerodynamic forces produce opposing moments, causing the blade to seek at equilibrium "an optimum pitch angle".

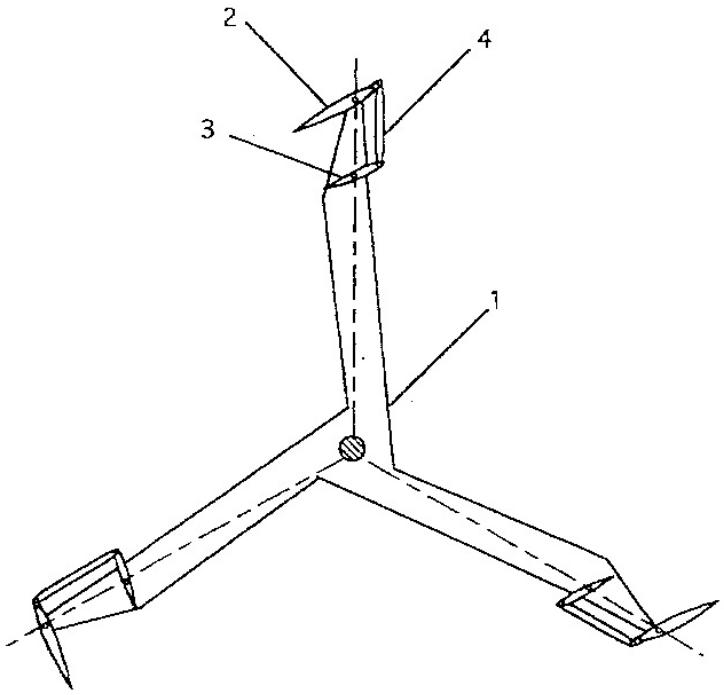

Figure 2.7: Patent sketch of Verastegui's aerodynamic stabiliser design (Verastegui, 1996)

The exact theory by which this is achieved is not disclosed, though a momentum type analysis included in the patent is used to derive predictions of peak power coefficient of 0.70 for the design, which exceeds the Betz limit for maximum theoretical C_p of 0.593.

In addition to his work on the Cycloturbine described above, Drees (1979) also patented a passive variable-pitch turbine in which the blades are not balanced about their pivot point. In the simplest form of the invention, the blades are allowed to swing inwards through 90° to act as drag translators at very low tip speed ratios. As speed increases, centrifugal force holds the blades out in a zero-pitch position against stops. Thus the design seeks to make use only of the start up drag-dominant mode and the lift-dominant running mode of the standard

Darrieus turbine, without any means of extending the lift-based operation down to intermediate tip speed ratios. As such is seems unlikely to achieve self-starting.

Zheng (1984) recognised the need to have a progressively diminishing amplitude of pitch response with increasing turbine speed for a given wind speed. His design has no means of providing a restoring moment on the blade to balance aerodynamic moments, but instead features a weighted 'guide' piece that progressively narrows the angle through which the blade is allowed to swing (see Figure 2.8). It is not clear whether this design concept could work, however from a practical standpoint the repeated impact of the swinging blade on the hard stops is likely to be problematic.

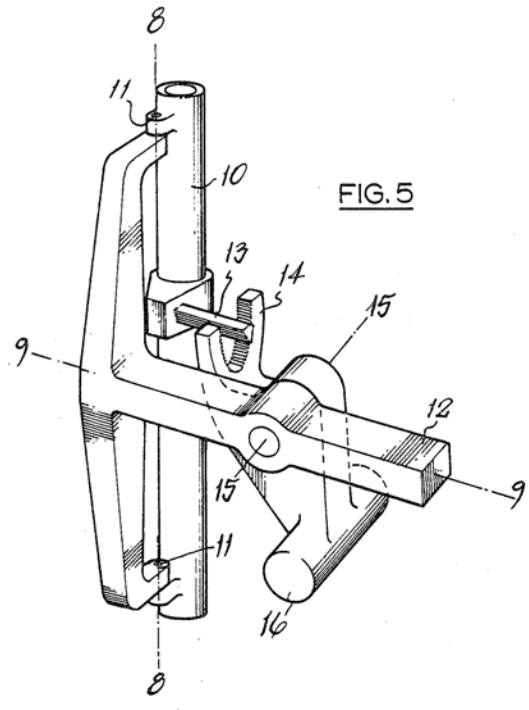

Figure 2.8: Sketch of the key mechanism of Zheng's variable pitch stop design (Zheng, 1984)

Martin (1989) patented a turbine in which cambered blades are free to pivot about a point near the leading edge and are balanced using a counterweight about a point on the chord line but forward of the pivot axis.

Bayly and Kentfield (Bayly, 1981; Bayly and Kentfield, 1981) performed a theoretical and experimental study on a turbine design they called a "Cyclobrid". This was a passive-pitching turbine essentially identical in concept to that patented by Sicard (1977), but apparently conceived independently by Kentfield (1978). Kentfield however used stops to limit the travel of the blades, thus allowing the turbine to start from rest (see Figure 2.9). Bayly produced a momentum type mathemat-

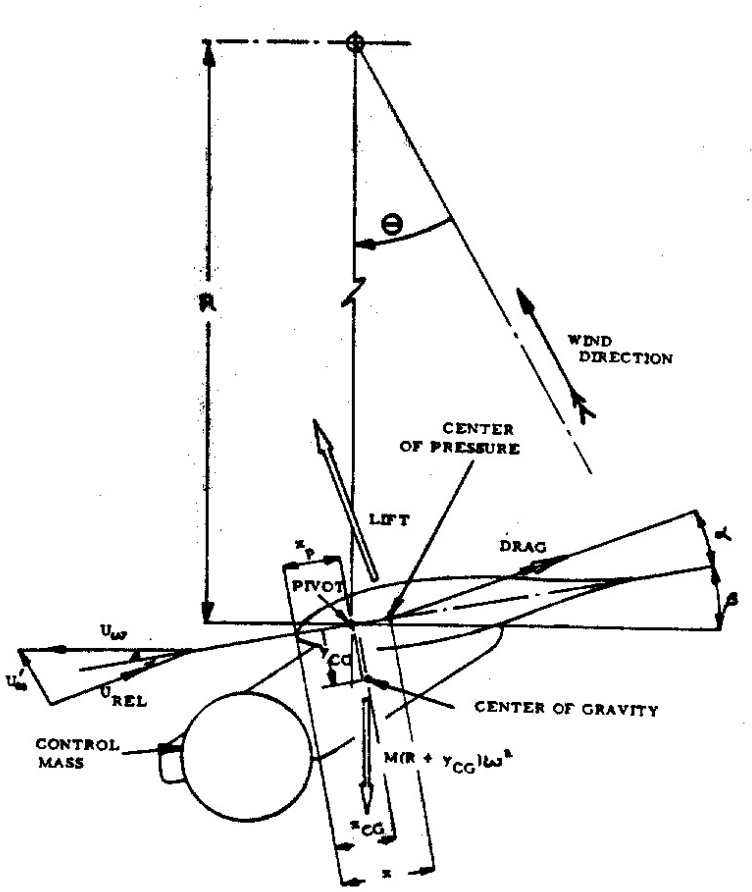

Figure 2.9: The 'pendulum' type inertial design of Kentfield (1978)

ical model for the turbine and tested a 15 foot (4.57 m) diameter prototype. The mathematical model indicated good running efficiency for the design.

The full-scale prototype turbine tested in the field achieved reliable self-starting and a peak efficiency of 0.36 at a tip speed ratio of 3.7, which are in reasonable agreement with predictions of the mathematical model. This work demonstrated the ability of the passive variable-pitch systems to marry self-starting ability with good running speed efficiency. It also demonstrated the ability of an inertial type pitch control system to produce appropriate pitch response over a range of turbine speeds.

Kirke (1998) conducted a study on self-starting vertical axis wind turbines as a PhD thesis. Kirke performed an extensive survey of previous active and passive variable pitch VAWT designs and his thesis is the most detailed and systematic work on passive variable-pitch turbines found in the literature. He considered passive variable-pitch Darrieus type turbines as just one of a number of options available for achieving self-starting, but devoted most of his attention to them and in particular the design he developed with Lazauskas (Kirke and Lazauskas, 1991). The design concept is shown in Figure 2.10.

Kirke's design is very similar in concept to that of Liljegren (1984), though much simpler in execution. A single T-shaped stabiliser mass is used to oppose the pitching of the blade, which is balanced about a point on the chord line near the leading edge. No springs are used to assist the masses at low speeds in this case. This design produces a restoring moment that is proportional to the centrifugal force but is independent of the pitch angle.

Unlike Liljegren's design, Kirke provided the ability to adjust the moment arms at which the two masses acted independently, as well as the respective pitch

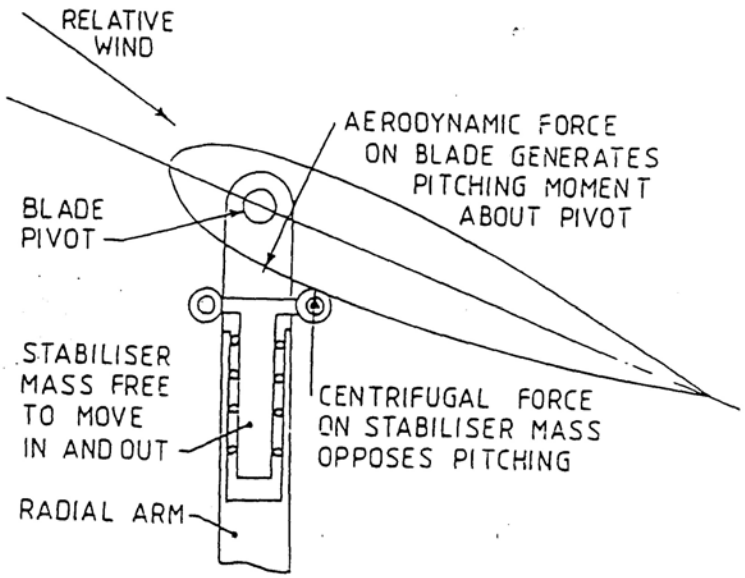

Figure 2.10: The Kirke-Lazauskas inertial design (Kirke, 1998)

limits. This allows the pitch response to be biased in one direction or the other. Unlike the 'pendulum' type of inertial system tested by Bayly and Kentfield (1981), Kirke's design has a threshold of restoring moment that must be exceeded by the aerodynamic moment on the blade before any pitching will occur. This feature is desirable because it prevents small oscillations at high speeds that occur with pendulum type designs and allows the turbine to function as a standard fixed-blade Darrieus turbine at high running speeds. However at lower TSR when the pitch response amplitude is large there will be an impact between the blade and the stabiliser mass each time the blade swings through the zero pitch position, as the mass switches contact points and is asked to change direction instantaneously. Thus the contact points between blade and mass would need to be cushioned in some way to avoid damaging impact loading and prevent 'bouncing' in the pitch response.

It should also be noted that compared with the Kentfield 'pendulum' type design, Kirke's separation of the pivoting blade and the sliding stabiliser mass does not necessarily result in a reduced moment of inertia of the blade or faster pitch response. The radial movement of the stabiliser mass associated with blade pitching adds to the effective mass moment of inertia about the pivot axis. It can be shown that this effect is equivalent to lumping the stabiliser mass at the contact point. This additional inertia was not included in the mathematical model (Kirke and Lazauskas, 1992).

The model was of the momentum type and was validated through wind tunnel testing of a model turbine. He also built and tested in the field a 6 metre diameter turbine based on the same design. Some discrepancy was found between predicted and measured results for this case. Both the wind tunnel and field testing demonstrated the ability of the design to achieve self-starting and his results lend further weight to the argument for inertial type pitch control.

2.1.3 Summary

From the wide range of often ingenious ideas embodied in the above designs a number of common themes emerge. By definition, all passive variable-pitch turbines rely on aerodynamic forces to effect the change in blade pitch.

Drees and Evans produced designs in which the blades are not independent, but instead move collectively. Martin, Drees and Zheng produced designs that rely purely on aerodynamic forces to move the blades. While centrifugal force is used to limit or prevent pitching at high speeds, it does not continuously influence the pitch response.

All the remaining passive designs regulate the pitch response using a restoring moment on the blades that counteracts the tendency of the wind to disturb the

blade from its neutral position. Brenneman and Cameron produced designs in which the restoring moment is provided by purely elastic means. Sharp, Sicard, Kentfield and Kirke relied on inertial forces in their designs. Brenneman and Liljegren also produced designs that used a combination of the two.

While Brenneman talks about elastic and inertial means of pitch control as being different means of producing essentially the same effect, the major difference between them is that the restoring moment provided by the elastic means (as embodied to date) is independent of the turbine speed. Inertial loads on the other hand are inherently proportional to the square of the turbine speed. The only designs demonstrated to be effective to date (Bayly and Kentfield, 1981; Kirke and Lazauskas, 1993) have utilised inertial pitch control. It will be shown that such a relationship should be the starting point for effective pitch control, though deviations from it may be required to optimise performance over the entire speed range.

The number and variety of the designs described above indicates the need for a systematic approach to the treatment of the problem of self-starting. Most of the above designs appear with minimal theoretical basis presented in the patent and no supporting work appearing in the literature. The aerodynamics and dynamics of passive variable-pitch mechanisms are too complex to be effectively handled without detailed quantitative analysis. The development of mathematical tools to predict what is desirable pitching behaviour and what designs might go closest to realising this is the primary aim of the present work.

2.2 Review of Mathematical Models for Variable-Pitch Darrieus Turbines

The two most studied and best validated approaches to the mathematical modelling of Darrieus turbines are momentum models and vortex models. Momentum models are fast and provide reasonably accurate prediction of steady state average turbine output. Vortex models are claimed to be more accurate at predicted instantaneous blade loads, but are much more computationally expensive.

2.2.1 Momentum models

Momentum models were developed for standard fixed-blade Darrieus turbines. They are based on the calculation of flow velocity through the turbine by equating the streamwise aerodynamic force on the blades with the rate of change of momentum of the air.

The first application of momentum theory to the modelling of VAWTs is attributed to Templin (1974). He used a single streamtube encompassing the entire turbine within which the momentum balance was calculated. The flow velocity within the streamtube was assumed to be uniform. Wilson and Lissaman (1974) assumed a sinusoidal variation in inflow velocity across the width of the turbine to account for non-uniform flow. In order to account for this effect more fully, Strickland (1975) extended the model so that the flow through the turbine is divided into multiple independent streamtubes. The momentum balance is carried out separately for each streamtube, allowing an arbitrary variation in inflow. Paraschivoiu (1981) allowed for the difference between the upwind and downwind passes of each blade by dividing each streamtube into an upwind half and a downwind half, in the

so-called 'Double Multiple Streamtube' (DMS) model. The momentum balance is carried out separately for each half of the streamtubes.

Two models have been found in the literature that apply momentum methods to the performance prediction of passive variable-pitch Darrieus turbines. This involves the added complexity of calculating the pitch response of the blades, which is both affected by and affects the flow velocity. The momentum model developed by Bayly (1981) is a two-dimensional model that predicts aerodynamic loads and blade pitch response. It makes a number of simplifying assumptions that are addressed in the current work. A single streamtube spanning the frontal area of the turbine is used, with a sinusoidal variation in flow induction factor across it, according to the method of Wilson and Lissaman (1974). The variation of streamwise velocity across the rotor is thus assumed a priori rather than calculated. Further, the use of a single streamtube does not allow any difference in flow velocity between the upwind and downwind passes of the blades. When the turbine is heavily loaded this simplification is no longer valid, as the flow is considerably decelerated by the time it reaches the downwind pass. Blade aerodynamic loadings are calculated using tabulated lift coefficients and centre of pressure locations measured under static conditions. Drag is calculated using an empirical expression, similarly for static conditions. Empirical corrections are made for the average Reynolds number and finite aspect ratio, but no attempt is made to take into account the difference between static and dynamic conditions. Also, since he only had data for angles of attack less than 20°, Bayly was unable to calculate performance at tip speed ratios less than three, which is the very area of interest for a self-starting turbine.

The instantaneous torque is taken to be the product of the tangential component of the aerodynamic forces on the blade and the radius of the turbine. No account is taken of the effect of the inertia of the pitching blade assembly on the reaction forces at the pivot. It will be seen that these forces, while integrating to almost zero over the course of a revolution at steady-state, may instantaneously be of the same order of magnitude as the aerodynamic tangential force.

Bayly comments on the problem of significant scatter in the experimental torque coefficient data. He attributes this principally to the fluctuating wind measurements that are used to non-dimensionalise the output torque. However he also suggests that "unwanted blade oscillations" may contribute to scatter. While the momentum model predicts steady-state blade pitch response, several revolutions are required to converge to steady-state from an arbitrary starting condition even in a steady wind. Accordingly he says

> "it seems logical then that the ever-changing speed and direction of the real wind would prevent a Cyclobrid turbine from ever reaching steady-state operation. Blade angles may be transiently favourable or unfavourable causing fluctuations in power coefficient."

This suggests the need to develop a mathematical model capable of examining the transient as well as the steady-state behaviour of this type of turbine.

Bayly further comments that the mathematical model predicts small amplitude high frequency oscillations superposed on the base pitch response. Previously Kentfield (1978) measured blade pitch response on a wind tunnel turbine by viewing a small protractor mounted on a blade under stroboscopic lighting, however such an approach was unable to detect high frequency oscillations. The existence of these oscillations could only be confirmed by the continuous measurement of

pitch angle as a function of azimuth. This task has been undertaken in the current work.

Kirke and Lazauskas (1992) developed a more sophisticated model of the Double Multiple Streamtube type. It incorporates flow velocity differences between upwind and downwind blade passes, flow curvature and dynamic stall. It is specifically designed to predict the blade pitch response for the control method shown in Figure 2.10. Kirke (1998) obtained reasonably accurate predictions of the performance of a 2 metre diameter turbine tested in a wind tunnel.

He also compared the results of the mathematical model with measured performance of a 6 metre diameter demonstration turbine based on the same principle operating in the field. He was unable to achieve the same level of agreement in this case, with the mathematical model significantly over-predicting the experimental results. He suggested a number of possible causes for the discrepancy, including underestimated parasitic drag and the difficulty of measuring the temporally and spatially fluctuating wind accurately, as reported by Bayly.

He suggests two further possible causes of discrepancy: the effect of the wake of the blades in the upwind pass on those in the downwind pass; and the effect of high frequency wind speed fluctuation. Neither of these effects can be accounted for by a momentum theory mathematical model, which predicts time-averaged performance. Kirke performed a simplified analysis of the effect of turbulence that indicated the potentially large influence of this factor on average performance. However a more complete investigation of this effect is only possible with an analysis tool able to deal with transient performance. This was the reason for the development of a vortex method for passive pitching turbines.

2.2.2 Vortex models

Vortex models are potential flow models based on the calculation of the velocity field about the turbine through the influence of vorticity in the wake of the blades. Discrete vortices are shed into the wake as the bound circulation at the blades changes in order to maintain total conservation of vorticity as dictated by Kelvin's theorem. The velocity field is the summation of the induced velocities of all vortex points, as calculated by the Biot-Savart law.

Early applications of vortex theory to Darrieus turbines were made by Larsen (1975), Fanucci and Walters (1976), and Wilson (1978). Both Larsen's and Wilson's models were applied to variable-pitch Darrieus turbines. Larsen studied what he termed a 'cyclogiro', in which the blades periodically flipped from a set positive pitch angle to a set negative angle and back each revolution. He used a simplified wake with only two vortices shed into the wake each revolution at the blade flipping points, and calculated an average velocity by which to convect the vortices downstream. Wilson (1978) analysed a 'giromill' with a preset schedule of pitch angle variation. He again used a simplified analysis in which the pitch angle was assumed to be varied to keep the circulation constant in magnitude, but flipping twice per cycle in sign, for each revolution. The steady state performance was calculated by representing the blade effect on the flow using circular vortex sheets on the blade orbit and straight sheets extending downstream from the transverse extremities of the orbit. The influence of these sheets on the flow at the blades could be calculated analytically.

Strickland et al. (1979, 1980, 1981) produced a more sophisticated vortex model for a fixed-blade turbine and compared results with instantaneous blade forces measured on a model turbine in a tow tank. Strickland incorporated blade stall using

published lift and drag coefficients, modified to account for unsteady aerodynamic effects including dynamic stall. He used a free wake in which the discrete vortices convect downstream with the free stream and under their mutual influence. The detailed account of the method given in the 1981 report was used as the basis for the implementation of the vortex model in the present work.

Strickland found that the major weakness of his method was in the calculation of the unsteady aerodynamic loads on the blades. His use of an empirical method derived for helicopter applications to modify published static lift and drag data was not able to capture all the details of the instantaneous blade loads measured in his experiment.

Wilson et al. (1983) abandoned the use of aerofoil coefficient data and used an analytical method, mapping the aerofoil onto the circle plane, to calculate aerodynamic forces. They coupled this method with a standard free vortex wake representation. This method however only deals with attached flow and so does not handle stall.

The complexity of the flow around a blade in Darrieus motion has prompted recent efforts to apply computational fluid dynamics approaches to the problem. Allet et al. (1999) modelled the flow about a rotating Darrieus blade using a finite element method to solve the Reynolds-averaged Navier-Stokes equations. Ponta and Jacovkis (2001) solved the 'constant-curl Laplacian equation' for the flow in the vicinity of the blade using the finite element method. Such methods are very demanding in terms of computation time, and it was felt that due to the added requirements of calculating blade pitch motion, the use of such methods in the current case was not realistic. Instead semi-empirical unsteady aerodynamics

treatments were used, despite their limited ability to model this highly complex phenomenon.

Work on 'fixed-wake' or 'prescribed-wake' vortex models has been performed by Wilson and Walker (1983) and Jiang et al. (1991). These methods aim to reduce the computational expense involved in calculating the induced velocity at every vortex point due to every other vortex point at each time step by assuming a fixed wake geometry and incorporating momentum theory to assist in calculation of the convection velocity. Such methods were not pursued in the present work as the greatly increased computing power available now was judged to render the effort not worthwhile. Similarly time-saving techniques such as the 'vortex-in-cell' method described by Baker (1979) and implemented by Vandenberghe and Dick (1986) were not used.

The extension to existing Darrieus vortex models developed here is the capacity to calculate the pitching motion of all the blades under the influence of the aerodynamic forces. No previous effort to do this has been found in the literature.

2.2.3 Summary

Numerous designs of passive variable-pitch Darrieus turbines have been conceived, but most lack rigorous theoretical grounding or experimental validation. The most thorough existing works in the field were produced by Bayly (1981) and Kirke (1998). These authors have produced momentum type mathematical models to predict the performance of their own specific design of passive variable-pitch turbine.

In order to examine the issue more generally so that different designs may be compared and new designs tested, a model that allows for different methods of pitch control is required. This has been produced in the current work. Each of

these authors also commented on the need to examine the transient behaviour of their turbines as a suspected cause of discrepancy between theoretical results and field experimental data. For this purpose, a vortex type mathematical model has been extended to deal with passive variable-pitch turbines.

Chapter 3

Passive Variable-Pitch Design Concepts

3.1 Introduction

Given the variety and complexity of the existing passive variable-pitch designs reviewed in Chapter 2, it was desired to assess the relative merits of different existing designs in a systematic manner. The common elements of existing passive variable-pitch designs were identified as:

- Provision of a rotational 'pitch' degree of freedom for each blade;
- Reliance on aerodynamic forces acting on the blade to produce changes in the blade pitch angle to reduce angle of attack;
- Provision of some regulating or moment about the pitch axis to produce pitch response of the appropriate phase and amplitude for improved performance.

Taking this arrangement as a starting point, the desirable nature of the regulating moment was investigated to assess which of the designs was most suitable for achieving self-starting and if a new design concept could be produced for improved performance.

Each blade was regarded as a rotating mass / torsion spring / damper system. The torsion spring was regarded as completely general, providing a restoring moment on the blade whose magnitude was some function of the blade pitch angle

and the turbine speed. These two quantities were chosen as they can be sensed directly and therefore passively. Speed, or more specifically the square of the speed, is sensed as centrifugal force.

The evaluation and conceptual design process then involved three steps:

- To determine the nature of desirable pitch response and its variation with tip speed ratio;
- To determine a suitable relationship between blade pitch, turbine speed and restoring moment for the 'spring' to best approximate such a pitch response;
- To identify a design that can approximate this relationship, based on the orientation of the blade relative to the rotor arm, the centrifugal load reacted at the blade connection and the aerodynamic forces acting on the blade.

Certain features of Darrieus turbine operation may be identified without any mathematical model. By the nature of the vector addition of free wind and blade velocity, the amplitude of the oscillation in angle of attack on a fixed blade reduces with increasing tip speed ratio. This was illustrated in Figure 1.7. At sufficiently high tip speed ratios (TSRs) the amplitude of the oscillation is small enough that the stall angle of the blades is never exceeded. It is at these speeds that the standard Darrieus turbine operates. While the ability to vary pitch enables stalling to be reduced at lower tip speed ratios, as explained in Section 1.4, at high tip speed ratios no pitching is desirable as any pitching reduces the angle of attack below stall so that lift is reduced. Thus the desired amplitude of pitch response reduces with tip speed ratio until it almost is zero at design running speeds.

The magnitude of driving aerodynamic pitching moment about the pivot axis depends on the strength of aerodynamic forces, which are proportional to the square of the relative flow velocity. As tip speed ratio increases, the relative flow

velocity at the blade becomes almost proportional to the rotational velocity of the turbine. Thus the magnitude of the aerodynamic moment, which seeks to reduce the angle of attack, is approximately proportional to the square of the turbine speed. As was mentioned in Chapter 2, almost all the documented passive variable-pitch turbines used some form of regulating moment to balance the aerodynamic loads that move the blades. In order to keep the motion of the blade in phase with the variation in angle of attack, a restoring moment, such as a torsional spring, is applied to the blade to move it always back toward the angle at which the blades of a standard Darrieus turbine are fixed.

Figure 3.1 illustrates a number of design concepts for passive variable-pitch turbines. Figure 3.1(a) shows the general mass/spring/damper arrangement that all designs were regarded as in essence.

The designs of Bayly & Kentfield (Figure 3.1(b)) and Kirke & Lazauskas (Figure 3.1(c)) employed inertial loads to play the role of the torsion spring in providing restoring moment. By their nature, the magnitude of this restoring moment is proportional to the centripetal acceleration, and so relates directly to the square of the turbine speed. Thus the ratio of the magnitudes of the driving aerodynamic moment and the restoring inertial moment remains relatively constant over the entire speed range. The demonstrated potential of these two designs made the square law relationship between restoring moment and speed the starting point for evaluation in this study.

It was then examined whether deviations from this basic relationship might yield improved performance. Specifically it was suspected that greater control at high tip speed ratios was required to effectively lock the blade and prevent pitching, without compromising starting performance.

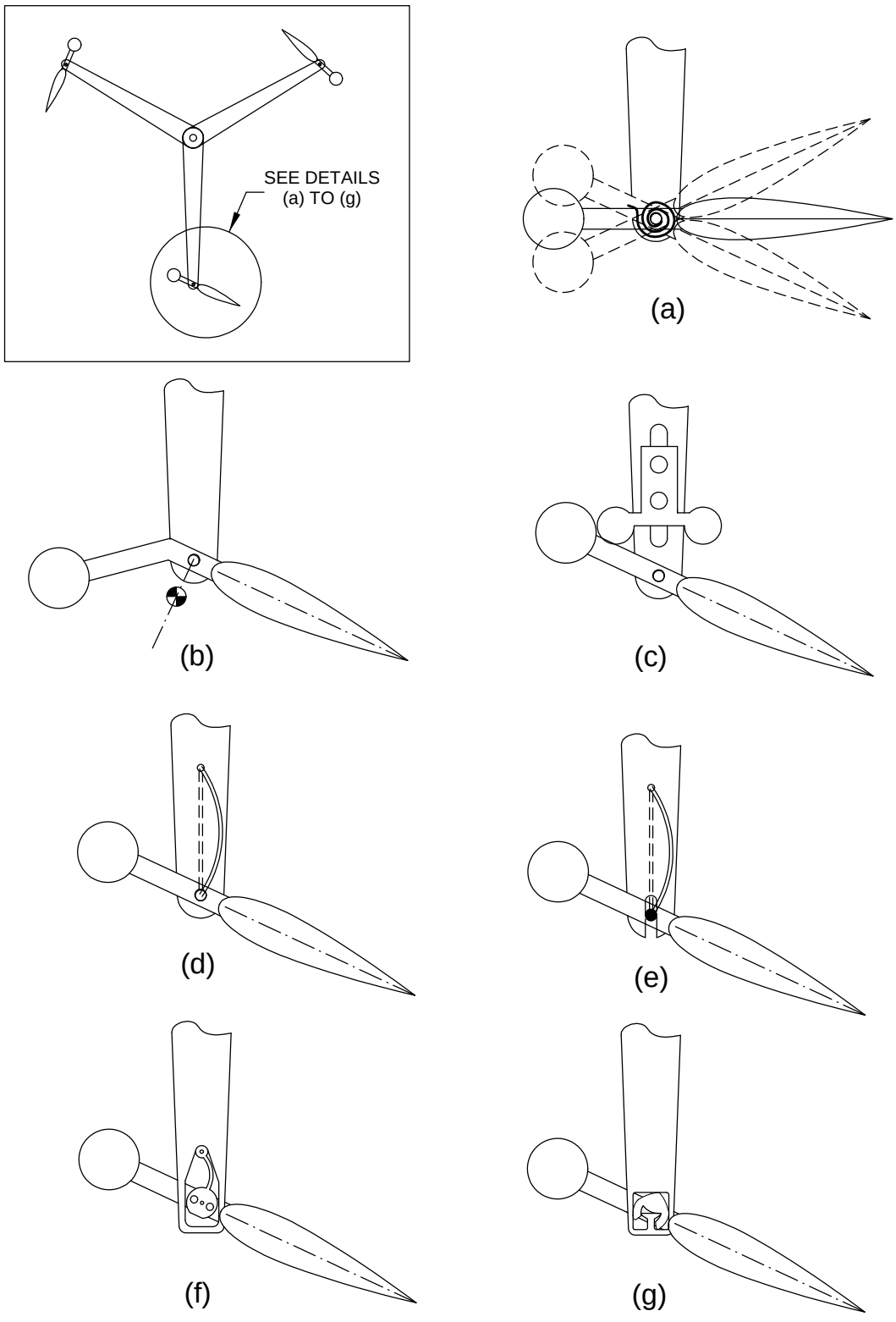

Figure 3.1: Passive variable-pitch design concepts

3.2 Elastomeric Pitch Control Concept

3.2.1 Origin of concept

The above reasoning led to the idea of designing an elastic type pitch regulation whose stiffness increased with centrifugal force. The concept differs from that of Brenneman's elastic design, shown in Figure 3.1(d), by making the radial centrifugal load be taken through the spring itself, rather than by a bearing. This is done by removing the radial constraint on the axis of the blade, while retaining the tangential constraint, as shown in Figure 3.1(e). The torsional stiffness of the elastic part can then increase with the centrifugal load. The idea of designing a mounting piece made from an appropriate elastomer and shaped to produce the desired stiffening effect was conceived. By constraining the piece within a radial slot, tangential loads can be transmitted to the rotor without affecting the blade pitch. As speed increases, the elastomeric piece stretches, progressively stiffening in the torsional sense, until it makes contact with the flat end of the slot, at which point further pitching is prevented. This allows the turbine to function like a standard fixed-pitch Darrieus turbine at running speed. This concept is illustrated in Figure 3.1(f).

The concept relies upon the ability to design the flexible blade mounting part to achieve the desired relationship between radial load and torsional stiffness. Both the material and the geometry of the part can be tailored to achieve this.

Initially a geometry with two curved members coupling the mounting pin with the blade was envisaged. At low speed, pitching of the blade would occur primarily through bending of the curved members. As speed increased and the tensile load arising from centrifugal force increased, the curved arms would straighten. This would mean that pitching would require stretching of the arms, rather than

bending, which would provide greater resistance. As centrifugal force increased further, the end of the elastomeric part would eventually make contact with the radial end of its housing, preventing further pitching. This, conceptually, fulfills the required trend of increasing torsional stiffness with increasing speed, and the prevention of pitching at design running speeds.

Concurrent with this work, a finite element analysis of possible geometries for an elastomeric blade mount was conducted at the University of New South Wales by Azim (2001). The highly non-linear nature of the problem made the analysis difficult, however he concluded that progressive torsional stiffening of an elastomeric part is possible. As a result of his investigation Azim recommended that the elastomeric mounting part have a curved end profile. This would allow a more gradual torsional stiffening after the mounting part had stretched to make contact with the end of its housing. Once contact is made, as centrifugal loads rise the load taken through compression increases while the tensile load remains fairly static. He modelled this further stiffening as arising from progressive compression of the elastomer, resulting in a contact patch whose area increased with centrifugal load. He states that

> "The profile of the base of the mount is very critical when the compressive forces dominate. This profile can be used to tailor the response of the mount..."

These recommendations were incorporated into the design process for the geometries that were tested on the wind tunnel prototype turbine. These are discussed in Section 3.4.

The appeal of this design concept is the potential to tailor the pitch response of the blades more generally than can be achieved with a purely 'inertial' design. The

response of the blades and the performance of the turbine could be determined entirely through the geometry and material of the blade mounting part. Different geometries could be designed for different wind speed regimes in different locations. The parts could be easily and cheaply manufactured and replaced. They also would remove the need for rotating element or journal bearings and offer greater simplicity than is achieved by most existing designs.

All of this however relies on the ability to arrive at a geometry and material that produces the desired pitch response.

3.2.2 Initial geometry testing

Experimental work was conducted on an initial test geometry. A rig was constructed to allow loading of a blade mounting piece simultaneously in tension and torsion.

The initial geometry chosen for testing is shown in Figure 3.2. It featured two curved arms designed to straighten and stiffen with increasing tensile load. It had two holes through which the blade spars were to pass. They were not symmetrical about the centreline of the elastomeric part in order to accommodate the offset of the blade. It was intended that the leading edge of the blade would be located near to the centre of the elastomeric part. Two spars protruding from the end of the blade, one of 20 mm diameter and a 10 mm dilater pin near the nose, would transmit force and moment to the elastomeric mounting part. The blade would be balanced so that the centre of mass lay on the centreline of the elastomeric part.

The part was made at full scale for the prototype turbine being designed and was 15 mm thick. It was made from soft 60 durometer polyurethane, cast in a hard polyurethane mould. The mould was made by casting about a master copy NC milled in High Density Polyethylene (HDPE). This technique is simple

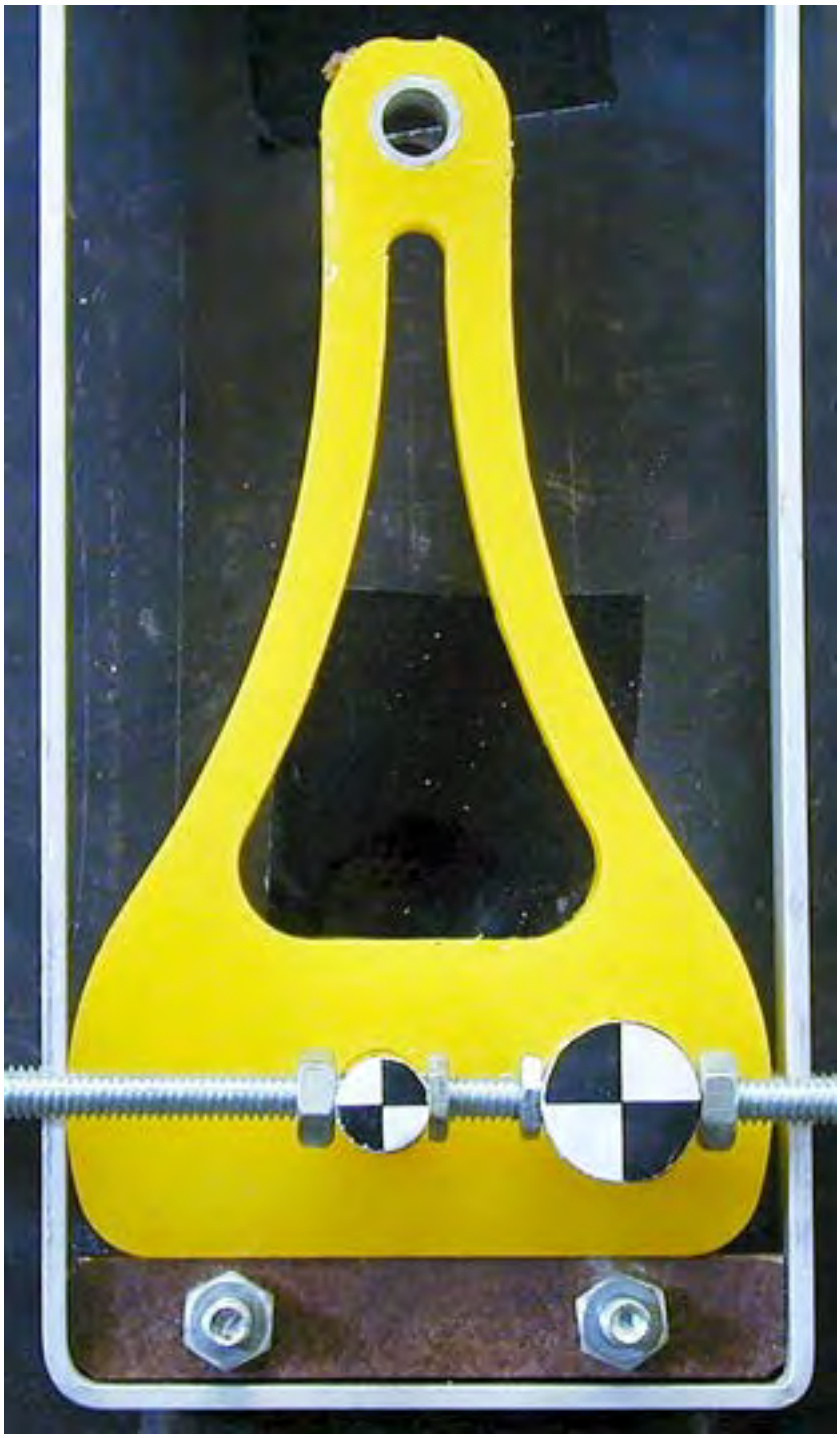

Figure 3.2: The initial elastomeric test piece

and inexpensive and produces parts of acceptable dimensional accuracy for this purpose.

Masses were suspended from a crossbar attached to two pins representing the blade. Different masses and positions on the crossbar were used to produce different total tensile load and moment about the centre point.

The results for five tensile loads are shown in Figure 3.3. Applied moment about the centre point is plotted against the resulting angular deflection. The following conclusions can be drawn from the results:

- Stretching around the spar holes in the elastomeric piece caused asymmetry in the results. The offset angle under zero moment became increasingly negative as tensile load was increased.
- The elastomeric component was not stiff enough in tension. While torsional stiffness was of the right order, the part stretched excessively in tension, resulting in contact being made with the end of the housing at a load of only 58.8 N. This corresponds to a turbine speed of approximately 40 rpm, or a tip speed ratio of approximately 0.6 in a wind of 7 m/s.
- No appreciable torsional stiffening occurred with increasing tensile load prior to contact being made with the end of the housing. The geometry of the part failed to deliver the progressive stiffening in tension that was intended.

Because stiffening was only evident as a result of compression in the elastomeric part, a further set of measurements was taken with no initial clearance between the part and the end of the housing. This was designed to examine the purely compressive behaviour of the piece. The results are shown in Figure 3.4.

Asymmetry in the results is clearly visible. Not only does a zero offset angle develop under zero moment with increasing compressive load, but the slope of the moment-angle curve is different under positive and negative moments.

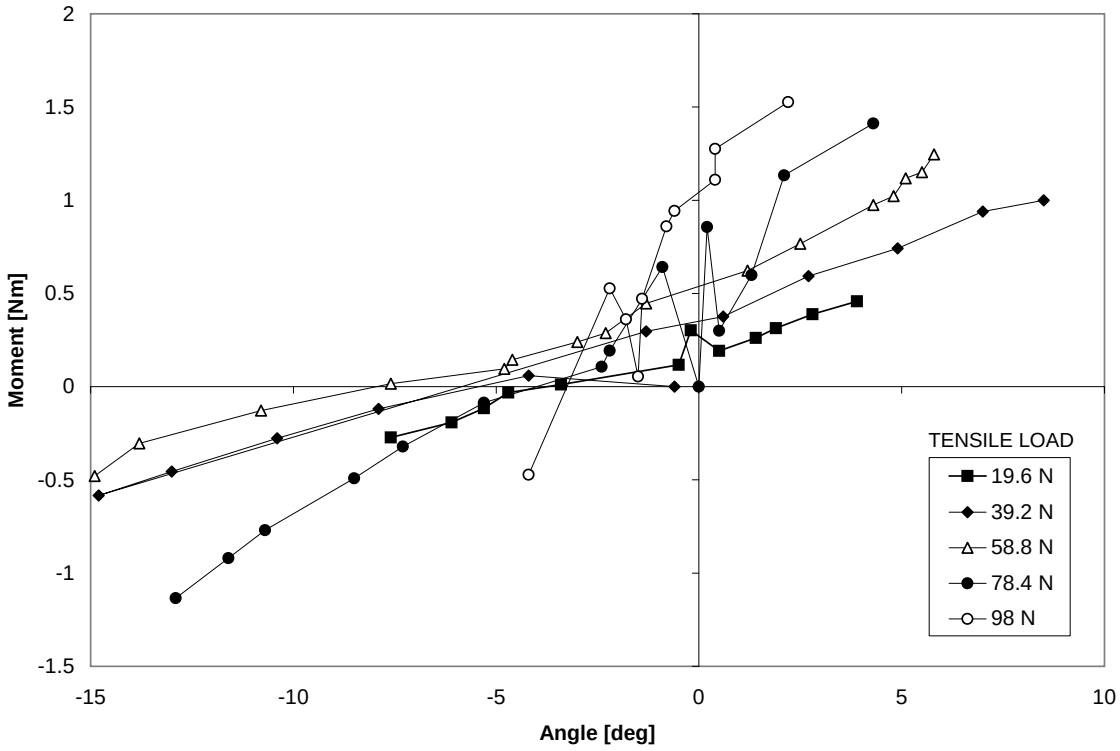

Figure 3.3: Results of testing of initial geometry

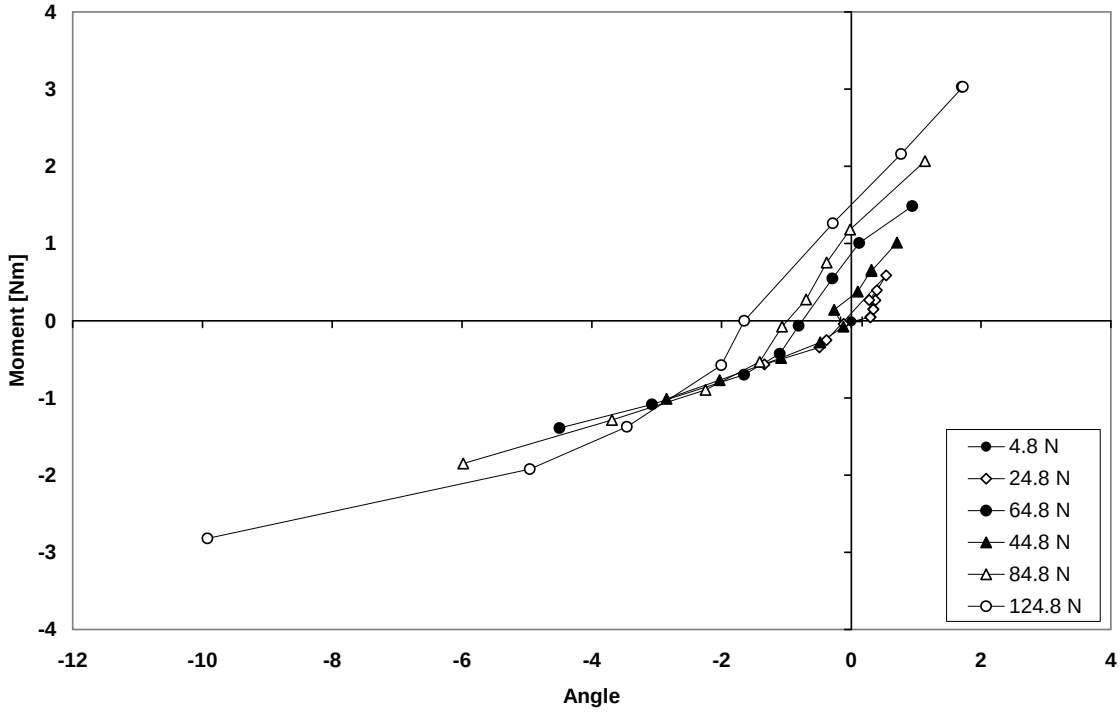

Figure 3.4: Results of testing of initial geometry in compression only

There is also no significant torsional stiffening with increasing compressive load. It seems that torsional stiffening is only available with this geometry as a status change, from purely tensile loading to combined tensile/compressive, when the part makes contact with the end of its housing.

These tests also made it clear that it would be difficult to achieve the low torsional stiffness needed at start up with the tensile stiffness needed to delay contact with the end of the housing until a suitably high running speed. If compressive contact is made at too low a speed pitching is inhibited when it is still required for self-starting to occur.

3.3 Rolling Profile Pitch Control Concept

3.3.1 Origin of concept

The results of the experimental work described in Section 3.2.2 and the finite element analysis by Azim (2001) lead to a focus on the outer radial portion of the mounting part and its behaviour under compression.

The conclusion that the end should be rounded rather than square, so that pitching was not halted immediately on contact, lead to the idea of using the exact shape of the end to dictate the pitch response. A rounded end would allow the blade to pitch by 'rolling'. It was realised that the curvature of the end profile would determine the amount of pitching that was permitted, even in the absence of any elastic constraint. As the profile tends toward a straight line, the resistance to pitching increases.

3.3.2 Derivation of mathematical basis

Referring to Figure 3.5, consider a two dimensional body with a curved convex end profile in the vertical plane, in rolling contact with the ground under the influence

of gravity. In the absence of external forces, the body will seek an equilibrium position with its centre of mass, the contact point with the ground and the local centre of curvature all lying on a vertical line. So long as the mass centre is below the centre of curvature, the body will roll back to this position from a disturbance. Accordingly, in order to maintain equilibrium at some other angle, an applied moment is required. For a general profile as shown in Figure 3.5, the magnitude

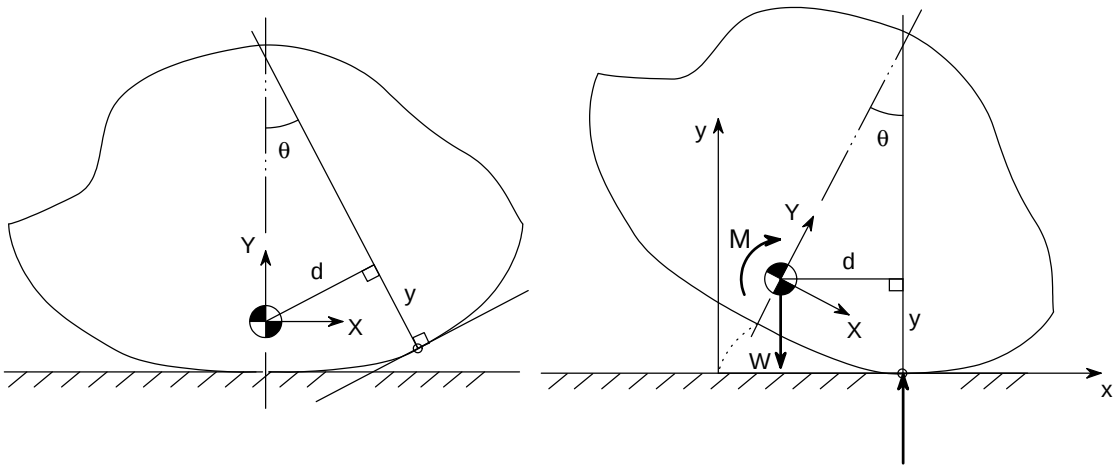

Figure 3.5: Rolling profile concept

of the moment M is proportional to the weight force W and the horizontal offset, d, of the mass centre from the normal through the point of contact. The moment M required to maintain a given angle θ (defined as the angle between the contact point normal for $M = 0$ and the current contact point normal) is therefore a function of the geometry of the profile. This profile can then be generated relative to the mass centre to produce a desired relationship between the applied moment and the resulting equilibrium angle. This is analogous to a torsion spring whose stiffness characteristic may be non-linear, can be tailored precisely and need not be symmetrical about its undisturbed position.

The method of generating the required profile for a specified moment-angle relationship is then required. A coordinate system attached to the profile body

with origin at the mass centre and X- and Y-axes parallel and perpendicular to the ground surface respectively when the profile is in the neutral position is defined, as shown in Figure 3.6. The final goal is a description of the required profile in the Cartesian X-Y coordinates. However the profile is most simply specified in terms of the three coordinates θ, d and y shown in Figure 3.6. θ is the disturbance angle from the neutral position. d is the 'horizontal' or distance parallel with the ground from the mass centre to the contact point. y is the 'vertical' or normal distance of the origin from ground at the given disturbance angle θ. Any combination of θ, d and y specifies a point in the plane. The profile curve is described parametrically in terms of d and y, taking θ to be the parameter.

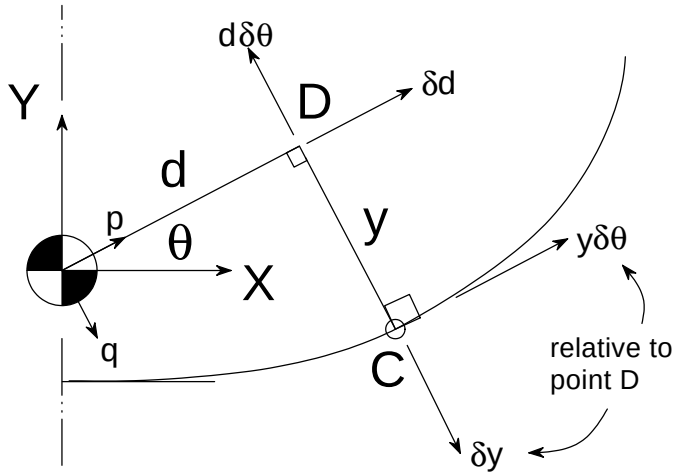

Figure 3.6: Derivation of profile. The infinitesimal displacements of the point C are shown in terms of variation in the d, y, θ coordinates.

Since for a given weight force the restoring moment at a given disturbance angle θ is proportional to d, the chosen relationship between restoring moment and θ, $M(\theta)$, may be treated as a relationship between d and θ. The input to the process is then a function of the form:

$$d(\theta) = \frac{M(\theta)}{W} \tag{3.1}$$

It then remains to find the appropriate variation of y with θ to make the profile smooth and continuous, with the tangent at any angle θ to the X-axis meeting the curve at the required distance d from the origin. Referring to Figure 3.6, consider a coordinate system p-q at the X-Y origin, rotated so that the angle between the X-axis and the p-axis is θ_c. The required contact point for the angle θ_c is at $p = d(\theta_c)$, $q = y(\theta_c)$ and the tangent to the curve must be parallel with the p-axis. This is achieved by satisfying:

$$\left.\frac{\partial q}{\partial \theta}\right|_{\theta_c} = 0 \tag{3.2}$$

From Figure 3.6 it is seen that

$$\delta q = \delta y - \delta\theta d \tag{3.3}$$

Dividing Equation (3.3) by $\delta\theta$ to produce a differential equation, the required function for y is seen to be:

$$\frac{\partial y}{\partial \theta} = \frac{\partial \theta}{\partial \theta} d$$

or

$$\frac{\partial y}{\partial \theta} = d(\theta) = \frac{M(\theta)}{W} \tag{3.4}$$

The required profile is thus defined by a simple differential equation. There is a family of parallel curves that satisfy the equation for any given function $M(\theta)$. A specific profile is determined by the choosing a value of $y_0 = y(0)$.

If the moment-angle function $M(\theta)$ is analytic and integrable, then the profile may be found analytically, else it may be generated numerically. Once the function $y(\theta)$ is found and y_0 chosen, the Cartesian coordinates of the profile may be easily

extracted:

$$X(\theta) = d(\theta)\cos\theta + y(\theta)\sin\theta \tag{3.5}$$

$$Y(\theta) = d(\theta)\sin\theta - y(\theta)\cos\theta \tag{3.6}$$

3.3.3 Application of concept to wind turbines

This concept is employed to govern the motion of the blades of the turbine. This is illustrated in Figure 3.1(g). The design utilises a profile attached to each blade that rolls on a flat vertical surface that is part of the rotor. This surface is tangential to the circular path of its midpoint. The blade assembly is free to move in a fashion determined by the rolling contact of the profile on the flat surface. Were

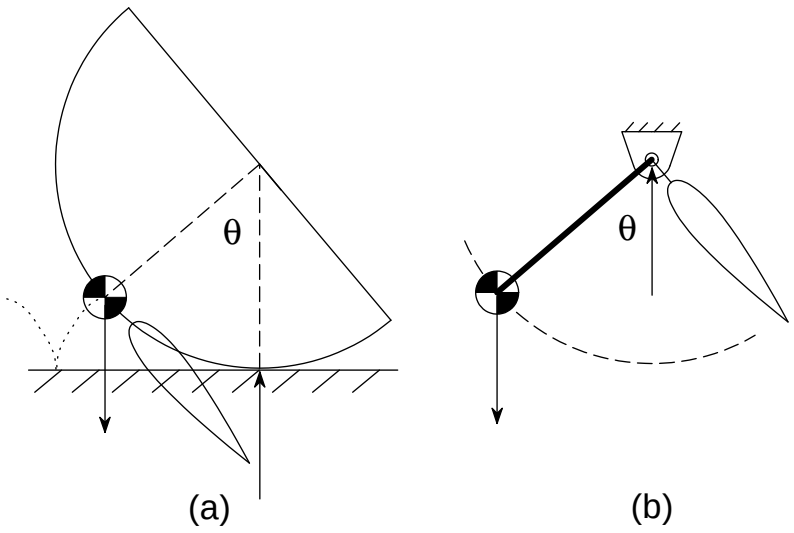

Figure 3.7: Comparison between rolling profile (a) and pendulum (b) concepts

the turbine to be spinning in a vacuum at constant speed, the blade would orient itself so that the centre of mass of the blade assembly lay on the radial line through the point of contact of the profile. Here centrifugal 'force' replaces gravity in the

original example. The shape and position of the rolling profile can be adjusted so that the blade assembly adopts the desired neutral orientation.

It may be noted that for application to the vertical axis turbine, the surface on which the profile rolls should ideally follow a circular arc with centre of curvature at the turbine axis, rather than being flat. However the small size of the arc subtended by the landing makes the difference negligible.

The restoring moment is a function of the separation between inertial force resultant and the reaction force. For a simple circular profile at constant rotational speed this separation is a function of $\sin\theta$, as it is for the pendulum design, as shown in Figure 3.7. Instead of the mass centre moving relative to the pivot axis in a circular arc as it does for the pendulum, with the rolling profile it is the contact point that does most of the moving. For a circular profile the mass centre's path relative to the rotor is a cycloid. The mass centre need not be located on the circumference of the profile itself. It is the distance from the centre of curvature to the mass centre that determines the restoring moment. The locus of the mass centre is then a general trochoid, whose form is determined by the value of y_0 (see Figure 3.8).

While the relationship between d and θ, and therefore the restoring moment under static conditions, is unaffected by the value of y_0, the dynamic response of the profile body is significantly affected. For the pendulum type design (Figure 3.7(b)), the mass centre is constrained to move in a circular arc centred on the pivot axis. This case is equivalent to the limit of the circular rolling profile with the offset y_0 equal to the negative of the mass centre radius, giving a rolling radius of zero. This is then an ideal pin joint. Pitching of the blade in this case involves a significant 'horizontal', or on the turbine, tangential, motion of the centre of mass.

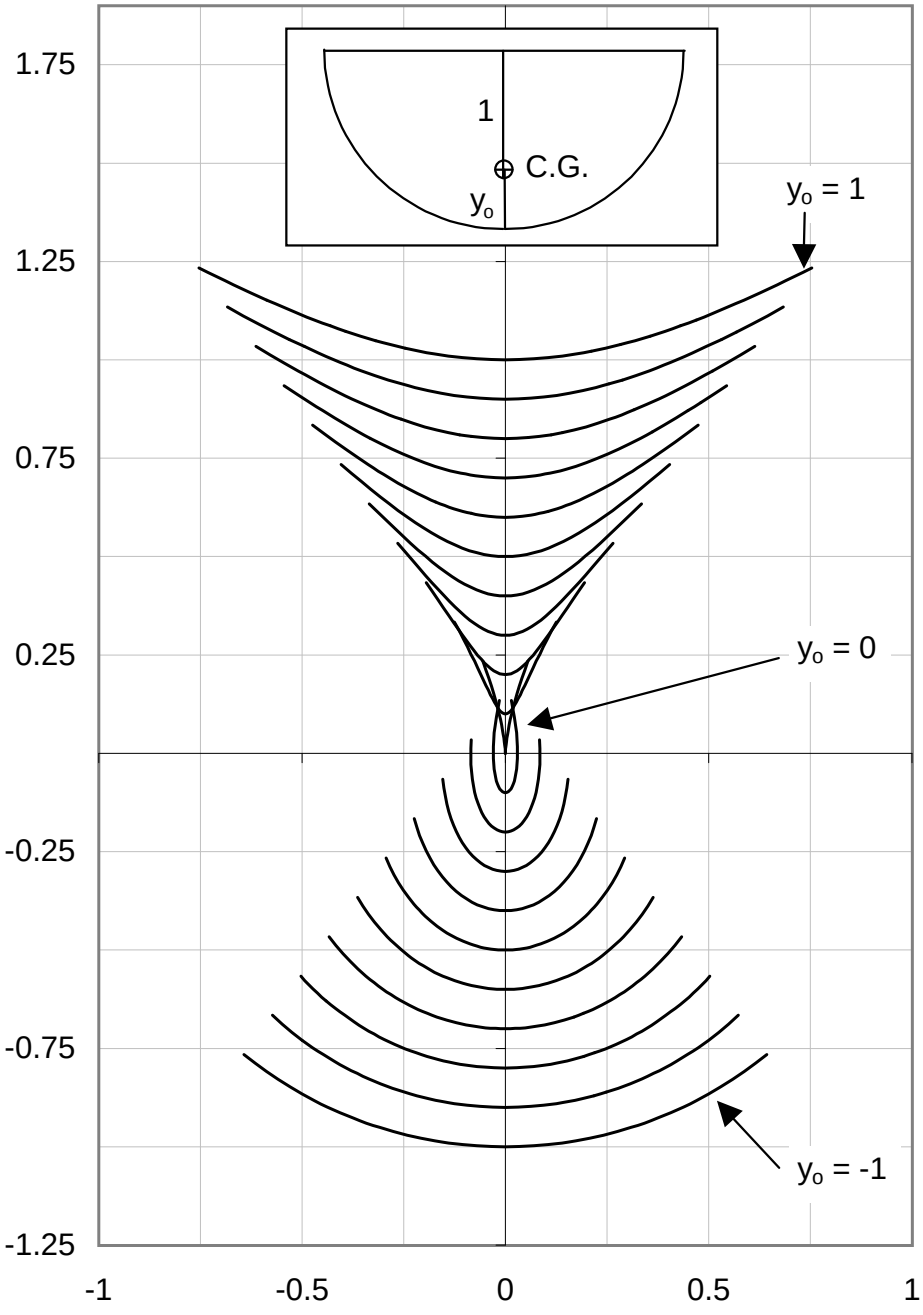

Figure 3.8: Variation with offset y_0 of the locus of the centre of gravity (C.G.) of the profile relative to the rotor. The C.G. is at unit radius. The general form of the loci for a circular profile is the trochoid, with the special case for $y_0 = 0$ being the well-known cycloid. The locus for the pendulum is that corresponding to $y_0 = -1$, which gives zero rolling radius, or a pin joint. All loci are for the disturbance angle range $\pm 40°$.

The inertial effect of this motion is reflected in the polar mass moment of inertia relative to the pivot axis, which increases with the square of the offset of the mass centre. The corresponding circular rolling profile offering the same static restoring moment, but with offset $y_0 = 0$, is able to greatly reduce the tangential travel of the mass centre. Note however that the radial travel is the same.

The tangential component of aerodynamic force on the blade is transmitted principally through friction between the cam and the flat surface on which it rolls. The radial centrifugal force on the blade is several orders of magnitude greater than the tangential aerodynamic force at running speeds, so a large coefficient of friction should not be required.

It is possible however to constrain the profile tangentially using its housing within the end of the rotor arm. The profile may be made to roll on a flat 'landing' on a radial post, as shown in Figure 3.9(b). If the width of the landing is made equal to the arc length of the profile over the chosen angular range, then the edges of the landing may be used to constrain the profile radially. As shown in Figure 3.9(a), the ends of the landing trace out on the profile body involutes to the profile curve. If the profile part is designed with extensions following these involutes, its tangential position is always constrained for no-slip rolling contact. There must be slip between the edges of the landing and the profile part, so the edges must be slightly rounded to accommodate this.

Alternatively, or in addition, the tangential constraints may be provided on the outer surfaces by making them offset a constant distance from the inner involutes. This means the profile part is able to be constrained between the parallel sides of the housing, against which it has to slide as pitching occurs. A careful choice of materials is required to allow such sliding without excessive friction and wear.

The radial location of the part may also be constrained using the housing. This may be necessary at start up where there is no centrifugal load to keep the rolling profile on the landing. Care must be taken with the design of the geometry to ensure that jamming does not occur.

It is also possible to combine the rolling profile concept with the elastomeric concept. At start up there is little or no centrifugal force to provide restoring moment and performance may be improved by providing some elastic restoring moment. If this is of a constant stiffness and does not increase with centrifugal load, then at running speeds it will be insignificant compared to the centrifugal based moment.

The profile material may be a hard elastomer, such as the polyurethane used in the prototype, or perhaps steel or other metal, depending on the wearing and friction properties.

The possibility of incorporating an overspeed protection feature into the design remains. Some flexibility, either in the rolling part itself or its attachment to the blade would allow the blade to flare outwards at high speed, producing extra drag to slow the turbine.

3.3.4 Potential advantages

Reduced mass moment of inertia

Compared with other inertial type pitch systems, the rolling profile concept has the potential to allow a reduced mass moment of inertia of the balanced blade about its centre of mass. This is advantageous because it improves the ability of the blade to respond quickly to aerodynamic forces. This reduction can be estimated by representing the blade assembly as a combination of the unbalanced blade and the counterweight, each of which has a known mass and moment of inertia (see

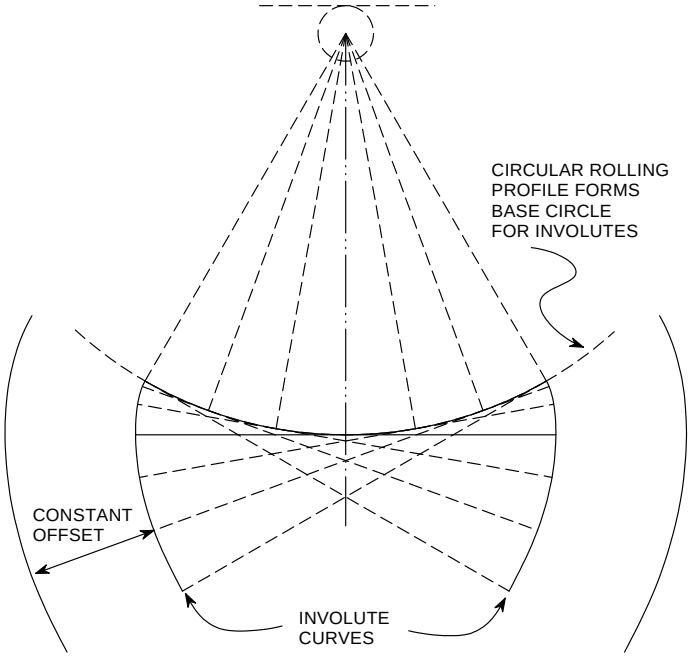

(a) Generation of profile involute curves

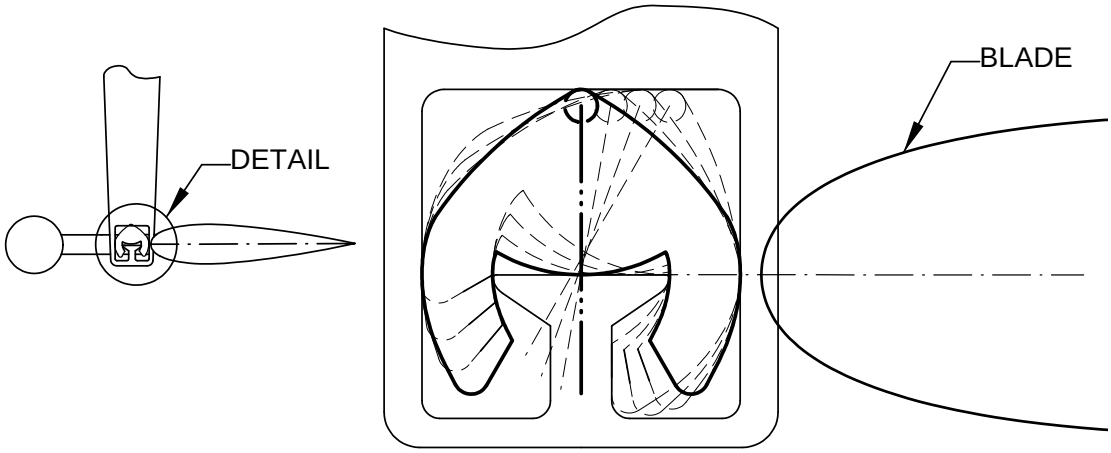

(b) Constraint of the rolling profile component (that is attached to the blade) using involute curves. The housing shown is within the end of the rotor arm.

Figure 3.9: Use of involute curves to provide tangential constraint for a circular rolling profile

Figure 3.10). The total mass moment of inertia about the pivot point is given by

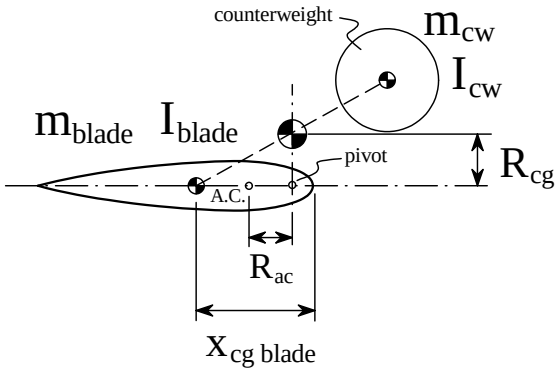

Figure 3.10: Calculation of the blade assembly moment of inertia

Equation 3.7.

$$I = I_{blade} + I_{cw} + \frac{m_{total}}{m_{cw}}(m_{blade}(R_{ac} - 0.25c + x_{cg_{blade}})^2 + m_{total}R_{cg}^2) \qquad (3.7)$$

where $x_{cg_{blade}}$ is the distance from the leading edge to the centre of gravity of the unbalanced blade.

For the pendulum design of Kentfield and Sicard, the moment of inertia that determines the pitching dynamic response is that about the pivot axis, found by the translation of axes theorem. For the rolling profile, the relevant moment of inertia is that about the contact point (this is discussed in detail in Appendix A). The inertia therefore changes slightly with the pitch angle and is a minimum when pitch is zero.

This means that for a circular rolling profile that produces the same restoring moment as a pendulum under static conditions, the inertia of the blade may be reduced because the counterweight is on the chord line, not offset from it. This allows the blade to respond more quickly to driving aerodynamic loads.

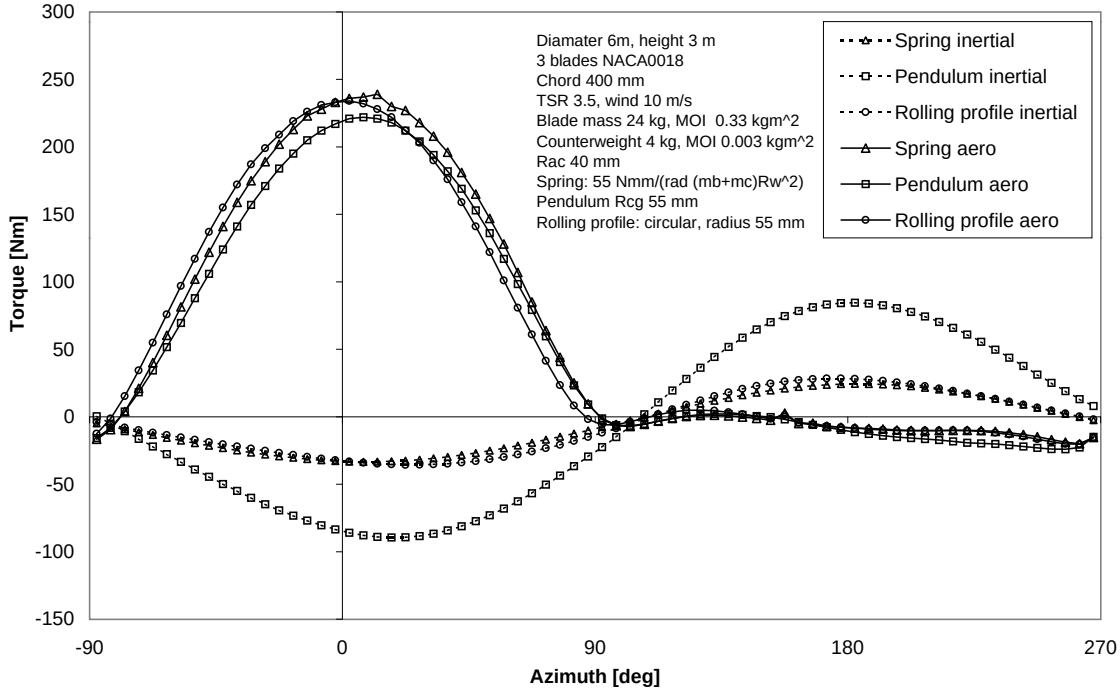

Figure 3.11: Comparison between the aerodynamic and inertial torque variation over a one blade's revolution for three different passive variable-pitch systems: spring, pendulum and rolling profile. All three have the same relationship between pitch angle and static restoring moment. Ta is the aerodynamic contribution to turbine torque. Ti is the inertial contribution due to the pitching blade, or due to the torsion spring.

Figure 3.11 shows the predicted torque variation for a blade for three different pitch control systems: a purely elastic, or torsion spring design; a pendulum type inertial design; and a rolling profile inertial design. All three are arranged so that the offset between the aerodynamic centre and the nominal pitching axis is the same, as is the restoring moment for a given pitch angle under static conditions. The polar moment of inertia of the balanced blade about the pitch axis in each case was calculated from the mass and moment of inertia of the blade and the counterweight. In this case the moment of inertia of the spring and rolling profile blades about the centre of mass is 3.17 kgm^2, while for the pendulum design, the fact that the counterweight is offset from the chord line means that the moment of inertia is higher: 3.77 kgm^2.

The predicted pitch responses at this tip speed ratio are almost identical for the spring and rolling profile turbines. The response is slightly different for the pendulum design due to its higher moment of inertia. The aerodynamic contributions to the torque are therefore similar. For a turbine of this solidity at this tip speed ratio, virtually all of the torque is generated between azimuth angles of -90° and 90°, in the upwind pass of the blade.

The sinusoidal variation in the non-aerodynamic torque component reflects the sinusoidal pitch response. The amplitude of this torque component is largest for the pendulum design. In the case of the elastic system, the torsion spring that provides the restoring moment exerts a reaction torque on the rotor that is proportional to the pitch angle. The amplitude of this reaction is smaller than the inertial reaction of the pendulum blade because the mass centre is not offset from the pivot axis.

The predicted inertial reaction for the rolling profile system is lower than for the pendulum design in this case. Its amplitude is slightly higher than is predicted for the spring case. Here the offset y_0 has been set to zero so that the centre of mass lies on the circular rolling profile. Because the point of rolling contact rather than the centre of mass does most of the movement, the reaction forces are much lower. If some positive y_0 value were used, the inertial reaction amplitude would increase. The kinematics of the rolling profile concept are described in more detail in Appendix A.

Customisation of profile

The application of the rolling profile concept to the wind turbine also allows the response of the blades at different wind and rotational speeds to be tailored by the

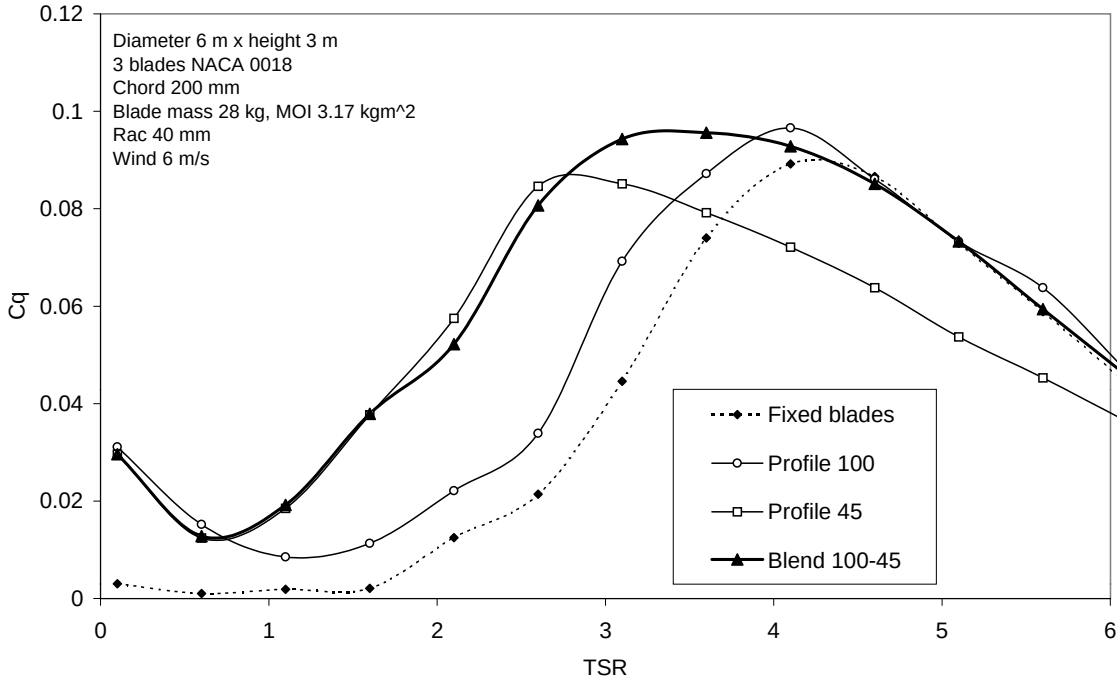

(a)Torque coefficient

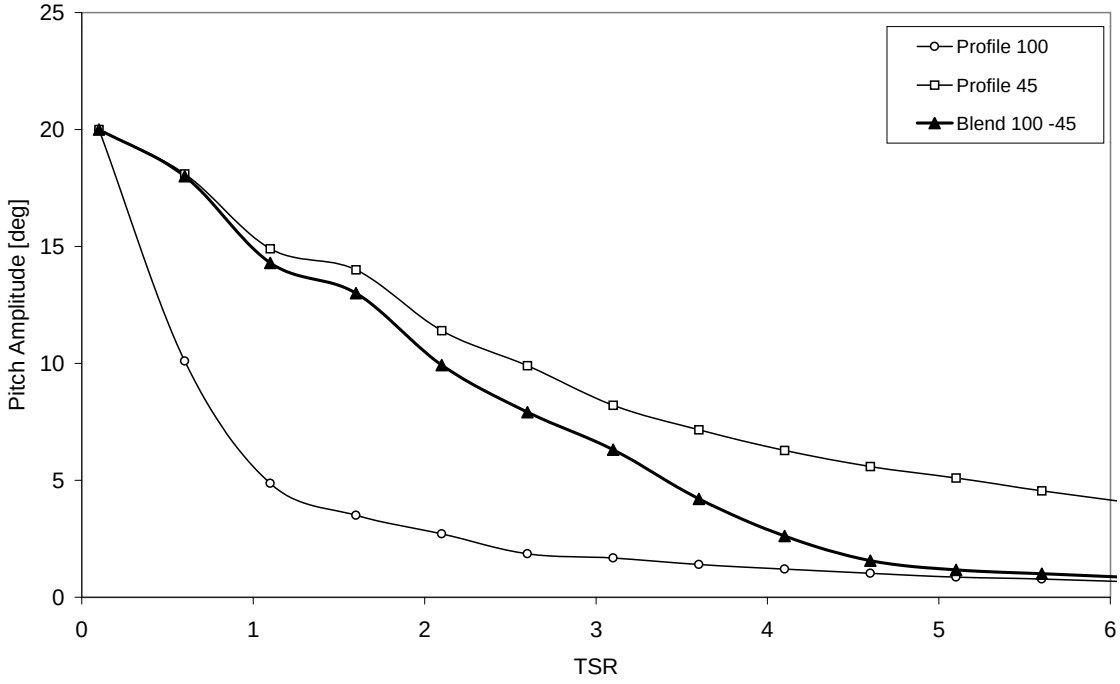

(b) Pitch amplitude

Figure 3.12: Example of predicted ability to tailor the rolling profile to produce different effective stiffness at high and low tip speed ratios

design of the profile. The stiffness may be made asymmetrical about the neutral position as it may be in Kirke's stabiliser mass design.

In addition there is the possibility of designing the profile to alter the response at different tip speed ratios. For example, if the region surrounding the 'nose' of the profile is flattened slightly, then the effective stiffness is increased over the range of a few degrees either side of the neutral position. This change can significantly affect the response of the blade at high tip speed ratios where the blade pitch amplitude is small, but has much less effect on the motion of the blade at slow speeds where the amplitude is large.

The performance predicted by the momentum theory mathematical model described in Chapter 5 for such a profile is shown in Figure 3.12(a). The predicted performance is shown for two rolling profiles which produce under static conditions a linear relationship between restoring moment and pitch angle. The 'stiffest' of these, labelled "Profile 100", produces a offset of $d = 100$ mm x θ. This profile is predicted to achieve the best peak efficiency at high tip speed ratios. This profile produces a pitch response whose amplitude diminishes rapidly with tip speed ratio, shown in Figure 3.12(b). The 'softest' profile, Profile 45, gives a greater amplitude at all tip speed ratios, resulting in improved intermediate speed performance, but significantly diminished peak performance.

The predicted performance for a profile that does not produce a simple linear relationship between restoring moment and pitch angle, but instead is 'stiffer' over the range of a few degrees either side of zero, is shown as "Blend 100-45". The blend profile is predicted to produce the best of the stiffest and softest linear profiles, combining the good intermediate TSR performance of Profile 45 with the good high TSR peak performance of Profile 100. The predicted pitch amplitude

for this profile is shown in Figure 3.12(b). The amplitude moves from being close to that for Profile 45 at intermediate TSRs to being almost equal to that for Profile 100 at high TSRs.

The $d - \theta$ relationship of the blend profile is shown in Figure 3.13(a), along side those of the two linear profiles. A relationship of the form

$$d = \frac{(K_1 - K_2)\theta}{(K_3\theta)^2 + 1} + K_2\theta \tag{3.8}$$

was used to blend between two linear relationships, where K_1 is the steeper slope, here 100 mm/rad, and K_2 is the lesser slope, 45 mm/rad. K_3 is a factor that controls the rate at which the blend between the two slopes occurs. Here K_3 was chosen by trial and error to be 40. This gives only a very small region either side of the zero pitch angle in which the slope is close to 100 mm/rad, before it diverges to asymptote towards the 45 mm/rad line. The form of this relationship was chosen because it is twice analytically integrable, allowing the equation of motion to be calculated.

The Cartesian coordinates of the profile can also be calculated analytically. The profiles for the two linear relationships and the blend are shown in Figure 3.13(b). This shows that the difference between the blend profile and the 45 linear profile is very small, only a fraction of millimetre. The magnitude of the difference in the performance predicted for such a small difference in the profiles is very surprising. It remains to be seen whether in reality performance is as sensitive to profile geometry as is predicted. It is possible that in practice, deformation of the profile around the contact point and any wear of the profile would have a significant impact on the blade pitch response. Some discussion on this point is given in Chapter 10.

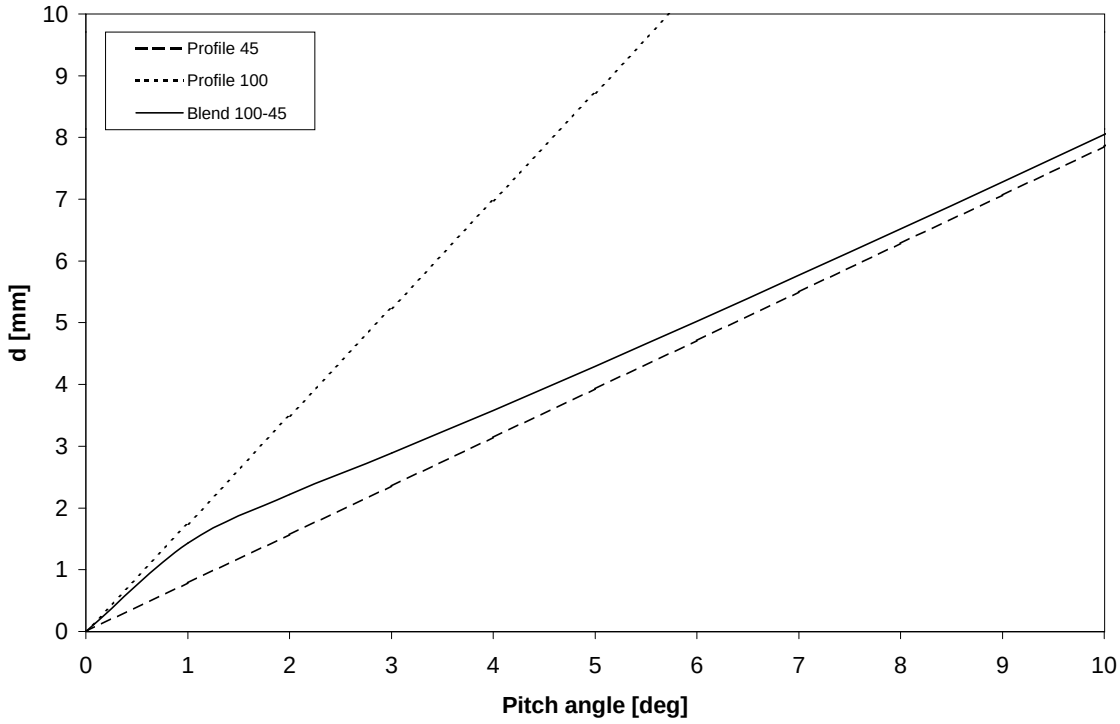

(a) $d - \theta$ relationships

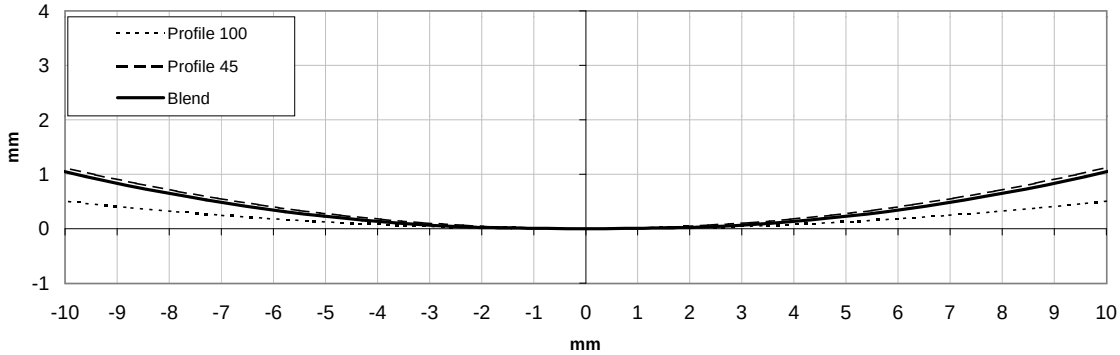

(b) The corresponding rolling profiles

Figure 3.13: Comparison of the $d - \theta$ relationships for the two 'linear spring' profiles, labelled Profile 100 and Profile 45 and the 'blend' profile with $d = \frac{(100-45)\,\theta}{(40\,\theta)^2+1} + 45\theta$ mm

3.4 Experimental Work

Three new geometries were designed on the basis of the initial experimental results, the recommendations of Azim (2001) and the rolling profile design concept described above. They are shown in Figure 3.14.

The first was designed along the same lines as the initial geometry and manufactured in the same grade of 60 durometer polyurethane, but modified to rectify some of the shortcomings observed.

- The blade design was modified so that equal-sized spars that were symmetrical about the centre of mass were used. This allowed the elastomeric mounting part to be made symmetrical about its centreline, eliminating the problems of asymmetry noted earlier. This required significant modification to blade design. An endplate was added that allowed the forward spar to be placed outside the blade section profile.
- The two curved arms of the original design were replaced with a single stem at the centreline. This produced a lower sectional moment of inertia and so lower bending stiffness for the same cross sectional area. This was an attempt to minimise the torsional stiffness while maximising the tensile stiffness.
- The end of the part was made curved instead of flat. This was designed to produce a more gradual stiffening once end contact did occur, by providing a contact patch that grew as the compressive load increased.

This geometry is hereafter referred to as 'Type A'. It is shown in place on the turbine in Figure 3.15 and in the test rig in Figure 3.16.

The other two geometries were based on a combination of the elastomeric and rolling profile concepts described above in Sections 3.2 and 3.3. They were made from a harder grade of polyurethane, of 90 durometer hardness, than the Type A

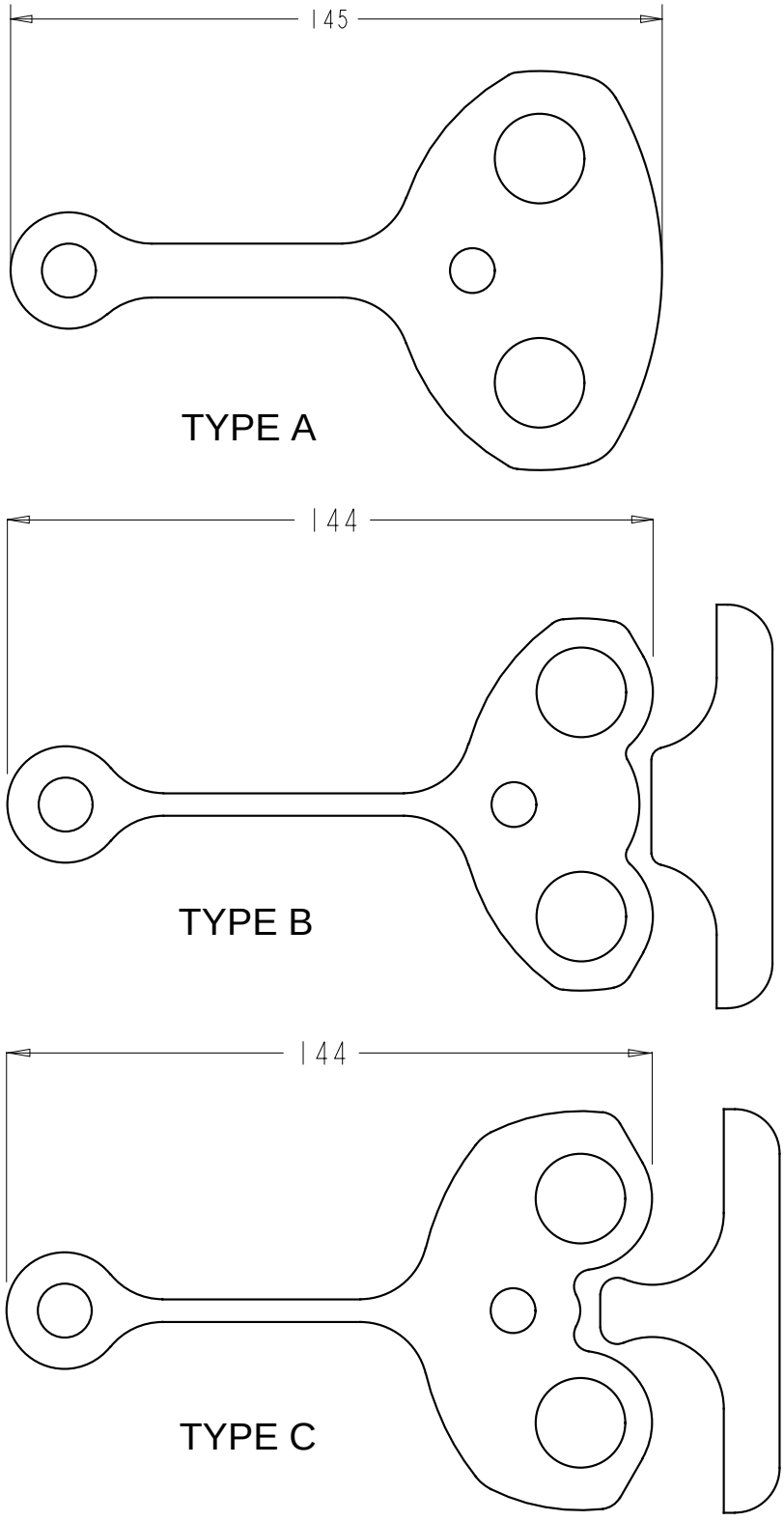

Figure 3.14: The three second-generation blade mounting part geometries.

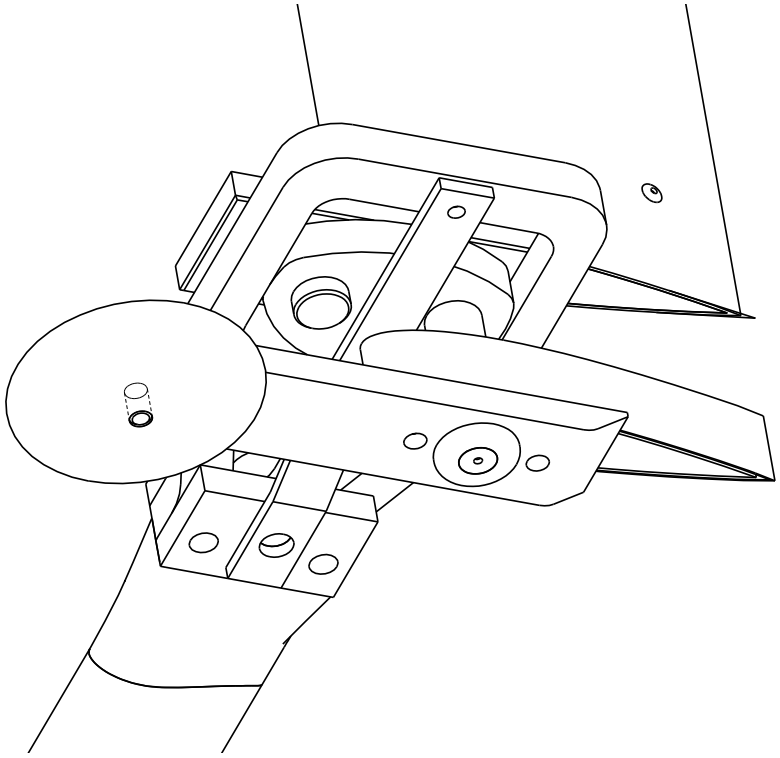

Figure 3.15: Pro/ENGINEER representation of the Type A geometry component in place on the prototype turbine.

part. Both feature a thin flexible 'stem' to provide elastic resistance to pitching. Each also has a rounded 'nose' part designed to provide further restoring moment through centrifugal force by rolling on a flat surface, as described in Section 3.3. They were designed to test the rolling profile concept.

For simplicity, each had a circular profile with an offset between the location of the centre of mass of the blade assembly and the centre of curvature of the profile of 7 mm. This value was chosen on the basis of mathematical modelling. The geometry labelled 'Type B' had a y_0 value of 13 mm, giving a radius of curvature of 20 mm for the profile. The 'Type C' part had $y_0 = 0$, for a radius of curvature of 7 mm. Each part should, according to the theory, provide the same static restoring moment for a given pitch angle, but the different y_0 values should produce different dynamic results.

Each was designed with a special mating part that was fastened to the end of the housing to provide the landing on which the profile rolled. These parts were manufactured in 95 durometer polyurethane.

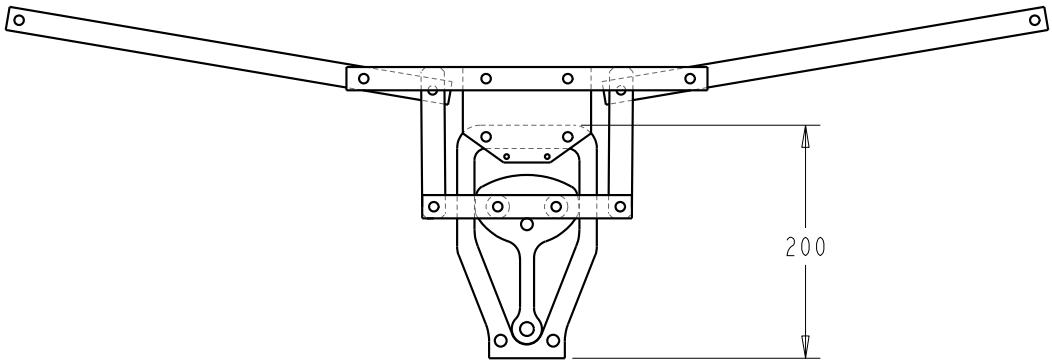

Figure 3.16: Test rig for elastomeric blade mounting pieces

A new test rig was designed to allow greater 'radial' loads to be applied to the parts (see Figure 3.16). This was achieved by a lever arrangement that magnified the applied weight force by a factor of five.

For each of the tested geometries, the deflection angles resulting from different applied moments were measured over a range of 'radial' loads. It was found that the moment-angle relationship in each case was fairly linear. The slope of the relationship, representing the linearised torsional stiffness, was estimated through regression for each geometry, at each 'radial' load. The results are shown in Figure 3.17.

Some scatter is evident in the results arising from friction between the polyurethane parts and the housing. This allowed the part to occasionally 'stick' at angles that were not the true frictionless equilibrium. This was not considered to be a significant problem as the vibration of the turbine in operation would reduce the tendency to stick.

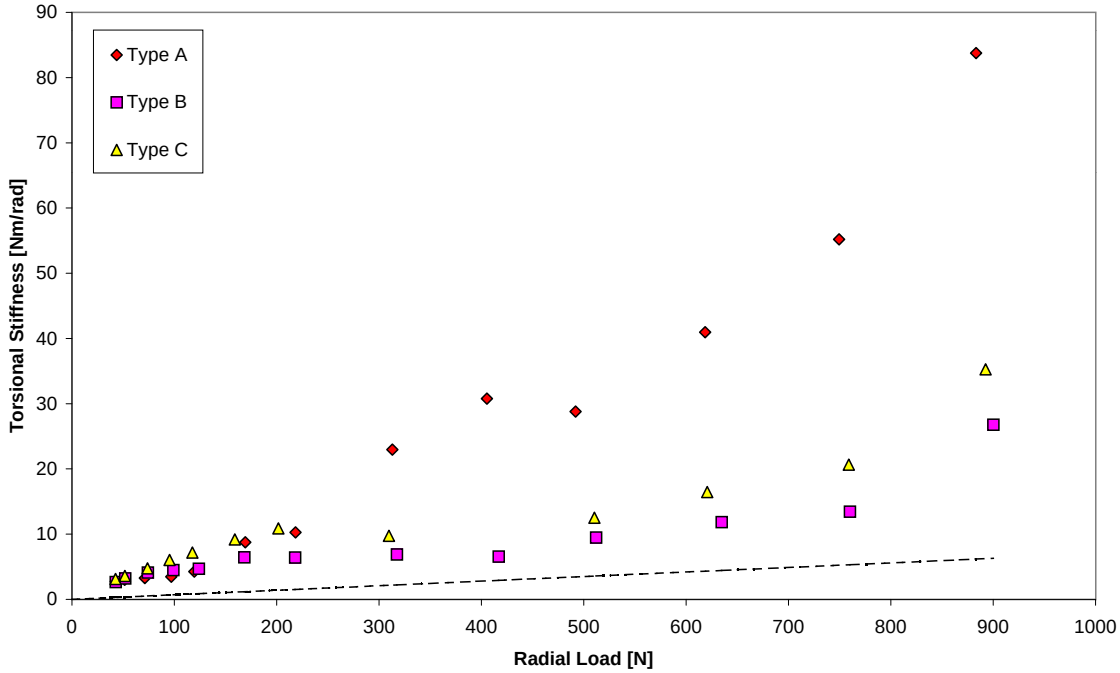

Figure 3.17: Results of testing of Type A, B and C geometries. The dashed line represents the theoretical linearised stiffness for the rolling profile alone.

It is clear that the Type A part is significantly stiffer in torsion that the other two parts. This time contact with the end of the housing was delayed until an applied radial load of approximately 125 N, but again the difficulty of decoupling this stiffness from the torsional stiffness is highlighted.

For reference the theoretical linearised stiffness for the rolling profile alone is plotted. It can be seen from Figure 3.17 that the slopes of the stiffness-load curves is approximately equal to that of the theoretical rolling profile, but that they are offset by different amounts. This is in keeping with the additional elastic constraint, which effectively adds a constant stiffness that is independent of radial load. The slightly higher stiffness of the Type C geometry reflects its slightly shorter flexible 'stem'.

Both Types B and C exhibit a departure from the basically linear range at loads above approximately 750 N, where the stiffness begins to increase more

rapidly. The reason for this additional stiffening is not known, but it may be due to compression of both parts at the rolling contact. This will be discussed further in Section 10.4.4.

3.5 Conclusion

Two distinct design concepts were conceived to allow the blade pitch response to be tailored on the basis of theoretical results. Each of these concepts differs from existing designs in the degree of control they offer over the relationship between blade restoring moment and centrifugal load.

Chapter 4

Development of a Pro/MECHANICA model of a passive variable-pitch turbine

4.1 Introduction

Preliminary investigation of passive variable-pitch turbine performance and dynamics was conducted using the commercial motion simulation software package Pro/MECHANICA, produced by Parametric Technology Corporation - website http://www.ptc.com. The package is used within the School of Mechanical and Manufacturing Engineering at UNSW in the Pro/ENGINEER integrated mode.

Pro/MECHANICA is able to simulate the motion of the turbine rotor and blades over time as a multi-degree-of-freedom mechanism under the influence of prescribed loads. It was used to investigate the general performance of the pendulum type inertial design and to gain insight into the dynamics of this type of turbine.

4.2 Pro/MECHANICA Model

Parts are created and assembled in Pro/ENGINEER, then converted to a mechanism with the desired degrees of freedom within Pro/MECHANICA.

The model created in Pro/ENGINEER and used in Pro/MECHANICA is shown in Figure 4.1. It was designed to represent the essential features of the turbine and the manner in which they are connected.

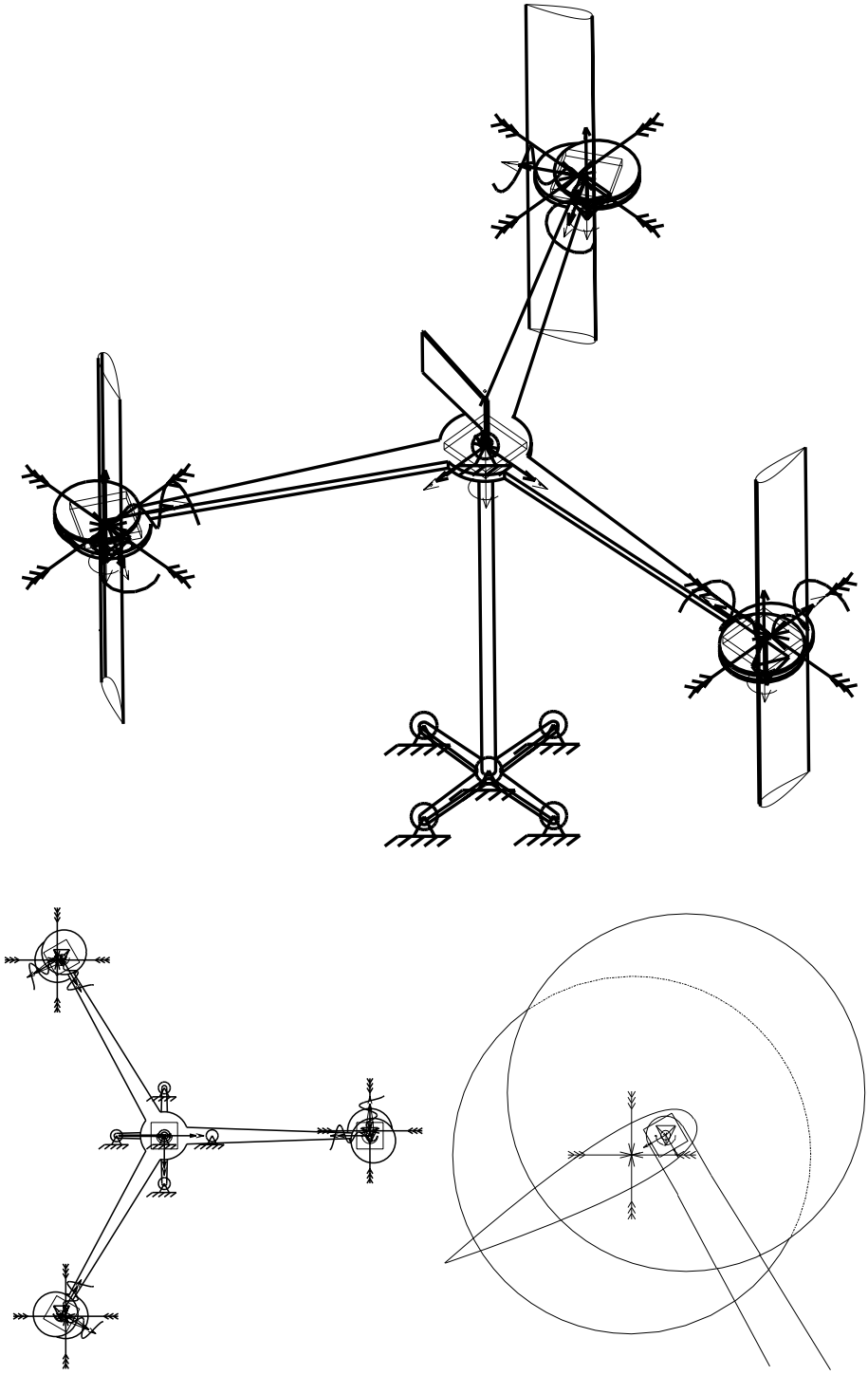

Figure 4.1: Pro/MECHANICA model of the pendulum type inertial turbine

In the initial version of the model, the rotor body was connected to the base via a "pin joint", giving it one rotational degree of freedom. The base is fixed as "ground". Each of the three blades is connected to the rotor by a pin joint, making the mechanism planar.

Each blade consists of two discs whose diameter and thickness can be adjusted to achieve any combination of mass and polar moment of inertia. The aerofoil-shaped features are massless surfaces and are purely cosmetic. One disc represents the mass of an unbalanced blade, centred at the aerodynamic centre of the aerofoil profile. As before, the distance between the aerodynamic centre and the pin joint axis is termed R_{ac}. The position of the other disc is adjusted so that the combined centre of mass lies on a line perpendicular to the blade chord line passing through the pivot axis. The offset of the centre of mass from the pivot axis is labelled R_{cg}. This arrangement causes the blade to seek a zero pitch angle under the action of centrifugal force.

This double disc model was designed to reflect the fact that blade mass and polar moment of inertia are constrained by structural design considerations, and so the parameters R_{ac} and R_{cg} cannot be adjusted independently.

Later the model was given two additional degrees of freedom of horizontal translation of the rotor hub. This freedom was designed to represent the flexibility of the turbine tower, so that the potential significance of this motion on the blade pitch response may be investigated.

4.2.1 Aerodynamic load simulation

While Pro/MECHANICA is well suited to investigation of the dynamics of the turbine mechanism, it is not designed to simulate aerodynamic loads. The aerodynamic forces experienced by each of the blades were approximated using a

combination of the standard loads available in Pro/MECHANICA based on two-dimensional blade element theory.

Pro/MECHANICA allows the user to create a set of "measures", which are either kinematic variables such as joint axis positions or velocities, or are values calculated from these via user-entered expressions. The values of measures are computed at each time step and can be used to control the magnitudes of loads applied to the mechanism.

For this analysis, measures were created to compute the magnitude and direction of the apparent wind on each blade at each time step, based on the blade's own velocity and the free wind velocity. The angle of attack, which takes into account the blade's instantaneous pitch angle, is then used to find the value of measures for lift, drag and pitching moment coefficients from a lookup table of values published for the NACA 0018 profile (Lazauskas, 2002).

Further measures are computed for the magnitude of lift and drag forces on each blade, based on the relative wind speed. It is not possible to adjust the direction of a force in Pro/MECHANICA during a run. Therefore the variable direction of the lift and drag forces on each blade was simulated using a set of four fixed force components. These forces are fixed in direction relative to the World Coordinate System (ground) and together can simulate any direction and magnitude of resultant force. They are applied to the aerodynamic centre of each blade, assumed to be fixed at the quarter chord. The key measures defined for each blade are shown in Table 4.1.

In this simplified analysis no account is taken of any reduction in wind velocity due to the force transmitted to the flow by the blades (so no energy is extracted from the air), nor for the effects of dynamic stall, flow curvature, finite

Measure	Definition
U	Free wind velocity Set manually prior to run
theta	Rotor azimuth angle. = Joint Axis Measure
azimuth	Theta normalised to 0 to 2π. = mod(theta + blade.theta0, 2π)
pivot	Blade pitch angle. = Joint Axis Measure
blade.theta0	Azimuth angle offset from the reference blade for this blade. Set manually
V	Speed of the blade. = if(omega<1e-5, 0, omega x radius)
Wx	X component of the relative wind at the blade. = -V cos(azimuth)
Wy	Y component of the relative wind at the blade. = V sin(azimuth) - U
W	Magnitude of relative wind. = sqrt(Wx^2 + Wy^2)

zp.alpha	Angle of attack on zero pitch blade.
	= if(W <1e-5, 0,
	if(V <1e-5, -$\pi/2-$ azimuth,
	if(mod(azimuth, π) == $\pi/2$,
	if($V < U$ && mod(azimuth, 2π) == $\pi/2$, -π, 0),
	if(cos(azimuth)< 0, acos($(W^2 + V^2 - U^2)/(2WV)$),
	-acos($(W^2 + V^2 - U^2)/(2WV)$)))))

alpha	Actual angle of attack. = zp.alpha - pivot
AoA	alpha normalised to 0° to 360°. = (alpha - 2π floor(alpha/(2π)) x $180/\pi$
Cl	Lift coefficient. = Look-up table, input AoA
Cd	Drag coefficient. = Look-up table, input AoA
Dx	Drag force due to Wx = 0.5 rho chord span Wx W Cd
Lx	Lift force due to Wx = 0.5 rho chord span Wx W Cl
Dy	Drag force due to Wy = 0.5 rho chord span Wy W Cd
Ly	Lift force due to Wy = 0.5 rho chord span Wy W Cl

Table 4.1: Key Pro/MECHANICA measures. Relevant measures are duplicated for each blade.

aspect ratio, wind shear or parasitic drag. These simplifications were considered justifiable because the aim of the exercise was to investigate the dynamics of the turbine rather than assess its efficiency. The assumption of constant wind velocity is significant not so much because of the consequent overestimation of average output torque (this could be corrected), but because of the variation in wind velocity both across the width of the turbine and between upwind and downwind passes that is neglected. This variation significantly effects the pitch cycle when the turbine is heavily loaded and the wind is greatly decelerated. Therefore the Pro/MECHANICA simulations were confined to low tip speed ratios and correspondingly small loads, where deceleration of the flow is minimal.

The turbine speed was chosen to give a relatively low tip speed ratio of 1.3 at a wind speed of 6 m/s. This speed is also in the operating region of interest for a study of self-starting ability.

4.3 Summary

A simplified model of a pendulum type inertial passive variable-pitch turbine was created in Pro/MECHANICA. The model may be used to study the dynamics of this type of turbine under the influence of simplified aerodynamic loads. As no account of flow deceleration is made, the model is not useful for predicting the operating output of the turbine, except at very low speeds. This model was used to conduct initial investigations of the relationships between key design parameters and blade pitch response. Results of its use are presented in Chapter 7.

Chapter 5

Development of a Momentum Theory Mathematical Model for Passive Variable-Pitch Darrieus Turbines

5.0.1 Background of momentum models

The development of momentum theory models for VAWTs has been discussed in Section 2.2.1. The model produced here was based on the Double Multiple Streamtube method set out by Sharpe (1990).

Momentum theory (or more specifically Blade Element/Momentum (BEM) theory) is based on obtaining two expressions for the streamwise force on the rotor. The force is given by the rate of change of momentum of the flow, which is equal to the overall change in velocity times the mass flow rate. The force is also equal to the average pressure difference across the rotor. Bernoulli's equation is applied separately to the flow upstream and downstream of the rotor, assuming energy is lost from the flow only at the rotor. These two equations produce the well-known result that the overall flow velocity change is twice the velocity change that has occurred by the time the flow passes the rotor.

Expressed in terms of the widely used 'flow induction factor' a, if the flow velocity at the rotor U is defined as

$$U = U_\infty(1 - a) \tag{5.1}$$

where U_∞ is the free stream velocity, then the final flow velocity in the far wake U_w is:

$$U_w = U_\infty(1 - 2a) \tag{5.2}$$

This result relates the streamwise force on the rotor to the flow velocity at the rotor.

A second expression relating these quantities is obtained using blade-element theory. The flow velocity at the blade is used to calculate the angle of attack and the known aerodynamic properties of the blade section are used to calculate the resulting streamwise force. Simultaneous solution of these two equations allows the calculation of the blade loads and the flow velocity given the blade speed and orientation. This is done using an iterative procedure.

In order to accommodate the variation in velocity across the rotor, the width is divided into a number of independent streamtubes, for each of which the momentum balance is carried out separately.

The Double Multiple Streamtube version developed by Paraschivoiu (1981) models the turbine's interaction with the wind in the upwind and downwind passes of the blades separately. The assumption is made that the wake from the upwind pass is fully expanded and the ultimate wake velocity has been reached before the interaction with the blades in the downwind pass. The downwind blades therefore see a reduced 'free-stream' velocity. This approach more accurately represents the variation in flow through the turbine.

5.0.2 Present extension

In the present work, the two-dimensional Double Multiple Streamtube model for Darrieus turbines has been extended to incorporate the prediction of blade pitch

response for a passive variable-pitch turbine. While similar work has been conducted by Bayly and Kentfield (1981) and Kirke and Lazauskas (1993), their work was limited in application to the specific design conceived by the respective authors. In order to evaluate particular designs and also to examine passive pitch systems more generally (so that different and new designs may be compared), a model that allowed for different methods of pitch control was required.

Accordingly the present model is able to deal with 5 different types of pitch control:

- General elastic pitch control, in which the blade is free to pivot about a specified point on the chord line, is balanced so that the centre of mass lies on the pivot axis and pitch is controlled by a torsion spring whose stiffness is a function of the turbine speed.
- 'Pendulum' type inertial pitch control, as designed by Sicard (1977), Kentfield (1978) and Brenneman (1983).
- 'Stabiliser mass' type inertial pitch control, based on the principle of the designs of Liljegren (1984) and Kirke and Lazauskas (1987).
- 'Rolling profile' type inertial pitch control, as described in Section 3.3
- 'Cycloturbine' type cam-driven preset pitch schedule, for comparison purposes. This includes fixed-pitch standard Darrieus turbines.

Any combination of the above passive pitch control types can be handled, for example a pendulum type inertial system can be supplemented with some elastic pitch control. The kinematics of these designs is discussed in Appendix A.

5.0.3 Basis of the mathematical model

In the Double Multiple Streamtube model for the Darrieus turbine, the flow through the rotor is divided into a number of independent streamtubes. In this

case the orbit of the single representative blade is divided into discrete 'nodes', separated by a constant angular distance labelled $\Delta\phi$. The pitch angle of the blade and the forces on it are calculated at each of these nodes. The nodes are also used as the boundaries of the streamtubes. This is illustrated in Figure 5.1. The

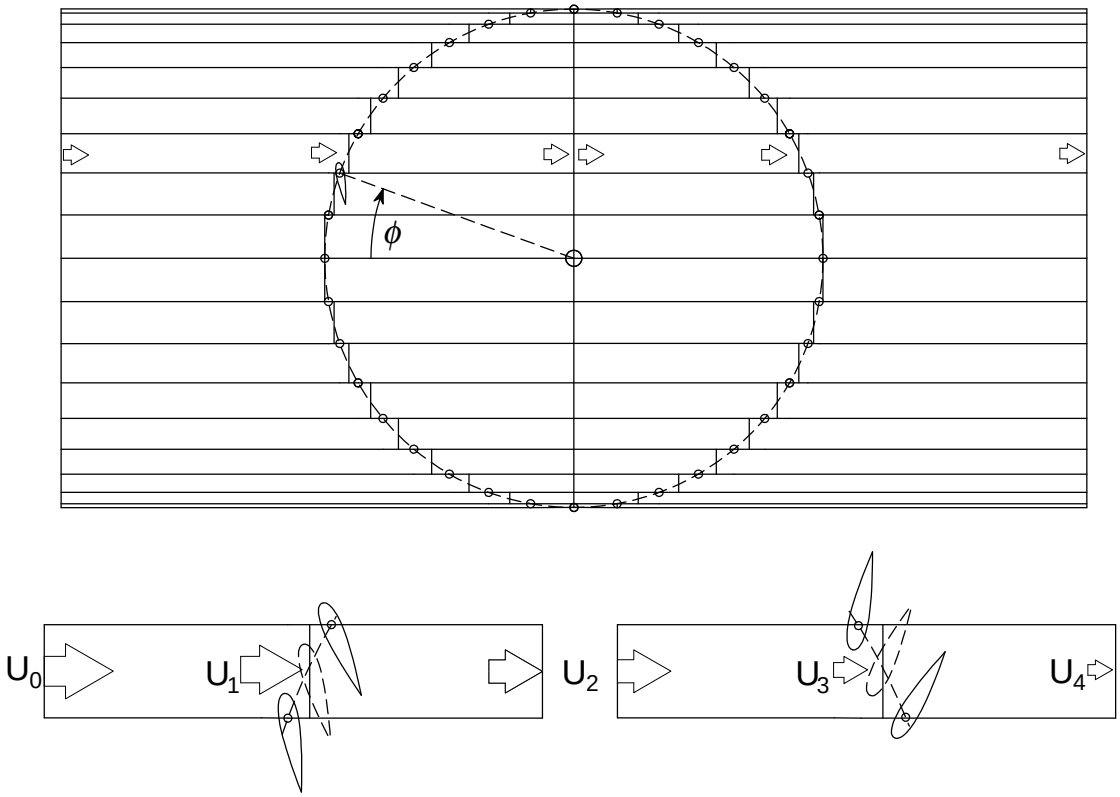

Figure 5.1: Illustration of the Double Multiple Streamtube concept. The flow through the rotor is divided into multiple independent streamtubes. The final wake velocity of the upwind half streamtube is taken to be the initial upwind velocity for the downwind half. The boundaries of the streamtubes lie on the equispaced nodes which discretise the orbit of the representative blade.

angle step between nodes is chosen to divide the revolution into an even number of nodes. For each node in the upwind half of the orbit there is a corresponding node directly downstream of it in the downwind half. Each streamtube may then be divided into a 'double streamtube', with the outlet velocity from the upwind half being the inlet velocity for the downwind half.

For a standard Darrieus turbine, the blade orientation within each streamtube is a function only of the azimuth angle. For a variable-pitch Darrieus turbine however, the additional degree of freedom means that the angle of attack for the segment cannot immediately be calculated and used for the iteration procedure described above. Instead, the blade pitch is affected by the aerodynamic forces on the blade, and the calculation of its position must be incorporated into the iteration. The process used is shown in Figure 5.2.

The motion of the blade and the forces on it are tracked around the orbit starting from the point at which the blade is advancing directly into the wind, at azimuth $\phi = -90°$. Each node is then handled in sequence, so that the upwind half of the orbit is completed and the outlet velocities are calculated and available to be used as the inlet velocities for the downwind half.

At each node, the velocity experienced by the blade there is taken to be that for the streamtube it is about to cross. An initial flow induction factor is assumed for the streamtube, usually zero, and the resulting forces on the blade calculated based on its current orientation.

Blade force is calculated using blade-element theory. The blade is treated as a two dimensional aerofoil profile and published lift, drag and pitching moment coefficients for the section are used to calculate aerodynamic forces and moments based on the angle of attack, relative flow velocity and blade Reynolds number. The coefficients for the NACA 0018 section used here are the data of Sheldahl and Klimas (1981), corrected by Lazauskas (2002). They provide data for the full 360° range of angle of attack at Reynolds numbers from 40,000 to 500,000.

Unsteady aerodynamics, including dynamic stall, greatly affect the performance of Darrieus turbines, especially at the low tip speed ratios that are the

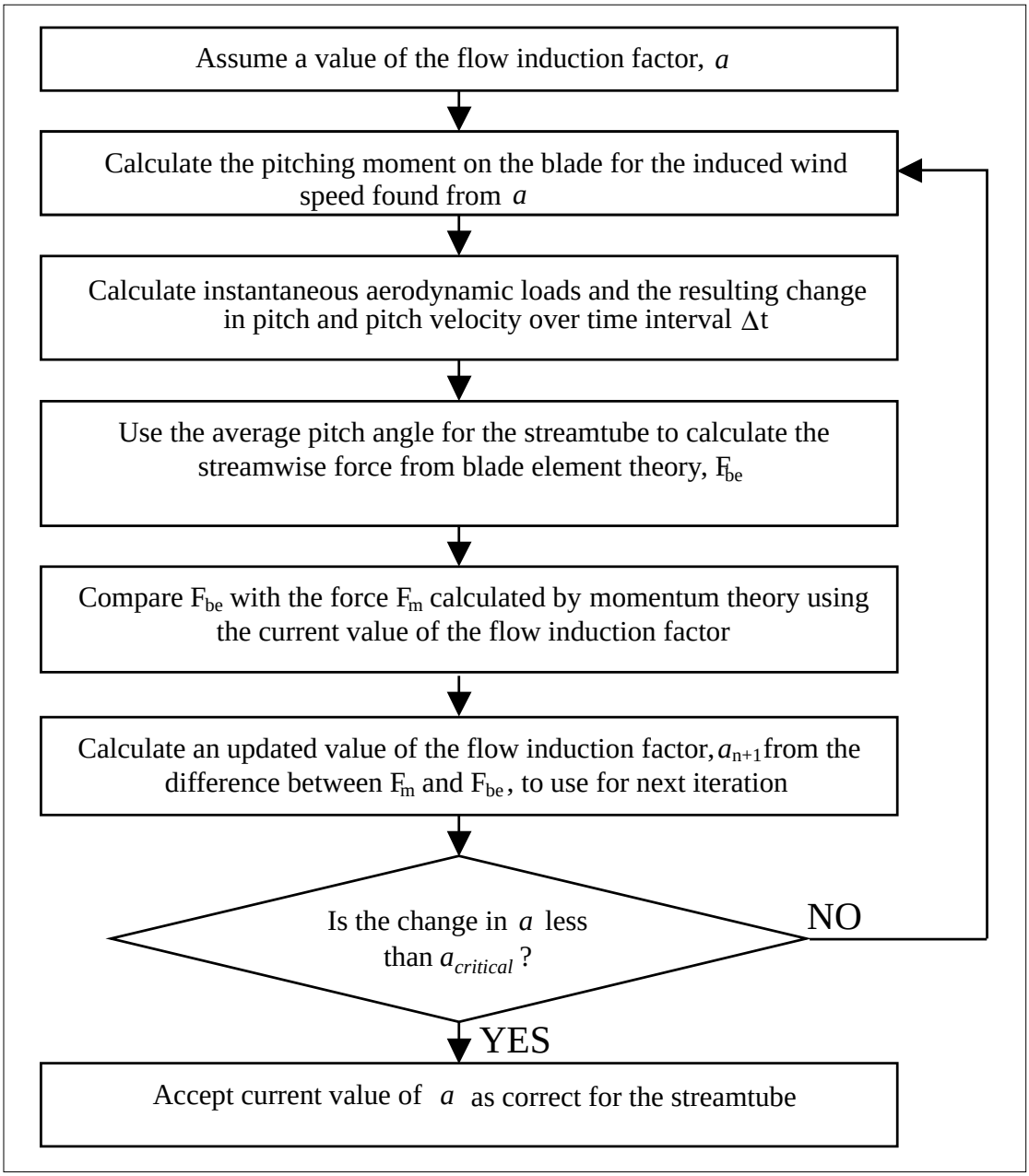

Figure 5.2: Iterative procedure used to calculate the flow velocity and blade motion within a streamtube

focus of the present work. Detailed discussion of the treatment of unsteady aerodynamics, for both the momentum and vortex models, is given in Section 5.1.

Once the aerodynamic loads have been calculated, the instantaneous pitching acceleration resulting from aerodynamic forces, any elastic forces and inertial forces is then calculated. The pitching acceleration depends on the kinematics of the particular variable-pitch design. Kinematics are treated in detail in Appendix A.

For example, the instantaneous pitching acceleration for a blade of the 'pendulum' inertial type of Sicard (1977) and Kentfield (1978) is given by:

$$\ddot{\theta} = \frac{\sum M - R_{cg} \sin\theta m R \ \dot{\phi}^2 - \{(I_{cg} + m R_{cg}^2) + m R_{cg} R \cos\theta\} \ \ddot{\phi}}{I_{cg} + m R_{cg}^2} \tag{5.3}$$

where $\sum M$ is the total aerodynamic and elastic moment acting on the blade; R_{cg} is the offset of the centre of gravity from the pivot axis; R is the turbine radius; θ is the current pitch angle and $\dot{\phi}$ is the turbine speed. I is the polar mass moment of inertia of the blade assembly about the centre of gravity and m is the blade assembly mass. Note that for the assumption of constant turbine speed made for the momentum model, the term in the numerator proportional to turbine acceleration $\ddot{\phi}$ vanishes.

A fourth-order Runge-Kutta numerical integration scheme (de Vahl Davis, 1991) is used to predict the pitch and pitching velocity for the blade at the next node, on the other side of the streamtube. The blade orientation at the midpoint of the streamtube is then estimated using the mean of the initial and final pitch angles (i.e. constant pitching velocity across the streamtube is assumed). The angle of attack based on this pitch angle at the midpoint is then used to calculate the blade element aerodynamic force for the streamtube. The difference between

blade element force and the momentum derived force for the assumed flow induction factor is then calculated and used to generate a new estimate of the flow induction factor. Here Newton's method (de Vahl Davis, 1991) is used to find the zero crossing of the function that is the difference between momentum and blade element estimates of streamwise force. The independent variable is the flow induction factor a. The process is repeated until the change in flow induction factor between iterations is acceptably small.

Once the flow induction factor iterations have converged and the blade pitch and velocity at the next node have been predicted, the forces on the blade at the current node are finalised and stored.

This process is repeated for each node until the entire revolution has been completed. Since the whole procedure began with an arbitrarily assumed pitch and pitching velocity (usually both zero), calculation must continue for several revolutions until a steady-state pitching pattern has been established. Equilibrium is checked by comparing the initial and final pitch angles and velocities, as well as the integrated torque for the revolution.

5.1 Unsteady Aerodynamics including Dynamic Stall

5.1.1 Introduction

Unlike the blades of a horizontal axis turbine, VAWT blades experience a constantly changing angle of attack and flow velocity even under steady operating conditions. While the static aerodynamic properties of the aerofoil sections typically employed for the blades are well documented, prediction of loads under dynamic conditions remains difficult.

The difference between static and dynamic loads is dependent on the rate of change of the angle of attack and is significant for Darrieus turbine operation. Noll and Ham (1982) state that maximum aerodynamic loads may be as much as three times greater under dynamic conditions than under static conditions, while the peak pitching moment may be up to five times greater.

Many authors (Klimas, 1982; Noll and Ham, 1982; Paraschivoiu and Allet, 1988; Jiang et al., 1991) emphasise the importance of accounting for unsteady aerodynamic loads from the perspective of structural design, fatigue life and drive-chain and generator sizing. The effect on overall turbine performance may also be significant. In general, the increased peak loads and delayed stall that are associated with dynamic conditions lead to an improvement in performance over that predicted using only static characteristics. Paraschivoiu and Allet state that:

> "[The effects of dynamic stall] can be seen in particular on the power performance curves, which exceed the steady-flow prediction for tip speed ratios of less than four. The ability to predict dynamic stall is therefore of crucial importance for optimising the Darrieus wind turbine."

Thus unsteady aerodynamics and specifically dynamic stall are important to the study of the low tip speed ratio performance of Darrieus turbines. While a passive variable-pitch turbine is designed to reduce the incidence of stalling at intermediate tip speed ratios, stall is inevitable at start-up and the timing and magnitude of the associated aerodynamic loads and moments can have a significant impact on the blade pitch history for the entire revolution. The average torque and not just the peak load is therefore sensitive to stall behaviour. Consequently

it is vital that unsteady aerodynamics be incorporated in any mathematical model of a passive variable-pitch turbine.

The following section covers the basic features of unsteady turbine blade aerodynamics and the available methods of quantifying their effect on turbine performance.

5.1.2 Attached flow unsteady aerodynamics

Unsteady aerodynamic forces may be divided into circulatory and non-circulatory components.

Circulatory unsteady effects

Unsteady circulatory effects for attached flow are:

- the change in circulation about the aerofoil due to the influence of vorticity in the wake;
- the change in circulation about the aerofoil due to the motion of the foil.

The latter effect is commonly included by calculating the circulation based on the angle of incidence at the 3/4 chord location, rather than the quarter chord location. Since the blade is rotating about the turbine axis and possibly also about its own pivot axis, the angle of incidence varies along the chord line. Fung (1955) presents a quasi-steady analysis of lift and drag for use in aeroelastic analysis, using classical thin aerofoil theory, where the influence of unsteady wake vorticity is neglected. He shows that for an aerofoil that is both pitching and plunging, the lift is proportional to the angle of attack at the 3/4-chord position. He presents a further analysis for an oscillating aerofoil without the quasi-steady assumption, based on complex potential flow and conformal mapping of a circle to a flat plate. This analysis confirms the significance of the 3/4-chord point, which Fung terms the "rear aerodynamic centre". Strickland et al. (1981) use a similar complex potential flow analysis for a flat plat in general motion presented by Milne-Thomson

(1968) to show that the additional circulation required to preserve the Kutta condition of a stagnation point at the trailing edge for a pitching aerofoil can be quantified by accounting for the downwash at the 3/4-chord point.

Some treatment of the vorticity shed in the unsteady wake of the aerofoil is also required. Under steady conditions vorticity is not shed into the wake. When a change in angle of attack occurs the circulation about the aerofoil must change to maintain the stagnation point at the trailing edge. In order to conserve total circulation according to Kelvin's theorem, vorticity of equal and opposite strength must be shed in to the wake. This wake induces a 'downwash' at the aerofoil (according to the Biot-Savart law) that effectively reduces the angle of attack, mitigating the change in lift. As this wake vorticity convects away from the foil, the induced downwash diminishes until the new steady-state lift is acting.

Theodorsen (1935) developed an analytic frequency-domain treatment of this wake-induced lift deficiency for a thin aerofoil undergoing small-amplitude harmonic motion in a steady flow.

Approximate analytic treatment of unsteady aerodynamic forces is made in the study of aeroelastic flutter (see for example Fung, 1955). The change in circulation in response to a step change in incidence is assumed to build up to its steady state value according to Wagner's function. This function accounts for the changing downwash at the aerofoil resulting from the wake that is shed from the trailing edge. This is akin to the influence of the 'starting vortex' shed from a wing at an impulsive start. Wagner's function starts at 0.5 at approaches 1 asymptotically. For an aerofoil in general motion, Wagner's function may be used to calculate the growth of circulation due to a step change in the downwash.

Similarly Kussner's function, as amended by Von Karman and Sears (1938) provides an analytic treatment of the transient lift on an aerofoil entering a sharp-

edged vertical gust. This analysis is based on the influence of the unsteady wake of the aerofoil, assumed to be planar (or linear, in the two-dimensional case) behind the foil.

Unsteady wake effects on attached flow behaviour may be incorporated using a semi-empirical unsteady aerodynamics model such as the Beddoes-Leishman model described in Section 5.1.3. However the complexity of the wake in the Darrieus turbine case makes the task of such methods very difficult. This topic is discussed further in the context of the free vortex mathematical model described in Chapter 6.

Non-circulatory unsteady effects

Non-circulatory aerodynamic loads are generally termed "added mass" forces. They arise from the acceleration of air due to blade motion and exist even in the absence of a free stream.

By contrast, Leishman and Beddoes (1986) use piston theory to calculate the non-circulatory, or impulsive, load on the blade. It is assumed to arise from a compression wave on one side of the blade with an expansion wave on the other, and allows the effects of compressibility to be included, which is important for helicopter applications, but should not be significant for wind turbines.

Quantification of unsteady effects in attached flow

Strickland et al. (1981) cite an analysis by Milne-Thomson (1968) for forces on a moving and rotating flat plate in potential flow. This analysis yields expressions for the additional circulation around the aerofoil due to its rotation, as well as the added mass forces that are independent of circulation. This results in expressions for the total normal and tangential (chordwise) forces. The tangential force is found to be proportional to the angle of attack at the mid-chord position. The

normal force consists of a term that is proportional to the angle of attack at the 3/4-chord position and an added mass term proportional to the normal acceleration of the foil. Strickland et al. state that an order-of-magnitude analysis justifies the omission of this added mass term. Likewise, the added mass pitching moment term is judged to be small.

They conclude that unsteady pitching and added mass effects may be treated in practice by:

- calculating the tangential force using the angle of attack at the mid-chord in the static look-up table of aerodynamic coefficients for the section;
- calculating the normal force similarly using the 3/4 chord angle of attack;
- assuming the pitching moment about the quarter-chord is negligible for attached flow.

This method has been adopted for both the momentum model and the vortex wake model described in Chapter 6.

Unsteady wake effects have been neglected in the momentum model due to the complexity of the wake structure and the difficulty in using a semi-empirical model based on a linear wake to represent its influence. Wake effects are modelled explicitly in the vortex model.

5.1.3 Dynamic stall

At zero incidence, a symmetric aerofoil generates no lift. As the angle of attack increases, the lift increases in an approximately linear fashion, until at a critical angle the flow begins to separate from the upper surface of the foil. Flow separation leads to the sudden loss of lift and increase in drag that is termed stall.

The angle at which stall occurs depends on the rate of change of the angle of attack. Traditionally, published lift and drag coefficients for an aerofoil section are

obtained from measurements made under quasi-static conditions. Under dynamic conditions stall occurs at a higher angle of attack than under static conditions, with an associated increase in the maximum lift attained. This phenomenon is termed dynamic stall.

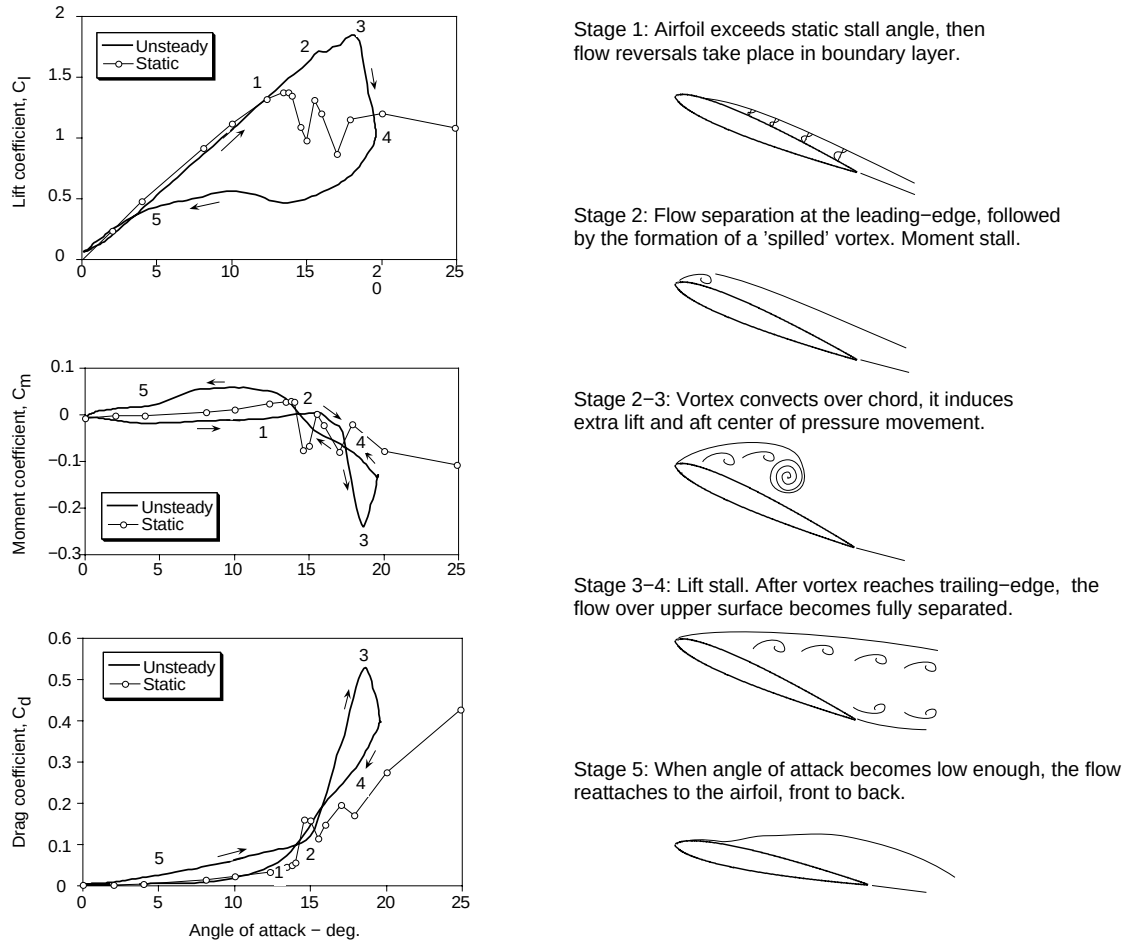

Figure 5.3: Schematic showing the features of the dynamic stall process. Reproduced from Leishman (2002)

Dynamic stall is characterised by the formation of a distinct vortex on the upper side of the aerofoil that detaches from the leading edge region and convects downstream over the surface of the foil. The convection of this vortex produces a rearward motion of the centre of pressure and a corresponding negative peak in pitching moment about the quarter chord. Once the dynamic stall vortex travels

past the trailing edge, lift drops sharply and the flow is fully separated. Upon return to lower angles of attack, reattachment of the flow may be delayed to a significantly lower angle than that at which separation occurred. These features are illustrated in Figure 5.3, reproduced from Leishman (2002).

Considerable experimental attention has been devoted to the topic of dynamic stall by measuring forces and pressure distributions on pitching aerofoils in the wind tunnel (for example Daley and Jumper, 1984; Francis and Keesee, 1985; Strickland and Graham, 1986; Lorber and Carta, 1988; Niven and Galbraith, 1997; Gracey et al., 1996, 1997). It is clear from this work that the magnitude of the delay of stall and the peak loads attained is a function of the pitch rate. There is however some disagreement in the literature as to the exact nature of this relationship. Lorber and Carta (1988) concluded from their experiments at low pitch rates that the angle at which moment stall occurs is linearly dependent on the pitch rate. However Gormont (1973) proposed a correlation that is based on Theodorsen's theory and is extended using experimental data from oscillating aerofoil tests. It suggests that the stall delay angle is related to the square root of the non-dimensionalised pitch rate. Experimental work by Daley and Jumper (1984), Francis and Keesee (1985) and Strickland and Graham (1986) appear to confirm this relationship. More recent work at the University of Glasgow (for example Niven and Galbraith, 1997; Gracey et al., 1996, 1997) suggests a combination of the two. For pitch rates that are high enough for fully dynamic stall, characterised by the formation of the stall vortex, the stall delay was found to be linearly proportional to pitch rate. At lower pitch rates, the stall is termed "quasi-steady", with no discernible stall vortex. In this region, their stall delay correlation includes a square root term.

Semi-empirical dynamic stall Models

Most of the work on the dynamic stall phenomenon appearing in the literature has been conducted by researchers in helicopter aerodynamics. Empirical dynamic stall models that have been applied to Darrieus wind turbines are the Massachusetts Institute of Technology (MIT) method (Johnson, 1970), Gormont or Boeing-Vertol method (Gormont, 1973), ONERA method (Petot, 1989) and Beddoes-Leishman (Leishman and Beddoes, 1986, 1989) method.

The MIT method was modified by Noll and Ham (1982) to include the empirical representation developed by Boeing-Vertol for the dynamic stall angle. They applied the method to the performance prediction of the variable-pitch Pinson 'cycloturbine' VAWT.

Boeing-Vertol - The Gormont, or Boeing-Vertol model is a simple empirical relation commonly used for Darrieus turbine analysis. The original Boeing-Vertol model was modified by Strickland et al. (1979) for use with their vortex code. It was used by Paraschivioiu et al. (1988) in their Double Multiple Streamtube code.

The model assumes that the lift-curve slope and the zero-lift angle for the aerofoil are unchanged by dynamic effects and it is the angle at which stall occurs and the peak lift coefficient attained that are modified. Effectively the linear region of the lift curve slope is extended beyond the static stall angle. A modified angle of attack is found for use in a look-up table of static lift and drag coefficients. The degree of stall delay is assumed to be proportional to a reduced pitch rate parameter

$$\sqrt{\frac{c\dot{\alpha}}{2W}}$$

where c is blade chord length, $\dot{\alpha}$ is the rate of change of angle of attack and W is the relative wind speed.

Paraschivoiu (1983) compared aerodynamic forces predicted by a Double-Multiple Streamtube model incorporating the Boeing-Vertol dynamic stall model with experimental data from a small straight-bladed Darrieus turbine in the wind tunnel. He reported small differences in the magnitude of the predicted steady state power coefficient when the dynamic stall model is included, but significant differences in instantaneous blade loads. He concluded that while the dynamic stall model provided large improvement over the static model, the results were still different from experimental data. The difficulty of obtaining accurate instantaneous force measurements should however be remembered.

The Boeing-Vertol model was implemented in both the momentum and vortex models presented here. The criteria for its use suggested by Strickland et al. (1979), that it be turned on when the angle of attack is above static stall or when the angle is decreasing below stall having been above it, were adopted.

It was found that this model caused significant reduction in the estimated torque, compared with the use of static lift and drag, at tip speed ratios where the maximum angle of incidence just exceeds the static stall angle. A small excursion beyond the designated static stall angle does not allow much time for increased peak lift before the angle of attack starts to decrease again, at which point the modified angle switches to be greater than the geometric angle and delays the reattachment of flow until angles much lower than the static stall angle. This phenomenon of delayed reattachment has been observed in experiments (for example Wickens, 1985).

Kirke (1998) used a momentum model for a passive-pitching VAWT that incorporated the Boeing-Vertol model as modified by Cardona (1984). Cardona recommended two modifications to the model used by Strickland:

1. that dynamic stall not be considered when the model predicts rapidly oscillating angle of attack and that the static coefficients be used instead;
2. that the average of the static and predicted dynamic values of lift and drag coefficients be used when the angle of attack is much greater than the stall angle.

The second modification was a response to the observed overprediction of peak tangential force by his free vortex VAWT model compared with the experimental results of Strickland et al. (1981).

The first modification may have been a method for dealing with the numerical instability that the vortex model is prone to when a rapid change in angle of attack occurs. This will be discussed in more detail in Section 6.3.

Details of the model are given in Appendix B.

MIT - Noll and Ham (1982) modified the original MIT model developed by Johnson (1970) for application to wind turbines and presented predicted results for a small Darrieus turbine. Details of the method are given in Appendix B.

The original MIT method was developed for helicopter aerodynamics. It was based on the delay of stall to a prescribed elevated angle of attack at which point peak values of lift and moment were instantaneously attained and held until the angle of attack began to decrease again. The coefficients then decayed exponentially with time until the static stall angle was reached. The values of the peak lift and moment were given as a function of the reduced pitch rate

$$\frac{\dot{\alpha}c}{W}$$

derived from experimental results.

Noll and Ham modified the method to calculate the dynamic stall angle using the Boeing-Vertol empirical method, in which the stall delay is a function of the square root of the reduced pitch rate.

Static sectional coefficients are used while the angle of attack is below static stall. When it exceeds static stall but is still below dynamic stall, C_L is calculated from

$$C_L = a_s \sin \alpha \tag{5.4}$$

where a_s is the lift curve slope at static stall. When the dynamic stall angle is reached the dynamic stall vortex is assumed to commence its motion from the leading edge. In this region the lift coefficient continues to be calculated from Equation (5.4) until either it reaches an empirically derived maximum value, or the angle of attack starts to decrease again.

In Noll and Ham's method the attainment of peak angle of attack marks the commencement of the exponential decay of lift and pitching moment coefficients from the peak value down to the static stall values.

A number of modifications to this method to make it suitable for application to the starting performance of Darrieus turbines are suggested. These are detailed in Appendix B.

Beddoes-Leishman - The Beddoes-Leishman method is based on an indicial aerodynamic response function, which is defined as the response to a step change between two steady-state conditions. The theory is that if the indicial response is known, the total response to an arbitrary time history of input (i.e. angle of attack) can be obtained using superposition.

The model is composed of three distinct sections:

- an attached flow region;
- a separated flow region where the effect of trailing edge separation is modelled;
- a dynamic stall region, where the effect on lift and moment of the formation, convection and detachment of the dynamic stall vortex are modelled.

Beddoes and Leishman used an indicial response function for the normal force in attached flow on an aerofoil composed of two parts: a non-circulatory component that acts instantaneously and then decays exponentially towards zero; and a circulatory component builds up from zero to asymptotically approach the steady state value. Time constants for these processes are obtained empirically for a specific aerofoil shape and a range of Mach numbers.

5.1.4 Comparisons

Paraschivoiu and Allet (1988) compared predictions from the Boeing-Vertol dynamic stall model and those from the MIT model as modified by Noll and Ham (1982) with experimental data from the Sandia 17m turbine for the normal force and average torque. Both models overestimated the maximum normal force on the upwind side of the rotor, but the MIT model successfully predicted no dynamic stall on the downwind pass, whereas the Boeing-Vertol model did. Paraschivoiu and Allet point out that Noll and Ham assume that the coefficients return to the linear (unstalled) domain when the angle of attack returns to below the static stall angle, however the experimental data indicates that flow remains separated until well below static stall.

The experimental data was from free wind operation and the tip speed ratio was not stated. The Boeing-Vertol method's use in the Double Multiple Streamtube

model was limited to those zones determined to have low turbulence from water-tunnel observations. Turbulence is stated to delay the dynamic stall phenomenon and the static aerofoil characteristics are used where turbulence is high.

Major and Paraschivoiu (1992) preformed a comparison between the Gormont, MIT and an indicial method based on the Beddoes-Leishman model and experimental data from the Sandia 17m turbine. They found that for some cases the indicial and Gormont methods predicted the occurrence of dynamic stall when the MIT model agreed with experiment in predicting a static stall case. Nevertheless they concluded that the indicial method offers a better representation of dynamic stall than the other two, thus allowing more accurate local blade load prediction.

5.1.5 Summary

Three dynamic stall models were implemented in the code for the momentum theory model and the vortex theory model to be described in Chapter 6. These were:

- The Boeing-Vertol method;
- The Boeing-Vertol model with modifications suggested by Cardona;
- The MIT model modified by Noll and Ham.

Details of these methods are given in Appendix B. The three models were implemented for comparison and are selectable via the GUI in the program. The Beddoes-Leishman model has not been implemented because it was not clear that its much greater complexity would result in greater stability and accuracy. However this model, or any improved model that is developed in the future, could be implemented as an additional module.

5.2 Sample Results

The momentum theory model was used to generate predictions of power coefficient for a passive variable-pitch turbine. The results from three dynamic stall models are shown in Figure 5.4.

The significant difference between the three dynamic stall models is clearly visible at tip speed ratios less than 5.5 for the case of fixed blades and 4.5 for the variable-pitch turbine. All three models produce significant increase in predicted power coefficient for the TSR range 1 to 3 compared with the static case where dynamic stall is ignored. At higher speeds the MIT model tends to converge with the static prediction, while the Boeing-Vertol model predicts first a lower C_p before converging at a higher TSR.

At intermediate tip speed ratios the dynamic stall models all produce an increase in the predicted integrated torque for the revolution by delaying stall and increasing the proportion of time for which flow remains attached. At higher tip speed ratios, the Boeing-Vertol model predicts a reduced output. At these speeds the angle of attack is, at its extremes, just exceeding the static stall angle each revolution. The dynamic stall model is activated whenever the static stall angle is exceeded and when the angle of attack is decreasing below stall having been above static stall. In this operating region, this results in only a small extension of the attached flow time when angle of attack is increasing, while dynamic stall hysteresis, resulting in delayed reattachment of flow as the angle decreases again, produces a net increase in the amount of time that the blades are stalled. The integrated torque for the revolution suffers accordingly.

This phenomenon is not observed in the MIT model because it effectively switches off when the angle of attack drops below the static stall angle. While

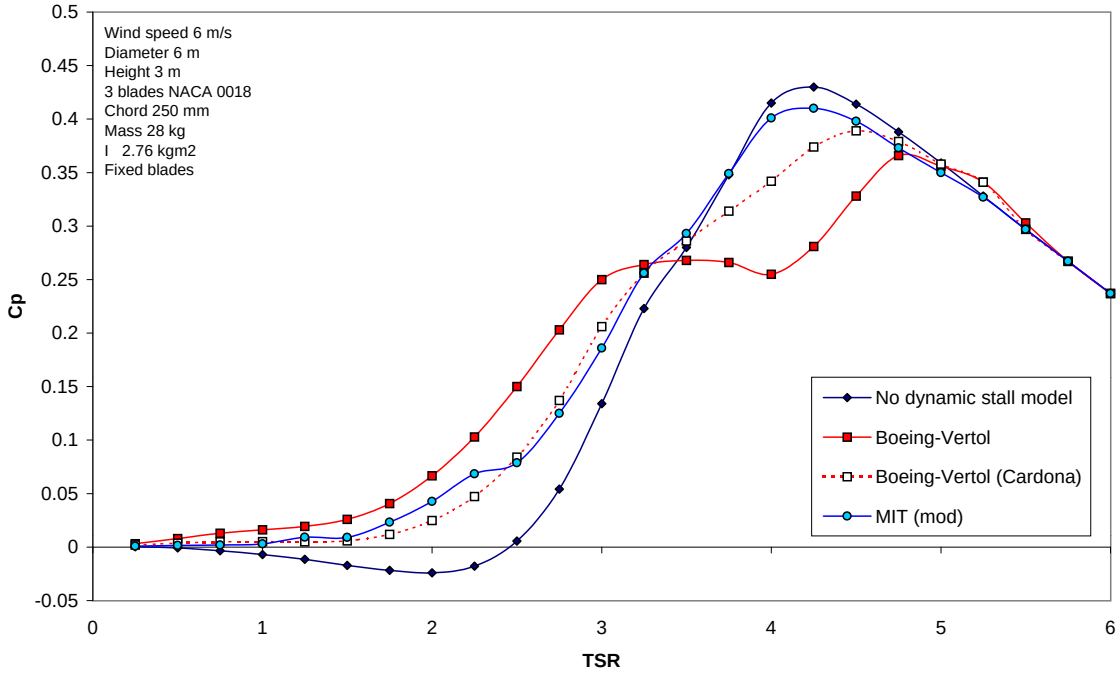

(a) Fixed blades

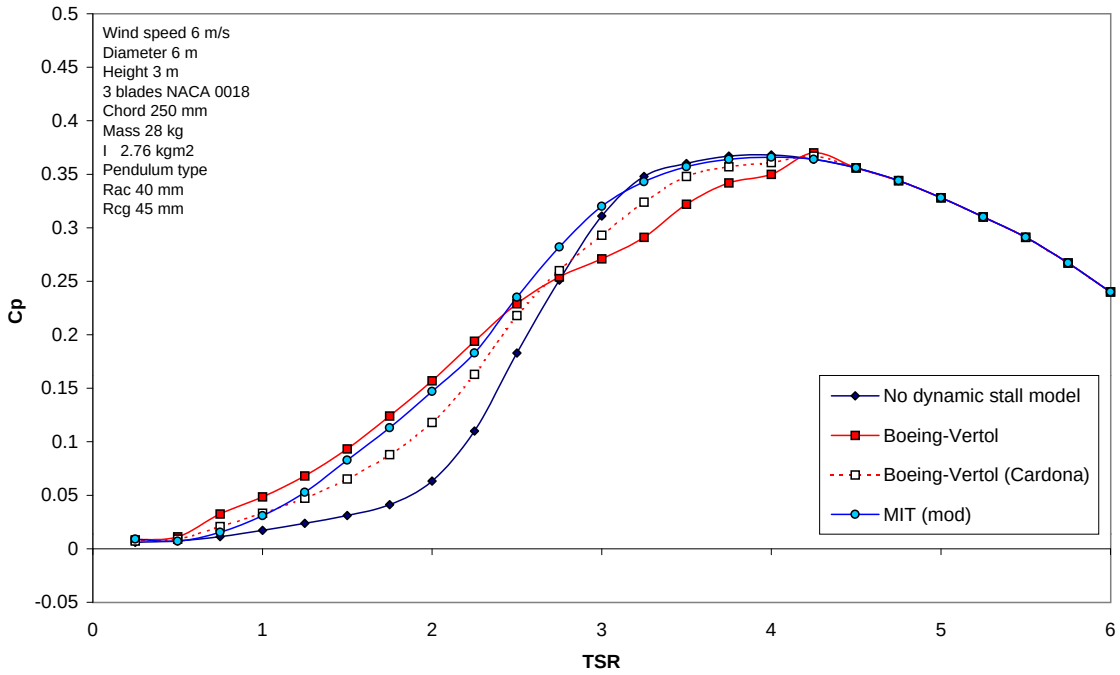

(b) Pendulum type passive variable-pitch

Figure 5.4: Predicted power coefficient against tip speed ratio showing significant variation between dynamic stall models.

hysteresis is a known feature of the dynamic stall process, from these results it appears to be overestimated by the Boeing-Vertol model in this form. The Cardona modified version mitigates this effect by simply using the mean of the modified and static coefficients. This produces results that are more like those of the MIT model at all speeds.

The effect of all of the dynamic stall models disappears when the tip speed ratio is sufficiently high to keep the angle of attack below the static stall angle at all times.

The effect of the passive variable-pitch system is also clearly seen from these results. The starting and intermediate tip speed ratio performance is significantly improved. For this choice of parameters, the peak power coefficient is reduced because some pitching is still occurring at the tip speed ratio at which this occurs (approximately 4). This reduces the amplitude of the periodic variation in angle of attack well below stall, reducing the lift produced. A trade-off between starting and high-speed performance is necessary and may be controlled by the choice of the blade mass centre offset parameter R_{cg}, which determines the strength of the restoring moment.

5.2.1 Summary

The treatment of unsteady aerodynamic effects is the greatest difficulty facing mathematical models of vertical-axis wind turbines. The approach of starting with static empirical lift and drag data and modifying it according to the rate of change of angle of attack cannot hope to accurately capture the full complexity of the unsteady aerodynamics. However a more fundamental computational fluid dynamics (CFD) approach remains excessively expensive and impractical in such

models. Accordingly the shortcomings of more economical treatments must be tolerated.

The MIT model was favourably compared with the Boeing-Vertol model by Paraschivoiu and Allet (1988). Comparisons with published experimental data presented in Section 6.4 indicate the modified MIT model is the most suitable of those tested. The Boeing-Vertol method predicts significant reduction in turbine power when the angle of attack just exceeds the static stall angle.

5.3 Limitations of Momentum Theory

Equation 5.2 implies that if the flow is decelerated to less than half its initial magnitude by the time it reaches the rotor, then in order to satisfy the momentum balance, the flow velocity in the far wake must be negative and there must be a point somewhere upstream of that at which velocity is zero. Clearly this result is not physically realistic. Wilson and Lissaman (1974) state that the momentum analysis should not be considered valid for $a > 0.5$.

In reality, the assumption of lossless expansion of the flow on the downstream side of the rotor needed to apply Bernoulli's equation is not justified when the rotor is heavily loaded. When the deceleration is large, the flow through and around the rotor becomes turbulent, resulting in significant loss of energy. This operating state is termed the 'Turbulent Wake State' by Stoddard (1976). Momentum theory predicts that as the flow induction factor increases above $a = 0.5$ towards $a = 1$ the streamwise thrust (proportional to the pressure drop across the rotor) will decrease towards zero. Experimental work by Glauert (1926) on free-running windmills indicates that in fact the thrust increases in this region, until at $a = 1$ the thrust is akin to that on a solid disc that allows no flow to pass through and about which there is large scale turbulence and recirculation.

In order to accommodate the breakdown of momentum theory in this region the modification suggested by Sharpe (1990) is used. A straight line is fitted through experimental data to produce an empirical expression for the streamwise thrust coefficient C_T in terms of the flow induction factor a (see Figure 5.5).

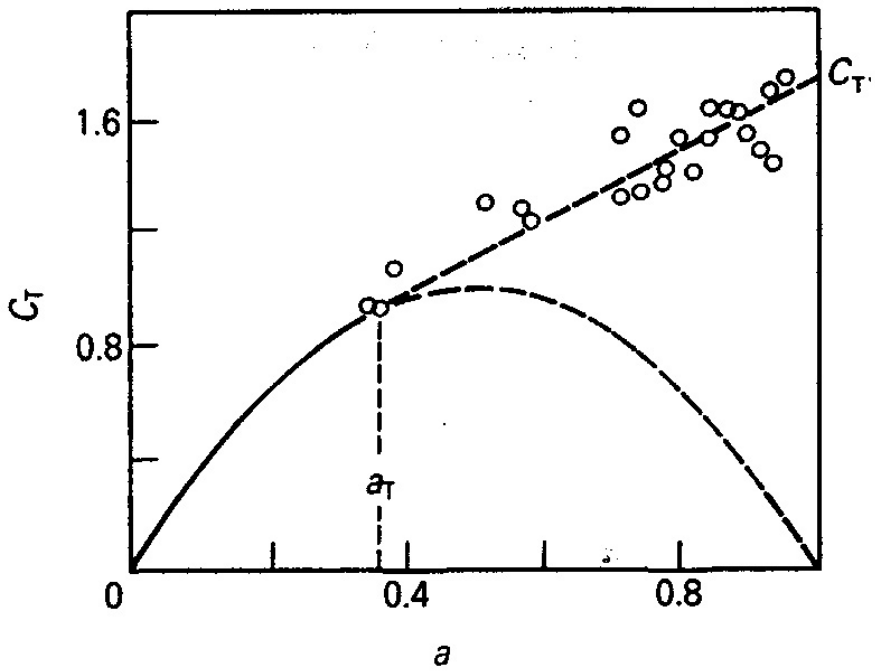

Figure 5.5: The empirical modification to momentum theory used by Sharpe (1990) to deal with heavily loaded rotor operation

Instead of the standard expression for C_T:

$$C_T = 4a(1-a) \tag{5.5}$$

in the region $a_T < a < 1$, C_T is given by:

$$C_T = C_{T1} - 4(C_{T1}^{0.5} - 1)(1-a) \tag{5.6}$$

where

$$a_T = 1 - 0.5C_{T1}^{0.5}$$

and C_{T1} is 1.816. This value approaches the drag coefficient for a solid disc perpendicular to the flow.

While this modification avoids the obvious impossibility of wake reversal and allows the model to be used for $a > 0.5$, the predicted power may still not be accurate. Stoddard (1976) states that:

> "Entrance into Turbulent Wake by a wind generator brings with it reversals in induced velocity (bound circulation along the blade), high turbulence, vibration, and a precipitous decrease in shaft torque."

In addition, the relationship between the pressure on the downstream side of the rotor and the far wake final velocity is now lost, as Bernoulli's equation cannot be used. While for a horizontal axis rotor, this does not matter as the wake velocity is of little concern, for the double multiple streamtube approach used here, the wake velocity calculated from the upwind pass of the blades is used as the input velocity for the downwind pass.

The modification allows the blade-element force iteration process to converge to flow induction factors greater than 0.5, whereas without it no convergence can be reached in this region due to the negative slope of the C_T curve. However the wake velocity will still be predicted as negative for $a > 0.5$. In reality the wake velocity will approach zero as a approaches 1, but turbulence and recirculation will dominate.

So while the modified momentum theory predicts smooth deceleration of the flow right up to complete blockage, the real situation is very much more complicated, and the turbine output in this operating region is likely to be significantly

overestimated. This fact provided further motivation for the development of a free vortex model for turbine performance.

5.4 Summary

An extended Double Multiple Streamtube type mathematical model has been produced as part of this thesis to predict the steady-state performance of passive variable-pitch Darrieus turbines. The model is able to handle the specific kinematics of five different passive designs. The inertial reactions on the rotor produced by the pitching blades are accounted for in the model. A modified version of the MIT model is used to treat dynamic stall.

The speed of the model enables it to be used to investigate the effects of variation of design parameters. Use of the model to develop a parameter selection strategy for passive variable-pitch turbines is described in Chapter 7.

Chapter 6

Development of a Free Vortex Mathematical Model for Passive Variable-Pitch Darrieus Turbines

6.1 Background to Vortex Methods

Vortex methods are a more complex and computationally expensive alternative to blade-element/momentum methods. The benefit is that they are able to handle more general scenarios than can momentum methods, with fewer limitations. They have been widely applied to helicopter, HAWT and Darrieus VAWT rotor analysis. A review of vortex methods applied to wind turbines is given by Leishman (2002).

Vortex methods assume incompressible, potential flow in the wake. A Lagrangian approach is used, tracking discrete vortex sheet segments in the wake of the rotor. Rather than referring to momentum, the velocity at any point in the flow field can be calculated by applying the Biot-Savart law.

6.1.1 Reasons for using a free vortex method

The free vortex wake model used here and extended for passive variable-pitch turbines is based on the 2 dimensional method for the Darrieus turbine developed by Strickland et al. (1979, 1980, 1981). They list the deficiencies of momentum models as:

- The breakdown of momentum theory at large tip speed ratios;

- The inaccuracy of predicted blade loads due to the quasi-steady approach and inability to deal with details such as individual blade wakes and flow normal to the free stream;
- Inability to model the structure of the near wake for the purpose of wind farm layout.

The first two issues are relevant in the current work.

The breakdown of momentum theory at high tip speed ratios has been discussed in Section 5.3. Vortex methods do not suffer from this limitation. While the area of interest here is starting and intermediate TSR performance, where momentum theory breakdown is not expected to be a problem, it is still possible for large flow deceleration to be predicted for high solidity rotors.

Given that the output of a passive pitch turbine is highly dependent on the blade pitch response, the accuracy of the predicted instantaneous aerodynamic loads is critical to the overall accuracy of the method.

A further motivation for developing a vortex method was the desire to investigate the transient behaviour of the turbine and average output under turbulent wind conditions. Turbulence was identified by both Bayly (1981) and Kirke (1998) as a likely cause of the often significant discrepancies found between their predictions and field turbine experimental results. Momentum methods calculate steady-state performance both in terms of the induced inflow velocities and the blade pitch response for a constant wind. These states may take several revolutions to develop. In turbulent wind conditions with constantly varying velocity and direction of flow, the turbine may spend little or none of its time at the predicted steady-state condition. Drees (1978) states that the Cycloturbine tested at Pinson Energy Corp. recorded a maximum power coefficient C_p of 0.45 in "very

smooth wind conditions", while a "nominal" C_p of 0.3 is maintained in gusty conditions. The time-marching free vortex method, which tracks the motion of discrete vorticies in the wake, is naturally able to deal with transient behaviour.

A two-dimensional free vortex mathematical model for passive variable-pitch turbines was accordingly developed. While three-dimensional vortex models have been produced for Darrieus turbines (see Strickland et al., 1980), the added computing cost and coding complexity were not considered justified in this case. The model has been used to investigate the significance of rotor speed variation in the prediction of starting performance and to examine the turbulent wind performance of a turbine connected to a load. The circumstances under which the order of magnitude greater computational expense justify its use over a momentum model are also examined.

6.2 Free Vortex Aerodynamic Model

The turbine blades are represented by bound or lifting-line vortices whose strengths are determined using aerofoil coefficient data and the calculated relative flow velocity and angle of attack. The bound vortex strength Γ_B is related to the flow at the blade via the section lift coefficient:

$$\Gamma_B = \frac{1}{2} C_L c W \tag{6.1}$$

where C_L is the lift coefficient, c is the blade chord and W is the local relative flow velocity. Blade stall is accommodated through the use of empirical lift, drag and pitching moment coefficients.

In the wake, potential flow is assumed. Discrete vortices are shed into the wake at regular intervals, whose strength is equal to the incremental change in the bound vorticity at the blade in order to satisfy Kelvin's theorem, namely the

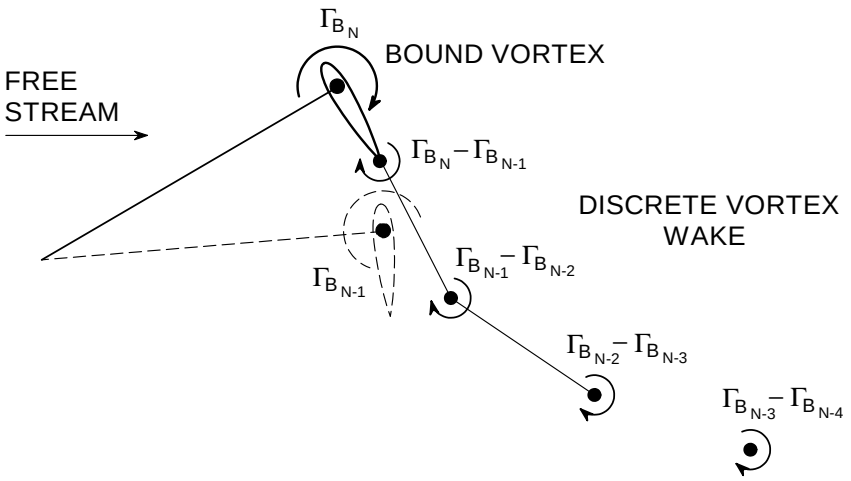

Figure 6.1: Discrete vortex representation of the unsteady blade wake

conservation of total system circulation (see Figure 6.1).

$$\Gamma_{W_N} = \Gamma_{B_N} - \Gamma_{B_{N-1}} \tag{6.2}$$

The velocity induced by the shed vortices is calculated at the turbine blades as well as at the locations of all of the wake vortices using the Biot-Savart law. Expressed in the $z = x + iy$ plane, the complex velocity induced by a point vortex at z_v of strength Γ_W is:

$$q(z) = \frac{-1}{2\pi i}\left(\frac{\Gamma_W(z - z_v)}{|z - z_v|^2}\right) \tag{6.3}$$

To remove the singularity at z_v, a smoothing factor δ is used to give a finite core radius, producing vortex 'blobs'. The simple core function is that used by Krasny (1987).

$$q(z) = \frac{-1}{2\pi i}\left(\frac{\Gamma_W(z - z_v)}{|z - z_v|^2 + \delta^2}\right) \tag{6.4}$$

The maximum induced velocity occurs at a radius δ, which is the 'core' radius. Following the method of Strickland et al. (1980), the core radius is chosen so that the maximum velocity induced by a vortex blob is equal to the velocity on either side of the trailing edge at the time that it is shed. From the definition of vorticity it may be seen that for an infinite vortex sheet the local vorticity is equal to the difference in tangential velocity immediately above and below the sheet. For a vortex blob at the trailing edge this velocity difference is taken to be twice the maximum induced velocity:

$$\gamma = 2V_{max} \tag{6.5}$$

By Kelvin's theorem, the strength of the vortex sheet arising from the trailing edge of a blade in motion is equal to the rate of change of bound vorticity relative to the rate of vortex sheet generation:

$$\gamma = \frac{\mathrm{d}\Gamma_B}{\mathrm{d}s} \tag{6.6}$$

where s is the path distance along the sheet. Using the maximum induced velocity from Equation (6.4), with Equations (6.5) and (6.6) we get:

$$\delta = \frac{\Gamma_W}{2\pi}\left(\frac{\mathrm{d}\Gamma_B}{\mathrm{d}s}\right)^{-1} \tag{6.7}$$

Then for discretised time, approximating Γ_W by $\Delta\Gamma_B$ and $\frac{\mathrm{d}\Gamma_B}{\mathrm{d}s}$ by $\frac{\Delta\Gamma_B}{\Delta s}$ we get:

$$\delta \approx \frac{\Delta s}{2\pi} \approx \frac{R\omega\Delta t}{2\pi} \tag{6.8}$$

where R is the turbine radius and ω is the rotor speed. The vortex core size is thus a function of the time interval Δt between vortices.

6.2.1 Treatment of unsteady aerodynamics

The same treatment methods used for the momentum model described in Section 5.1 were used for the vortex model. There are however different factors to be considered in the implementation of some of the semi-empirical dynamic stall models in a free vortex scheme. Semi-empirical models such as the Boeing-Vertol model incorporate the effect of the unsteady wake implicitly as they were developed on the basis of tests on oscillating foils in the wind tunnel, on which the measured forces were affected by the unsteady wake. Semi-empirical methods such as the Beddoes-Leishman model, which were developed from a theoretical basis that attempted to reflect the relevant physical processes, incorporate Duhamel summation of Kussner function indicial responses to a discretised history of changing angle of attack (refer to Leishman and Beddoes, 1989). As such it explicitly incorporates the effect of the unsteady wake.

Strickland et al. (1980) stated that the treatment of unsteady circulatory lift is handled automatically in an approximate fashion in a free vortex scheme by the downwash induced at the blade by the discrete vortex points tracked in the wake. The wake vorticity that is shed in response to step change in angle of attack mitigates the magnitude of that change. As the discrete vortex convects away from the blade, this 'downwash' reduces towards zero and the angle of attack approaches a steady state value. Thus the time-dependent nature of the response is inherently handled in an approximate way by the discrete vortex wake model, rather than by an empirically derived analytic method.

If a semi-empirical unsteady aerodynamic model is applied where the wake vorticity is modelled explicitly, the unsteady wake effects may in fact be treated twice. Jiang et al. (1991) recognised this in the application of the Beddoes-Leishman

model to their fixed-wake vortex model for VAWTs. However they reconciled this duplication by pointing out that the discrete vortex modelling of each blade's wake included the effect of wake influence on the other blades and on the same blade at subsequent crossings, while the semi-empirical unsteady aerodynamics model of course did not. They stated,

> "the degree of overlap [between the two methods] is considered small enough to be insignificant in the present analysis".

The geometry of the wake of a wing oscillating in a wind tunnel is very different from that in the case of the Darrieus turbine, even for similar histories of angle of attack experienced at the blade. For the former, the wake may have sinusoidal oscillations but is still basically linear in structure and is carried directly away from the aerofoil. For a Darrieus turbine, especially at high tip speed ratios, the wake is coiled into a much smaller space in the immediate vicinity of the blades and is repeatedly crossed. Thus its influence may be expected to be significantly different from that in the wind tunnel. If the only input to the semi-empirical unsteady aerodynamics model is the angle of attack history, then no account can be taken of the actual wake geometry.

For dynamic stall experiments in the wind tunnel the specified angle of attack is the geometric angle of the chord line with the free stream velocity, accounting for the aerofoil's own plunging and/or pitching velocity. No account is taken of the induced velocity or downwash at the foil due to the unsteady wake, as this cannot be measured directly and is indeed the very factor whose influence is being predicted.

In a discrete vortex wake model of a Darrieus turbine the influence of the unsteady wake on the angle of attack at the blade is already calculated. If a

semi-empirical model that is validated using wind tunnel data is to be applied to the calculation of unsteady lift on a Darrieus turbine blade then the influence of the wake should not be included in the calculation of angle of attack, so long as the semi-empirical model can accurately reproduce the effect of the omitted wake. However because such models assume an essentially linear wake shape, then it is unlikely that this will be done accurately.

Alternatively the effects of the unsteady wake could be omitted from the semi-empirical unsteady aerodynamics model and this aspect left to the influence of the discrete vortex wake. Leishman and Beddoes (1989) model the effect of the wake as the induction of a change in the effective angle of attack experienced at the blade. This change affects the unsteady lift under attached flow conditions, as well as delaying the onset of stall. This change in angle of attack is handled automatically by the discrete vortex wake. In addition to this however, they account for a time lag in the leading edge pressure response used to detect the onset of leading edge stall. They state that:

> "this mechanism significantly contributes to the overall delay in the onset of dynamic stall"

Further, there is a lag in the unsteady boundary layer response that further delays trailing edge separation. Both of these effects are separate from the wake effect and so are not modelled by the discrete vortex wake.

Modification of the angle of attack alone also cannot produce the increased maximum lift coefficients observed under dynamic conditions. In the Beddoes-Leishman model, this increased lift is provided to some extent by the extension of the linear lift slope region through the delay of trailing edge separation, but also through the addition of lift generated by the:

"excess accumulation of circulation lift that is retained in the vicinity of the airfoil..."

This circulation is transferred to the dynamic stall vortex that detaches from the leading edge and convects downstream over the upper (low pressure) surface of the blade before being shed into the wake. This aspect of dynamic behaviour is also not accounted for purely by modification of angle of attack. Hence ideally the non-wake dynamic effects should still be modelled separately and the wake effects left to the discrete vortex modelling of the wake.

The preceding discussion only applies to the circulatory lift component of the unsteady blade loading. The non-circulatory components, such as added mass effects, are not handled by the discrete vortex wake. Accordingly, in the present analysis, the angle of attack history incorporating the influence of the discrete vortex wake is used as input to the modified MIT dynamic stall model. Given the approximate nature of the semi-empirical model, any duplication of treatment of wake effects is regarded as insignificant.

6.3 Extension of the Vortex Method for Passive Variable-Pitch VAWTs

The basic Darrieus free vortex model is modified here in a number of ways.

Strickland et al. (1981) used a look-up table for lift and drag coefficients against angle of attack up to 180° for the NACA0012 section. No pitching moment coefficients were used. The aerodynamic coefficients were for a single Reynolds number. For the Darrieus turbine, not only does blade Reynolds number change appreciably with varying wind speed and tip speed ratio, but it also changes within each revolution. Accordingly tabulated coefficients spanning Reynolds numbers from

40,000 to 500,000 were used in the present model (data from Sheldahl and Klimas, 1981, presented in Lazauskas, 2002). At each timestep the Reynolds number based on blade chord and local relative flow velocity, as well as the angle of attack, is calculated. The appropriate lift, drag and pitching moment coefficients are then obtained from the tabulated data using bi-linear interpolation.

In the present work, the model has been coded in Visual C++ for Windows. The source code developed for this thesis is included on a CD inside the back cover of this thesis. A graphical user interface (GUI) has been implemented to facilitate the adjustment of parameter values. An animated display (see Figure 6.2) of the turbine and the vortex wake is generated so that the evolution of the wake and the motion of the blades can be viewed.

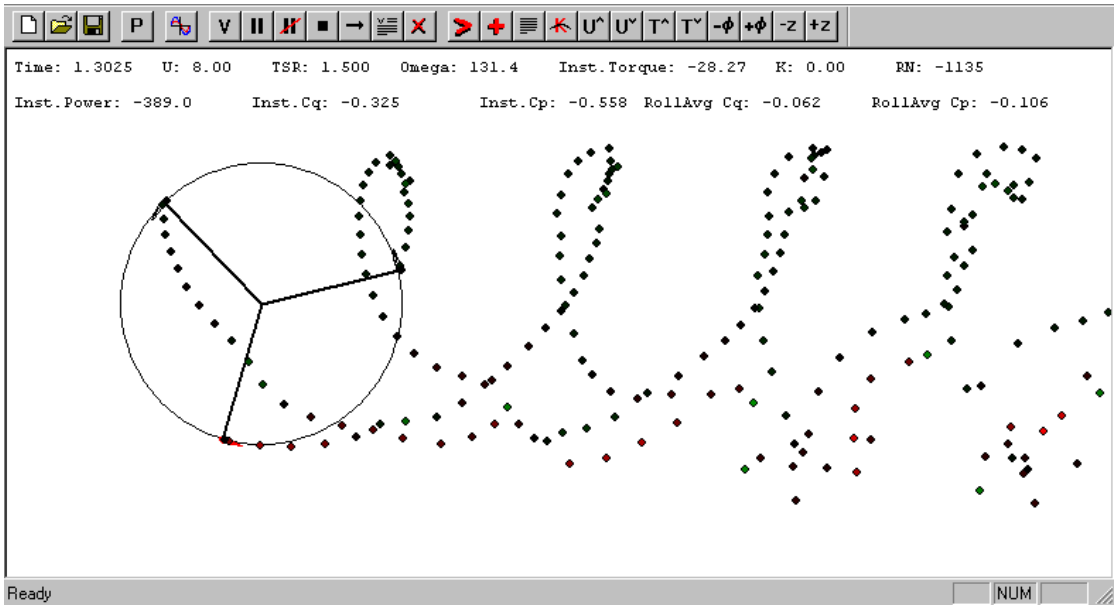

Figure 6.2: Screen capture of the animated output of the free vortex model

Strickland et al. (1979) used a prediction-correction method to calculate the strength of the bound vortex at each time step. The induced velocity at the blade element is calculated using the wake vortex positions and the bound vortex strengths at the other blade elements at the previous time step; the bound vortex

strength is calculated on the basis of this induced velocity; the induced velocities at all blade elements is then updated for these new values and the bound vortex strengths then recalculated.

Here a full iterative scheme is used to calculate bound vortex strength at each step. The reason for this is that problems were encountered with oscillation in the bound vortex strength. Any sudden change in the angle of attack, and hence change in bound vortex strength, produces a correspondingly large change in the strength of the wake vortex of opposite sense, following Equation (6.2). This wake vortex, which is still close to the blade at the following time step, induces a correction in the angle of attack at the blade, causing a change in bound vortex strength of the opposite sign. A wake vortex corresponding to this change is then shed, continuing the oscillation at the next time step. This process is usually instigated by the sharp change in lift occurring at blade stall. A string of wake vortices of alternating signs then results, along with a sharply oscillating angle of attack and lift history.

This instability is exacerbated by the use of a semi-empirical dynamic stall method, such as the Boeing-Vertol model, which is dependent on the instantaneous rate of change of angle of attack. If this is estimated using a simple first order backward difference then the oscillation in lift due to oscillation in angle of attack is amplified. A higher order backward difference estimate reduces the sensitivity of the value to the instantaneous angle.

In order to decouple the rate of change from the latest estimate of angle of attack completely, an approximate closed-form expression was derived. If the effect of changing rotor speed and non-uniformity in the wind field is neglected, the analytic expression for the instantaneous angle of attack may be differentiated

to obtain an estimate of the rate of change. The angle of attack on a blade at zero pitch is given by:

$$\alpha_0 = -(\gamma + \phi) \tag{6.9}$$

γ is the clockwise angle between the chord line and the relative wind vector and is calculated in the code by $\gamma = \text{atan2}(-W_x, -W_y)$. W_x and W_y are the x and y components of the relative wind velocity. They are given by:

$$\begin{aligned} W_y &= U_y + \dot{\phi} R \sin\phi \\ W_x &= U_x - \dot{\phi} R \cos\phi \end{aligned}$$

U_x and U_y are the components of the free wind velocity at the current blade position, ϕ is the blade's azimuth angle and R is the turbine radius. Differentiating (6.9) with respect to time and subtracting the pitching velocity $\dot{\theta}$:

$$\dot{\alpha}_0 = -\dot{\phi}[\dot{\phi} R(U_x \cos\phi - U_y \sin\phi - \dot{\phi} R)/W^2 + 1] - \dot{\theta} \tag{6.10}$$

where $W = \sqrt{W_x^2 + W_y^2}$.

This expression ignores the effect of the movement of the blade through a non-uniform and unsteady flow field, as well as specific local events such as wake crossings. However as the empirical angle modifying correlation for which the value is used as an input is itself inexact, it is felt that this error is not significant.

The MIT dynamic stall model is also inherently less sensitive to the instantaneous rate of change of the angle of attack and was found to be more stable.

This instability was treated by placing the next vortex to be shed at the trailing edge and including its influence in the calculation of the flow at the lifting-line. Since the strength of the trailing edge vortex is related to the velocity it induces at the lifting line by Equations (6.2) and (6.1), an iterative process is used to

calculate it and the bound vortex strength at each time step. This stabilises the calculation of bound circulation. Damped simple iteration, a technique in which each new estimate of the convergence variable is moderated by a comparison with the previous estimate (see de Vahl Davis, 1991), is used to treat the same instability previously exhibited over successive time steps, now shown over successive iterations at each time step.

This process also allows wake vortices to be shed less frequently than every time step if desired. The string of vortices shed by each blade is a discrete representation of the continuous vortex sheet that is shed as a result of the ever-changing angle of incidence experienced by the blade through each revolution. It is the nature of this representation that a large number of vortices of small strength is not necessarily preferable to a smaller number of vortices of greater strength. It has been shown by Moore (1981) that dividing the sheet into more vortices only serves to exacerbate the problems of instability that eventually appear in the modelling of the roll-up of such sheets. In addition, CPU time increases with the square of the number of vortices. Therefore it is desirable to make the time interval between shedding of vortices larger than the time step required for accurate numerical integration of the equations of motion of the turbine mechanism, even with a fourth-order scheme.

It was discovered however that decoupling the vortex and turbine motion integration time steps caused problems. Because the velocity induced by a vortex blob according to Equation (6.4) is inversely proportional to the distance from it, its effect on the velocity at the lifting line diminishes as it is convected away from the blade. If a vortex is shed at each time step, the closest (most recently shed) vortex is always at approximately the same distance from the lifting line and so the effect is relatively smooth. If a vortex is shed only every third time step, wake vorticity for three time intervals is accumulated in a single vortex blob and

when it is shed, there is a significant and abrupt change in the flow induced at the lifting-line. This effect decays as the vortex is convected away until another vortex is shed and another spike in the angle of attack at the lifting-line occurs.

By maintaining a trailing edge vortex whose strength is calculated iteratively to satisfy Equation (6.2) at each time step, the spikes in the flow produced each time a vortex is shed are smoothed. The trailing edge vortex is shed into the wake after a set interval, to be replaced by a new trailing edge vortex, initially of zero strength. This method effectively represents the most recently shed portion of the blade wake by a discrete vortex blob at the trailing edge.

The blade incidence history may be further smoothed by representing this nearest wake region using straight vortex sheet segments, in the manner of Fink and Soh (1978). The two most recently shed free wake vortices are replaced by straight vortex sheet segments joining them and the trailing edge, (see Figure 6.1) in the calculation of the velocity induced at the lifting-line. These segments are desingularised in the same manner as the vortex blobs, as suggested by Krasny (1987). This ensures that the sensitivity of the lifting-line circulation to the wake strength is not exaggerated by the concentration of the most recently shed part at the trailing edge.

6.4 Validation Using Published Results

Several researchers have compared their vortex models with the experimental results obtained by Strickland et al. (1981). A rotor with 1, 2 or 3 straight fixed-pitch blades of NACA 0012 section was tested in a water tow tank. The turbine had the following parameters:

Blade chord	9.14 cm
Turbine diameter	1.22 m
Blade length in water	1.1 m
Tow tank depth	1.25 m

Strain gauges were used to measure the normal and tangential forces on the blades. Dye injection in the water was used to observe the 'streak line' of particles passing over the trailing edge. Images of the streak lines were compared with predicted wake structures from the VDART2 program. Reasonable agreement between analytical and experimental results was achieved, though some areas of discrepancy existed. The primary area of difficulty appears to lie with the dynamic stall model. Strickland resorted to modifying the empirically derived stall delay time constants of the Boeing-Vertol model in order to obtain better agreement with experimental data. Even so there are major areas of discrepancy and no single set of values could be found to best fit all tested operating points.

Cardona (1984) published results from a modified vortex model that included the effects of flow curvature and modified the application of the Boeing-Vertol dynamic stall model. He claimed this improved agreement, though there are still regions of significant discrepancy.

Ponta and Jacovkis (2001) recently developed a vortex model incorporating a finite element calculation of the blade forces and near flow field. The free vortex model is used to compute the 'macro' flow field and its results are used as boundary conditions for the 'micro' local blade model, which is based on a finite element solution of the constant-curl Laplacian equation. The velocities in each region are calculated iteratively at each time step to find the bound vorticity. Surface pressures and shear forces calculated by a viscous boundary layer model are then

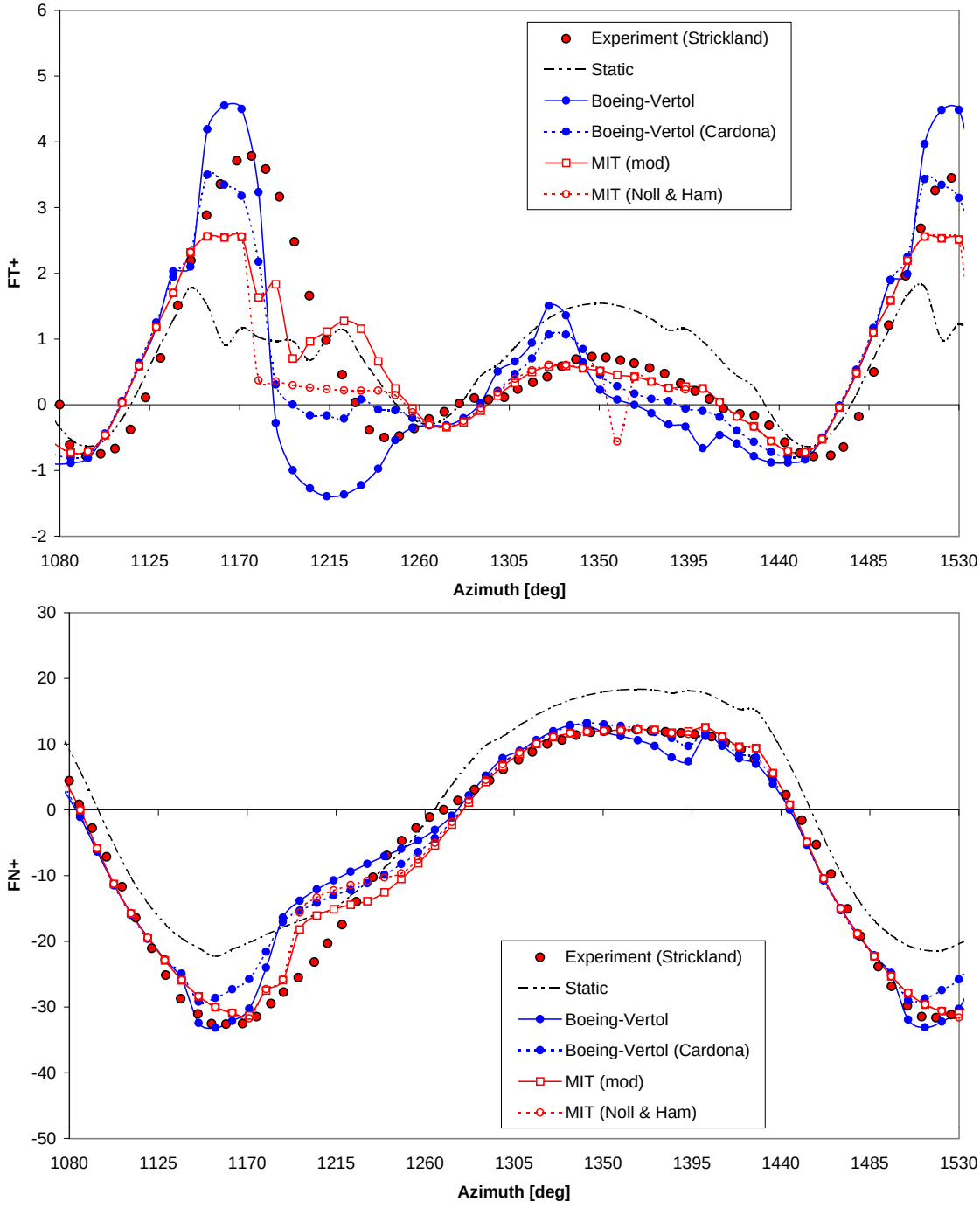

Figure 6.3: Comparison of predicted non-dimensionalised tangential and normal forces $FT+$ and $FN+$ for three different dynamic stall treatments with the experimental data of Strickland et al. (1981). 1 blade, TSR = 5.

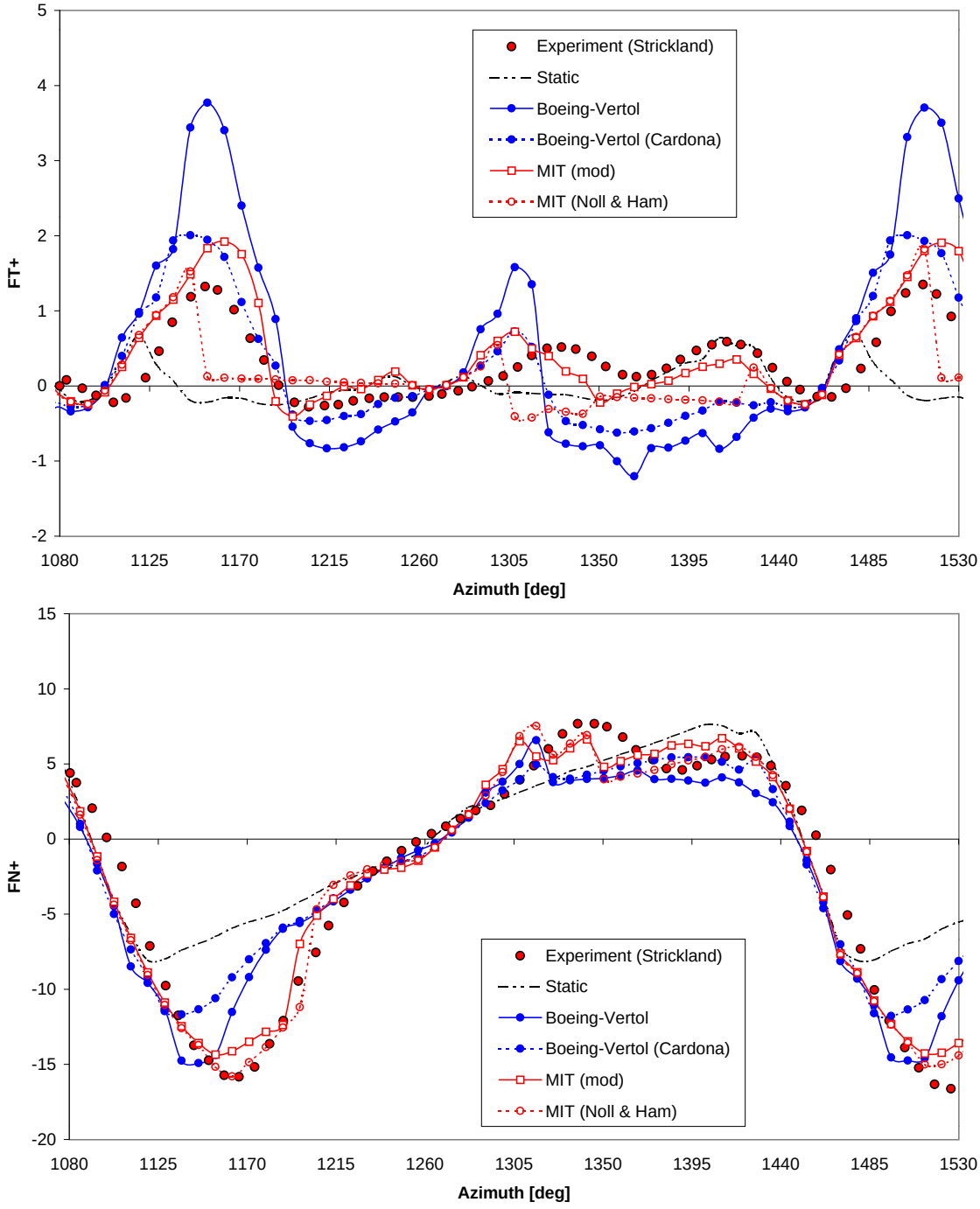

Figure 6.4: Comparison of predicted non-dimensionalised tangential and normal forces $FT+$ and $FN+$ for three different dynamic stall treatments with the experimental data of Strickland et al. (1981). 2 blades, TSR 2.5

used to compute blade forces. The circulatory and added mass effects are thus accounted for naturally and there is no reliance on experimental static aerofoil coefficients. The finite element model however is only applied prior to stall. Once separation is detected, the method reverts to the standard vortex model using aerofoil coefficients and so the issue of dynamic stall, which appears to be the most problematic, is not addressed. Nevertheless the results obtained for normal and tangential blade forces and wake structure visualisation show good agreement with Strickland's experimental data.

Tangential and normal force predictions for two tip speed ratios tested by Strickland et al. are shown in Figures 6.3 and 6.4. The degree of agreement in general is reasonable considering the simplifying assumptions made. Primary among these is the assumption of 2 dimensionality, which is dubious as the experimental rig had a blade length of 1.1 m and a gap of 15 cm to the bottom of the tank. The effect of the trailing tip vortex is not accounted for in the model.

Results for the dynamic stall models implemented in the code are compared. These are the Boeing-Vertol model; the Boeing-Vertol model as modified by Cardona; the MIT model as modified by Noll and Ham; and the MIT model with present modifications. All of the above models were used in conjunction with the measures to account for finite aspect ratio, flow curvature and dynamic effect. Included for reference are the predictions using the unmodified static section coefficients.

For the TSR = 5 case shown in Figure 6.3 none of the dynamic stall models are able to accurately predict the upwind (left hand half of the graph) pass peak. The Boeing-Vertol model overestimates the peak and then predicts a significant undershoot to negative values on the descending side that does not appear in

the experimental values. The Cardona modification mitigates this effect, but still underpredicts the duration of the peak. Noll and Ham's MIT model underpredicts the size of the peak and then exhibits an extended period of almost zero tangential load that does not occur in the experiment. This is the post-stall region in which the tangential load would be exactly zero were it not for the slight angle of attack and drag coefficient modifications for finite aspect ratio and flow curvature. The modified MIT method designed to remedy this shows improved but still imperfect agreement with measured values. The descending portion of the tangential force curve around azimuth = 1200° shows artifacts of the model's representation of lift decay and flow reattachment after stall that appears to be problematic. The MIT models give by far the best agreement with experimental values for tangential force in the downwind pass (azimuth 1260° - 1440°).

Note that if no account is taken of dynamic effects then the upwind tangential force peak is greatly truncated, indicating stall.

All three models give good agreement with normal force data at TSR = 5, though the fact that these forces are an order of magnitude greater than the tangential loads makes the agreement appear better. Again all three models have difficulty matching the smooth decline from the negative peak at azimuth 1170° (the upwind most point of the orbit) that was measured by Strickland et al.. The measured values seem to indicate that no blade stall occurred at this TSR, despite the fact that if no dynamic stall model is used, the tangential and normal force peak in the upwind half of the revolution is truncated to less than half of the measured peak, indicating flow separation. All the literature surveyed on dynamic stall indicated the presence of significant hysteresis in lift, drag and moment coefficients, with reattachment delayed to lower angles of attack than under static conditions.

This separation and delayed reseparation is apparently triggered when the angle of attack reaches a maximum and starts to decrease, even if stall would not have occurred at this angle had pitching continued beyond it. The experimental results seem to indicate that flow separation has not occurred at any stage, despite the excursion to angles greater than the static stall angle. This phenomenon is not predicted by any of the dynamic stall models examined. Nevertheless the quality of agreement is reasonable.

Agreement for the TSR = 2.5 case shown in Figure 6.4 is not as good, with all dynamic stall models overpredicting the upwind tangential force peak at azimuth 1160°. The Cardona modified Boeing-Vertol model show and the modified MIT model show best agreement here, but the MIT model shows much better agreement over the rest of the revolution.

The MIT models show the best level of agreement for normal force. Again the inadequacy of ignoring dynamic effects at this TSR are highlighted.

Figures 6.5 and 6.6 show comparisons between vortex model predictions with the various dynamic stall models and the experimental results published by Paraschivoiu (1983). He presented normal and tangential force coefficient data for a small straight-bladed turbine operating in air.

Blade chord	6.1 cm
Turbine diameter	0.61 m
Blade length	0.61 m
Blade section	NACA 0018

In general the level of agreement with these results is not as good as with those of Strickland et al. The modified MIT model gives a marginally better prediction of the measured results than the other models, however there are still

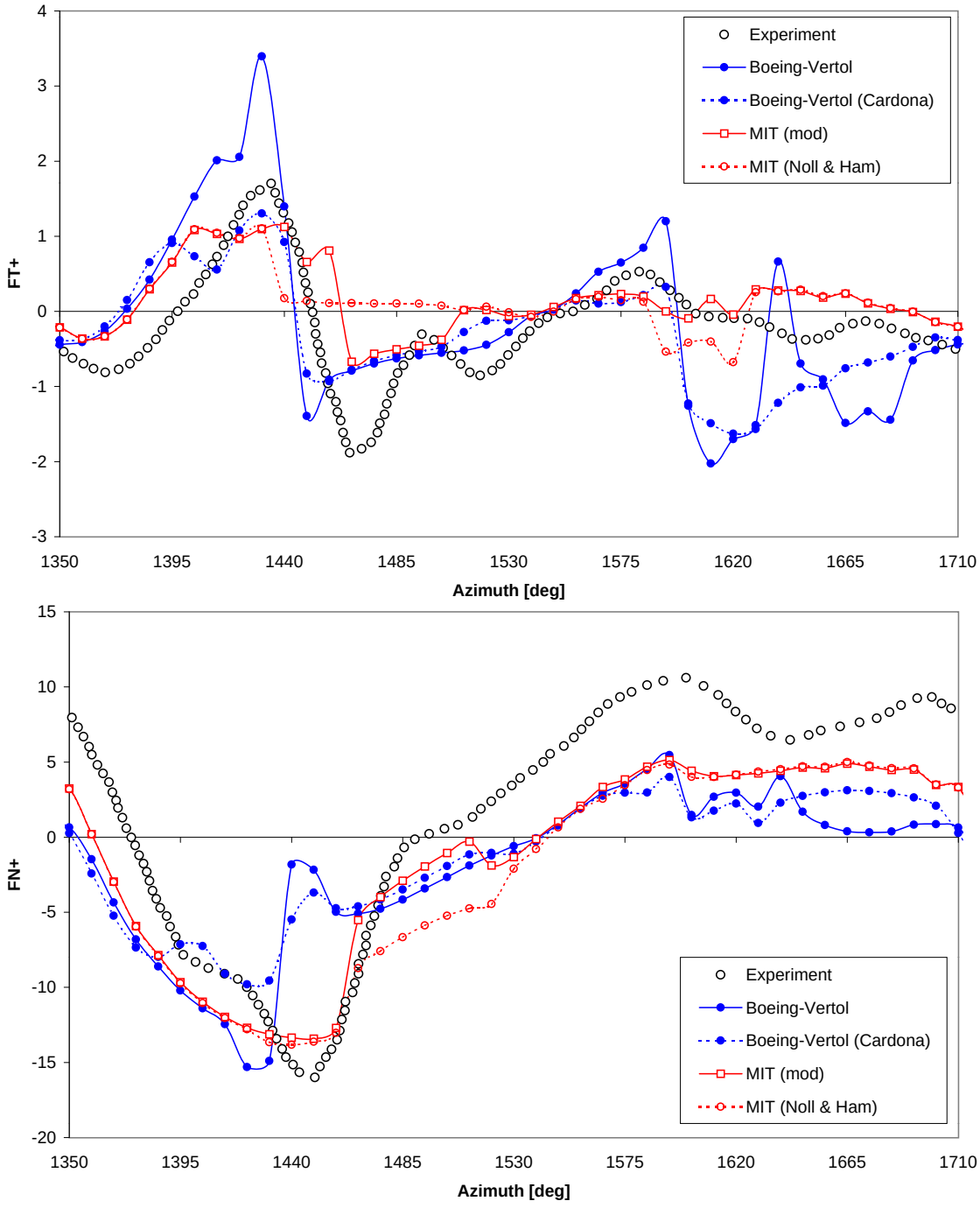

Figure 6.5: Comparison of predicted non-dimensionalised tangential and normal forces $FT+$ and $FN+$ for three different dynamic stall treatments with the experimental data of Paraschivoiu (1983). 2 blade, TSR = 3.

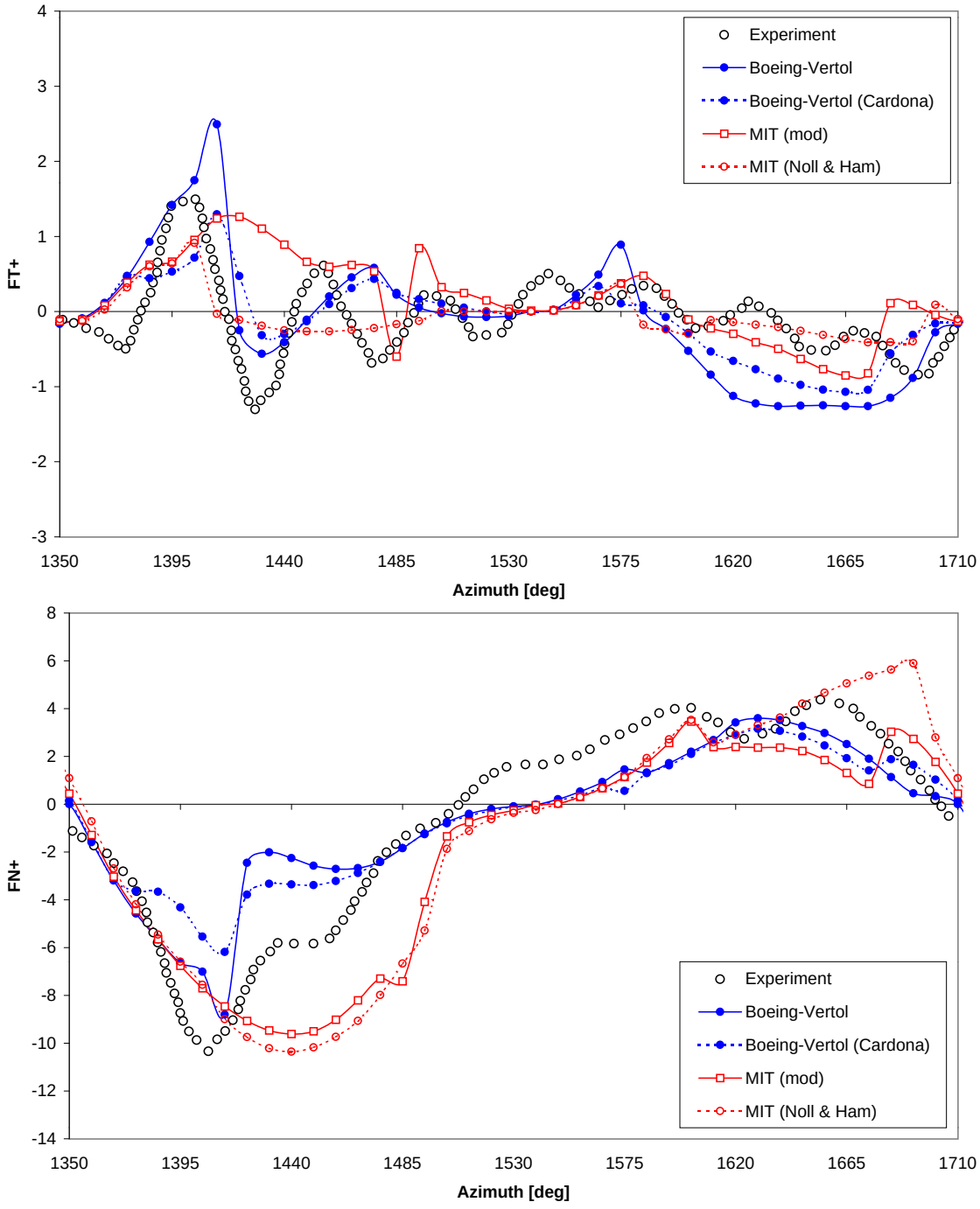

Figure 6.6: Comparison of predicted non-dimensionalised tangential and normal forces $FT+$ and $FN+$ for different dynamic stall treatments with the experimental data of Paraschivoiu (1983). 1 blade, TSR 1.5

areas of significant discrepancy. The measured tangential force data for TSR 1.5 in Figure 6.6 shows an oscillation that may be due to some vibration in the turbine. The MIT model, both in its unmodified and modified forms, grossly overpredicts the upwind (negative) peak in the normal force, while the Boeing-Vertol models underpredict.

Overall it is concluded that the MIT method, with modifications described in Appendix B, offers the best agreement with experimental results of the models tested. However none of the models is able to capture all of the details of the blade force histories measured in the experiment.

6.5 Limitations of Vortex Methods

While vortex methods incorporate a good deal more of the complexities of Darrieus turbine aerodynamics than momentum models, they still rely on significant simplification. Potential flow is assumed in the wake and the effect of viscosity in the blade aerodynamics is included through empirical force coefficients. The present model is two dimensional. For a turbine with straight blades of large aspect ratio, this simplification is acceptable. While the affect of finite aspect ratio is accounted for in the modification of sectional lift and drag coefficients, spanwise flow and trailing tip vortices have not been included. Turbine shaft or tower shadow has also been neglected in the present model.

The primary area of limitation is still the handling of unsteady aerodynamics, as it has been for more than twenty years. It is clear that researchers have investigated many different approaches to the modelling of this area that is so important for accurate prediction of Darrieus turbine performance. These range from the entirely empirical to complete first-principles CFD approaches, with almost every possible blend of the two in between. Clearly a compromise must be

reached between accuracy and simplicity. Because the real flow is so complex, the diminishing returns of accuracy gained for ever greater investment of effort in first principles approaches make the use of semi-empirical methods attractive.

Even so, the free vortex method is still expensive in terms of computing requirements. The repeated use of the Biot-Savart law is the main cause of this expense. For example if 200 discrete vortices are maintained for each of three blades, $600^2 = 360,000$ Biot-Savart induced velocity calculations are required at each time step. The method is several orders of magnitude more time consuming than the momentum method and it is not practical to perform comprehensive optimisation studies using it. This task remains the domain of more economical methods, for conditions under which their accuracy is known and acceptable.

6.6 Motion Simulation Model

Existing momentum theory methods assume constant turbine speed and steady-state operation. These assumptions are limiting in the study of the self-starting performance of passive variable-pitch turbines.

The steady-state pattern of pitch angle variation predicted under the assumption of constant turbine speed may be slightly different from the actual pitch variation for a turbine with finite rotor and load inertia where speed ripple is likely to exist. The angular acceleration of the turbine rotor affects, and is affected by, the pitching motion of the blades.

In addition, for the study of starting performance, the turbine will naturally be accelerating, rather than operating at steady-state. Further, the passive variable-pitch mechanism is intended to be applied to small stand-alone systems, almost certainly driving non-constant speed and maybe non-electrical loads. Therefore in fluctuating wind, turbine speed will almost always be changing. Acceleration

will be shown to have significant effect on the predicted pitch pattern and on the average torque over a single revolution.

In addition to transient blade motion, the unsteady wake may also affect aerodynamic loads. When the turbine is heavily loaded, the deceleration of the flow is significant. It may take a finite time for the wake to fully develop and if the turbine speed and the wind speed are varying, the instantanteous performance at a given tip speed ratio may be different from that at steady state with a fully developed wake.

In order to accommodate these factors, turbine acceleration must be included in the mathematical model. It is then necessary to model the entire turbine as a single mechanism with multiple degrees of freedom. This differs from the initial approach of assuming a constant turbine speed (effectively infinite rotor or load inertia) and tracking the motion of a single blade under the influences of aerodynamic, elastic and inertial forces. This single degree of freedom system permitted the use of Newton's vector method to arrive at the differential equation of motion by use of a free body diagram. If the turbine speed is allowed to vary however, it becomes necessary to calculate the rotor acceleration at every time step, since this both affects and is affected by the motions of all of the blades at that instant. It is therefore no longer possible to model only a single blade and to take its motion as representative of the remaining blades.

The principle of virtual work is much better suited to deal with this multi-degree-of-freedom system than is Newton's approach. It enables the motions of interconnected bodies to be tracked without reference to any joint or constraint forces. D'Alembert's principle allows application of the virtual work principle to dynamic systems by including inertia forces. The Lagrangian form of the virtual

work principle, which uses a set of generalised coordinates to describe the system position, is used to produce a set of differential equations of motion, one equation for each degree-of-freedom. The linear set of differential equations is solved to calculate the instantaneous accelerations of all generalised coordinates.

A numerical integration scheme is then used to predict the change in positions and velocities of all bodies in the system during a timestep. As for the momentum model, a fourth-order Runge-Kutta scheme is used for this purpose.

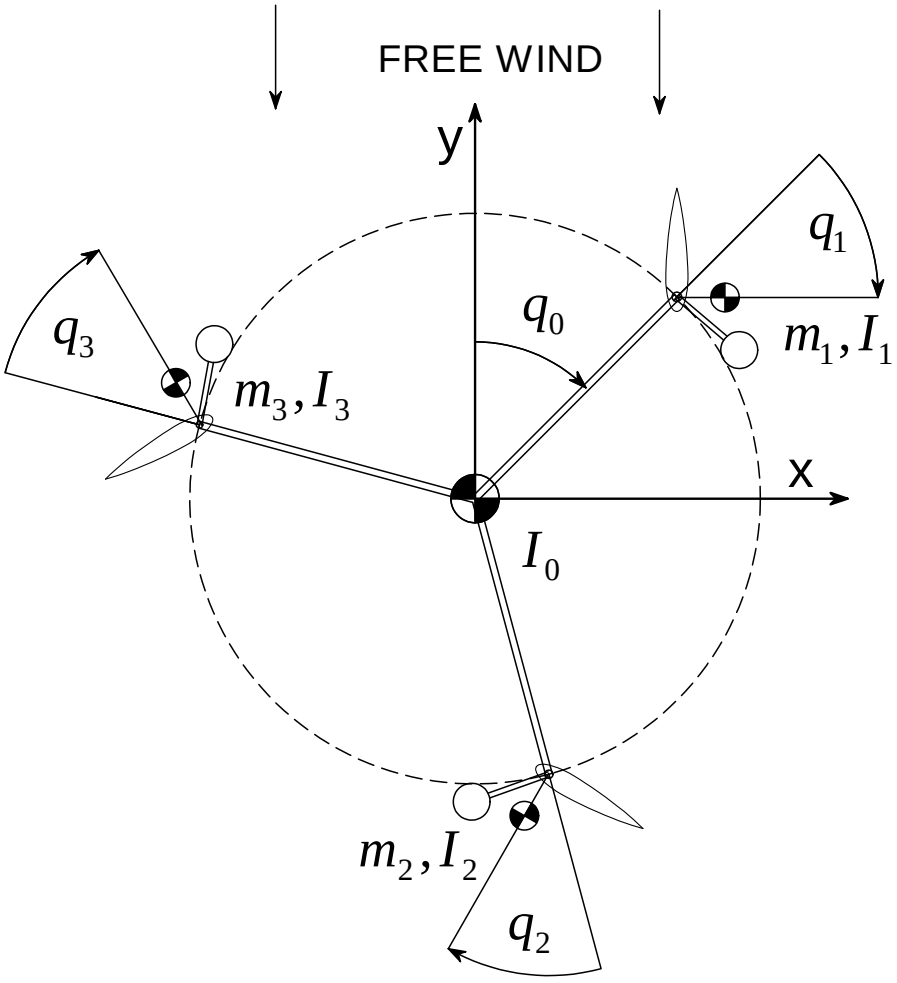

Figure 6.7: Schematic of turbine mechanism defining the generalised coordinates q for a turbine of the pendulum type.

For the pendulum type configuration studied by Bayly and Kentfield (1981) the turbine may be modelled as an open-loop planar mechanism - effectively a

number of double pendula connected at the turbine shaft (see Figure 6.7). A set of F = n+1 generalised coordinates is used for a turbine having n blades: one for the pitch angle of each blade and one for the rotor azimuth angle. q_0 is defined as the azimuth angle of the reference blade, being the clockwise angle specifying the orbital position of the blade relative to the wind direction. q_1 to q_n are the blade pitch angles.

The notation used by Paul (1979) is adopted, but the equation is reformulated here in matrix form. The velocity coefficients for the M = n+1 members relate the velocity of the mass centres of the members to the rate of change of each of the F generalised coordinates. The coefficients are termed U, V and Ω for the x, y and clockwise directions respectively, as defined in Figure 6.7. For example, the coefficient U_{ij} gives the influence of the rate of change of the generalised coordinate q_j on the x-direction velocity of the i-th member of the assembly. That is:

$$\dot{x}_i = \sum_{j=0}^{n} U_{i,j} \cdot \dot{q}_i \tag{6.11}$$

or in matrix form

$$\begin{pmatrix} \dot{x}_0 \\ \dot{x}_1 \\ \vdots \\ \dot{x}_n \end{pmatrix} = \begin{pmatrix} U_{00} & U_{01} & \dots & U_{0n} \\ U_{10} & U_{11} & \dots & U_{1n} \\ \vdots & \vdots & \ddots & \vdots \\ U_{n0} & U_{n1} & \dots & U_{nn} \end{pmatrix} \cdot \begin{pmatrix} \dot{q}_0 \\ \dot{q}_1 \\ \vdots \\ \dot{q}_n \end{pmatrix}$$

In matrix notation:

$$\dot{\mathbf{x}} = \mathbf{U} \cdot \dot{\mathbf{q}} \tag{6.12}$$

The rotor centre of mass is assumed fixed at the origin and has zero velocity at all times, so all coefficients relating to its translation are zero. The change in the pitch angles of the blades has no kinematic effect on the rotor speed. Therefore all coefficients concerning the rotor are zero, except that relating the generalised coordinate for the azimuth to the rotor position, which is one.

$$\begin{aligned} U_{0j} &= V_{0j} = 0 \quad \text{for} \quad j = 0, 1, 2, ...n \\ \Omega_{00} &= 1 \\ \Omega_{0j} &= 0 \quad \text{for} \quad j = 0, 1, 2, ...n \end{aligned}$$

The velocity of the mass centre of the each blade is affected by both the rotor azimuth and that blade's pitch angle, but is independent of the pitch angles of any other blade. For the 'pendulum' type inertial pitch control design shown with three blades, the velocity coefficient matrices are:

$$\mathbf{U} = \begin{pmatrix} 0 & 0 & 0 & 0 \\ A(q_0, q_1) & B(q_0, q_1) & 0 & 0 \\ A(q_0, q_2) & 0 & B(q_0, q_2) & 0 \\ A(q_0, q_3) & 0 & 0 & B(q_0, q_3) \end{pmatrix} \tag{6.13}$$

$$\mathbf{V} = \begin{pmatrix} 0 & 0 & 0 & 0 \\ C(q_0, q_1) & D(q_0, q_1) & 0 & 0 \\ C(q_0, q_2) & 0 & D(q_0, q_2) & 0 \\ C(q_0, q_3) & 0 & 0 & D(q_0, q_3) \end{pmatrix} \tag{6.14}$$

$$\mathbf{\Omega} = \begin{pmatrix} 1 & 0 & 0 & 0 \\ 1 & 1 & 0 & 0 \\ 1 & 0 & 1 & 0 \\ 1 & 0 & 0 & 1 \end{pmatrix} \tag{6.15}$$

where

$$\begin{aligned} A(q_0, q_i) &= R\cos(q_0 + \phi_i) + R_{cg}\cos(q_i + q_0 + \phi_i) \\ B(q_0, q_i) &= R_{cg}\cos(q_i + q_0 + \phi_i) \\ C(q_0, q_i) &= -R\sin(q_0 + \phi_i) - R_{cg}\sin(q_i + q_0 + \phi_i) \\ D(q_0, q_i) &= -R_{cg}\sin(q_i + q_0 + \phi_i) \end{aligned}$$

These kinematic relations may be replaced by those applicable to any other design. These are given in Appendix A.

ϕ_i is the azimuth angle of blade i when q_0 is zero. For the three bladed turbine $\phi_i = 0°$, $120°$, $240°$ for $i = 1, 2, 3$ respectively. The elements of these matrices must be updated for the current values of the generalised coordinates at each timestep.

The accelerations of the mass centres of the members are also defined in terms of coefficients. For example in the x-direction:

$$\ddot{x}_i = U_i + \sum_{j=0}^{n} U_{i,j} \cdot \ddot{q}_i \tag{6.16}$$

The coefficients summed in the second term are the velocity coefficients defined above. The first term is the acceleration coefficient for the i-th member, which is a function of both the generalised velocities and displacements. In matrix notation,

the x-direction acceleration is given by:

$$\ddot{\mathbf{x}} = \mathbf{U}' + \mathbf{U} \cdot \ddot{\mathbf{q}} \tag{6.17}$$

Similar equations exist for the y and clockwise directions. For the rotor, the acceleration coefficients are all zero. The acceleration coefficient matrices are:

$$\mathbf{U}' = \begin{pmatrix} 0 \\ E(q_0, \dot{q_0}, q_1, \dot{q_1}) \\ E(q_0, \dot{q_0}, q_2, \dot{q_2}) \\ E(q_0, \dot{q_0}, q_3, \dot{q_3}) \end{pmatrix} \tag{6.18}$$

$$\mathbf{V}' = \begin{pmatrix} 0 \\ F(q_0, \dot{q_0}, q_1, \dot{q_1}) \\ F(q_0, \dot{q_0}, q_2, \dot{q_2}) \\ F(q_0, \dot{q_0}, q_3, \dot{q_3}) \end{pmatrix} \tag{6.19}$$

where

$$\begin{aligned} E(q_0, \dot{q_0}, q_i, \dot{q_i}) &= -R_{cg}(\dot{q_0} + \dot{q_i})^2 \sin(q_i + q_0 + \phi_i) - \\ &\quad R\,\dot{q_0}^2 \sin(q_0 + \phi_i) \\ F(q_0, \dot{q_0}, q_i, \dot{q_i}) &= -R_{cg}(\dot{q_0} + \dot{q_i})^2 \cos(q_i + q_0 + \phi_i) - \\ &\quad R\,\dot{q_0}^2 \cos(q_0 + \phi_i) \end{aligned}$$

All the angular acceleration coefficients are zero. Again, the form of these coefficients is specific to the pendulum type turbine. Expressions for the other types of turbine discussed in this thesis are given in Appendix A.

To treat an elastic type system, the expressions are the same, but the mass centre radial offset R_{ac} may be set to zero. The spring moment on each blade is included as an external moment with magnitude calculated based on the instantaneous pitch angle. An equal and opposite moment must be applied to the rotor.

For the rolling profile design concept, the appropriate kinematic relationships must be used to define the velocity and acceleration coefficients. These are given in Appendix A.

External forces are also expressed in generalised terms. The generalised force component Q_j corresponding to q_j is defined by:

$$Q_j = \sum_{i=0}^{n} (X_i \cdot U_{ij} + Y_i \cdot V_{ij} + M_i \cdot \Omega_{ij}) \tag{6.20}$$

or in matrix notation:

$$\mathbf{Q^T} = \mathbf{X} \cdot \mathbf{U} + \mathbf{Y} \cdot \mathbf{V} + \mathbf{M} \cdot \mathbf{\Omega} \tag{6.21}$$

where $\mathbf{X}$,$\mathbf{Y}$ and $\mathbf{\Omega}$ are vectors containing the x, y and clockwise external forces and moments acting at the centre of mass of each of the members. In this case these are the aerodynamic forces and pitching moments acting on the blades. The external forces acting directly on the rotor are the neglected but a load torque may be applied.

Paul defines a vector C whose elements represent the inertia forces on the members due to centripetal and Coriolis accelerations. The term corresponding to

the q_j is given by:

$$C_j = \sum_{i=0}^{n} (U_i' m_i U_{ij} + V_i' m_i V_{ij} + \Omega_i' J_i \Omega_{ij}) \tag{6.22}$$

In matrix notation:

$$\mathbf{C^T} = \mathbf{U'}^{\,\mathbf{T}} \cdot \mathbf{m} \cdot \mathbf{U} + \mathbf{V'}^{\,\mathbf{T}} \cdot \mathbf{m} \cdot \mathbf{V} + \mathbf{\Omega'}^{\,\mathbf{T}} \cdot \mathbf{J} \cdot \mathbf{\Omega} \tag{6.23}$$

using the diagonal mass and inertia matrices defined as:

$$\mathbf{m} = \begin{pmatrix} m_{rotor} & 0 & 0 & 0 \\ 0 & m_{blade} & 0 & 0 \\ 0 & 0 & m_{blade} & 0 \\ 0 & 0 & 0 & m_{blade} \end{pmatrix} \tag{6.24}$$

$$\mathbf{J} = \begin{pmatrix} J_{rotor} & 0 & 0 & 0 \\ 0 & J_{blade} & 0 & 0 \\ 0 & 0 & J_{blade} & 0 \\ 0 & 0 & 0 & J_{blade} \end{pmatrix} \tag{6.25}$$

where the J terms are the polar mass moments of inertia about the respective centres of mass.

The generalised inertia matrix is the square FxF symmetric matrix whose elements are defined as:

$$I_{rj} = \sum_{i=0}^{n} (U_{ir} m_i U_{ij} + V_{ir} m_i V_{ij} + \Omega_{ir} J_i \Omega_{ij}) \tag{6.26}$$

in matrix notation:

$$\mathbf{I} = \mathbf{U^T} \cdot \mathbf{m} \cdot \mathbf{U} + \mathbf{V^T} \cdot \mathbf{m} \cdot \mathbf{V} + \mathbf{\Omega^T} \cdot \mathbf{J} \cdot \mathbf{\Omega} \tag{6.27}$$

The above matrices are used to form the equation of motion derived from Lagrange's form of d'Alembert's principle:

$$\sum_{i=0}^{n} \left(Q_i - C_i - \sum_{j=1}^{F} I_{ij} \cdot \ddot{q}_j \right) \cdot \dot{q}_i = 0 \tag{6.28}$$

The matrix form of the equation of motion is:

$$(\mathbf{Q} - \mathbf{C} - \mathbf{I} \cdot \ddot{\mathbf{q}}) \cdot \dot{\mathbf{q}} = \mathbf{0} \tag{6.29}$$

The instantaneous accelerations may be found by solving the equation for $\ddot{\mathbf{q}}$. For general velocities, Equation (6.29) requires:

$$(\mathbf{Q} - \mathbf{C} - \mathbf{I} \cdot \ddot{\mathbf{q}}) = \mathbf{0} \tag{6.30}$$

The solution is found by performing Gaussian elimination on the augmented matrix:

$$[\quad \mathbf{I} \quad | \quad (\mathbf{Q} - \mathbf{C}) \quad]$$

with matrices updated for the instantaneous positions, velocities and external forces. The position and speeds at time t+Δt can be found through numerical integration. Here a fourth-order Runge-Kutta numerical integration scheme is used.

6.7 Constrained Cases

For comparison purposes it is sometimes desirable to simulate the performance either of a fixed bladed turbine whose speed is allowed to vary, or of a passive variable-pitch turbine whose speed is held constant. For these constrained cases the general procedure above is modified to remove the redundant degrees of freedom.

For the first case the system reverts to a single degree-of-freedom. The blades may be fixed or their motion may be prescribed as a function of the azimuth, as for a cycloturbine. The generalised force for the rotor degree of freedom is calculated as normal, but an additional external load is added to account for the moment on the blades that is now transmitted directly to the rotor and the moment required to produce the prescribe blade motion.

For the second case, because the rotor speed is prescribed, the top row of the normal augmented matrix is removed and the remaining rows (one for each of the blades) are row-reduced to find the pitching accelerations.

6.7.1 Calculation of turbine torque

At any instant there is a certain torque applied to the turbine by aerodynamic loads on the blades. Because the blades of a passive variable-pitch turbine are free to move, not all of this torque is automatically available at the turbine shaft. The shaft torque may be found by calculating the reaction forces acting on the rotor itself at the blade connections. Since the Lagrangian analysis does not calculate the internal reactions of the mechanism, these must be found by performing a separate kineto-static analysis for each blade.

The joint reactions include the inertial loads due to the oscillating blades as well as the aerodynamic forces on them. Both Bayly and Kentfield (1981) and Kirke and Lazauskas (1992) neglected inertial effects of the swinging blades on the rotor

torque. Both considered the blade inertia in predicting the pitch response, but assumed that only the aerodynamic forces on the blade contributed to torque, as is true for a fixed bladed turbine. At high speeds and for heavy blades, fluctuating tangential inertial loads may be significant. In a detailed study of turbine dynamics including possible speed ripple, the inclusion of such loads may be important. Also, while for a periodically oscillating blade at steady-state the fluctuating tangential reaction at each blade pivot due to the inertia of the blade should integrate to almost zero, it is possible for some net energy to be imparted or lost through hysteresis in the aerodynamic loads.

Where the blade has a fixed pivot axis, the torque contributed by the blade is equal to the product of the tangential reaction force at the connection and the turbine radius. For the rolling profile type design, because the contact point moves fore and aft, the torque contribution also involves the normal reaction force. The total rotor torque at any instant is the sum of these contributions from all blades.

Whether or not the turbine accelerates under the influence of the torque depends on the load connected to the shaft. Speed may be held constant either through an actively controlled load or an effectively infinite inertia passive load. If the load torque at that speed is less than the torque applied to the rotor by the blades then the turbine will accelerate. In this case the power generated by the turbine is split between the load and acceleration of the rotor. In either case useful work is performed. The self-starting of the turbine is the focus of this work and is a task that otherwise must be performed by an external energy source.

In order to obtain a measure of turbine performance that accounts for both of these outputs, the total torque is taken to be the sum of the load torque at the shaft and the torque used to accelerate the turbine. This is calculated as the turbine

acceleration multiplied by the total turbine and load inertia. For this purpose the blades and rotor are considered as a single body. This provides an smoothed estimate of the torque, as the instantaneous motion of the blades relative to the rotor is neglected.

Alternatively, the total torque may be estimated by performing the kineto-static analysis of the blades to find the joint reactions assuming the rotor acceleration to be zero. This method allows the fluctuating inertial reactions arising from pitching acceleration to still be included. If these fluctuating loads happen to integrate to some non-zero value over a complete revolution then this is included in the torque.

6.8 Validation of Motion Simulation Code using Pro/MECHANICA

In order to validate the motion simulation part of the code, results were compared with those generated by the commercial motion simulation package Pro/MECHANICA. A simplified scenario was modelled, consisting of three blades mounted on a rotor, with a constant magnitude downwind force applied to each blade. Body masses and moments of inertia were matched and the time step in each set at 0.02 s. A damping moment of 0.05 Nm/rad/s was applied to the pitch axes. The radial location of the mass centre of the blade with respect to its pivot axis was adjustable, as was the location of the 'aerodynamic centre' or point of application of the constant wind force.

The motion of the blades and the rotor was tracked for 315 time steps. The predicted pitch angles for the three blades are shown in Figure 6.8. Note that for clarity the vortex program's results have been thinned, only every tenth time step

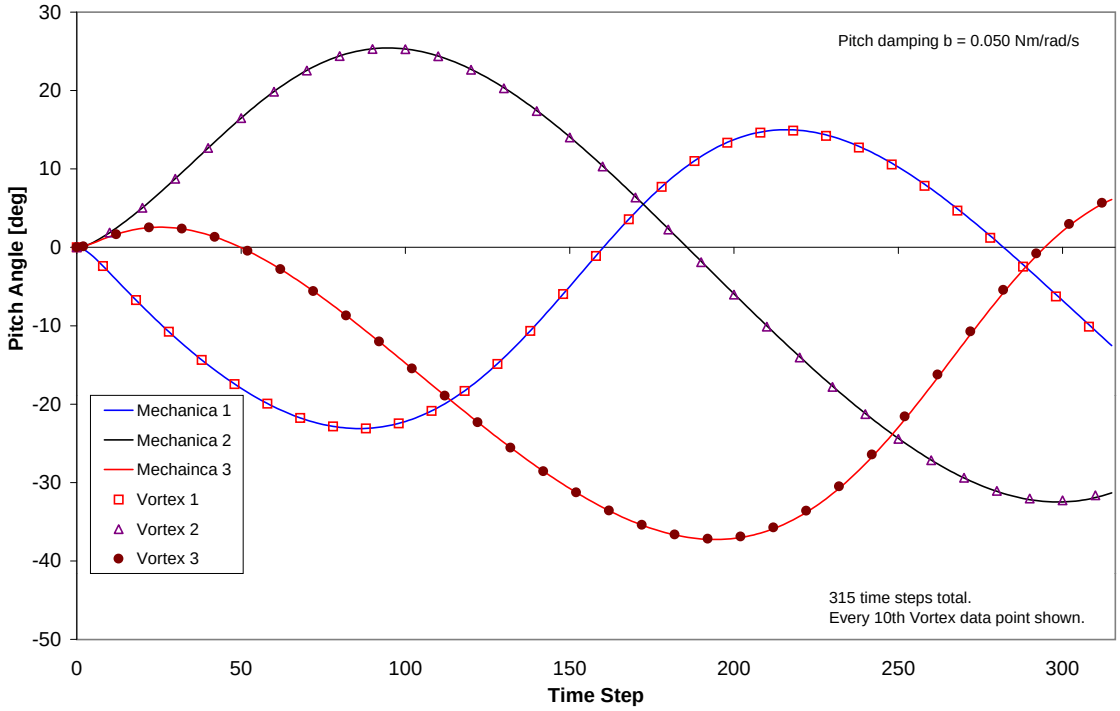

Figure 6.8: Comparison of Pro/MECHANICA and vortex code predicted pitch responses for constant wind force. Note that the vortex data has been thinned for clarity.

is shown. The maximum discrepancy in pitch angle at the end of 315 time steps is 0.33°. This level of agreement gives confidence that the motion simulation module of the vortex code is free from errors.

6.9 Comparison with Momentum Method

Simulations were run for a turbine of the pendulum type, shown in Figure 6.7, with the parameters shown in Table 6.1. R_{ac} is the distance from the pivot axis to the aerodynamic centre, assumed to be at the quarter chord, and its value determines the magnitude of aerodynamic pitching moment. R_{cg} is the distance from the pivot axis to the centre of gravity of the blade assembly and it determines the magnitude of the restoring moment on the blade.

Diameter:	6 m
Height:	3 m
Blades:	3 NACA0018
R_{ac}:	20 mm
R_{cg}:	45 mm
Blade chord:	400 mm
m_{blade}:	28 kg
J_{blade}:	2.7 kgm^2
J_{rotor}:	500 kgm^2

Table 6.1: Turbine parameters for DMS - vortex model comparison

The present vortex method and the Double Multiple Streamtube method described in Chapter 5 were used to predict turbine performance at a wind speed of 10 m/s and two different tip speed ratios.

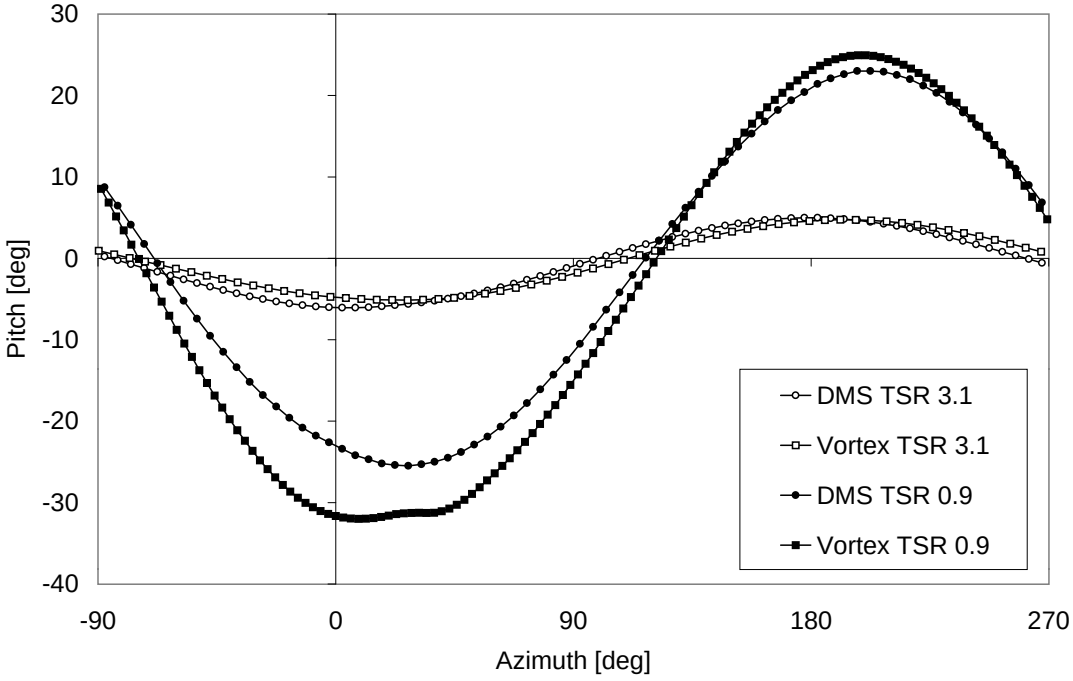

Figure 6.9: Predicted pitch response for vortex method and Double Multiple Streamtube (DMS) method.

The predicted pitch responses are shown in Figure 6.9. At TSR = 3.1 the turbine is at steady state, connected to a load whose torque is proportional to the square of turbine speed. At TSR = 1 the turbine is accelerating when connected

to the same load. The steep positive slope of the torque-speed curve prevents the turbine from having a stable operating point at this TSR. Instead it is accelerating up to the stable operating point at TSR = 3.1

At TSR = 1 the difference in pitch response predicted by the DMS and vortex methods is largely due to the acceleration of the turbine. When using the DMS model to study the starting behaviour of this type of turbine, stable operation is assumed at all speeds, even if this is not possible when connected to a realistic passive load. The difference in pitch response between steady-state and transient cases is clear at this TSR. The difference is partly due to the different velocity field predicted for the transient case, but is largely due to the effect of acceleration of the rotor. The TSR increased from 0.89 to 1.03 during the course of this revolution. The average torque calculated for the revolution by the DMS model is 277 Nm, while the average torque for the transient vortex case is 343 Nm, including torque driving the load and accelerating the turbine. The significant difference between the two values is due to the difference in pitch response, especially in the azimuth range -90° to +90°, which is the upwind half of the orbit. The greater pitch amplitude in this region reduces the amount of time spent by the blade in stalled conditions, increasing the time spent developing useful torque.

The difference in the pitch responses at TSR = 3.1 is largely due to the difference in the velocity fields predicted by the models. The difference in average torque is much smaller at this speed: 438 Nm for the DMS model and 417 Nm for the vortex model.

The torque variations for one of the blades is shown in Figure 6.10.

While the momentum model is much simpler than the vortex model, it achieves good agreement in the calculation of integrated quantities such as average torque

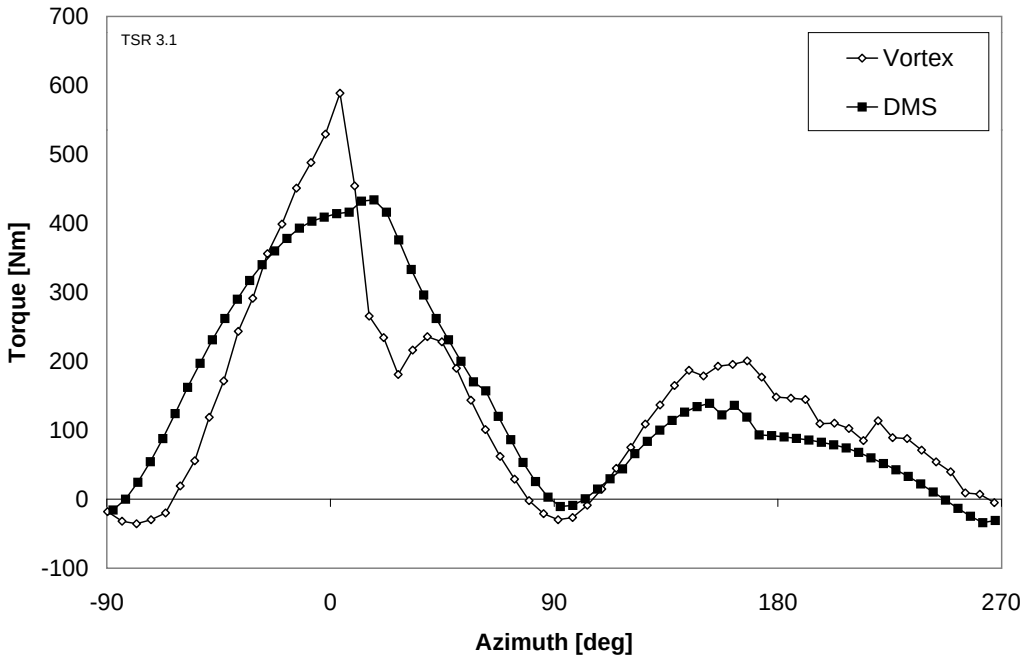

(a)

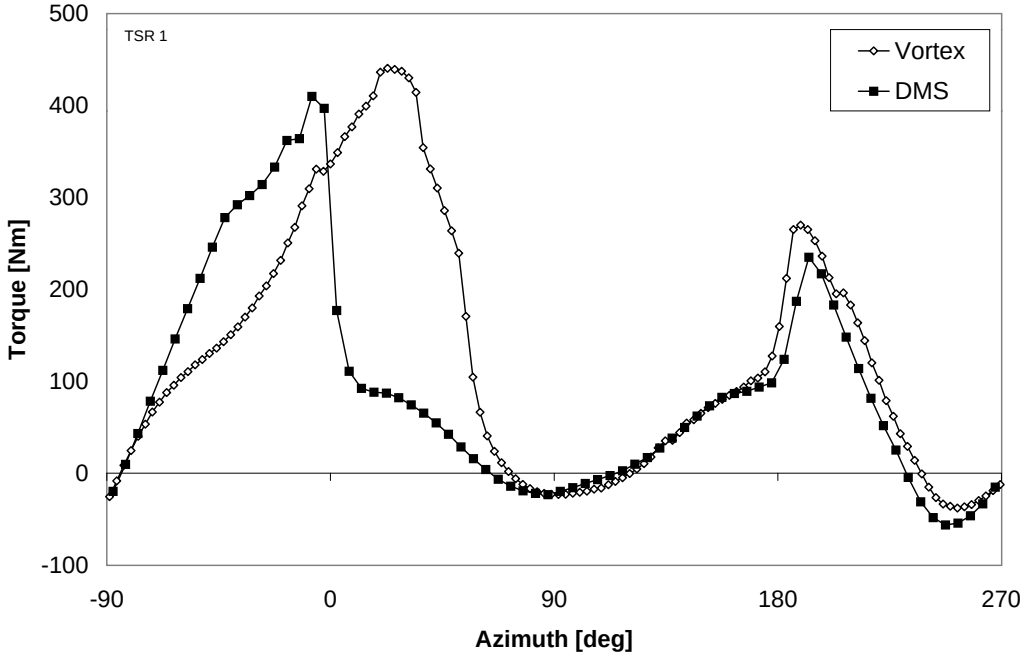

(b)

Figure 6.10: Predicted torque variation for vortex method and Double Multiple Streamtube (DMS) method. (a) TSR = 3.1; (b) TSR = 1.0

at steady-state. However the prediction of starting performance using a steady-state analysis may lead to significant discrepancies, not only in the instantaneous

quantities, but also in averaged values. The free vortex model is better suited to study of this aspect of turbine performance, which is critical to variable-pitch turbines of this type.

6.10 Conclusion

A free vortex wake model has been developed for passive variable-pitch Darrieus turbines. The model incorporates a motion simulation module that treats the entire turbine as a multi-degree of freedom mechanism. The model provides the more accurate and detailed aerodynamic load prediction commonly claimed for standard vortex codes in comparison with momentum models. It also allows prediction of transient turbine performance, which is important in the study of self-starting ability as well as turbulent wind output.

Chapter 7

Development of a Parameter Selection Strategy for Passive Variable-Pitch Systems

7.1 Introduction

The passive variable-pitch systems examined in Chapter 3 each consist in essence of a blade free to pitch under the influence of aerodynamic forces, regulated by some restoring moment, be it elastic or inertial in origin. For each specific design, the magnitudes of the aerodynamic and restoring moments may be adjusted by selection of the values of a number of design parameters. The predicted performance has proven to be very sensitive to the values of these parameters. A logical basis for the selection of appropriate values was therefore sought.

7.2 Study of Blade Pitch Response Using Pro/MECHANICA

7.2.1 Introduction

The Pro/MECHANICA model of a three-bladed pendulum type passive variable-pitch turbine described in Chapter 4 has been used to study the effect of variation in key design parameters on the blade pitch response. The polar moment of inertia of the blade assembly and the magnitude of the aerodynamic and inertial moment arms were varied and the predicted pitch responses in a steady wind were compared.

7.2.2 Simulation method

The Reynolds number for the simulations was assumed to be constant at 80,000, based on a blade chord length of 150 mm and a free wind speed of 6 m/s. The lift and drag coefficients used to calculate the aerodynamic forces on the blades were those published by Lazauskas (2002) based on the data of Sheldahl and Klimas (1981) for the NACA 0018 profile at this Reynolds number.

The model described in Chapter 4 allowed the variation of the blade polar moment of inertia for a given mass. It also allowed the parameters R_{ac} and R_{cg} to be varied. These are the distance from the pivot axis to the aerodynamic centre for the blade (assumed to be at the quarter chord) and the distance from the pivot axis to the centre of mass respectively. These moment arms determine the relative strengths of the restoring inertial moment and the driving aerodynamic moment on the blade.

Eight different blade parameter sets were examined. The ratio of aerodynamic moment to inertial moment was kept constant by fixing the ratio $R_{ac} : R_{cg}$ (see Figure 7.1). The value of this ratio was arrived at by a process of trial and error as one which produced favourable results over a range of tip speed ratios.

Each configuration tested is identified by the value of the normalised aerodynamic centre offset, $\bar{R}_{ac}$ defined as R_{ac}/c, where c is the blade chord. Here $c = 150$ mm with turbine radius, $R = 860$ mm. The polar mass moment of inertia of the blade assembly about the pivot axis varies with $\bar{R}_{ac}$ as shown in Figure 7.1.

For each configuration the steady state blade pitch cycle was obtained with the tower vibration degrees of freedom locked. Initially this was attempted by setting an arbitrary load magnitude on the turbine shaft and an arbitrary initial turbine

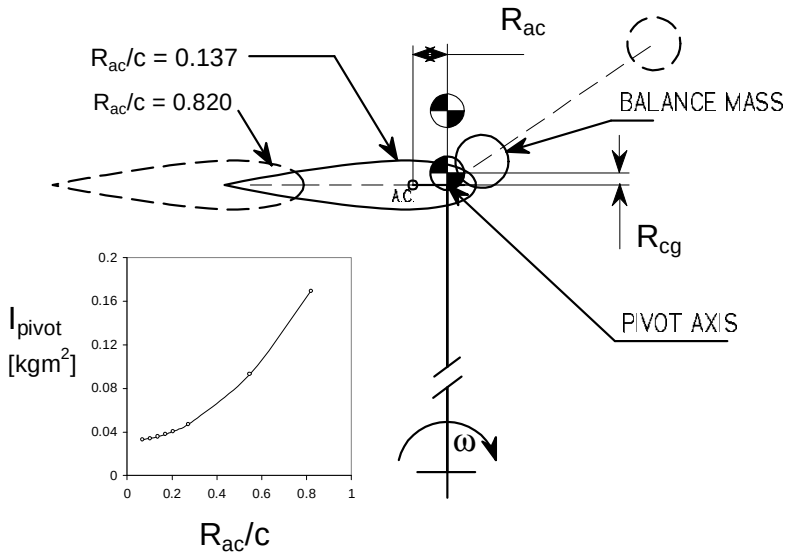

Figure 7.1: Definition of parameters R_{ac} and R_{cg}.

velocity and allowing the turbine to proceed towards an equilibrium velocity and pattern of pitch variation.

No equilibrium was reached without viscous damping in the blade pin joints. A damping moment of 20 Nmm/(rad/s) was accordingly applied. It was discovered that this approach still did not readily yield a steady-state operating point, especially for large values of R_{cg}, with correspondingly large polar moments of inertia.

In addition, for much of the speed range the turbine torque curve increases sharply with speed, precluding the possibility of a stable operating point. Consequently a "driver" was used to fix the turbine speed at a predetermined value and the turbine was allowed to run until the blade pitch cycles reached steady state.

The simulation time required to reach steady-state increased with the value of $\bar{R}_{ac}$ of the blade configuration. The arrangements with the largest inertia required an initially larger damping coefficient, which was then progressively reduced with time until the final value of 20 Nmm/rad/s was reached.

Once steady-state had been reached, blade pitch cycles and driver shaft torque histories were recorded for a simulation run of 5 seconds (500 timesteps at 0.01s) for each configuration.

7.2.3 Results

Fixed speed steady-state tests

Figure 7.2 shows the average torque for each configuration. It was found that there was a threshold value of $\bar{R}_{ac}$ below which torque was (highly) negative. Above the threshold, torque was positive, but decreased with increasing $\bar{R}_{ac}$ to a minimum before rising slightly again. The reason for this distribution is apparent from the

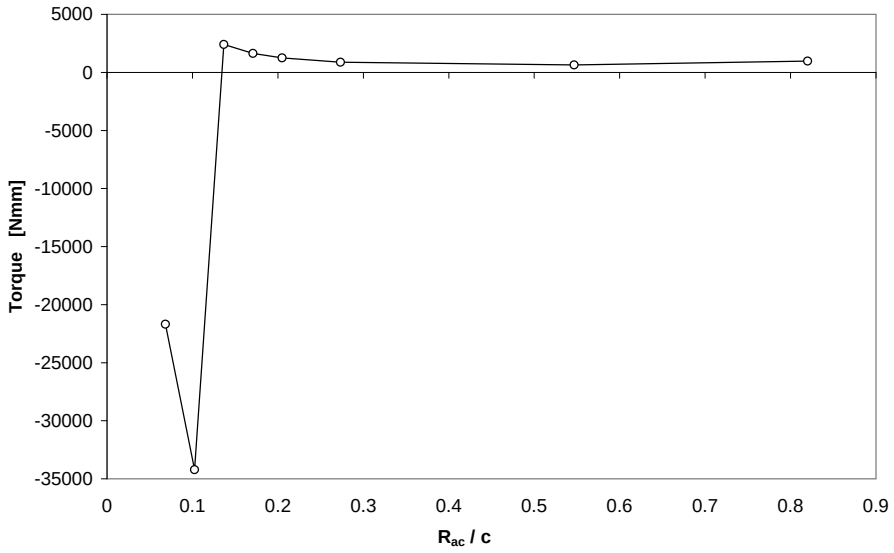

Figure 7.2: Pro/MECHANICA steady-state average torque results

steady state pitch cycles for the various configurations shown in Figure 7.3. For all cases the pitch response is essentially sinusoidal. As $\bar{R}_{ac}$ is decreased from the maximum value the amplitude of the pitch response increases. However for those cases where $\bar{R}_{ac}$ is less than 0.137 the amplitude increases markedly and the phase of the response changes. The sharp drop in torque that corresponds to this change

is due to the fact that the pitch response becomes significantly out of phase with the variation in incident wind direction.

As was shown in Figure 1.4 (page 11), the angle of attack variation on a fixed blade is almost sinusoidal for tip speed ratios greater than one. In order to maintain angles of attack of the correct sign for positive thrust to be generated, the pitch response of the blades must be similarly sinusoidal and, ideally, in phase with the zero-pitch angle of attack. If the phase angle between zero-pitch angle of attack and pitch angle becomes too large, the blade then experiences angles of attack of the wrong sign to produce lift with a forward component. Figure 7.4 shows the variation in angle of attack on one of the blades for two of values of $\bar{R}_{ac}$ tested. The configuration with the greater pitch amplitude ($\bar{R}_{ac} = 0.103$) is almost completely out of phase with the zero-pitch angle of attack.

The amplitude and phase of the blade pitch responses varies with the polar moment of inertia in a fashion consistent with the variation in natural frequency of the blade assembly.

While the turbine speed is constant, each blade can be regarded as a pendulum suspended in an inertial field, where centrifugal force takes the place of gravity. Ignoring the small variation in this acceleration with radius (and so with pitch angle) for small angles the damped natural frequency is

$$\omega_d = \sqrt{\left[\frac{mR_{cg}R\dot{\phi}^2}{I + mR_{cg}^2}\right] - \left[\frac{b}{2(I + mR_{cg}^2)}\right]^2} \tag{7.1}$$

where m is the mass of the blade assembly; R is the turbine radius; $\dot{\phi}$ is the turbine speed; b is the pitch axis damping coefficient; I is the blade moment of inertia about its centre of mass. For small damping the natural frequency is an almost

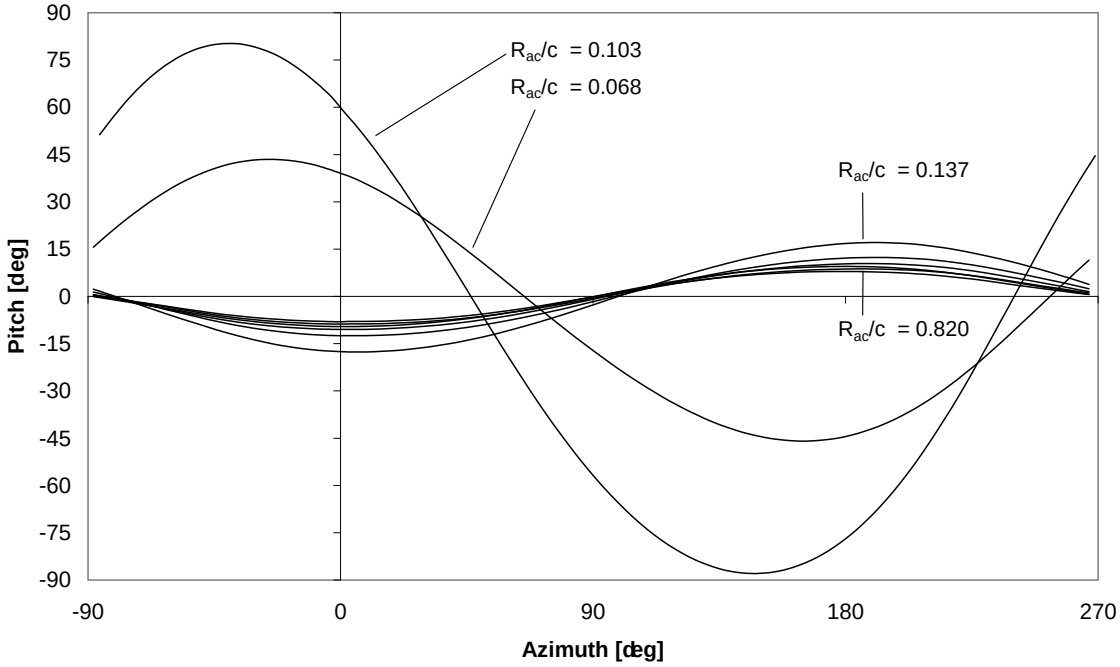

Figure 7.3: Pro/MECHANICA steady-state pitch responses

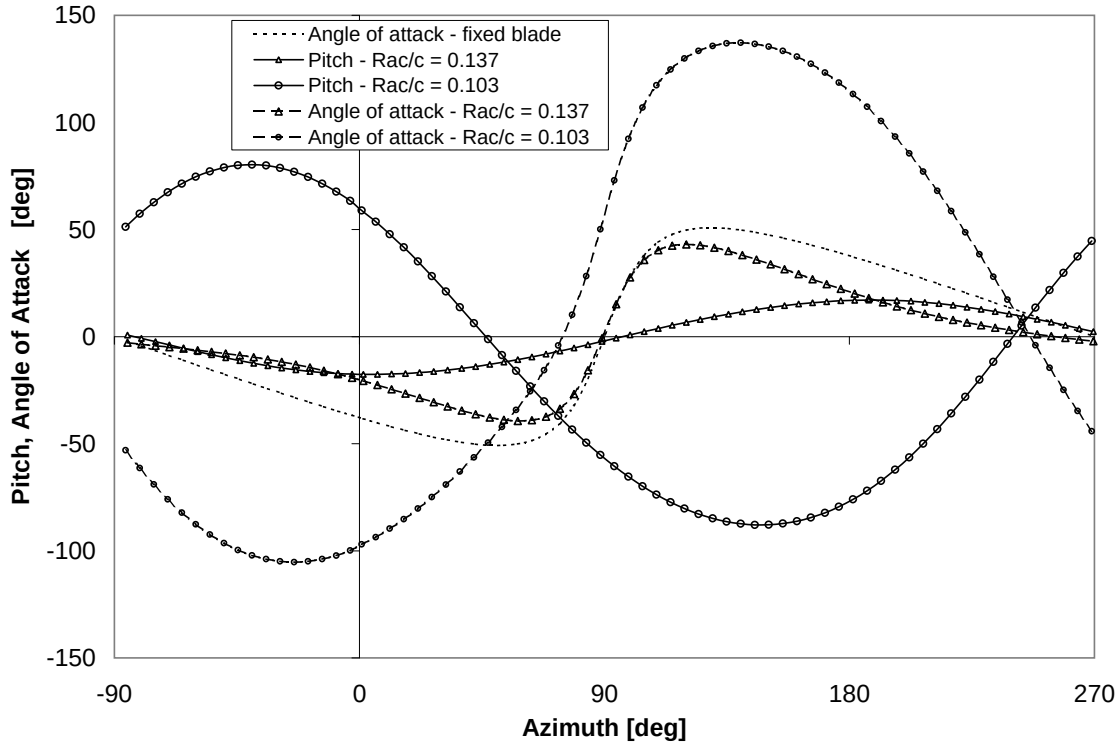

Figure 7.4: Comparison of the Pro/MECHANICA steady-state pitch and angle of attack patterns for two values of $\bar{R}_{ac}$.

linear function of the rotor speed, so frequency ratio ω/ω_d is almost independent of speed.

The blade pitch response is akin to that of a single degree-of-freedom system being excited by an approximately harmonic driving force. While the natural frequency is higher than the running speed (the frequency ratio is less than one), the motion of the blades is close to being in phase with the driving aerodynamic force. However once the natural frequency drops through and below the running speed, the response amplitude increases greatly and the phase angle passes through 90° toward 180°. This is shown in Figure 7.5. According to Equation 7.1 the frequency ratio is one when $\bar{R}_{ac}$ is equal to approximately 0.1.

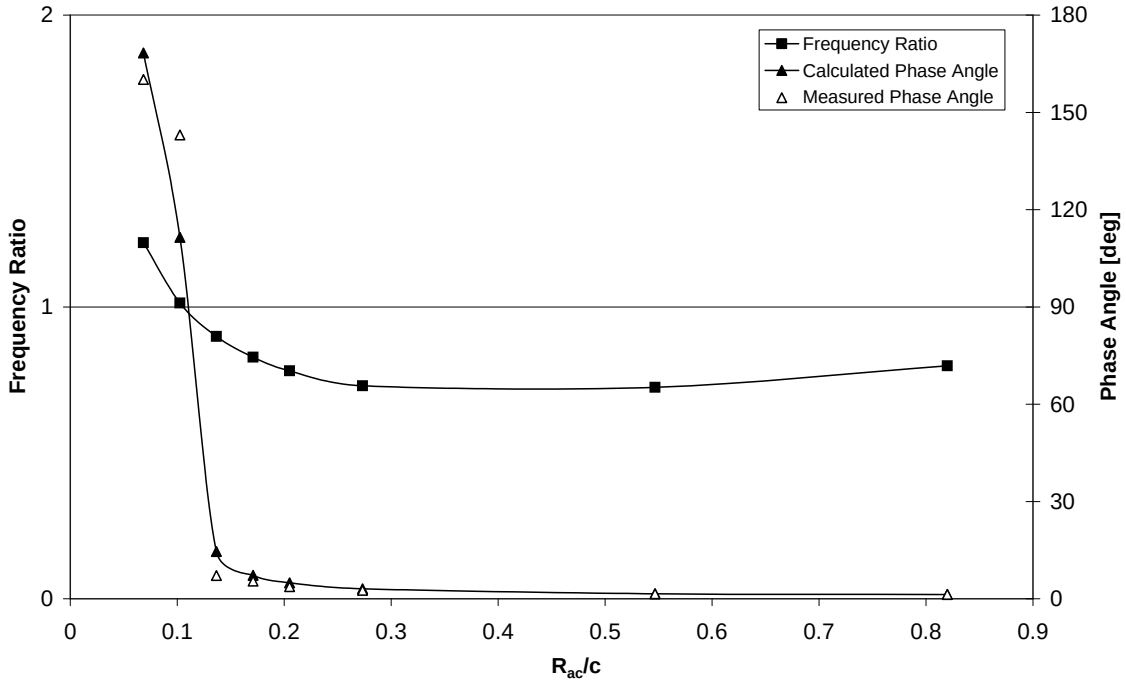

Figure 7.5: Calculated mass-spring-damper system frequency ratio and phase angles. The pitch response phase angles estimated from the zero-crossings are also shown.

The greatest output torque achieved here is at $\bar{R}_{ac} = 0.137$, for which the frequency ratio is 0.90. This point represents a trade-off between the large pitching

amplitude and small phase angles required to prevent stalling of the blades over a significant portion of the revolution.

Variable speed steady-state tests

In order to investigate the significance of rotor speed fluctuations, further simulations were performed for two of the configurations with the driver removed. Turbine average speed was held (approximately) constant over the 5 second run by applying a shaft torque proportional to the square of the turbine speed, in the style of a hydraulic load. The magnitude of the load was set so as to produce an average torque equal to the average torque that the driver had applied when holding the turbine at that constant speed.

Results for the these runs were almost identical to those with the driver in place. This finding reflects the small magnitude of speed fluctuations. Fluctuations have a three per period cycle for the three bladed turbine. It is apparent that interaction between blades and rotor is minimal at steady-state because the effect of each blade, which may be quite significant, tends to be cancelled out by those of the other blades.

Transient response results

Further simulation runs were then conducted with the blades started from the zero pitch position and allowed to progress towards steady state over 15 seconds. This was done for two values of $\bar{R}_{ac}$ (0.137 and 0.820), first with speed fixed at 9 rad/s and then with an initial velocity of 9 rad/s and the same hydraulic load as before. The pitch angle histories (for one of the blades) are shown in Figure 7.6. It can be seen that the interaction between blade and rotor for $\bar{R}_{ac} = 0.137$ is minimal and steady state operation is already being approached after 15 seconds.

By comparison the pitch histories for the driver and free cases for $\bar{R}_{ac} = 0.820$ diverge markedly, indicating the effect on pitch of fluctuation in rotor speed.

The turbine accelerations for steady state and transient cases are shown in Figure 7.7. For $\bar{R}_{ac} = 0.137$, (b), the magnitudes of the acceleration variations are not greatly different. For $\bar{R}_{ac} = 0.820$ however the transient case exhibits significantly larger acceleration peaks than the steady state case. It is also the only case for which a regular three per revolution pattern (reflecting the three blades) has not developed by the end of the 6th revolution. This reflects the stronger coupling between blade pitch speed and turbine speed associated with larger moments of inertia I_{pivot} and greater mass centre offsets (R_{cg}).

While minimisation of I_{pivot} and R_{cg} does not appear to be critical to steady state performance, it does affect transient performance and especially the time taken to adjust to a change in conditions, such as a change in wind velocity. The performance of the turbine in the turbulent conditions inevitably encountered in the field is likely to be highly dependent on these parameters.

Turbine shaft reaction forces

The shaft radial reaction forces predicted by Pro/MECHANICA for two parameter sets ($\bar{R}_{ac} = 0.137$ and 0.820) are shown in Figure 7.8. These results are for the constant speed (driver) simulation runs at steady-state pitch patterns. It can be seen that the maximum reactions are significantly higher for the turbine with blades of greater mass moment of inertia. This indicates the significance of blade inertial loads, showing that load fluctuations do not arise only from aerodynamic forces.

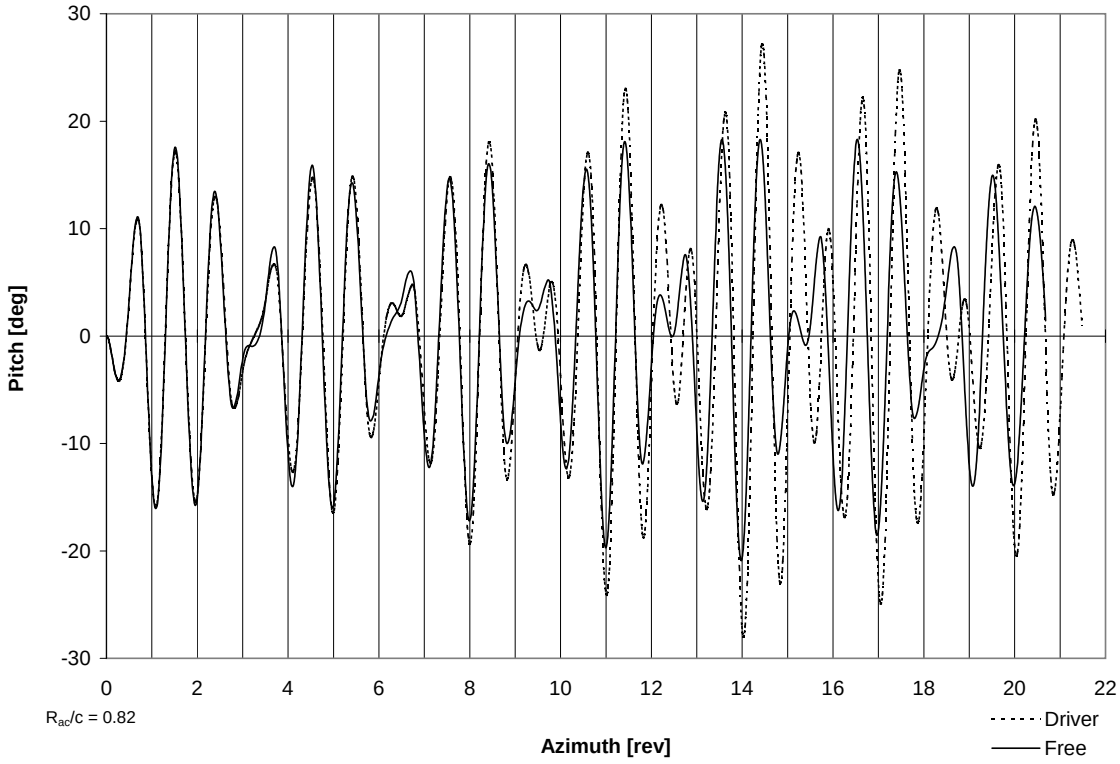

(a)$\bar{R}_{ac} = 0.820$

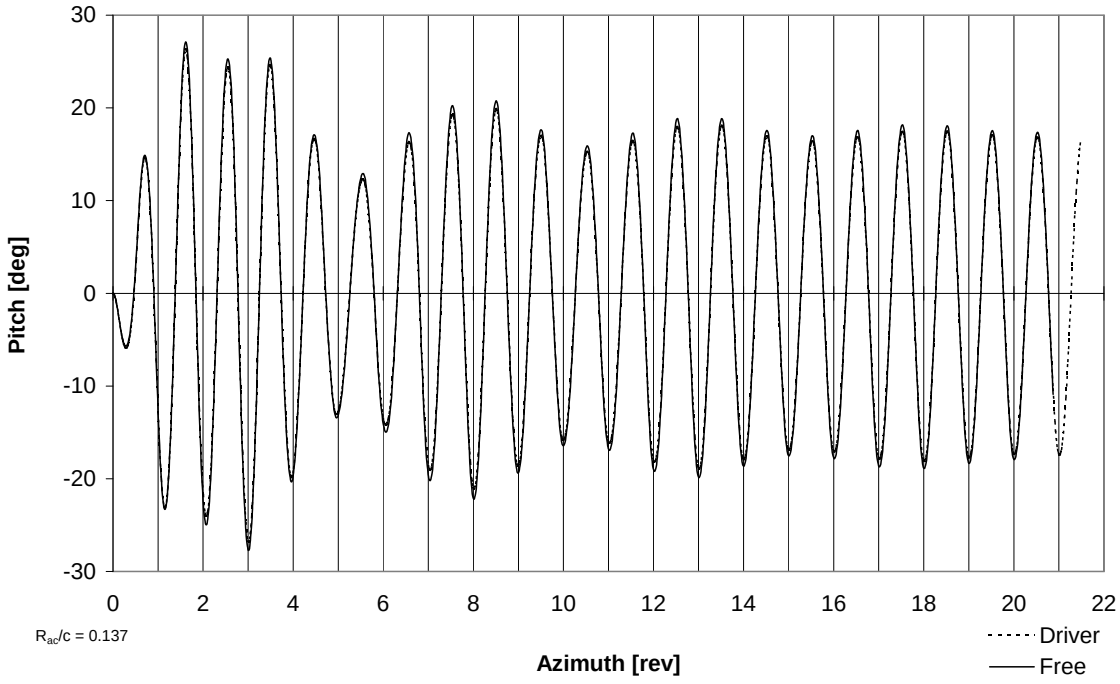

(b)$\bar{R}_{ac} = 0.137$

Figure 7.6: Pro/MECHANICA transient pitch responses for two parameter sets for the constant speed 'Driver' case and the variable speed 'Free' case.

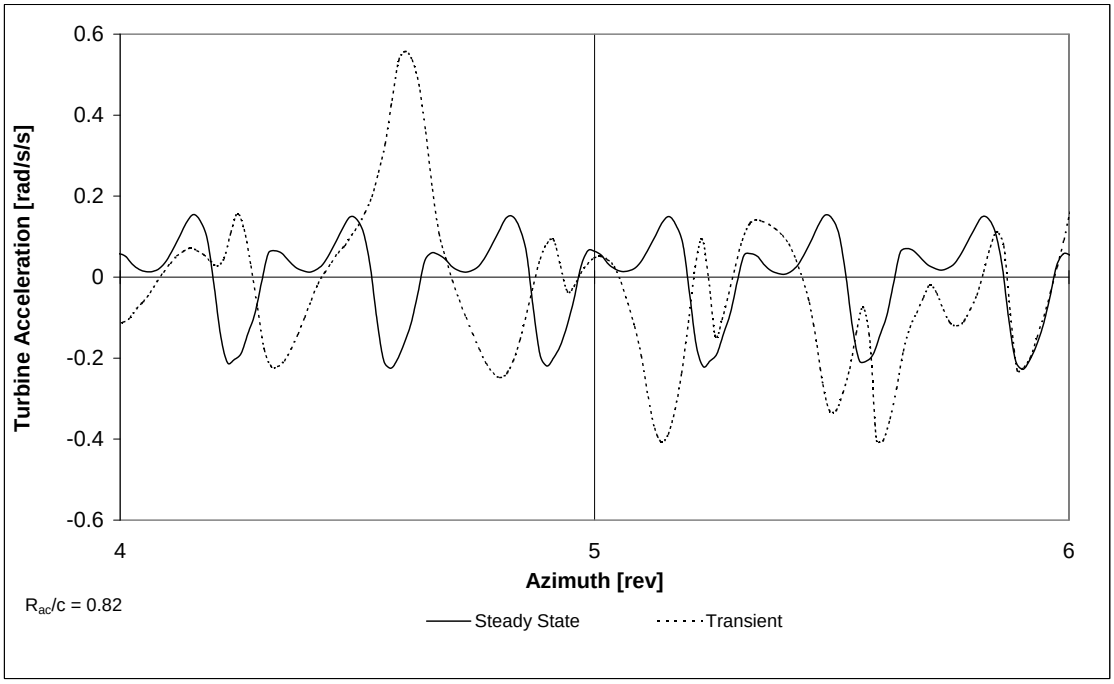

(a)$\bar{R}_{ac} = 0.820$

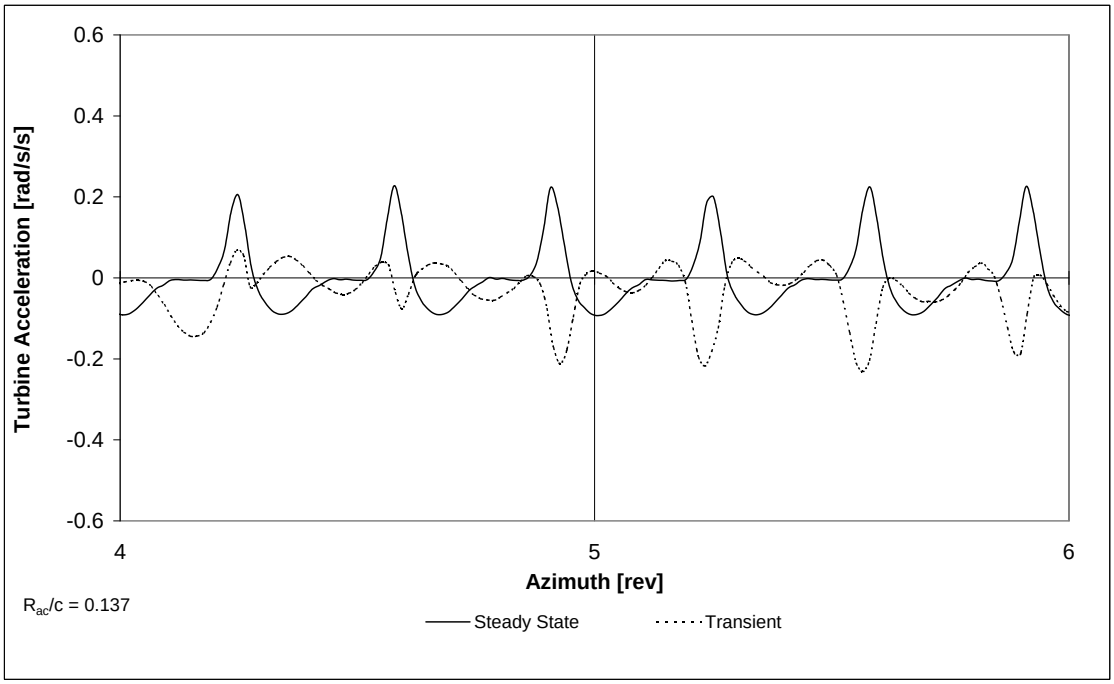

(b)$\bar{R}_{ac} = 0.137$

Figure 7.7: Pro/MECHANICA turbine acceleration fluctuations over two consecutive rotor revolutions for two parameter sets.

The influence of tower stiffness was investigated by freeing the two planar translation degrees of freedom at the rotor main bearing and applying a"point-to-point" spring load between the centre of the rotor and the centre of the base. The motion of the turbine under different values of stiffness of this spring was examined. The shaft load was removed and the turbine allowed to accelerate from an initial speed of 9 rad/s at a free wind speed of 6 m/s. The most successful set of blade parameters ($\bar{R}_{ac} = 0.137$) and the appropriate initial blade velocities and positions found from the steady-state analysis were used. The predicted shaft reaction force magnitude fluctuations for three values of spring stiffness are shown in Figure 7.9.

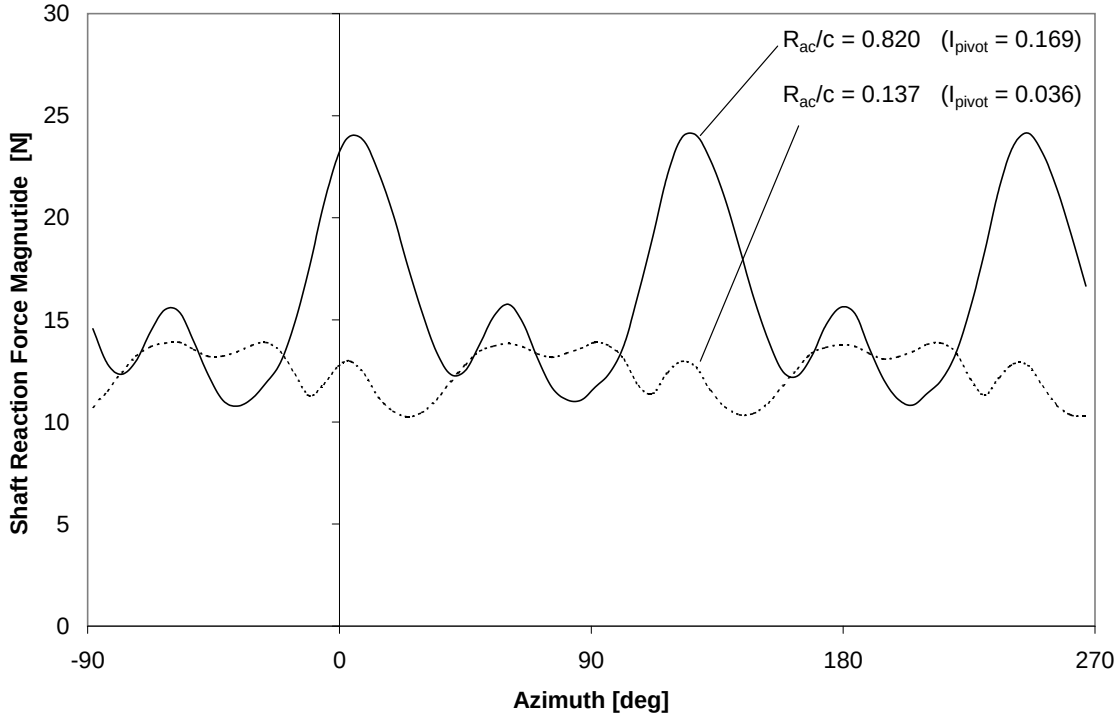

Figure 7.8: Pro/MECHANICA turbine shaft reaction force magnitude fluctuations for a locked rotor axis with two different blade inertias.

The stiffest spring (300 N/mm) kept total rotor axis displacement to less than 0.1 mm, resulting in a reaction force of approximately 30 N. The softest spring

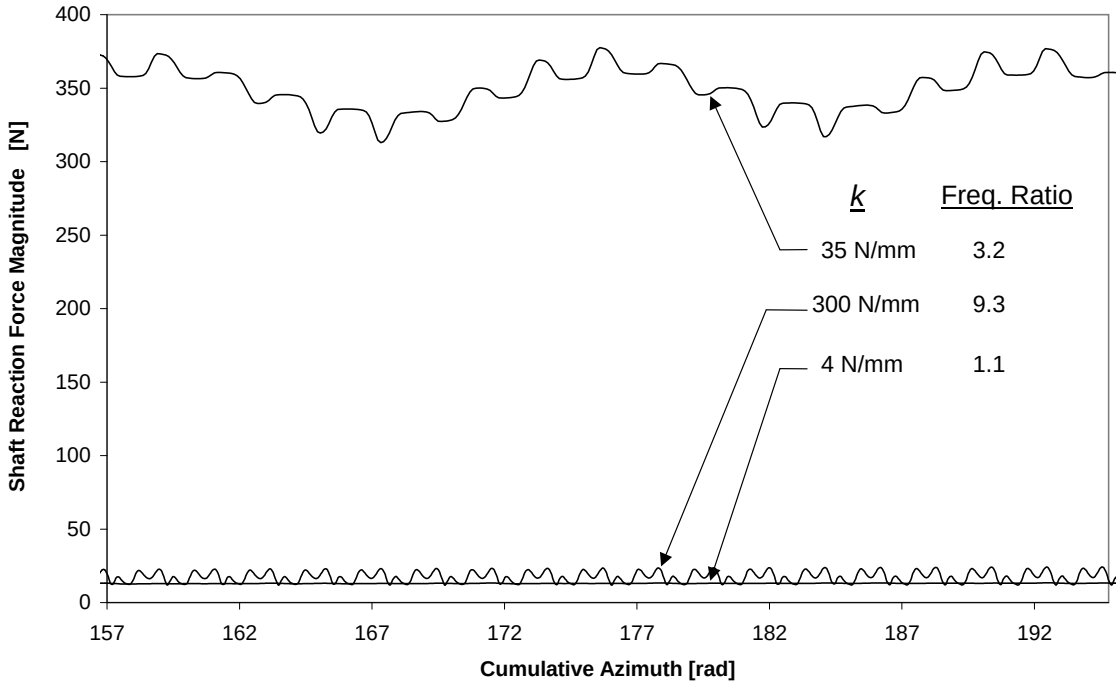

Figure 7.9: Pro/MECHANICA turbine shaft reaction force magnitude fluctuations for three values of 'tower' stiffness.

(4 N/mm) resulted in an almost steady downwind displacement of the axis of approximately 3 mm and a corresponding reaction of approximately 12 N. The intermediate spring (35 N/mm) produced the largest displacement - approximately 10 mm and a corresponding force of 350 N. This displacement rotated at the rotor speed. This spring stiffness corresponds to a simple translatory natural frequency based on the rotor mass of approximately three times the rotor speed. The 4 N/mm spring gives a natural frequency close to the rotor speed. The relative displacements for the two stiffnesses indicates that the primary excitation of the system occurs at three times the rotor speed, arising from the fluctuating aerodynamic and inertial loads on the three blades of the turbine.

These results are for a simplified turbine/tower analysis where the mass of the tower is not included. The trend of the results should not be altered by a change of mass, only the speeds at which resonances lie. The results indicate that the inertial

effects of the pitching blades of this type of turbine produce fluctuating reaction loads at the shaft, at a frequency equal to the rotor speed times the number of blades (blade pass frequency). The magnitude of these inertial effects is dependent on the mass moment of inertia of the blades.

7.2.4 Summary

Pro/MECHANICA was used to examine the dynamic behaviour of a pendulum type inertial passive variable-pitch turbine. Simulations were conducted for a range of blade parameters at a steady state operating point with a wind speed of 6 m/s and a tip speed ratio of 1.3. It was found that best performance was obtained when the blade parameters were set so that the natural frequency was approximately 10% higher than the rotational speed of the turbine.

Rotor speed fluctuation at steady state was found to be small and the effect on blade pitching was negligible, due to the mutual cancellation of inertial reaction forces at the pivots of the three blades. Under transient conditions interaction between blades and rotor was again minimal for the best blade parameter set but was evident for the blade with the largest moment of inertia. It is concluded that response time to changes in wind speed will be minimised by minimisation of blade moment of inertia (I_{pivot}) and mass centre offset (R_{cg}).

Fluctuating turbine shaft reaction forces were found to be stronger for blade arrangements with larger moments of inertia, further indicating the desirability of minimising the blade inertia. The simulation indicates the possibility of large displacements and reaction forces at the main bearing when the tower stiffness places the natural frequency close to the blade pass frequency.

7.3 Parametric Study of an Elastic Passive Pitch System using the Momentum Model

In order to undertake a more comprehensive study of parameter selection on turbine performance, the momentum theory mathematical model described in Chapter 5 was used. The quantities most critical to turbine performance are the strength of the driving aerodynamic moment and the strength of the restoring moment. These quantities are most easily examined in the context of an elastic-type passive variable-pitch turbine, where the restoring moment is produced by a spring. In this case adjustment of the spring stiffness does not affect the mass moment of inertia of the blade assembly as it does in an inertial-type system.

7.3.1 Selection of restoring moment parameter

A turbine with the parameters shown in Table 7.1 was tested. These parameters are based on those quoted by Kirke (1998) for his demonstration turbine.

Parameter	Value
Diameter:	6 m
Height:	3 m
Blades:	3 (NACA0018)
Blade chord:	400 mm
Aerodynamic moment arm R_{ac}:	25 mm
Inertial moment arm R_{cg}:	0 mm
Blade mass m_{blade}:	28 kg
Blade mass moment of inertia I:	2.55 kgm^2
Damping coefficient, b:	2 Nm/(rad/s)

Table 7.1: Turbine parameters used for DMS study

The restoring moment on the blade was assumed to be provided by a torsion spring, which applied a moment linearly proportional to the pitch angle. The spring constant is labelled K. The steady-state performance of the turbine was

predicted at tip speed ratios (TSRs) ranging from 0.2 to 5 for different values of K at a wind speed of 7 m/s.

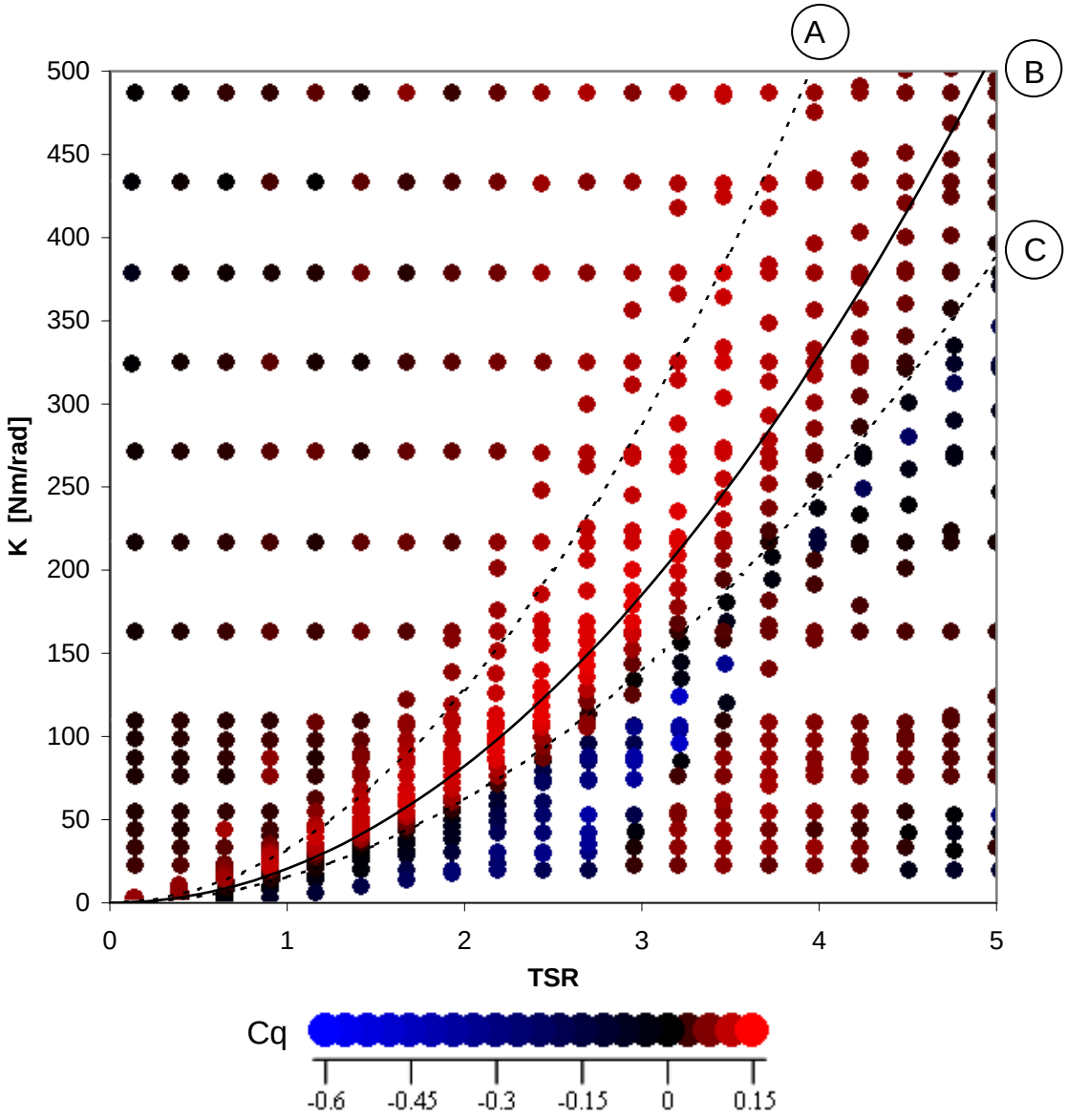

Figure 7.10: Steady-state torque coefficient C_q predicted by the momentum model for a range of TSR and torsion spring constant K. Each dot represents an operating point and C_q is indicated by the colour. The three reference curves shown are:

$$\begin{aligned} A &: K = 0.070\, m_{blade} R\dot{\phi}^2 \\ B &: K = 0.045\, m_{blade} R\dot{\phi}^2 \\ C &: K = 0.034\, m_{blade} R\dot{\phi}^2 \end{aligned}$$

Figure 7.10 shows clearly that the torsion spring stiffness K should be approximately a function of the square of the tip speed ratio. The red band of high torque is very narrow for low speeds (TSR$<$ 1.5), but broadens at higher speeds. At tip speed ratios greater than approximately three, the spring stiffness may increase toward infinity with almost no change in torque. This reflects the small pitch amplitude at these speeds, making the turbine behave much like a standard Darrieus turbine (which may be regarded as having blade springs of infinite stiffness).

Shown for reference are three curves representing different relationships between K and turbine speed. These are of the form $K = aF_R$, where $F_R = m_{blade}R\dot{\phi}^2$ is the centrifugal load on the blade and a is a constant. The significance of the form of this relationship is that inertial pitch control systems naturally provide a restoring moment that scales with centrifugal force. If an elastic-type system were to be used the torsional stiffness should somehow be made to increase with centrifugal load. This is the aim underlying the elastomeric pitch control concept explained in Section 3.2. Designs using a simple spring with a constant stiffness, such as those of Brenneman (1983) and Leigh (1980) shown in Section 2.1.2, will clearly not be as effective, based on these results.

An inertial system like the pendulum type of Sicard (1977) and Kentfield (1978) has a sine relationship between pitch angle and restoring moment; however over small angles it may be regraded as linear. An inertial system may then be regarded as equivalent to an elastic system in which the stiffness increases with centrifugal force. These results indicate a clear basis for implementing such a torsion spring stiffness function.

If the spring constant can be made to vary in such a fashion with rotor speed then significant torque can be developed at all tip speed ratios. The predicted

torque-TSR curves for the three relationships A, B and C shown in Figure 7.10 are shown in Figure 7.11. Also shown is the predicted torque curve for fixed blades.

Spring characteristic C is too soft, and falls off the high torque 'ridge' evident in Figure 7.10. This is especially true at tip speed ratios between 0.5 and 1.5.

Spring A is marginally too stiff and improved torque at virtually all tip speed ratios is gained by using spring B.

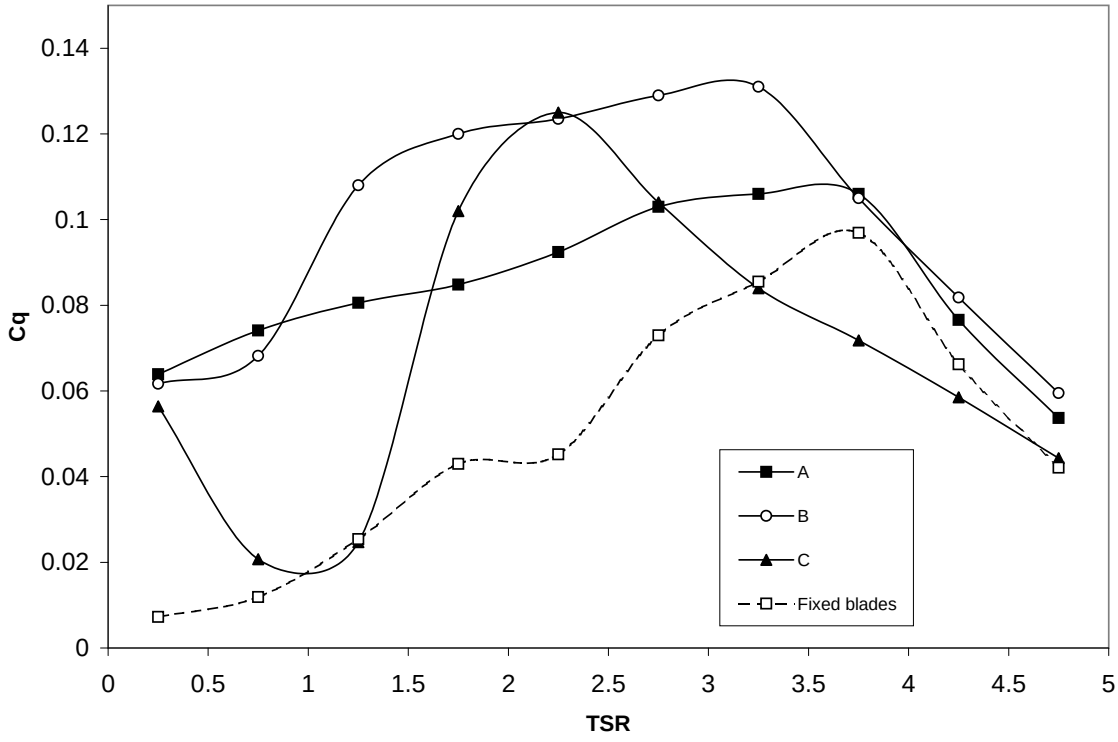

Figure 7.11: Torque coefficient C_q predicted by the momentum model for the three spring characteristics shown in Figure 7.10. For reference the prediction for a fixed-bladed turbine is also shown.

The reason for the nature of this relationship is evident from the different pitch responses of the blade for the three spring characteristics. These are shown in Figure 7.12.

It is evident that the amplitude of the pitch response at all tip speed ratios reduces with increasing spring stiffness. More importantly, the phase lag of the response is smaller for the stiffer springs. As shown in Figure 1.4, the angle of

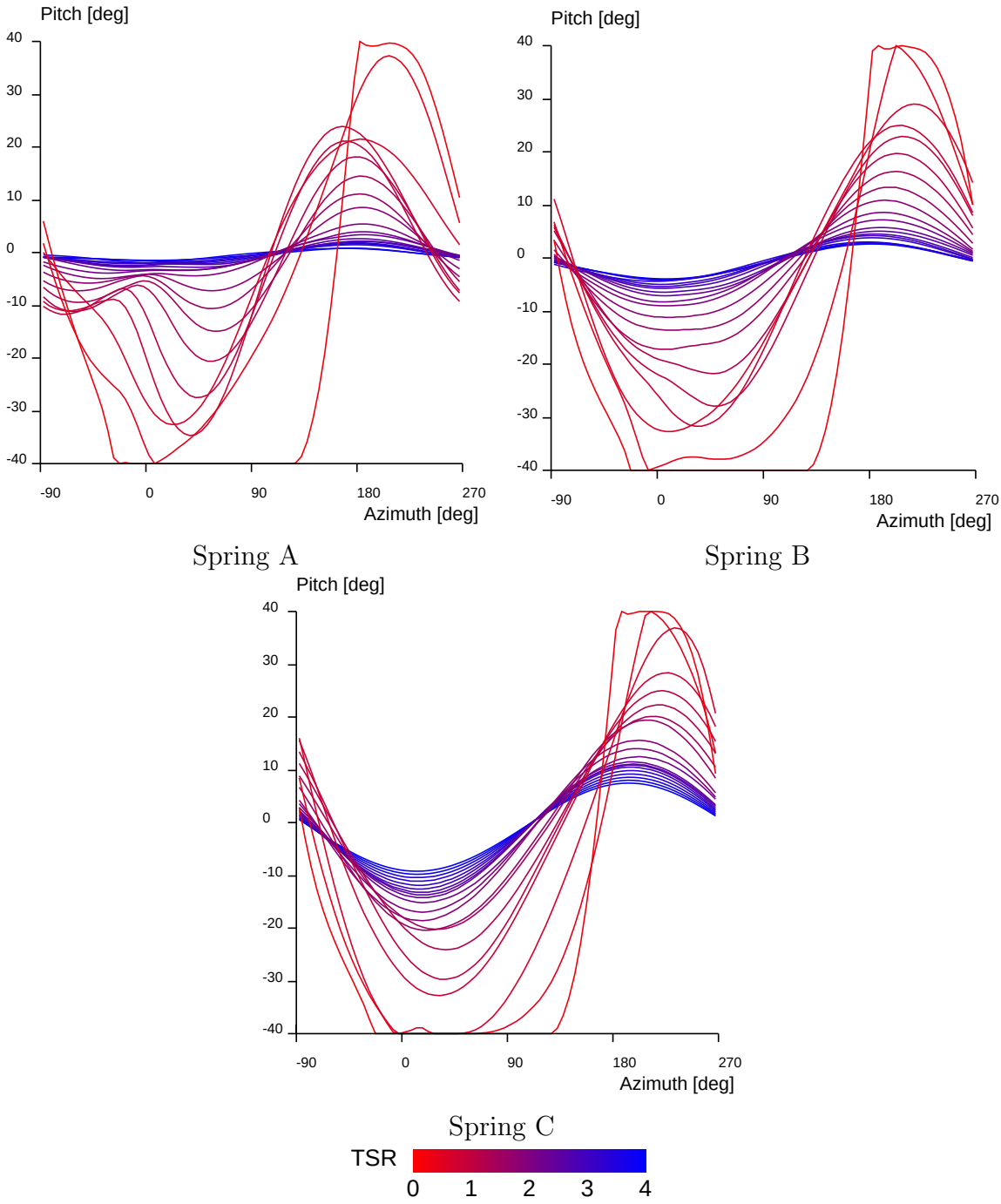

Figure 7.12: Pitch response variation with TSR (indicated by colour) for the three spring characteristics A,B and C shown in Figure 7.10.

attack variation that drives the pitch response is approximately a sinusoid with zero crossings at azimuth angles 90° and 270°. The pitch response to this variation should be as close to being in phase as possible. The predicted response for Spring C, which is the softest spring, shows that for TSR less than one, the pitch angle is still significantly positive at azimuth 270°. This causes the angle of attack on the blade to be temporarily negative, resulting in severe negative thrust and thus negative torque.

The stiffer springs A and B show a smaller phase lag and correspondingly better torque at low TSR in Figure 7.11. At the lowest TSR tested of 0.2, all three springs produce similar torque. This is because at this low speed the blade swings from one limit to the other (here set to ±40°). The limits effectively supplement the springs and prevent the blade from ever becoming too far out of phase.

As discussed in Section 7.2.3, insight into the pitch response can be gained by regarding the blade as a single degree of freedom spring/mass/damper system. The small angle natural frequency for constant rotor speed is (see for example Thomson (1993)):

$$\omega_n = \sqrt{\frac{K}{I}} \tag{7.2}$$

K is the spring stiffness, I is the mass moment of inertia of the blade assembly. The damped natural frequency is given by:

$$\omega_d = \sqrt{\left(\frac{K}{I}\right) - \left(\frac{b}{2I}\right)^2} \tag{7.3}$$

where b is the damping coefficient.

The response to a harmonic excitation force of frequency ω of such a system is of the form:

$$\theta = X \sin(\omega t - \beta) \tag{7.4}$$

The response phase angle β for such a system for a harmonic driving force is given by:

$$\tan \beta = \frac{b\ \omega}{K - I\omega^2} \tag{7.5}$$

The amplitude of response to a harmonic excitation is given by:

$$X = \frac{M}{\sqrt{(K - I\omega^2)^2 + (b\,\omega)^2}} \tag{7.6}$$

where M is the amplitude of the harmonic driving moment. The amplitude may be expressed in terms of the natural frequency ratio $\frac{\omega}{\omega_n}$ and damping ratio ζ:

$$X = \frac{M}{\sqrt{(1 - (\frac{\omega}{\omega_n})^2)^2 + (2\zeta(\frac{\omega}{\omega_n}))^2}} \tag{7.7}$$

These relations are illustrated in Figure 7.13.

If $K = amR\omega^2$ is proportional to the square of turbine speed as it is in this case, with small blade damping, the frequency ratio (of turbine speed to natural frequency) is virtually constant for all but very low speeds.

$$\frac{\omega}{\omega_d} \approx \frac{\omega}{\omega_n} = \omega\sqrt{\frac{I}{K}} = \omega\sqrt{\frac{I}{amR\omega^2}} = \sqrt{\frac{I}{amR}} \tag{7.8}$$

Recall that a is a constant defining the spring stiffness. Also note that in the discussion of natural frequency the notation $\omega = \dot{\phi}$ has been adopted for the turbine speed.

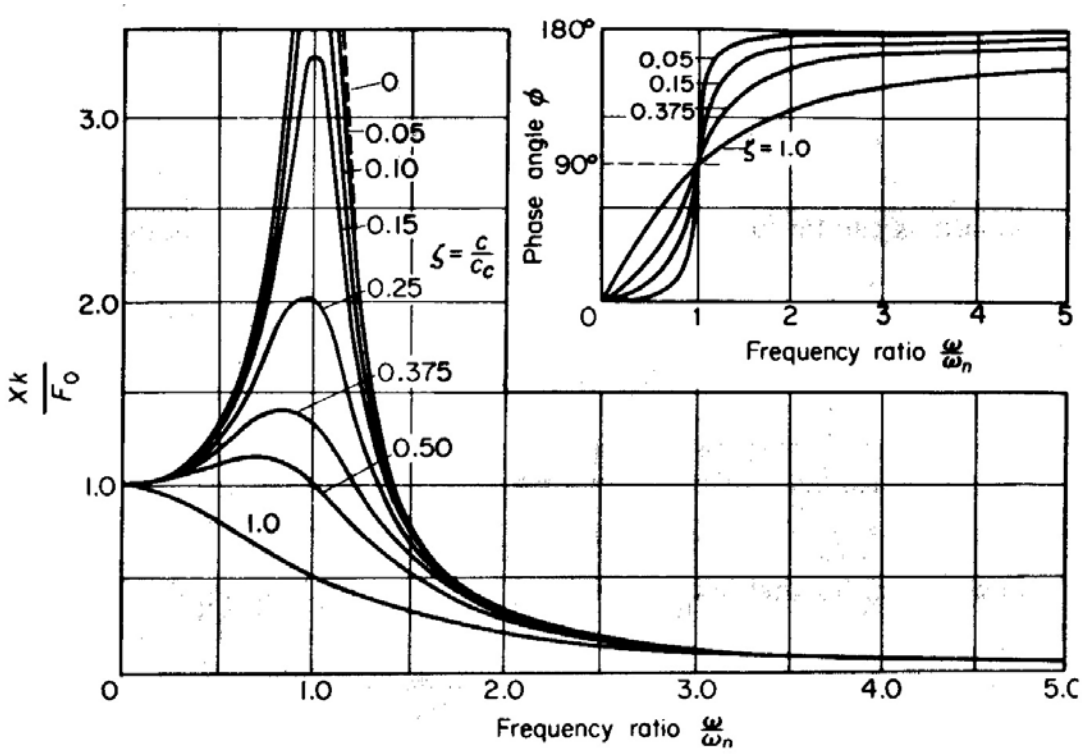

Figure 7.13: Non-dimensionalised response amplitude and phase angle for harmonic excitation for a single degree of freedom spring/mass/damper system. Reproduced from Thomson, W., *Theory of Vibration with Applications*, 4th ed. Chapman & Hall, 1993.

Figure 7.14 shows that Spring C is closest to the damped natural frequency at speeds above TSR = 0.5 in this case. The torque coefficient results shown in Figure 7.10 are plotted again in terms of the damped natural frequency. It is clear from this plot that maximisation of torque at all tip speed ratios is achieved by a constant frequency ratio of approximately 0.82 in this case.

The relationship between frequency ratio and the theoretical phase angle for the spring/mass/damper system is shown in Figure 7.15. Since the damping coefficient is constant, the damping ratio decreases as turbine speed increases. The phase angle therefore is greatest at low speeds. The response lags the driving force by $\pi/2$ radians at resonance (frequency ratio of 1), and the proximity to the natural frequency produces large phase angles even at TSR = 4.

While the stiffest spring, A, puts the blade furthest from the natural frequency and thus produces the smallest phase angle, the reduced amplitude of response at this frequency ratio is detrimental. At low and intermediate tip speed ratios, the natural variation in relative wind direction requires a large pitching amplitude to produce useful torque. If the pitch amplitude is too small, little improvement over a fixed-blade turbine is gained.

In summary, it is desirable to minimise the natural frequency ratio in order to minimise the phase angle between aerodynamic driving moment and the pitch response. If the blade operates too close to or above its natural frequency, the pitch response lags the wind incidence variation by so much that the sense of the lift produced is opposite to that needed and severe negative torque results. A frequency ratio of one is a 'hard boundary' beyond which torque drops very rapidly to negative values.

It is also in general desirable to maximise the pitch response amplitude. For intermediate tip speed ratios, at which improved performance is the primary focus of this work, output is generally improved by maximising the pitch amplitude, so long as the phase angle remains small. A large pitch response reduces the amplitude of the variation in angle of attack experienced by the blade, which reduces the proportion of time spent in blade stall. If the pitch response amplitude is too small, the performance of the turbine approaches that of a fixed bladed turbine. The region of excessively low frequency ratio constitutes a 'soft boundary', as performance is gradually diminished.

A balance must therefore be struck between an adequately large pitch amplitude and an adequately small phase angle. This compromise is assisted by maximising the aerodynamic driving moment and minimising the blade inertia.

For example, if R_{ac} could somehow be increased without changing I, the response amplitude could be increased without increasing the frequency ratio and so the phase lag. The desirability of finding blade materials and a design that minimise mass and moment of inertia is clear. For whatever mass properties are given, R_{ac} and the inertial or the elastic stiffness may be adjusted to produce a natural frequency ratio that represents an appropriate balance between amplitude and phase.

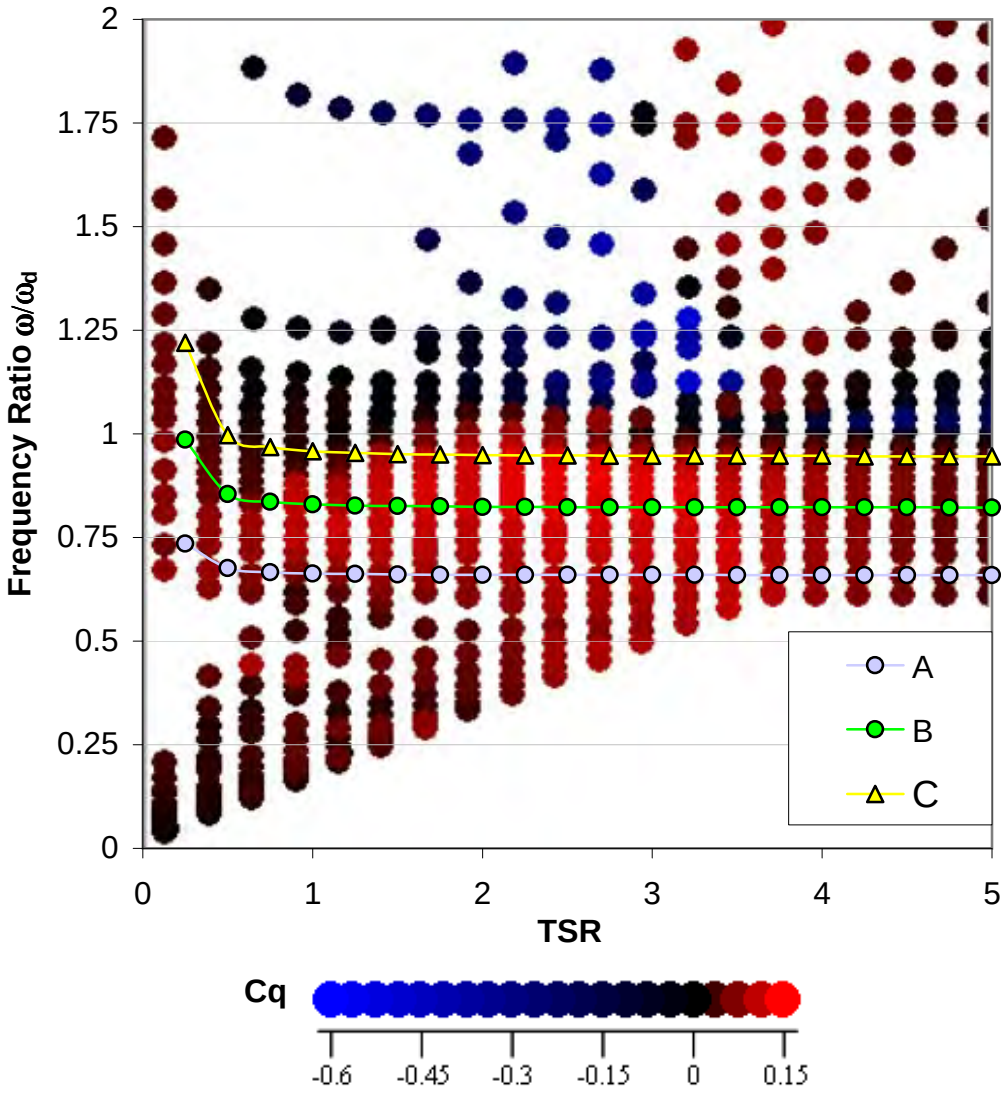

Figure 7.14: Spring/mass/damper frequency ratio for the three spring characteristics A,B and C. The torque coefficient is shown by colour as a function of the frequency ratio.

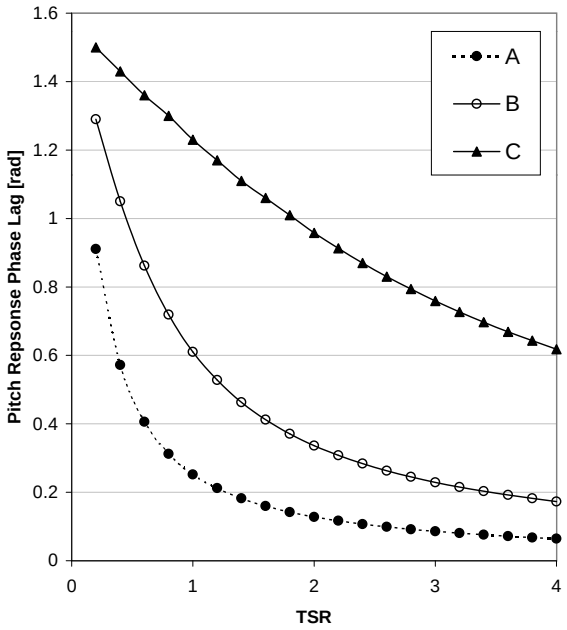

Figure 7.15: Spring/mass/damper theoretical harmonic excitation response phase angle for the three spring characteristics A,B and C.

7.3.2 Selection of aerodynamic moment arm R_{ac}

The foregoing analysis was conducted with the aerodynamic moment arm R_{ac} set at 25 mm. R_{ac} is the distance from the pivot axis to the aerodynamic centre. Assuming that the driving aerodynamic moment is predominantly provided by the lift force, the moment is given by:

$$M_{aero} \propto \frac{1}{2}\ \rho\ c\ L\ C_L\ W^2 R_{ac} \tag{7.9}$$

where ρ is the air density, c is the blade chord, L is the blade length, C_L is the lift coefficient and W is the relative flow velocity.

For a given blade and counterweight the mass moment of inertia of the blade assembly, I, is a function of R_{ac}. I may be estimated by Equation 3.7:

$$I = I_{blade} + I_{cw} + \frac{m_{total}}{m_{cw}}(m_{blade}(R_{ac} - 0.25c + x_{cg_{blade}})^2 + m_{total}R_{cg}^2)$$

From Equation7.6, the response amplitude is proportional to:

$$X \propto \frac{\frac{1}{2}\ \rho\ c\ L\ C_L\ W^2 R_{ac}}{\sqrt{(K - I\omega^2)^2 + (b\,\omega)^2}} \tag{7.10}$$

So for a given blade, increasing the aerodynamic moment arm R_{ac} linearly increases the strength of the aerodynamic driving moment, but also increases the polar moment of inertia according to Equation 3.7. As R_{ac} approaches zero, M_{aero} approaches zero but the moment of inertia approaches a finite minimum. The response amplitude therefore approaches zero. As R_{ac} goes to infinity, I becomes almost proportional to R_{ac} according to Equation 3.7. The response amplitude therefore again approaches zero. At some intermediate value of R_{ac}, the ratio $R_{ac} : I$ is a maximum. Using Equation 3.7 this value, labelled R_{ac}^*, is found to be

$$R_{ac}^* = \sqrt{\frac{\frac{m_{cw}}{m_{total}}(I_{blade} + I_{cw}) + (m_{blade}(-0.25c + x_{cg\,blade})^2 + m_{total}R_{cg}^2)}{m_{blade}}} \tag{7.11}$$

If damping is zero, the response amplitude for a spring/mass/damper system given by Equation 7.6 is a maximum at R_{ac}^*. For non-zero blade damping, the amplitude is reduced and the value of R_{ac} giving maximum amplitude increases. For small damping ratios the ratio $R_{ac} : I$ gives a good indication of the response amplitude. Figure 7.16 shows the pitch response amplitude over a range of tip speed ratios predicted by the momentum model for values of R_{ac} between 25 mm and 200 mm. Also plotted is the variation of the ratio $R_{ac} : I$ with R_{ac}. The value of R_{ac}^* given by Equation 7.11 is 100 mm in this case, which is the location of the peak $R_{ac} : I$ value. The variation pitch response amplitude at each tip speed ratio mirrors the variation in $R_{ac} : I$. The elastic restoring stiffness is adjusted for each value of R_{ac} to maintain the same frequency ratio.

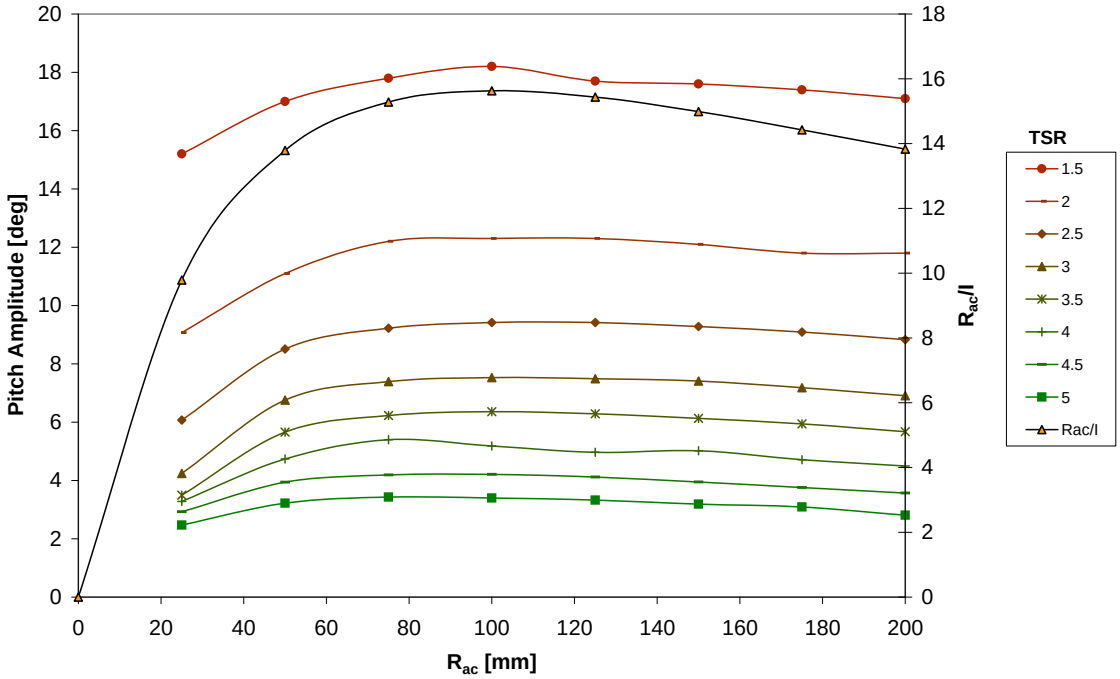

Figure 7.16: Pitch response amplitudes predicted by the momentum model for values of R_{ac} between 25 mm and 200 mm. The elastic restoring moment is adjusted to maintain the frequency ratio at 0.82 in each case. The variation of the ratio $R_{ac} : I$ with R_{ac} is also plotted.

Figure 7.17 shows the variation in the stiffness of the restoring spring that is required to maintain the frequency ratio at a value of 0.822 for the turbine parameters given in Table 7.1. For any value of R_{ac}, the spring stiffness is assumed to be proportional to the square of the turbine speed.

Figure 7.18 shows the performance predicted by the momentum model for the turbine with R_{ac} varied between 25 mm and 200 mm and the spring stiffness varied as shown in Figure 7.17. For all cases the frequency ratio is the same. The variation in performance reflects the variation in response amplitudes, as shown in Figure 7.16, as well as variation in damping ratio, which affects the phase angle. In general, the larger pitch amplitudes produce improved performance at lower tip speed ratios, but degrade higher speed performance. The value of R_{ac} chosen for the analysis shown in Figure 7.10 of 25 mm produces a smaller amplitude

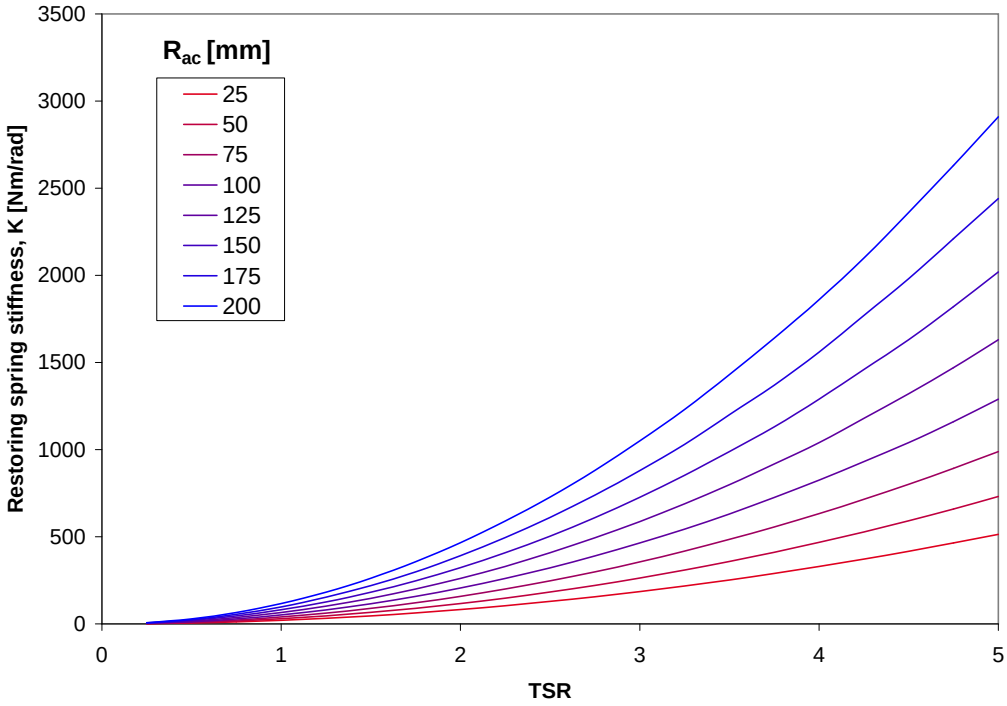

Figure 7.17: Variation in stiffness of the 'ideal restoring spring' required to keep the frequency ratio constant for a range of values of R_{ac}.

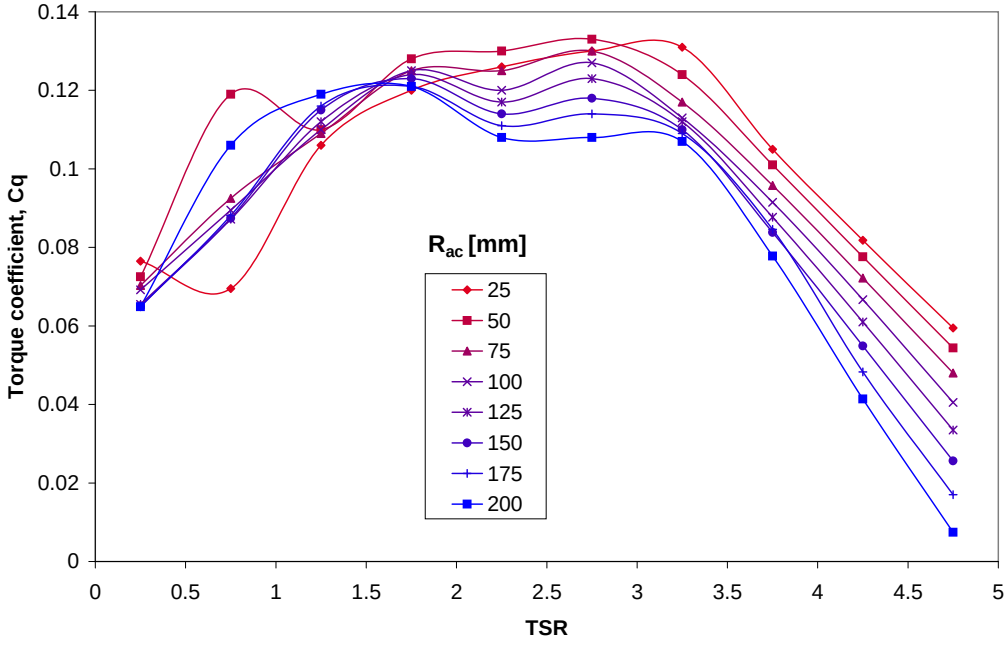

Figure 7.18: Torque coefficients predicted by the momentum model for a range of values of R_{ac} with the elastic restoring moment adjusted as shown in Figure 7.17 to keep the frequency ratio constant.

than would be produced by larger values of R_{ac}. In this case, improved overall performance results. The value chosen for a particular turbine would depend on its specific combination of parameters, such as the blade and counterweight mass and moment of inertia, blade centre of gravity location, aerofoil profile and chord length and so on.

A large R_{ac} makes the driving aerodynamic moment large relative to the resistance of friction and damping. However there are a number of constraints that limit the value of R_{ac}. For a large R_{ac}, the pitching motion of the blade results in significant translatory motion of the aerodynamic centre. The angle of attack experienced by the blade is then modified by its own motion. This increases the aerodynamic damping on the blade that arises from its positive lift curve slope (this phenomenon is discussed further in Section 7.3.3).

Secondly, a large R_{ac} also places the pivot axis a long way forward, outside the blade profile. This presents problems from a design point of view. The blade connection components are then not concealed within the blade and require fairing to reduce parasitic drag. Further, the large moment arm at which the counterweight acts results in large bending loads on the member on which the weight is mounted. It is likely that such structural considerations would take precedence over aerodynamic optimisation in most cases.

7.3.3 Blade damping

The current analysis suggests that deliberate damping of the blade motion is not desirable. Damping serves to reduce the amplitude of the pitch response as well as increasing the phase lag. If the amplitude is too great, then in general it would be better to reduce it by reducing the aerodynamic centre moment arm, R_{ac}, to reduce the driving moment, rather than to add damping. This does not affect

the phase of the response and results in a reduced mass moment of inertia for the blade assembly.

Kirke (1998) stated that the blades on his demonstration turbine were heavy enough to require damping, by means of damping cylinders that were also used to limit the blade travel.

Even if some form of damping is not included deliberately, it is assumed that some damping of the blade pitch motion will arise naturally. Such damping would exist within the blade connection itself and as aerodynamic damping.

Hansen (1995) concluded that aerodynamic damping on horizontal axis wind turbine blades arises primarily from the positive lift-curve slope of the aerofoil. If the blade 'flaps' normal to the rotor plane in the upwind direction, the blade's own velocity increases the angle of attack, resulting in increased lift that opposes the flap motion. Conversely, if the blade moves downwind, the angle of attack is decreased, resulting in a loss of lift. This effect is inherently related to the transverse velocity and produces positive damping of blade flap motion. This damping is not related to viscosity of the air and arises in a potential flow analysis. It is dependent on the fact that lift is proportional to angle of attack. If the blade is operating near its stall angle, the negative slope of the lift curve beyond stall can result in 'negative damping', which produces instability.

Aerodynamic damping of this form should emerge naturally from the calculation of aerodynamic loads so long as the angle of attack takes into account the motion of the blade. This damping does not need to be included in the damping coefficient.

Aerodynamic damping arising from the viscosity of the air would need to be accounted for in the damping coefficient, but this effect is likely to be small. Fung

(1955) does not include a separate viscous aerodynamic damping term of this form in his text on the theory of aeroelasticity.

The value of the damping coefficient is therefore determined mainly from the structural damping of the blade connection. This damping may well not be viscous, but instead may be structural (force proportional to displacement). According to Cook (1995), structural damping is difficult to model mathematically, and it may be idealised as viscous damping so long as it is small ($< 10\%$).The amount of structural damping that exists would depend on the exact design of the blade connection. For an elastic type system, especially one using an elastomeric material, the damping may be significant. However for a purely inertial system where nominally no deformation of material is involved, damping would seem to be very low.

Bayly (1981) included a damping term in his analysis, though did not comment on its physical origin. He found that the predicted blade pitch pattern would not converge for critical damping ratios less than 0.1. He tested damping ratios between 0.1 and 2, and concluded that the value of the damping ratio does not have a strong influence on performance at tip speed ratios greater than 3.5 (this was the lower limit of his range of study). It seems logical that the influence of damping should decrease with increasing tip speed ratio, as the amplitude of the pitch response naturally decreases with speed.

Kirke (1998) and Lazauskas (1992) make no mention of a damping term in their mathematical model.

It was found that the value of the damping constant may have a significant effect on predicted blade pitch response patterns and on the average torque for the revolution, especially at low and intermediate tip speeds. Increased damping

alters the frequency ratio, decreasing the amplitude and increasing the phase angle of the response.

Damping also accelerates convergence of the pitch response to the steady state pattern. It was found that instead of converging to a single steady state pitch response, the blade often settled into a two-revolution period cycle, with the revolution-average torque alternating between two distinct values. Less commonly, a three revolution cycle may develop. When this occurred, the check for steady-state convergence would fail, as this was based solely on comparing the torque coefficient values for the two most recent revolutions.

Increased damping reduces the tendency for multiple-revolution cycles to develop, but also significantly changes the predicted pitch pattern and average torque (see Figure 7.19). It may also be noted that the general trend is for the torque to decrease with increasing damping.

For the purposes of these analyses, the damping coefficient has been set to the lowest value possible that allows convergence to a single torque to occur at most tip speed ratios. Where a two-revolution pattern persists, an average of the alternating torque values is taken. This value approximates the steady-state average torque that would be produced by a turbine with such a two-revolution period.

It is not clear whether multiple-revolution pitch cycles occur in reality. In the field, even if the actual damping were low enough for such patterns to develop, it is likely that continual changes in conditions would not allow precise repetition of any pattern, whether it had a period of one or two revolutions.

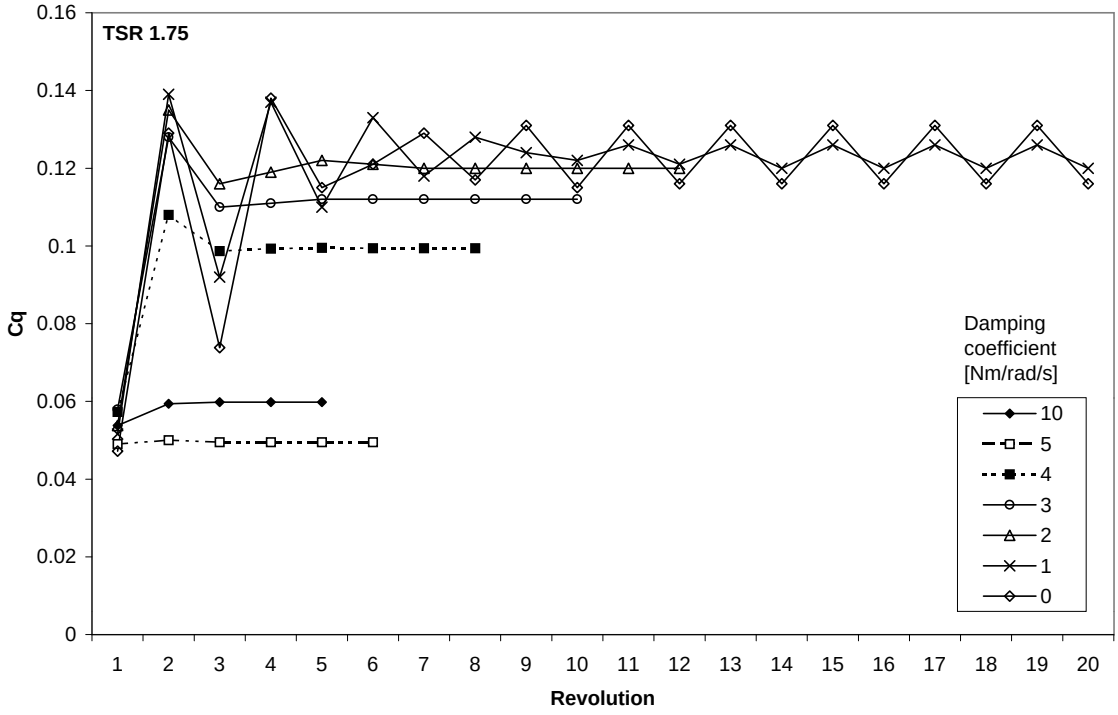

Figure 7.19: Comparison of the convergence of predicted torque coefficient Cq with successive revolutions for different blade damping coefficients.

7.4 Validity of the Spring/Mass/Damper Analogy

The analogy of a mass/spring/damper system response to harmonic forcing is clearly a simplification of the real situation. Specifically, the aerodynamic forces and moments that drive blade pitching do not vary in a simple sinusoidal fashion, especially for TSR$<$ 1 and around blade stall. Aerodynamic forces on the blade always cause it to seek zero angle of attack. As the amplitude of the pitch response increases, the angle of attack experienced by the blade tends to zero and so does the lift force that causes the pitching. If the inertia of the blade causes it to overshoot, the angle of attack will switch sign and begin to reduce the pitch angle. The pitch response amplitude is therefore limited by the amplitude of the variation in angle of attack that would be experienced by a fixed blade at that tip speed ratio. The

harmonic forcing spring/mass/damper analogy also breaks down as this point is approached.

However the analogy is a useful starting point in the design of passive variable-pitch turbines for which the restoring moment is roughly proportional to the blade pitch angle.

There are designs for which this approximation is not applicable. The stabiliser mass concept used in the designs of Liljegren (1984) and Kirke and Lazauskas (1991) produce a restoring moment that is constant in magnitude at a given turbine speed and is independent of the pitch angle. It is difficult to predict the behaviour of such a system based on the replacement of the stabiliser mass with a spring. At best, the stabiliser mass restoring moment could be taken as a kind of average of a torsion spring moment taken over the pitch amplitude. However the stabiliser mass moment at pitch angles close to zero is very much greater than would be applied by the spring and conversely, the mass moment at the extremes of pitch would be less than the spring moment.

In Section 3.3.4 the concept of tailoring the shape of the rolling profile was explained. The shape of the profile may be designed so that the relationship between pitch angle and restoring moment is not linear. In terms of the present analogy this is akin to providing a torsion spring with a non-linear stiffness characteristic. If the slope of the moment-angle curve is made to decrease with increasing pitch angle, then the blade should feel an effectively stiffer spring when its pitch amplitude is small than when the amplitude is large. Theoretically this should enable the performance of the turbine to be improved, by effectively blending a relatively 'soft spring' at low tip speed ratios, where the pitch amplitude is large, with a 'hard spring' at high tip speed ratios where the amplitude is small.

In some respects the mass stabiliser concept is an extension of this idea. The 'average' stiffness of the torsion 'spring' felt by the blade depends on the amplitude of the pitch response. At small amplitudes the mass acts like a very stiff spring, while at large amplitudes it is more like a soft spring (see Figure 7.20).

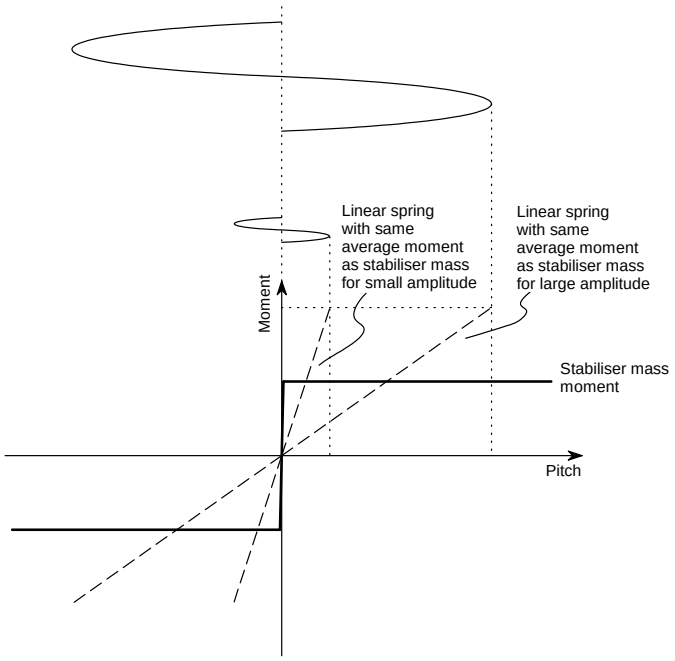

Figure 7.20: Stabiliser mass torsion spring analogy

For this reason, the stabiliser mass concept is able to allow large pitch amplitudes at low speeds to provide good starting torque, while effectively locking the blade to zero pitch at high speeds, so the turbine acts like a standard Darrieus. There is a threshold of restoring moment that has to be overcome in order to move from zero pitch prevents small oscillations. While this is a desirable trend, the variation in effective stiffness with pitch amplitude in some instances may be excessive. Kirke (1998) states in his conclusion that a large pitch amplitude, up to 45°, is an advantage at low tip speed ratios, but that mathematical modelling indicated that a higher maximum efficiency (attained at high tip speed ratios) was produced by a smaller pitch amplitude (typically less than 10°). It is possible that

the limiting of blade pitch to relatively small angles (using stops) was found to be advantageous because the stops supplemented the stabiliser mass at intermediate tip speed ratios, preventing the blade motion from becoming too far out of phase with the wind.

7.5 Summary

Most of the passive variable-pitch design concepts discussed in Chapters 2 and 3 are able to be approximated by a simple mass/spring/damper. The mass stabiliser designs of Lilegren and Kirke are difficult to characterise in this way because the restoring moment is constant and not proportional to the pitch angle.

The following conclusions have been reached on the basis of this analysis:

- **The magnitude of the restoring moment should be approximately proportional to the square of the rotor speed.** For small damping, this makes the natural frequency of the blade almost proportional to speed and the frequency ratio almost constant. Inertial-type designs naturally produce such a moment.
- **The 'stiffness' of the restoring moment should be chosen so that the frequency ratio is less than one.** This prevents the blade motion from being completely out of phase with the driving aerodynamic moment.
- **The frequency ratio must be high enough to produce an adequate pitch response amplitude, but low enough to keep the phase angle of the response small.** If the frequency ratio is too near one, the pitch response approaches 90°. If the frequency ratio is too low, the blade does not pitch sufficiently and no great improvement over a fixed-bladed turbine

is obtained. The exact value depends on the specific turbine parameters and the degree of damping in the blade mechanism.

- **There is a value of the aerodynamic moment arm R_{ac} for which the ratio $R_{ac} : I$ is a maximum.** This value should yield the greatest amplitude of pitch response and should allow the use of the lowest frequency ratio. A smaller value may however yield better overall performance, especially at higher tip speed ratios. It is likely that structural design considerations would override aerodynamic optimisation in the selection of R_{ac}.
- **The above conclusions, based on the modelling of each blade as a spring/mass/damper system, provide starting points for more detailed analysis using a mathematical model such as the momentum model.** The complexity of Darrieus turbine aerodynamics makes the design process difficult. The analogy is especially tenuous at tip speed ratios less than one. Also specific design concepts such as the mass stabiliser design are not readily treated in this manner.

Chapter 8

Analysis of Turbulent Wind Performance

8.1 Introduction

One of the advantages of the free vortex wake mathematical model over the momentum model is its ability to handle unsteady conditions. While the self-starting ability of passive variable-pitch turbines in steady wind has been the focus of this thesis, the performance of this type of turbine in a turbulent wind has also been studied.

Both Bayly (1981) and Kirke (1998) identified unsteady wind and its effect on blade pitch response as an area requiring further study.

8.2 Performance in a Wind of Varying Velocity

Simulation runs using the vortex model were conducted for a turbine operating in a free wind of fixed direction but sinusoidally varying velocity.

Nattuvetty and Gunkel (1982) performed an analysis of the performance of a cycloturbine in varying wind. The pattern of pitch variation is predetermined for the cycloturbine and is independent of tip speed ratio. The present analysis takes into account the gradual change in pitch response that occurs with changing wind conditions.

Since the power of the wind is a function of the cube of the wind speed, more energy passes through a fixed area in one period of a wind of sinusoidally varying

Parameter	Value
Type:	Rolling profile
Diameter:	6 m
Height:	3 m
Blades:	3 (NACA0018)
Blade chord:	400 mm
R_{ac}:	40 mm
Profile:	Circular arc - R_{cg} 55 mm
Blade mass:	28 kg
I_{pivot}:	3.19 kgm^2
Damping, b:	0.5 Nm/(rad/s)
Friction:	0.0003 Nm/N
Pitch limits:	$\pm 30°$

Table 8.1: Turbine parameters for variable velocity wind simulation. I_{pivot} is the mass moment of inertia of the blade about its nominal pivot point, the centre of mass.

velocity than for a steady wind of the mean velocity. In order to enable direct comparisons between steady and unsteady winds, the mean and amplitude of the sine function were selected to make the average power the same. That is, for the wind velocity given by:

$$U(t) = U' \ \sin(t\frac{2\pi}{T}) + \bar{U} \tag{8.1}$$

the steady wind U_0 that gives the same average power is found by:

$$\frac{1}{2}\rho A \left[\frac{1}{T}\int_0^T [U' \ \sin(t\frac{2\pi}{T}) + \bar{U}]^3 \ \mathrm{d}t\right] = \frac{1}{2}\rho A U_0^3 \tag{8.2}$$

where A is the swept area of the turbine and ρ is the air density. This gives:

$$U_0 = (\frac{3}{2}U'^2\bar{U} + \bar{U}^3)^{\frac{1}{3}} \tag{8.3}$$

A turbine with the parameters given in Table 8.1 was studied. A load was applied to the turbine with torque proportional to the square of turbine speed. This type of load allows the turbine to operate at constant steady-state tip speed

ratio and power coefficient regardless of wind speed. Such a load arises for example from the direct heating of water by an impeller attached to the turbine shaft (Nattuvetty and Gunkel, 1982). The magnitude of the load was chosen so that the steady-state operating point lies at close to the peak of the power coefficient - tip speed ratio curve. The steady-state efficiency was found using the vortex model by performing a simulation run with a constant wind speed of 7 m/s.

Several runs were then conducted using the vortex model with a sinusoidally varying wind. From Equation 8.3 the values $U' = 6.93$ m/s, $\bar{U} = 0.99$ m/s were found to give the same average power as a steady wind of 7 m/s, regardless of the period. The period of oscillation was varied between 2 and 50 seconds. The resulting oscillation of power transmitted to the load with time is shown in Figure 8.1. Since the load torque is proportional the square of the speed, the load power is proportional to the cube of the speed. The speed oscillates at the same frequency as the wind speed variation. Due to the inertia of the turbine and its load, the turbine speed lags the wind speed and as the frequency increases, the amplitude of the turbine speed oscillation diminishes, as the turbine is not able to respond to the rapid fluctuations.

Nattuvetty and Gunkel (1982) found that for a cycloturbine connected to a load of this type, all the operating points predicted by his analysis lay on a cubic curve on the power coefficient-tip speed ratio plot. This fact results from the use of the load torque to define the power coefficient. Under unsteady conditions, part of the total torque developed by the turbine drives the load while the remainder accelerates the inertia of the turbine and load. Because of this the total instantaneous power is different from the load power. In examining the self-starting ability of turbines, the total power was used because both the energy being fed to the load

and being used to accelerate the turbine were considered as useful. In the case of a statistically stationary varying wind, any work done in changing the turbine speed may be considered as lost. The use of the load power does produce apparently nonsensical instantaneous power coefficients greater than the steady-state optimum in a fluctuating wind. This occurs when the turbine speed lags a drop in wind speed due to inertia and is temporarily driving the load faster than is sustainable. The turbine soon decelerates however and then lags the wind speed when it rises again, resulting in a lower than optimum power coefficient. The turbine is never allowed to settle to steady-state and the average power delivered to the load is less than would be extracted from a steady wind of the same average power.

Rosen and Sheinman (1994) performed a simulation of a horizontal axis wind turbine in a sinusoidally varying wind. They found that for low frequency variation the average power coefficient was not significantly lower than for a steady wind. However as the frequency increased, the effect on efficiency become more pronounced. There was a frequency at which the deviation from steady wind performance was greatest and for higher frequencies, the performance recovered towards the steady wind level. This was explained as the turbine's inability to respond to such rapid variations in the wind. A similar trend was observed with the present results, shown in Table 8.2.

Results for two different total (turbine and load) mass moments of inertia (I_t) are presented. The lower inertia is for a turbine with a bare rotor plus load moment of inertia of 100 kgm^2, resulting in a total moment of inertia of 866 kgm^2. The heavier rotor has a mass moment of inertia of 1000 kgm^2, giving a total inertia of 1766 kgm^2. The remainder of the inertia comes from the blades.

Period s	$I_t = 866$ kgm^2 Cp_{avg}	Difference %	$I_t = 1766$ kgm^2 Cp_{avg}	Difference %
steady	0.405	0	0.405	0
2	0.392	-3.4	0.389	-4.0
3	0.375	-7.6	0.375	-7.5
5	0.385	-5.1	0.389	-4.0
8	0.391	-3.6	0.391	-3.6
10	0.393	-3.1	0.393	-3.1
20	0.388	-4.2	0.394	-2.8
50	0.393	-3.1	0.391	-3.7

Table 8.2: Average power coefficients for the turbine with two different values of rotor inertia in a wind of sinusoidally varying velocity magnitude.

The oscillating power output for the various frequencies tested are shown in Figure 8.1. The effect of turbine inertia is obvious, with the heavier rotor experiencing a smaller amplitude of speed (and therefore load power) oscillation at every frequency. The difference in average power produced by each turbine, shown in Table 8.2, is surprisingly small and for some frequencies, the heavier rotor actually results in higher predicted efficiency. This unexpected result contradicts the intuitive notion that reduced rotor inertia improves performance by allowing the turbine to better track fluctuations in wind velocity. Such a result may be possible if the load is not perfectly matched to the turbine to yield maximum efficiency.

8.3 Performance in a Wind of Varying Direction

A second set of vortex model runs was conducted for a wind of constant velocity magnitude but varying direction.

One of the attractions of the vertical axis format is that the turbine does not need to be oriented with the wind direction. While this feature simplifies the turbine design, it does not guarantee that changes in wind direction have no effect on performance. Passive variable-pitch turbines rely on the development of an

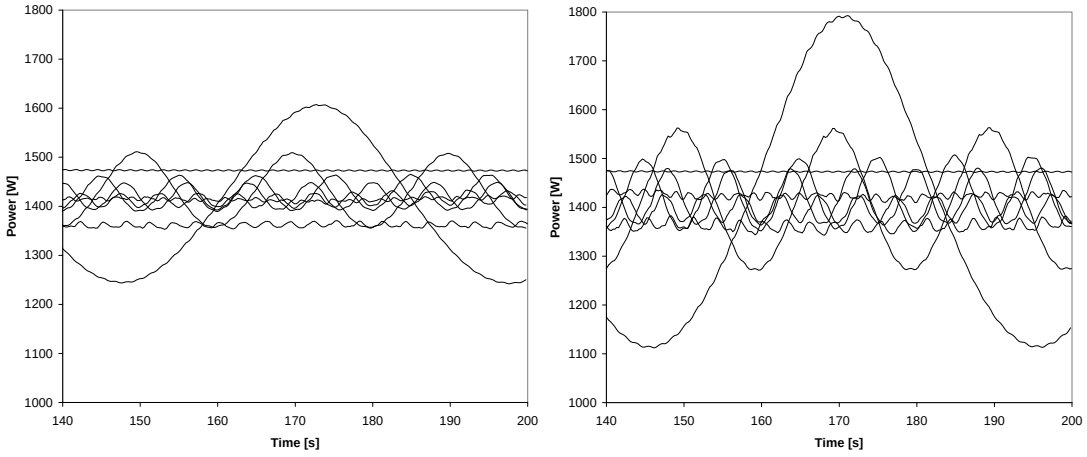

$I_t = 1766$ kgm^2 $I_t = 866$ kgm^2

Figure 8.1: Variation in power at steady-state in winds of fluctuating magnitude for two values of turbine mass moment of inertia. The different frequencies of oscillation are evident in the power fluctuations.

appropriate pattern of blade pitch response. This pattern is oriented relative to the wind direction and takes some time to develop. If the wind direction changes, the pattern of pitch must change in response and this change takes some finite time. In the interim, the phase of the pitch response is effectively changed. If the wind direction is constantly varying, then the steady-state pitch response pattern may never have a chance to develop, and the efficiency of the turbine may be diminished.

A turbine with the parameters given in Table 8.1 and with turbine inertia I_t equal to 1766 kgm^2 was simulated using the vortex model in a wind of constant magnitude but varying direction. The wind speed was set at 7 m/s and the direction varied sinusoidally between limits of $\pm 45°$. The frequency of the oscillation was varied between 2 and 20 seconds.

Once the turbine had reached steady-state, the average output power was calculated over an integer number of periods for each case. The results are compared with the steady-state power for a steady wind in Table 8.3. The trend of the

results is consistent with those for the sinusoidally varying velocity. The effect on average output is small for low frequency variation and increases as the frequency increases. For a period of 4 seconds, the blade pitch response was so disturbed by the wind variation that the turbine decelerated almost to rest. At frequencies higher than this however, the performance recovered, as the blades seemed to be unable to 'feel' such rapid variations.

Period s	Average power coeff. Cp_{avg}	Difference %
Steady	0.405	0
2	0.366	-9.7
3	0.111	-72.6
4	0.005	-98.7
5	0.395	-2.4
10	0.403	-0.6
20	0.409	+1.0

Table 8.3: Average power coefficient results for wind of constant velocity magnitude and sinusoidally varying direction.

Of interest is the slight improvement in efficiency predicted for low frequency (period 20 second) direction variation over steady wind performance. The result could be dismissed as a product of the numerical model with these specific initial conditions, however it is not inconceivable that the result could be real. Axial momentum theory for wind turbines states that the power coefficient can not exceed the Betz limit due to the deceleration of flow through the turbine. The flow velocity at the turbine is related to the flow velocity in the wake via Bernoulli's equation. In a wind of varying direction, the wake is no longer linear and stationary behind the turbine and this may allow a higher velocity to persist at the turbine for a given loading. This may allow a higher torque to be produced than could be with a fixed wake. Further work is needed to investigate this possibility further.

Figure 8.2 indicates the oscillation in output power resulting from a wind of varying direction. This oscillation reflects an increase in torque during periods in which the wind direction is moving in the same direction as the turbine rotation, and a decrease in the opposite direction. This behaviour may be explained by the effective phase change of the pitch response that results from the wind direction change. If the wind direction moves to a positive azimuth angle, the phase angle of the pitch response is effectively decreased. Since for a passive variable-pitch system the blades always lag the driving aerodynamic force function by some amount, this reduction in phase angle is generally favourable. Conversely, a negative change in wind direction exaggerates the phase lag, reducing torque.

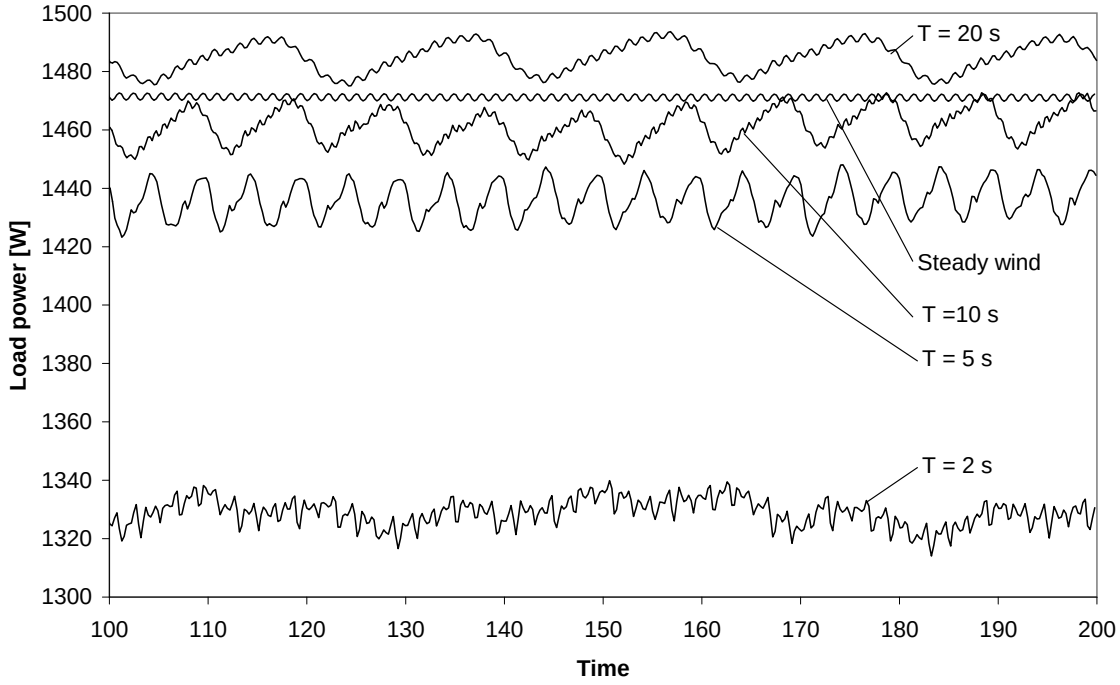

Figure 8.2: Fluctuating power transmitted to the load for a wind velocity of constant magnitude but direction varying sinusoidally between $\pm 45°$. The effect of different frequencies (indicated by the period T) is evident. The high frequency ripple superposed on all traces is due to the three blades of the turbine.

8.4 Performance in "Real" Wind

In order to simulate a real wind, the Dryden turbulence model was used to generate a time series of lateral and longitudinal free wind velocity components. The Dryden filtering technique presented by McFarland and Duisenberg (1995) was used to generate the velocity series from a random number input. A similar method was employed by Pesmajoglou and Graham (2000) in a study of horizontal axis wind turbines.

The input parameters for the filter - the longitudinal and lateral turbulence length scales and velocity standard deviations - were selected from data from the Engineering Sciences Data Unit (ESDU, 2001) for a surface roughness parameter of 0.03 corresponding to "typical farm land" at a height of 10 m. These parameters are shown in Table 8.4. The resulting velocity series is shown in Figure 8.3.

Nominal mean flow velocity:	7 m/s
Time interval:	1 s
Longitudinal turbulence length scale:	92 m
Lateral turbulence length scale:	22 m
Longitudinal velocity standard deviation:	1.28 m/s
Lateral velocity standard deviation:	1.00 m/s

Table 8.4: Turbulence parameters for "real" wind simulation

A number of factors influence the average output of a turbine in turbulent wind. The shape of the power coefficient-tip speed ratio curve is important. For a turbine operating at constant speed in a wind of varying velocity, the tip speed ratio will vary as the inverse of the wind speed. Because the power in the wind is proportional to the cube of the wind speed, the power coefficient that applies at the higher speeds has a disproportionately large influence on the average efficiency. For constant speed operation, the tip speed ratio is lower at these high wind speeds. Therefore if the power coefficient for a turbine decreases with increasing tip speed

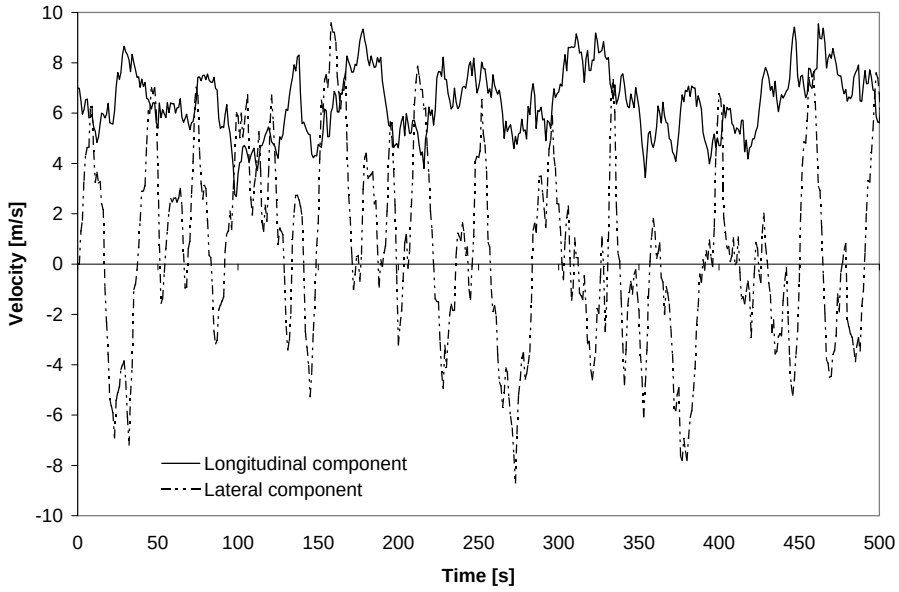

Figure 8.3: Longitudinal and lateral velocity components generated by the Dryden turbulence filter.

ratio in the range of interest, then the overall efficiency may actually be greater than that for the mean steady wind. The opposite is true for a positive Cp-TSR slope. The work of Rosen and Sheinman (1994) on horizontal axis wind turbines demonstrates this relationship.

Ideally, the turbine speed should be set so that it operates at close to the peak of the Cp-TSR curve as possible. In this case, any deviation in wind speed causes a reduction in power coefficient and so the overall efficiency will be reduced, as stated by Nattuvetty and Gunkel (1982).

For a turbine that is not constrained to operate at a constant speed, the inertia of the system becomes important. For a hydraulic type load, where the torque is proportional to the square of the speed, the turbine should operate at the same steady-state tip speed ratio, no matter what the wind speed. If it had zero inertia, the turbine would always be able to operate at this tip speed ratio even in a turbulent wind and would suffer no loss of efficiency. The slope of the Cp curve

would be irrelevant as the turbine would never leave its ideal operating point. However for a real turbine with non-zero inertia, the turbine speed lags the wind speed and it will be forced to operate at off-design tip speed ratios. For infinite inertia, the system returns to the constant speed case described above. The inertia of the system then determines to what extent the shape of the Cp-TSR curve affects the overall efficiency.

For these reasons Kirke (1998) recommended that in order to minimise the loss of efficiency that occurs in gusty conditions, the system inertia should be minimised and the Cp-TSR curve should be made as flat as is practicable.

The above factors apply to any type of wind turbine. A third factor may influence the performance of passive variable-pitch turbines. It has been assumed above that the shape of the Cp-TSR curve is constant, and that the instantaneous turbine output in unsteady conditions is always equal to the steady-state output that would develop were the current wind and turbine speeds to be held constant. However this is not necessarily the case for passive variable-pitch turbines. It has been shown that the performance of the turbine is very sensitive to the blade pitch pattern and that this pattern may take several revolutions to settle to its final form. It is possible then that this settling time might significantly influence the instantaneous output and also the overall average efficiency. It was desired to test whether differences in the moment of inertia of the blades would affect this settling time and would produce a measurable difference in average efficiency.

Four different passive variable-pitch turbines were tested in the turbulent wind field. The parameters of these turbines are presented in Table 8.5. The 'Elastic' and 'Pendulum A' turbines were selected to match as closely as possible the parameters for the original rolling profile turbine whose parameters are given in

Table 8.1. The blade mass moments of inertia (I_{pivot}) were calculated using Equation 3.7 in Section 3.3.4. It was found that because the Pendulum A turbine had a greater mass moment of inertia, it had a higher natural frequency ratio for the same restoring moment. In this case diminished performance resulted, so the Pendulum B turbine was included with an increased mass centre moment arm to match the frequency ratio of the other designs. The steady-state performance predicted for this design closely matched those of the Rolling Profile and Elastic designs (see Figure 8.4). It was desired to see whether the higher mass moment of inertia of the Pendulum designs would affect performance in a turbulent wind.

Parameter	Rolling profile	Elastic	Pendulum A	Pendulum B	Fixed blades
R_{ac} / mm	40	40	40	40	40
Restoring moment	55[a]	55[b]	55[c]	75[c]	-
I_{pivot} / kgm^2	3.19[d]	3.19	3.79	4.30	-
Load torque / (Nm/(rad/s)^2)	3.6	3.6	3.6	3.6	1.5

[a]Distance from centre of curvature to mass centre [mm]
[b]Torsion spring stiffness constant (stiffness proportional to centrifugal load) [(Nmm/rad)/N]
[c]Distance from pivot axis to mass centre [mm]
[d]Mass moment of inertia about the centre of mass

Table 8.5: Parameters of turbines simulated in a "real" wind. All other parameters are the same as for Table 8.1.

A fixed-bladed (standard Darrieus) turbine was also included in the comparison. The predicted steady state performance is included in Figure 8.4. Because the shape of the torque speed for the Darrieus turbine is different from that of the variable-pitch turbines, a different load characteristic was chosen to suit it. It was found that the operating point had to be located at a slightly higher tip speed ratio than would yield the greatest steady-state efficiency because the lack of torque at lower speeds made it difficult to converge to the steady-state. A load of 1.5 Nm/(rad/s)^2 was finally used.

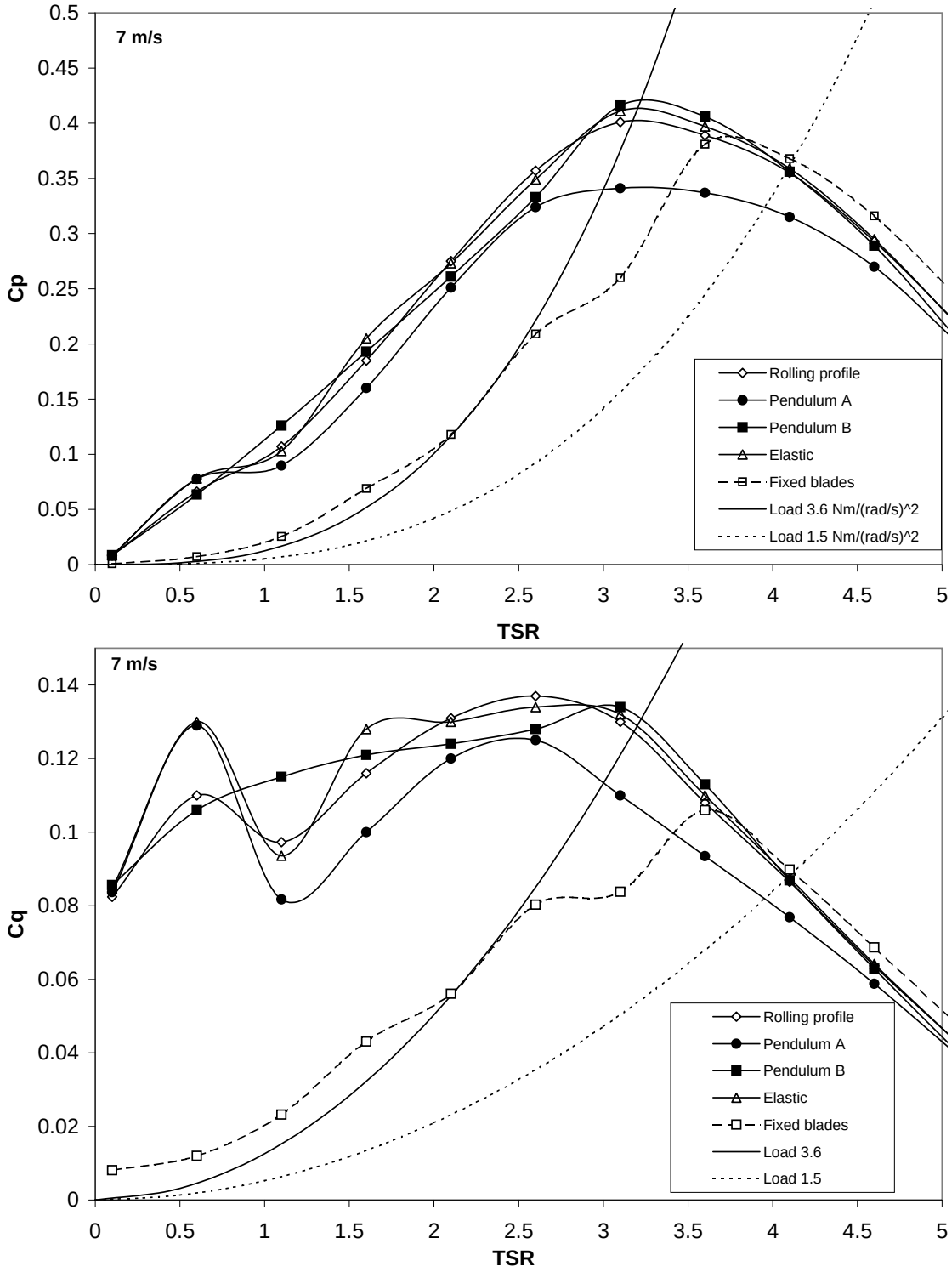

Figure 8.4: Momentum theory steady-state performance curves for the turbines listed in Table 8.5

The load power histories of the turbines over 500 seconds (some 26,000 time steps) is shown in Figure 8.5. The average power coefficients for the period are presented in Table 8.6. These values include the integrated load power and the change in kinetic energy of the turbine calculated from the difference between in initial and final speed. The runs were started with the turbines at approximately the steady-state speed for the equivalent steady wind of 7.7 m/s. This speed yields the same average power as the turbulent wind series. The average efficiency in the turbulent wind is compared with the steady-state power coefficient at this wind speed.

It is evident that the average power in a more realistic wind is reduced by a greater amount than in the simple sinusoidally varying cases. The rolling profile design is predicted to handle the turbulent wind slightly better than the other designs. The pendulum designs, with their greater blade inertia, suffered more in these conditions.

The predicted performance loss for the fixed-bladed Darrieus turbine is considerably greater than for the variable-pitch turbines, despite the fact that it does not suffer from any lag of blade pitch response. It appears that the sharper drop-off in torque at intermediate tip speed ratios characteristic of fixed-bladed turbines significantly affects the average efficiency in a turbulent wind, where sudden gusts force the turbine to operate for considerable periods in this region. Figure 8.4 shows clearly that while the torque produced by the variable-pitch turbines is maintained at low tip speed ratios, the Darrieus turbine curve drops sharply below the peak. The difference between the turbine torque and the load torque at a given tip speed ratio determines the acceleration of the turbine. It is clear that even for the smaller load (1.5 $Nm/(rad/s)^2$), the gap between turbine and load

torque curves below the intersection point is smaller than for the variable-pitch turbines. This means that when a gust of wind arrives and the tip speed ratio is momentarily reduced, less torque is available to accelerate the turbine. The Darrieus turbine is therefore less able to track variations in wind speed.

A simulation run was also conducted for the rolling profile and fixed bladed turbines with reduced rotor moment of inertia ($I_t = 866$ kgm^2 compared with $I_t = 1766$ kgm^2 as before). In this instance the lower inertia allowed the turbine with the rolling profile to track the wind velocity more effectively, reducing the variation in tip speed ratio and resulting in a clear improvement in performance. This is in line with expectation, unlike the results obtained for the sinusoidally varying wind speed presented in Section 8.2.

The difference in performance between the two fixed-bladed turbines is smaller than expected. It appears from Figure 8.6 that during gusts the lighter rotor allows the turbine to accelerate and extract more power, however this gain is offset by the deceleration of the rotor during lulls.

These results suggest that the shape of the turbine torque curve is the most important factor in determining the average efficiency of the turbine in turbulent conditions. The proportions of time spent at tip speed ratios above and below the equilibrium is influenced by the shape of the torque curve either side of the steady operating point.

8.5 Conclusion

Vortex model simulations of a passive variable-pitch VAWT were conducted for winds of sinusoidally varying magnitude and direction over a range of frequencies.

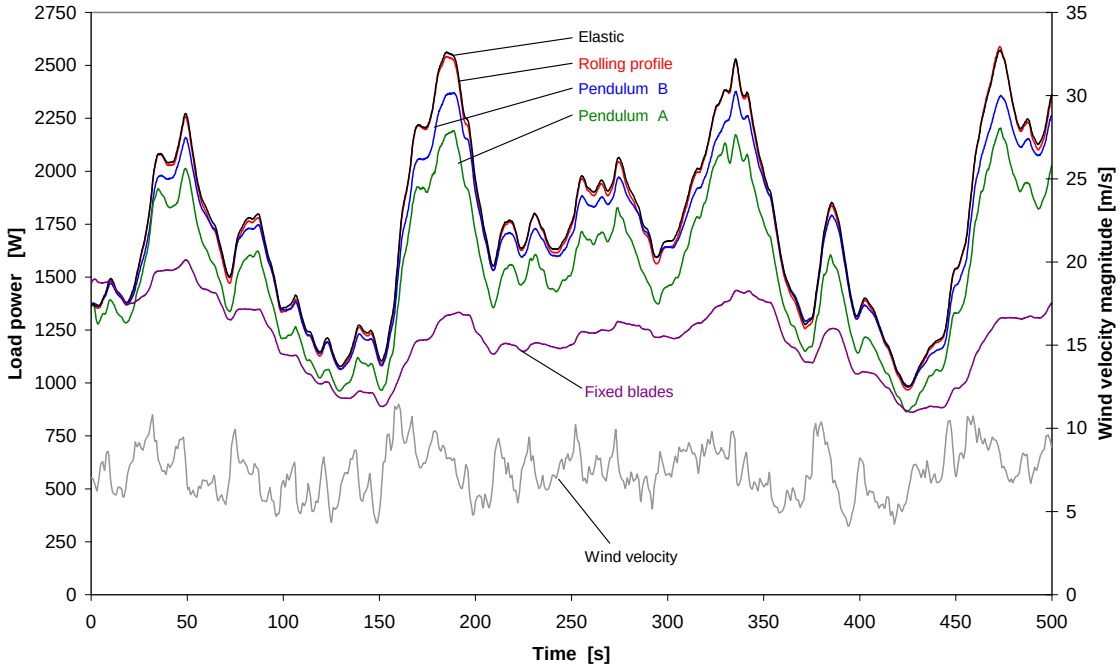

Figure 8.5: Load power generated by four passive variable-pitch turbine systems and a fixed bladed turbine in a simulated turbulent wind.

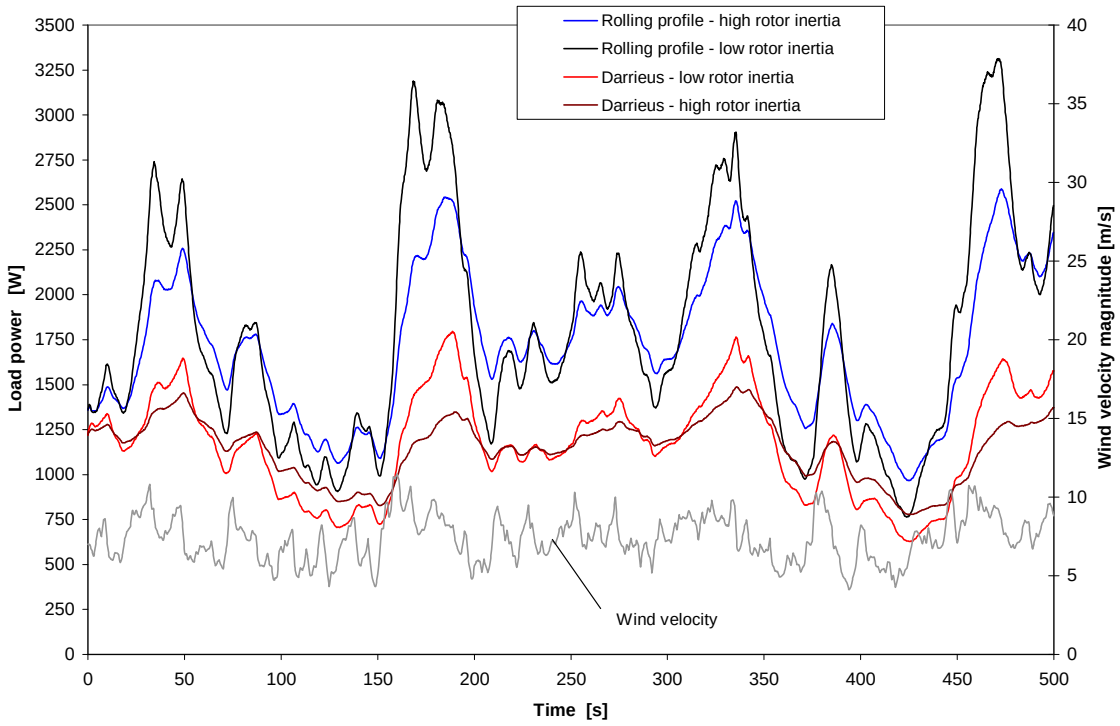

Figure 8.6: Comparison of the load power generated by the rolling profile turbine with two different rotor inertias. High inertia is $I_t = 1766$ kgm^2, low inertia $I_t = 866$ kgm^2

Average power coefficient Cp_{avg}	7.7 m/s steady	Turbulent wind	Difference %
Rolling profile	0.407	0.364	-10.5
Elastic	0.414	0.367	-11.3
Pendulum A	0.367	0.321	-12.5
Pendulum B	0.405	0.354	-12.5
Fixed blades	0.333	0.240	-27.9
Rolling profile - low inertia	0.407	0.373	-8.3
Fixed blades - low inertia	0.333	0.245	-26.3

Table 8.6: Average power coefficient results for five turbines in a turbulent wind

It was found that the deviation of average output from steady-wind performance increased with increasing frequency of variation up to a point, beyond which the turbine appeared to be unable to respond to such rapid variations.

Simulation of performance in a turbulent wind has indicated the importance of a 'flat' Cp-TSR curve to maximise total energy capture. In the current trial, turbulent wind efficiency was predicted to be 28% lower than steady wind efficiency for a Darrieus turbine. The corresponding difference for a rolling profile passive variable-pitch was 10.5%. Variable-pitch mechanisms are therefore not only important for self-starting, but can also significantly increase the average efficiency in turbulent conditions. Minimisation of the mass moment of inertia of the turbine and load appears to be of secondary importance, as does the minimisation of blade inertia.

Chapter 9

Experimental Evaluation of New Design Concepts

9.1 Introduction

In order to test the potential of the design concepts described in Chapter 3, a prototype turbine was designed and constructed for testing in the wind tunnel at UNSW. Testing was intended to assess the performance of the design concepts and of the mathematical models developed for them.

The development of a technique for measuring the pitch response pattern of at least one of the blades while the turbine was in operation was a priority. This information would provide insight into the performance of the turbine and the ability of the mathematical models to predict it.

Three options were considered for testing of a prototype turbine: wind tunnel testing, field testing and vehicle-mounted testing.

Wind tunnel testing offered the greatest control over flow conditions and was the simplest option. The drawbacks however were the limitation that the available test section placed on the size of the turbine and the effects of blockage. It was desired to maximise the size of the prototype to increase the Reynolds number of operation, reduce rotational speeds and in general be as close to full-scale as possible. However if the turbine were made too large for the test section, the flow field around the turbine would be affected by the walls of the section, altering its performance in ways that would be difficult to predict.

The option of field testing would remove the limitation on size and allow the turbine to be studied in the conditions in which it would ultimately operate. The inability to control or even accurately measure the free wind velocity and direction at the turbine however would make analysis of performance difficult. Only averaged quantities would be reliably obtained.

The third option of vehicle or trailer-mounted testing offered the possibility of controlling the wind velocity and direction, if still air conditions occurred. There remained the possibility of disturbed flow from the vehicle affecting turbine performance. Also practical considerations would limit the size of the turbine that could be tested in this fashion. A final major disadvantage was the likelihood that movement and vibration of the vehicle would significantly affect the pitch response patterns of the blades. Given the predicted sensitivity of turbine performance to the blade response pattern, this would be a major problem.

The final issue affecting any form of outdoor testing was that the photogrammetric pitch measurement method that was developed (which is described in Section 9.4.3) relied upon the ability to reduce ambient light. This could only be achieved in the wind tunnel. Accordingly, the wind tunnel was chosen as the most appropriate method of testing.

9.2 Prototype Turbine Design

A turbine was built for testing in the large test section of the closed-circuit wind tunnel at the UNSW. The size of the turbine was determined by the size of the available wind tunnel test section. As mentioned above, it was desired to make the turbine as close to a real operational size as possible within the constraints of the test section area. The smaller the turbine of a given solidity, the smaller the blade chord and therefore the smaller blade Reynolds number. This results in

earlier blade stall and reduced starting performance. If the blade chord is made large relative to the turbine radius to overcome this, the effect of flow curvature is amplified.

The turbine speed required to achieve a given tip speed ratio at a given wind speed is inversely proportional to the turbine radius. The centrifugal load on a blade is therefore inversely proportional to the square of turbine radius. Maximising the radius at which a blade of given length is mounted therefore reduces the bending loads on it, as well as increasing the swept area and power capacity of the turbine.

The test section available at UNSW is octagonal in cross section with a height and width of approximately 3 metres (see Figure 9.1). The turbine dimensions were chosen to be diameter 1.8 metres and height 1.3 metres, giving a swept area of 2.34 square metres.

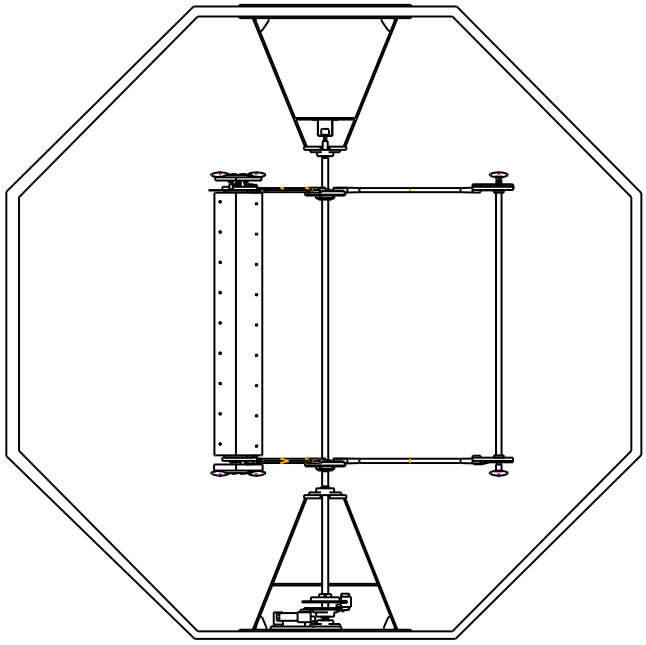

Figure 9.1: Turbine in the 3 metre high wind tunnel test section

The blade chord was set at 150 millimetres, giving an aspect ratio of 8.67. The turbine was designed with three blades, giving a solidity of $N_b c/R = 0.5$. This relatively high solidity was chosen to assist starting performance.

The NACA 0018 profile was chosen as the blade section. This section is commonly used for Darrieus turbines. Its relatively high thickness to chord ratio gives it good strength in bending and its aerodynamic properties are well documented.

The radial arms of the turbine were made from high strength aluminium grade 6061-T6. They were NC milled to an Eppler 862 non-lifting profile to reduce parasitic drag.

9.3 Blade Design

Unlike horizontal-axis turbines, the straight blades of a vertical axis turbine are loaded in bending by their self-weight under centrifugal force. Horizontal axis turbine blades take centrifugal loads in tension, which produces much lower maximum stresses. While aerodynamic forces produce bending loads, these are an order of magnitude lower than inertial loads at design speed.

The blade bending loads are a significant hurdle to be overcome in the design of a straight-bladed VAWT. The curved troposkien-shaped blades of large Darrieus turbines are designed to minimise bending loads, but blade articulation is then not possible.

Often blades designed for this type of turbine are based around a central structural spar, to which ribs are attached and around which a thin skin is fastened, to form the desired blade profile. The blade designs described by Bayly (1981) and Kirke (1998) are of this type.

Since the primary concern is bending stress due to the self-weight of the blades, the minimisation of mass and maximisation of cross-sectional area moment of

inertia are paramount. Apart from selecting a material with a high strength-to-weight ratio, these criteria require that material be located as far from the section neutral axis (the blade chord line) as possible. For a prismatic blade the ratio of area moment of inertia of the section to cross-sectional area, I/A, should be maximised. For this application, a solid section blade is far worse than a hollow blade, as material near the neutral axis adds mass without contributing much bending strength. It may be shown that for a given profile with constant wall thickness, the limit of I/A as wall thickness goes to zero is two times that for the solid section. This principle led to the adoption of a design in which the blade skin is the structural component, rather than an aerodynamic covering over a structural skeleton. Clearly design to avoid buckling failure must be done carefully in this case.

Often blades are constructed so that they are attached to the rotor at two points. In order to minimise bending stress, the mounting points are located at some distance in from the ends. For example Evans (1978) calculates that for a blade of uniform section, the bending moment at midspan and mounting points is made equal by locating the supports a distance of $L/(2+2\sqrt{2})$, approximately $0.207L$, in from each end. This reduces the maximum bending moment by a factor of 1/5.8 compared with simply supporting the blades at its ends.

In this case, because the focus of the project was on the design of the blade mounts, it was felt that it was desirable to have the blade mounted at its ends. This would allow easiest access to the blade connection area, which would require frequent adjustment. In addition, it allowed the blade to be mounted without breaking the skin - an important consideration if the skin is to be used as the structural member. Finally, it was intended to mount the turbine in the wind

tunnel using supports connected to the floor and ceiling, making end-mounting of the blade more desirable.

In order to reduce the bending moment in the middle of the blade, it was decided to utilise counterweights, cantilevered above and below the mounting points. The counterweights that are needed to balance the blade about its pivot axis can then serve two purposes. They will act as 'virtual' blade length outside the mounting points, playing the same role as the roughly 20% of the uniform section blade calculated by Evans (1978). This design is shown in Figures 9.2 and 9.3.

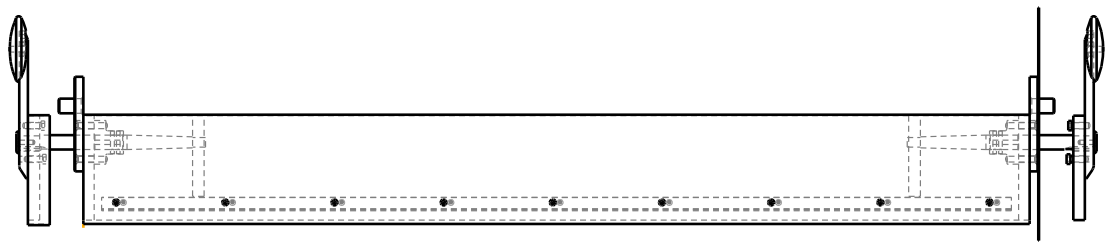

Figure 9.2: Blade design featuring cantilevered counterweights

The difficulty with this design is that the cantilevered spar on which the counterweight is mounted is subjected to significant bending and torsional loading. The spar must be made of a high strength material capable of withstanding these high loads. In this case high strength stainless steel - Sandvik SAF 2205 - was chosen. This has a high yield stress (450 MPa) and was selected for its corrosion resistance so that the turbine could be used for outdoor testing in the future.

An undergraduate thesis completed at UNSW by Dawson (2000) involved a detailed finite element analysis of different blade designs for this project using MSC/PATRAN and MSC/NASTRAN. His work indicated that the lowest maximum stresses could be obtained using a structural skin with no internal spars or ribbing. The skin could be aluminium or fibreglass. Dawson performed linear

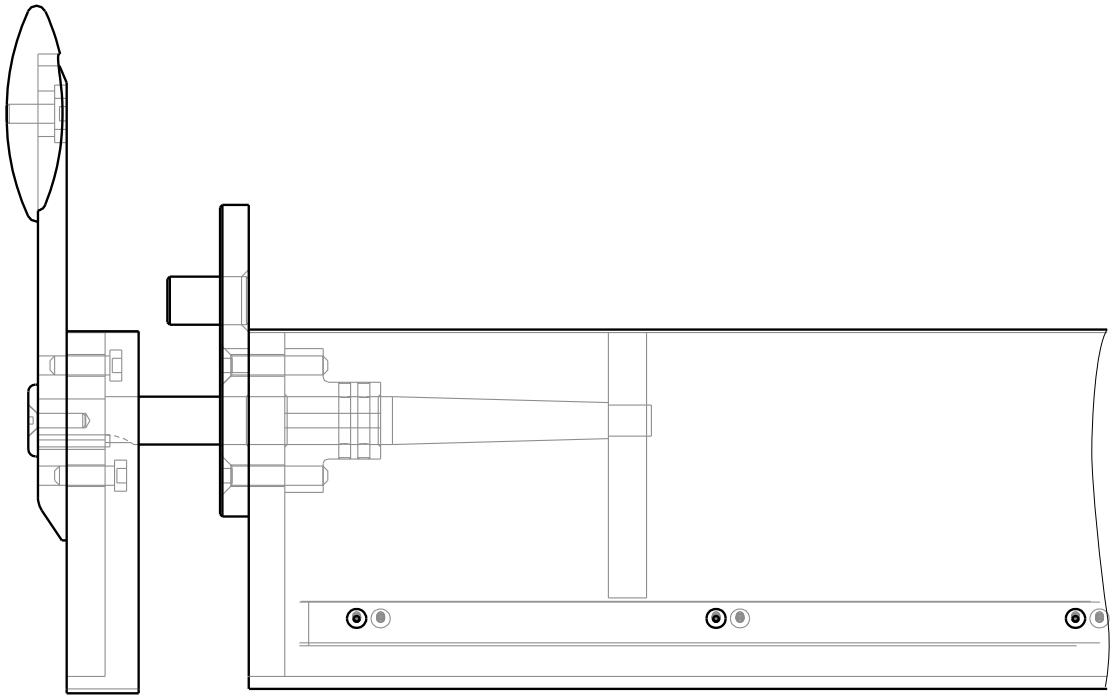

Figure 9.3: Detail of blade design concept showing cantilevered counterweight

static analyses to predict maximum Von Mises stress, as well as running buckling analyses to check for buckling failure.

Further finite element analysis using Pro/FEM was conducted by the author on the specific design chosen for the prototype turbine that was built for the wind tunnel. The mesh generated for the blade is shown in Figure 9.4. Symmetry was exploited to allow modelling of one half of the blade. A 'gravity' acceleration of 200 g was applied, corresponding to a rotational speed of approximately 450 rpm at a radius of 900 mm.

Skin material was chosen as 1.27 mm thick aluminium sheet. Carbon fibre was investigated as a possible material for blade manufacture, but the cost for the manufacture of three blades was found to be prohibitive. A relatively high-strength alloy - 6061-T6 - was chosen, giving a nominal yield stress of 240 MPa. A counterweight mass was chosen and its chordwise location adjusted so that the

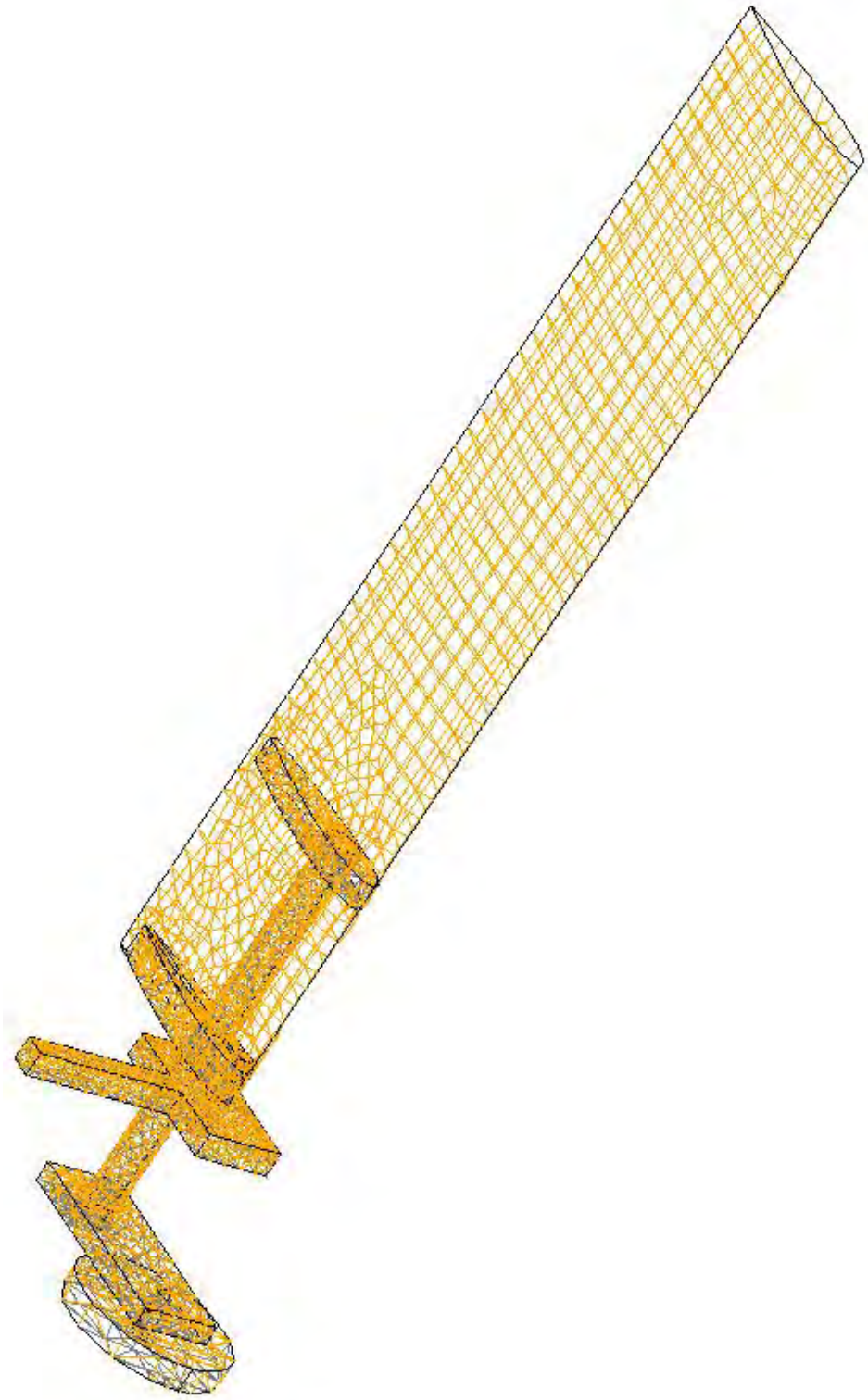

Figure 9.4: Finite element mesh

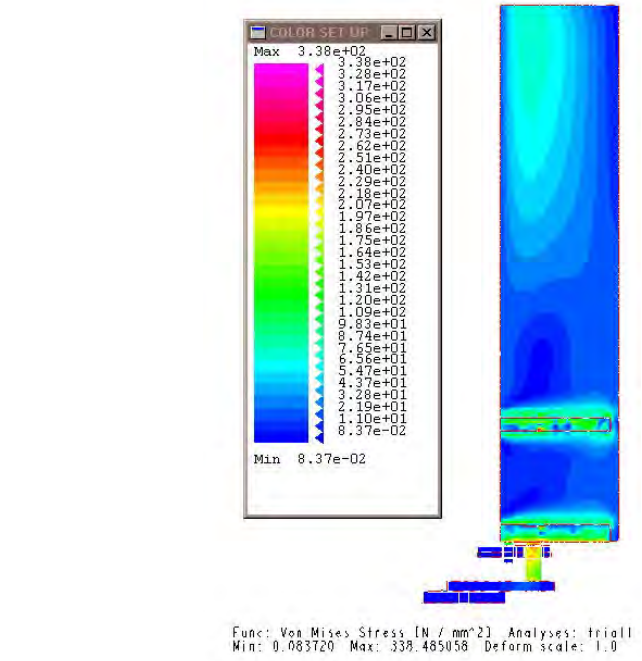

(a)

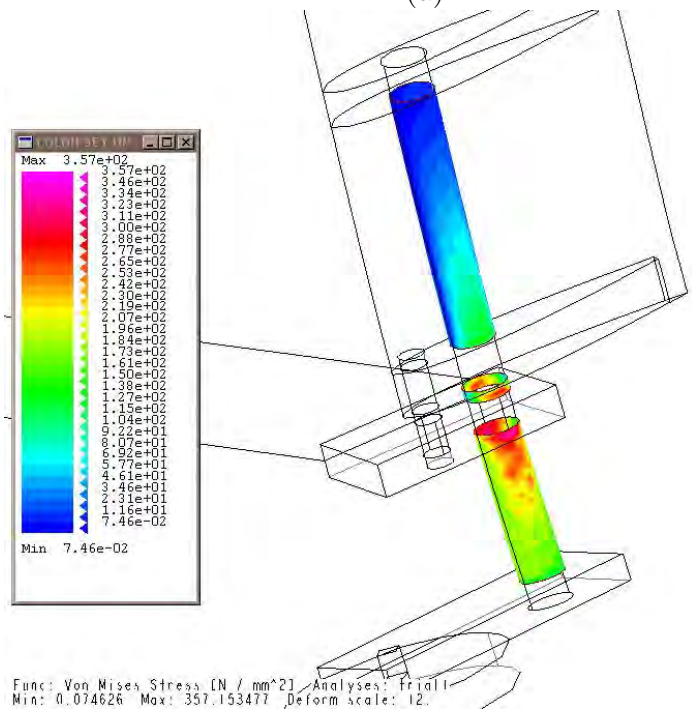

(b)

Figure 9.5: Colour fringe plot indicating predicted von Mises stress in the blade skin (a) and the counterweight spar (b)

centre of mass lay 20.5 mm ahead of the quarter chord location - a position that had been selected on the basis of momentum theory modelling. The degree of overhang on the mass was then adjusted so as to balance the safety factors with respect to yield in the blade skin and the counterweight spar.

The design relied upon the ability to form the sheet to the required profile with sufficient accuracy. The structural blade skin is thicker and stronger than a thin skin that would be used around a series of ribs. Tests were done in first rolling a flat piece of sheet to gain the general curvature of the sides of the aerofoil, then forming the nose by bending in a press using progressively smaller radius dies. Initial tests were encouraging. Ultimately the forming was done by a specialist sheet metal company using a similar technique. The sheet was rolled then bent to match as closely as possible a template of the desired NACA 0018 profile.

Ribs were NC milled to the correct profile from 15 mm thick 6061-T6 aluminium. One rib was located at each end of the blade, and another 150 mm in from each end. Each rib had holes to locate the spar on which the cantilevered counterweight was mounted. This assembly is shown in Figure 9.6. The formed blade skin was glued to all ribs and also rivetted to the end ribs to pull them into the correct profile. The assembly process is shown in Figure 9.7.

The trailing edge was closed using a 'V'-strip of aluminium sheet. The strip was glued and rivetted to each side of the blade skin and the edges of the sheet were then glued together at the trailing edge. Araldite 2015 was selected as a suitable adhesive, as it is slightly flexible, giving it greater toughness. Pictures of the formed blades and the assembly process are shown in Figure 9.7.

The blade in place on the turbine rig is shown in Figure 9.8. The Type A elastomeric blade mounting component is shown. The completed turbine rig, fixed

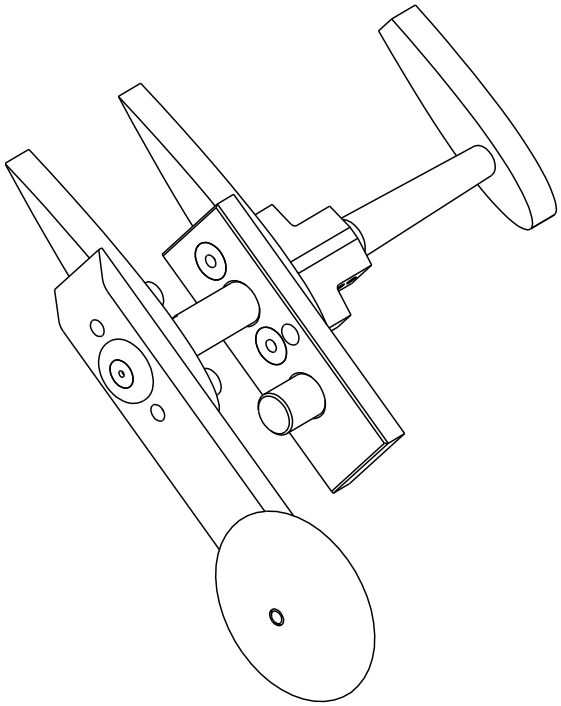

Pro/ENGINEER model

Finished assembly

Figure 9.6: Blade end assembly

(a) Application of glue to blade trailing edge

(b) Blade skin in mould used for clamping while the glue set

Figure 9.7: Construction of the blades

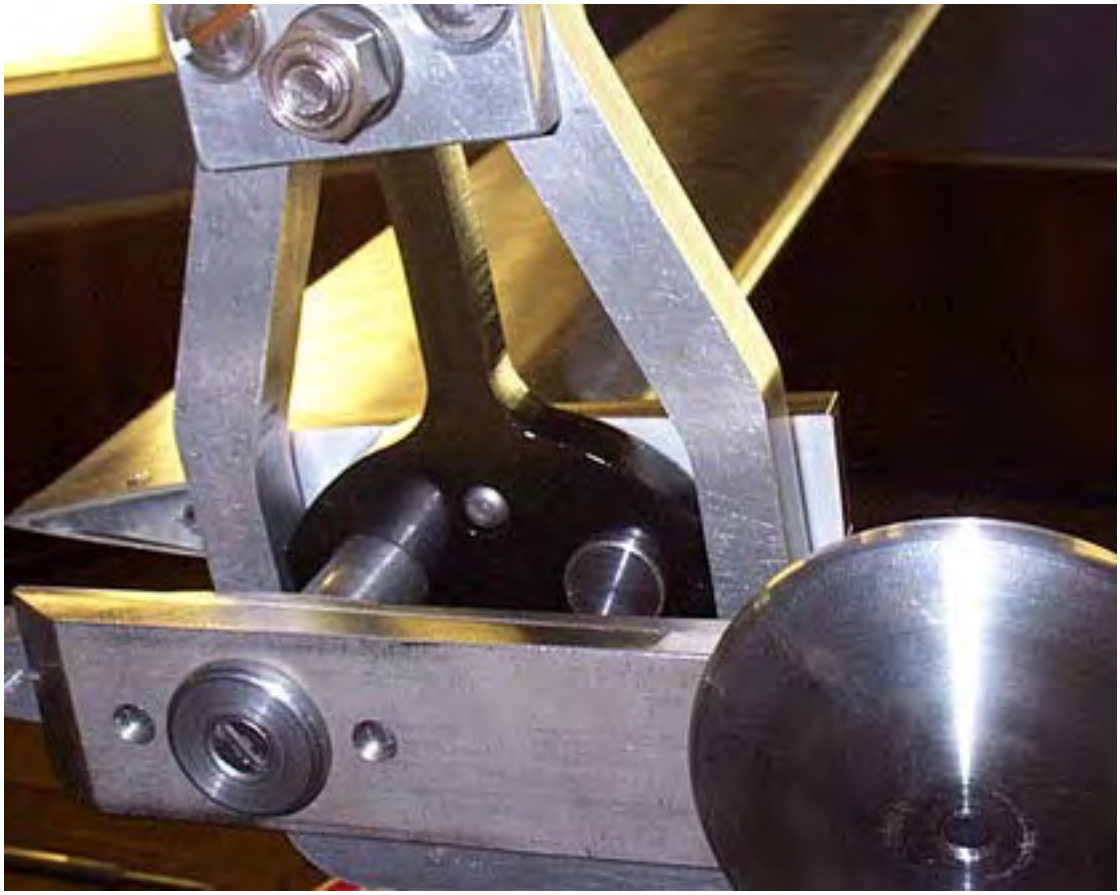

Figure 9.8: The 'Type A' elastomeric blade mounting component on the turbine rig.

inside the wind tunnel test section is shown in Figure 9.9.

9.3.1 Aerodynamic testing of blades

The major concern for the blade design chosen was whether the construction method would deliver sufficient accuracy in the blade profile from an aerodynamic standpoint. In order to test the aerodynamic properties of the blades, wind tunnel testing was performed to measure lift and drag coefficients. The test blade had the same chord length of 150 mm as the blades used on the turbine, but was cut shorter to fit inside the 3 x 4 ft (614 x 1218 mm) wind tunnel test section. The test blade was 1 m long, giving an aspect ratio of 6.67. The blades used on the

Figure 9.9: The author with the finished rig in the wind tunnel.

turbine were 1300 mm long, with an aspect ratio of 8.67. The test blade is shown in the test section in Fig. 9.10.

Lift and drag coefficients were measured at wind speeds ranging from 16 m/s to 36 m/s and at angles of attack from -15° to +50°. Forces were measured using a 6-component pyramidal balance. A calibration was performed with zero wind velocity to eliminate the effect of the mass of the blade. The results are shown in Fig. 9.11.

For comparison the data of Sheldahl and Klimas (1981) for the NACA 0018 section are also shown in Figure 9.11. These data were used in the mathematical models because they provide a complete range of values for all angles of attack and

Figure 9.10: Test blade mounted in the wind tunnel

over a large range of Reynolds numbers. It can be seen from Figure 9.11 that the lift and drag coefficients measured here are quite similar to the published values. At all tested Reynolds numbers, stall occurs at a higher angle of attack and occurs more suddenly than was measured by Sheldahl and Klimas. Correspondingly higher maximum lift coefficients were also recorded. As expected, the stall is delayed with increasing Reynolds number over this range.

The delayed stall may be a result of the manufacturing technique, which does leave slight artifacts of the forming process. A series of parallel bends are visible near the leading edge, which may serve to 'trip' laminar flow to become turbulent. There was however little measured increase in drag associated with this effect.

It was concluded on the basis of this testing that the chosen blade design and manufacturing technique produced blades of sufficient profile accuracy to be used as turbine blades.

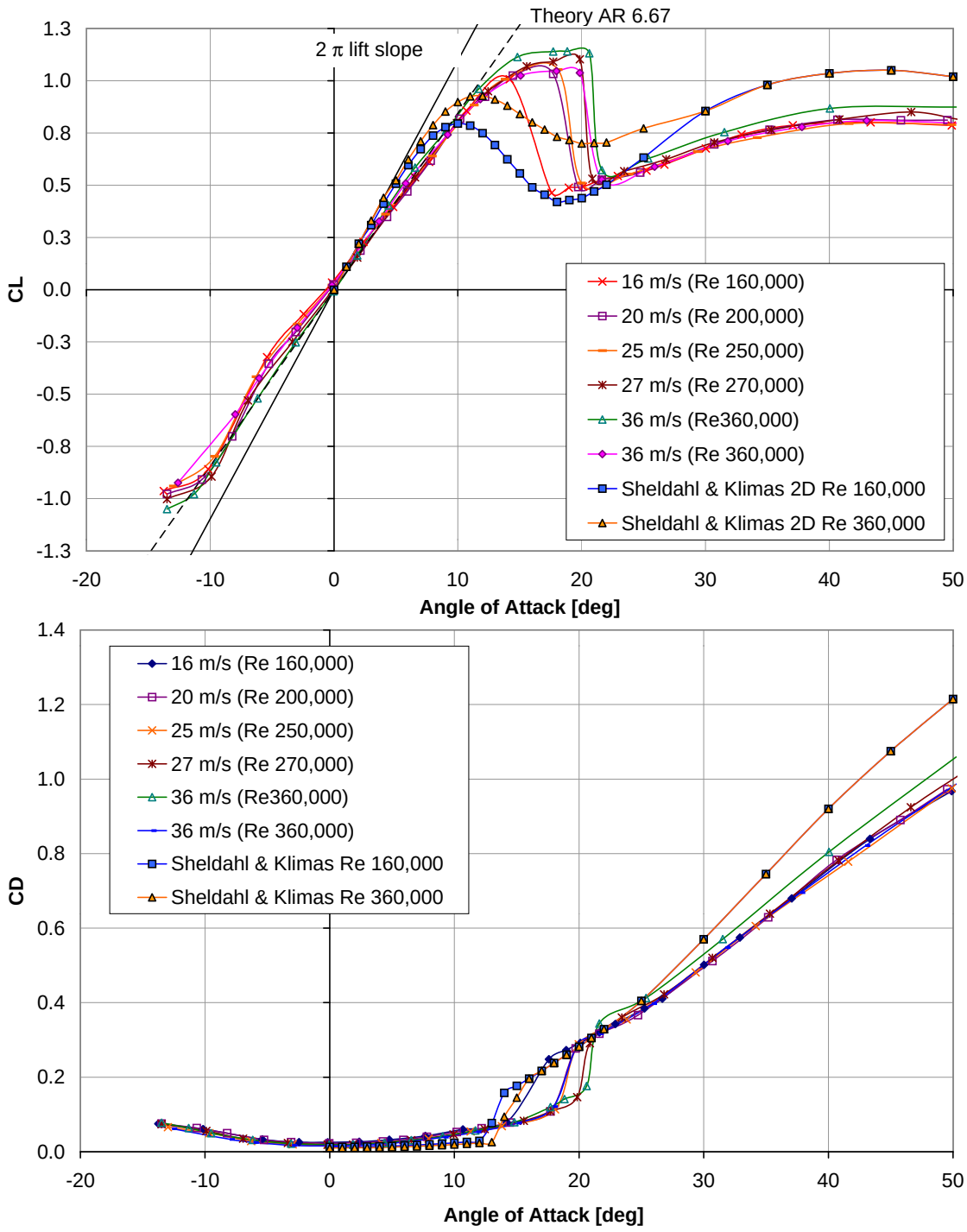

Figure 9.11: Measured lift and drag coefficients for a test turbine blade

9.4 Instrumentation

9.4.1 Torque and speed measurement

The quantities measured were the turbine rotational speed and torque. Speed was measured using a 720 pulse-per-revolution shaft encoder mounted at the top of the turbine shaft. Torque was measured using a load cell attached to a brake calliper that acted on a brake disc keyed to the shaft. Commercial panel meters were used for signal conditioning and digital conversion. The data was logged by a PC, which was connected to the panel meters via the serial port.

The turbine torque calculated is a combination of shaft torque measured by the load cell on the brake and torque that is accelerating the turbine. Acceleration torque was calculated by numerically differentiating the logged turbine speed data. Because numerical differentiation magnifies the small scatter in the measured speed values, the acceleration curve was smoothed by fitting a cubic spline through the velocity data. The data was thinned from the sampling frequency of approximately 3 Hz to a period of 5 seconds, which was judged sufficient to capture the features of interest in the speed history. The spline was then fitted through the thinned data points. The slope of the spline at the data points, which is naturally calculated in the process of fitting the spline, is then used as the acceleration at that time.

Torque is calculated by multiplying acceleration by the polar moment of inertia of the rotor and blades, calculated using the Pro/ENGINEER model.

The shaft or load torque measured by the load cell connected to the brake calliper exhibited considerable scatter resulting from slight misalignment between the disc, shaft and calliper. The fluctuating torque data was smoothed taking a rolling average.

The total torque produced by the turbine at any point in time was then taken to be the sum of the acceleration torque and the load torque. The non-dimensional

torque coefficient, C_q, is defined as:

$$C_q = \frac{T_{acc} + T_{load}}{\frac{1}{2}\rho A U_\infty^2 R} \tag{9.1}$$

where ρ is the air density, A is the swept area of the turbine, U_∞ is the free wind velocity and R is the turbine radius.

The torque coefficient calculated in this way reflects the total aerodynamic torque generated by the turbine at a given speed. If the turbine is at steady-state, the torque used to accelerate the turbine, T_{acc} is zero, and all the torque is used to drive the load. At tip speed ratios lower than the steady-state speed, the turbine will be accelerating and T_{acc} will be non-zero. This means that the torque coefficient calculated using Equation 9.1 is larger than that calculated using the load torque alone. In the study of the self-starting ability of turbines, the transmission of energy to the load is not considered to be the only useful work being done: the acceleration of the turbine to steady-state operating speed is a task that otherwise must be done using external energy. This measure of torque reflects the success of the blades in extracting energy from the wind. This is the aspect of turbine performance that is being studied.

9.4.2 Wind speed measurement

Initially the wind speed was measured manually using a fluid manometer connected to a static pitot tube mounted approximately one diameter upstream of the turbine axis in the wind tunnel. This was the furthest forward position possible. Later a digital micromanometer was used to measure the pressure differential from the pitot tube, allowing flow velocity data to be logged along with the torque and speed data.

Some scatter was observed in the logged data from the digital manometer. This scatter was due to signal noise, rather than being a reflection of the turbulence level in the test section. It may be seen that the scatter in the wind velocity measurement is evident only during periods when the mean velocity is constant. The same degree of scatter is evident at the end of the run even when the wind speed was definitely zero.

Separate turbulence measurements were carried out using a hot wire anemometer. The turbulence intensity was found to be between 1.0% and 1.3%.

To smooth the wind velocity data, a rolling average technique was again employed, over an interval of 100 samples. Torque coefficient C_q was calculated from Equation 9.1 using the smoothed wind speed. These values are then plotted against the current turbine speed, non-dimensionalised in the form of tip speed ratio. This allows results at different wind velocities to be compared.

9.4.3 Blade pitch measurement

The most difficult quantity to measure was the blade pitch angle. Several methods of measurement and data collection were conceived, involving linear or rotary variable displacement transducers, onboard microprocessors, slip rings or radio communications. Ultimately problems of complexity, invasiveness and inadequate sampling frequency forced the abandonment of such designs in favour of a simpler and more direct method.

The pitch measurement system presented a number of major difficulties. First, it must provide sufficient accuracy and resolution, both in terms of the pitch angle and the azimuth angle (the blade's position in its orbit) and it must be able to convey information from the rotating frame of reference of the turbine rotor to ground. While any of the transducers listed above could provide satisfactorily

accurate measurement of the instantaneous pitch angle, determination of the azimuth angle at which this pitch occurred was more difficult. A second transducer would be needed to sense the rotor position and the sampling of signals from the pitch and azimuth transducers would have to be accurately synchronised. The sampling frequency would also have to be sufficiently high to provide adequate azimuthal resolution at the highest turbine speeds. This would require a relatively expensive radio transmitter (and signal conditioning and A/D circuitry) to be mounted on the rotor. Slip rings would also require pre-amplification of the signal and be prone to signal noise. A further problem was the sensitivity of the blades' pitching behaviour to friction and interference from the transducer. Worse, in some variants of the new design, the pitching axis of the blade is not actually fixed with respect to the turbine rotor on which the blade is mounted. The sensor therefore must also be able to accommodate these additional translatory degrees of freedom.

On the basis of these constraints, it was decided to measure the blade pitch angle photogrammetrically by recording the motion of two target points on one of the blades. Instead of attempting to capture motion with a series of high speed images, the periodic nature of the pitching motion was exploited by using light emitting diodes (LEDs) as targets and recording their trajectories using a long exposure on a digital still camera.

This approach yields continuous position information for the targets around the entire cycle (see Figure 9.12). By comparison a video camera operating at 25 frames per second would only record one image every 48 degrees at a turbine speed of 200 rpm.

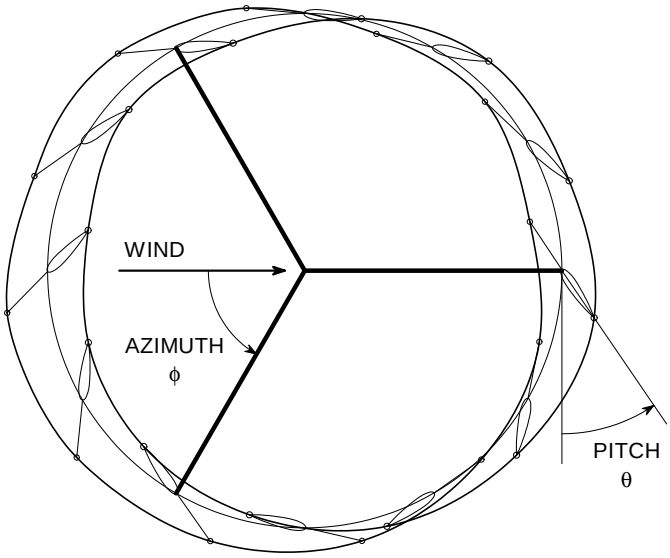

Figure 9.12: Variable pitch Darrieus turbine concept showing LED traces.

Two LEDs were mounted on the chord line of one of the blades, equidistant fore and aft of the axis of pitching, as shown in Figure 9.13. The trajectories of these points were then analysed to retrieve the blade pitch angle history over the duration of the exposure (see Figure 9.14). Assuming central projection, the world space trajectories can be found from the image traces with knowledge of the camera position and orientation. As physical measurement of the location of the camera was difficult, this data was estimated for each image using reference targets. For this purpose, two further LEDs were mounted on one of the radial arms of the turbine in the same horizontal plane as the blade LEDs. In the image these circular traces appear as ellipses whose proportions and positions, together with knowledge of the actual radii, reveal the viewing angle and distance. Once these quantities are found the pitch angle indicated by the blade LEDs can be determined.

Figure 9.13: The target LEDs mounted on one of the blades.

Determination of perspective transformation

It is well known that a circle appears as an ellipse in the image plane under perspective projection and that the centre of the circle is not projected to the centre of the ellipse in the image. Here the elliptical images of two concentric circular reference traces are used to determine the inverse perspective transformation needed to convert image coordinates into object space coordinates of points.

The perspective projection of an inclined circular trace of radius R in the X_2,Y_2 plane in object space onto the image plane is shown in Figure 9.15. The image plane x,y coordinate system and the object space X_2,Y_2,Z_2 coordinate system are defined such that their origins lie on the camera (z) axis and the X_2 and x axes

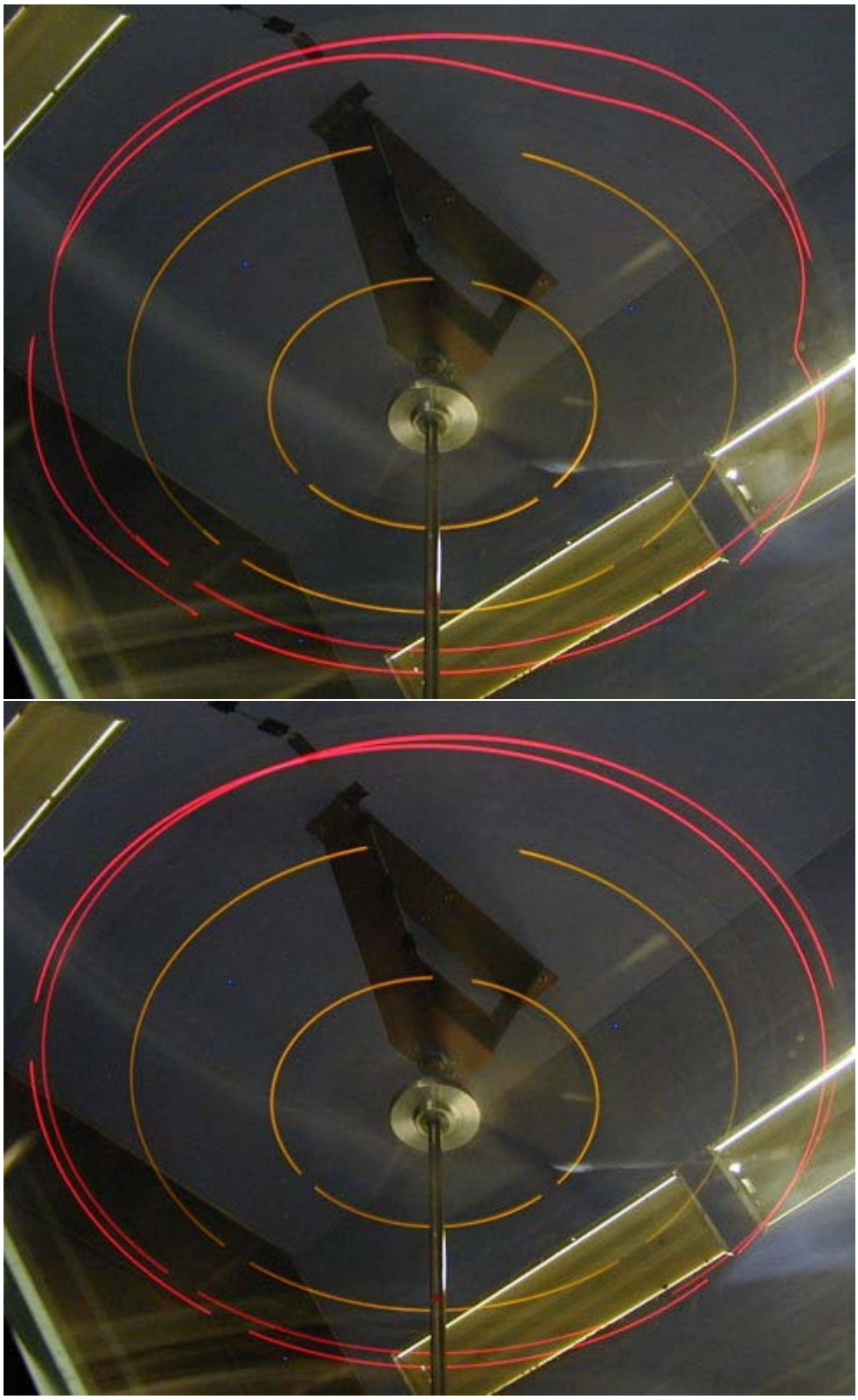

Figure 9.14: Two example images of LED traces for blade pitch measurement. The upper image is for a low tip speed ratio, the lower image for a high tip speed ratio.

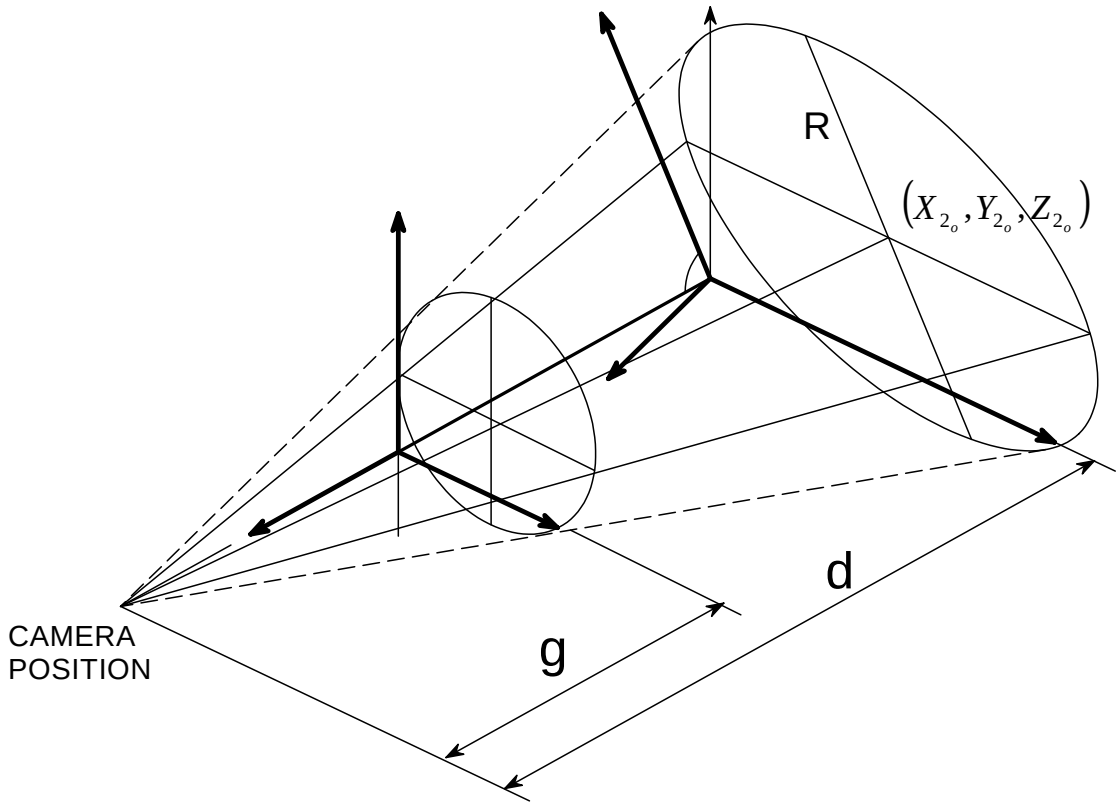

Figure 9.15: Projection of a circle in the inclined X_2-Y_2 plane onto the image plane x-y.

are both parallel with the line of intersection of the image plane and the plane containing the LED traces.

The first step then is to find algebraic expressions for the two ellipses. The process of obtaining the image coordinates of points on the reference ellipses was automated in order to speed up analysis and improve repeatability of results. A program was written in Visual C++ for Windows for the purpose of image analysis. Analysis was not conducted in real time for this application; instead images were stored and downloaded after each wind tunnel run.

A number of sample points need to be located on the traces. For this purpose the approach of Vincze (2001) was adopted. In order to obtain initial positions for the sample points, the parameters of the two ellipses (centre, major and minor semi-axes and rotation angle) are adjusted manually so that, when drawn on the

screen over the digital image, the ellipses coincide with the image traces as closely as possible. Sample points are then distributed at equal angular spacing around each ellipse. Pixels along a tracker line normal to the local tangent are then tested using an 8 x 1 Prewitt edge detection filter based on pixel intensity. The points of maximum and minimum intensity gradient are taken to be the inner and outer edges of the LED trace. The pixel closest to midway between the two edge pixels is then taken to be the location of the sample point on that tracker line. Since the analysis is not conducted in real time, it is possible to manually check each of the sample points to ensure that the detection has succeeded.

If detection fails, either due to a gap in the trace where a turbine blade passed in front of it or due to insufficient contrast in the image, the sample point on that tracker line is positioned either by interpolating between the two neighbouring points, or is positioned manually as close as possible to the centre of the trace using a magnified image.

Once the sample points have been located on the traces (12 points were found to be sufficient), ellipses are fitted to these points using Halir and Flusser's (1998) version of the direct least squares ellipse fitting method of Fitzgibbon et al. (1999). This method produces 6 coordinates to define the ellipse in polynomial form

$$Ax^2 + Bxy + Cy^2 + Dx + Ey + F = 0$$

Two approaches may be used to find the camera distance and angle from the reference ellipse coordinates.

The viewing parameters may be estimated using a direct geometric method. The 6 coordinates used to represent each ellipse in the horizontal and vertical screen axes are transformed by rotation to principal axes and the five parameters

of major and minor axis length, angle of orientation and location of centre are extracted for each.

For the general case of the circles' common centre not lying on the camera axis, the major axes of the elliptical images of the circles will be parallel neither with the x axis nor with each other. For strict central projection, a line constructed through the centre points of the two elliptical images will pass through the location in the image of the actual centre of the circles and proceed to the vanishing point for lines parallel with the Y_2 axis. The tangents to both ellipses at the points of intersection with this line should all be parallel with the X_2 axis. This is illustrated in Figure 9.16.

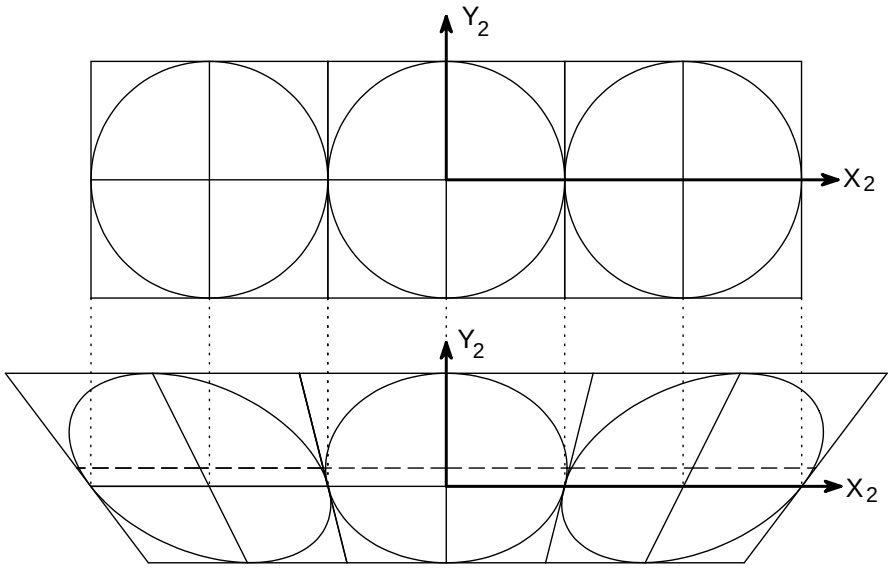

Figure 9.16: The perspective projection of circles and their bounding squares, rotated about the X_2 axis, which is parallel to the image plane. The dashed horizontal line indicates the vertical position in the image of the centre of all ellipses, independent of the X_2 coordinate.

Once the ellipses are identified in the image therefore, the line through their centres is found and the slope of the tangents at the intersection points determines the orientation of the x,y image coordinate system. The x-axis will not necessarily be horizontal in the image and so image coordinates must be found by a rotation

about the principal point from their pixel coordinates. Next the location in the image of the centre point of the circles is determined. Referring to Figure 9.17, the y-direction 'height' of each ellipse is defined as $2b$ and the y offset of the image of the circle centre from the ellipse centre is labelled δ. The values for the outer ellipse, subscripted 1, are shown. The x-direction 'width' of the ellipse at the location of the image of the circle centre is defined as $2r_s$. These 3 quantities are used to characterise each ellipse and to determine the viewing angle.

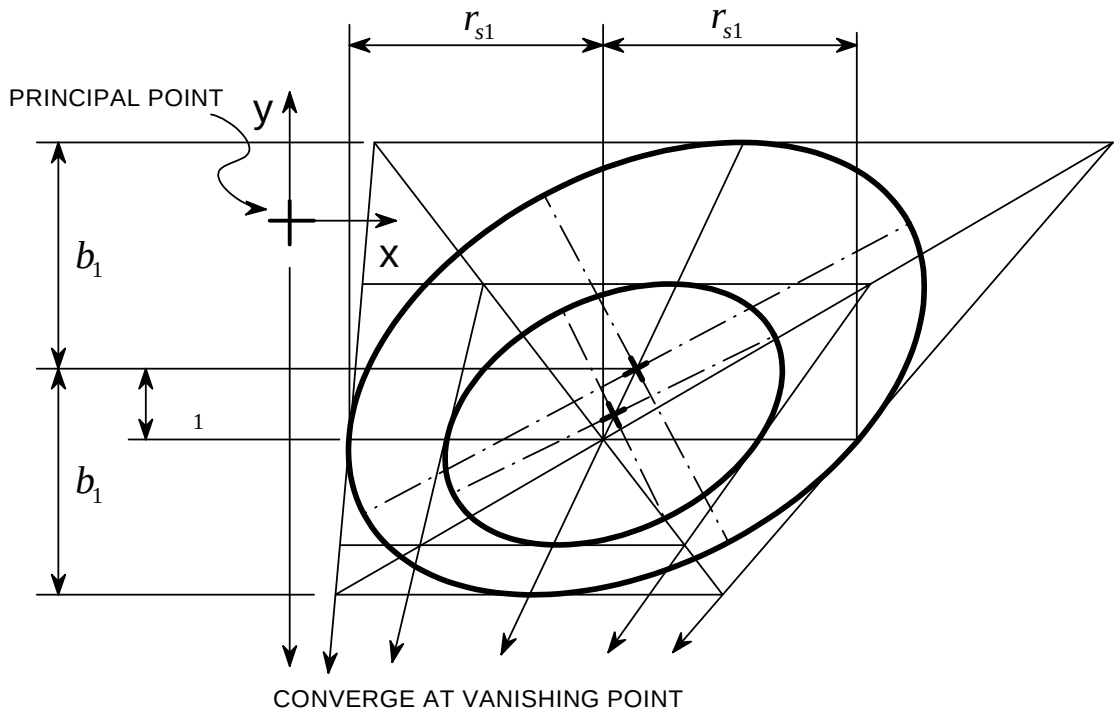

Figure 9.17: Elliptical images of concentric circular reference traces.

The location of the image of the circle centre is termed (x_o, y_o). The corresponding object space coordinates of the circles' centre are (X_{2o}, Y_{2o}, Z_{2o}). For the coordinate systems chosen the image y-coordinate is independent of the X_2-coordinate and the x-coordinate is proportional to the X_2-coordinate on lines parallel with the X_2 axis. That is, X_2 distances are mapped linearly to the image

plane. Therefore the values of b, δ and r_s defined above are independent of the value of X_{2o} and so can be found for the simplest case of $X_{2o} = 0$.

Using perspective projection, expressions for the image coordinates of the top, bottom and centre points of the circle can be found for general viewing angle θ, distance d and image plane distance g as defined in Figure 9.17. The quantities $(b + \delta)$ and $(b - \delta)$ can then be expressed in terms of θ, d, g, circle radius R and centre Y_{2o} and Z_{2o}. It is found that:

$$y_0 = \frac{g(Y_{2o}\sin\theta - Z_{2o}\cos\theta)}{d - Y_{2o}\cos\theta - Z_{2o}\sin\theta} \tag{9.2}$$

$$\frac{b+\delta}{b-\delta} = \frac{d - Y_{2o}\cos\theta - Z_{2o}\sin\theta + R\cos\theta}{d - Y_{2o}\cos\theta - Z_{2o}\sin\theta - R\cos\theta} \tag{9.3}$$

We also get directly

$$r_s = \frac{gR}{d - Y_{2o}\cos\theta - Z_{2o}\sin\theta} \tag{9.4}$$

From (9.2),(9.3) and (9.4) the viewing angle can be expressed as

$$\theta = \sin^{-1}\left(\frac{b^2 - \delta^2 - y_0\delta}{r_s b}\right) \tag{9.5}$$

and the viewing distance and the focal length are then

$$d = \frac{(b^2 - \delta^2)R}{r_s\delta\tan\theta} + \frac{Z_2}{\sin\theta} \tag{9.6}$$

$$g = r_s\frac{b}{\delta}\cos\theta \tag{9.7}$$

In using Equations 9.5, 9.6 and 9.7 to find θ, d, g and Y_{2o} for an assumed value of Z_{2o} (which may be defined as zero), we can measure b directly from the image, but do not yet know δ. If we have two ellipses that we know are the

images of concentric circles then we know that the image of the common centre lies somewhere on the line through the centres of the ellipses. The location of that point is then determined for a given value of the distance δ for either ellipse, as is the value of δ for the other ellipse. From Equation 9.3 we get for each ellipse

$$d - Y_{2o}\cos\theta - Z_{2o}\sin\theta = R\frac{b}{\delta}\cos\theta \tag{9.8}$$

Given that we know the ellipses are projections of two concentric coplanar circles of known radii, and as such d, Y_{2o}, Z_{2o} and θ are the same for both, the ratio of the two centre offsets δ_1 and δ_2 is from (9.8):

$$\frac{\delta_1}{\delta_2} = \frac{b_1 R_1}{b_2 R_2} \tag{9.9}$$

meaning that

$$\delta_2 = \Delta\delta\frac{b_2 R_2}{b_2 R_2 - b_1 R_1} \tag{9.10}$$

where $\Delta\delta = \delta_2 - \delta_1$ is the y-distance between ellipse centres.

Even if the actual radii of the circles are not accurately known, the location of the circle centre that makes the ellipses consistent with each other can be found using (9.3) giving

$$\frac{\delta_1}{\delta_2} = \frac{b_1 r_{s1}}{b_2 r_{s2}} \tag{9.11}$$

The values of r_{s1} and r_{s2} have to be identified at trial values of δ_1 and the corresponding δ_2, so that the values which satisfy (9.11) can be found numerically. The viewing angle and distance can then be calculated for each ellipse from (9.5) and (9.6).

These values will inevitably not be identical due primarily to random error in the sampling of the ellipses. Where the difference between the two values is small the averages of those for the two ellipses may then be used directly. If however the discrepancy is significant then a more systematic approach is required, as described below.

The elliptical image of a circle lying in a plane of constant Z_2 with known viewing angle and distance can be expressed in terms of d, g and θ. For a circle radius R centred at $(X_{2_o}, Y_{2_o}, Z_{2_o})$:

$$(X_2 - X_{2_o})^2 + (Y_2 - Y_{2_o})^2 = R; \quad Z_2 = Z_{2_o} \tag{9.12}$$

the image in the x,y coordinate system is found using:

$$X_2 = \frac{x(d\sin\theta - Z_2)}{y\cos\theta + g\sin\theta}; \quad Y_2 = \frac{yd - Z_2(y\sin\theta - g\cos\theta)}{y\cos\theta + g\sin\theta} \tag{9.13}$$

Substituting these expressions and expanding, the resulting ellipse is found to be:

$$Ax^2 + Bxy + Cy^2 + Dx + Ey + F = 0 \tag{9.14}$$

where

$$
\begin{aligned}
A &= (Z_{2_o} - d\sin\theta)^2 \\
B &= 2X_{2_o}\cos\theta(Z_{2_o} - d\sin\theta) \\
C &= \cos^2\theta(X_{2_o}^2 + Y_{2_o}^2 - R^2) + (d - Y_{2_o}\cos\theta - Z_{2_o}\sin\theta)^2 - (Y_{2_o}\cos\theta)^2 \\
D &= 2X_{2_o}g\sin\theta(Z_{2_o} - d\sin\theta) \\
E &= g\sin 2\theta(X_{2_o}^2 + Y_{2_o}^2 - Z_{2_o}^2 - R^2) - \\
&\quad 2gY_{2_o}Z_{2_o}\cos 2\theta + 2dg(Z_2\cos\theta - Y_{2_o}\sin\theta) \\
F &= g^2(X_{2_o}^2 + Y_{2_o}^2 - Z_{2_o}^2 - R^2) + Z_{2_o}g^2(Z_{2_o} - Y_{2_o}\sin 2\theta)
\end{aligned}
$$

For two ellipses of known radius, the twelve coefficients obtained from the digital image through the ellipse fitting method described above can be used in Equation 9.14 to yield twelve equations that may be solved simultaneously on a minimisation of error basis to estimate the values of d, g, θ, X_{2_o} and Y_{2_o}. This optimisation may be performed by a commercial software package such as Mathcad. The values obtained from the direct geometric method are used as initial estimates for the unknowns.

The advantage of these approaches is that they do not require physical measurement of the camera position and angle relative to the experimental rig, which is often difficult to perform in practice.

Calculation of pitch angle pattern

Once the viewing angle and distance have been calculated, any point on the image can then be projected back onto the inclined plane of the LED traces. The traces of the two blade-mounted LEDs are sampled in a similar manner to the two reference ellipse traces as described above, this time using 36 sample points. The image

coordinates of these points are then transformed to space coordinates, for a set value of the Z_2 coordinate, usually zero. Calculation of the pitch angle at any location in the orbit relies on knowledge of the actual separation of the leading and trailing edge LEDs on the experimental rig.

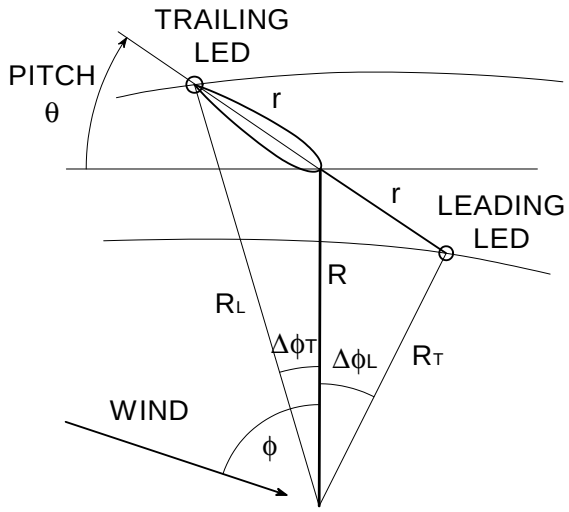

Figure 9.18: Geometry of the blade LED trajectories.

For a given azimuth (orbital) location of the pitch axis of the blade, the radial distance from the origin at which each of the two blade LEDs lies needs to be found. These radii are not the radii of the respective traces at the azimuth of the pitch axis, which is mid way between the two LEDs, but those at some azimuths slightly ahead of and behind the axis azimuth (see Figure 9.18). The angles by which the LEDs lead and lag the axis are not the same and depend on the pitch angle. An iterative procedure is therefore adopted to find the appropriate angles and radii.

The lead/lag angles are first approximated by the angle that would apply for zero pitch, knowing the separation of the two LEDs and assuming a nominal pitch axis radius. The radius of each of the traces at these locations is then

calculated. Linear interpolation (in terms of radius as a function of azimuth) is used to calculate the radius between sample points.

The actual radius of the blade pitch axis and the pitch angle are then calculated on the basis of these values. This estimate of the pitch allows calculation of new estimates of the lead/lag angles and so re-measurement of the trace radii. This process is repeated until the pitch angle converges. The pitch angle can thus be calculated at as many points around the orbit as desired and so a plot of pitch against azimuth angle obtained.

Validation of measurement method

The prototype wind turbine for which the method was developed is of radius 870 mm, height 1.3 m and blade chord length 150 mm. LEDs were mounted on one of the three blades, whose motion was taken as representative of all blades. The blade LEDs were 150 mm fore and aft of the pitch axis on the chord line. The two reference LEDs were mounted at radii of 0.364 m and 0.674 m respectively.

The camera was on a tripod outside the wind tunnel test section, looking up through a window at the LED plane, which was at the top end of the blades (see Figure 9.19). The viewing angle θ was approximately 50° and viewing distance 2.8 m to the centre of rotation in the LED plane.

A series of images was taken with the blade locked at known pitch angles ranging through ±25°. The results are shown in Figure 9.20. The calculated pitch angle should be constant for the revolution, but random errors in the sampling of the traces and small errors in the location of the turbine axis and the viewing angle produce non-constant results. The standard deviations of the pitch angle results range from 0.41° to 0.83°. Here the results have been corrected for zero

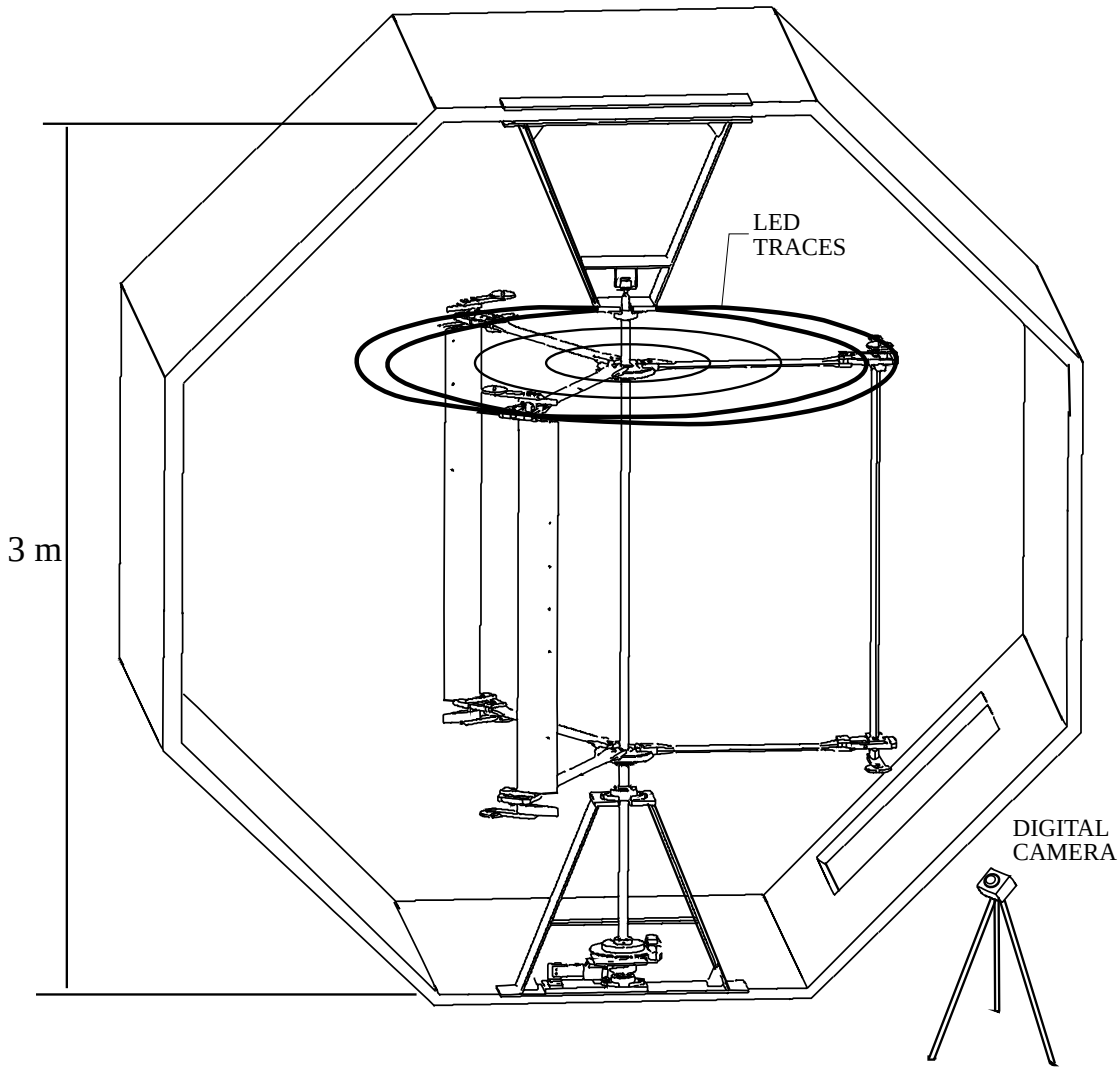

Figure 9.19: Illustration of prototype turbine mounted in the 3 metre wind tunnel test section. The digital camera was mounted on a tripod on the floor just outside the section looking through one of the viewing windows as shown.

offset resulting from slight misalignment of the blade LEDs with the reference edge that was used to set the blade pitch. The offset here was found to be 1.2°.

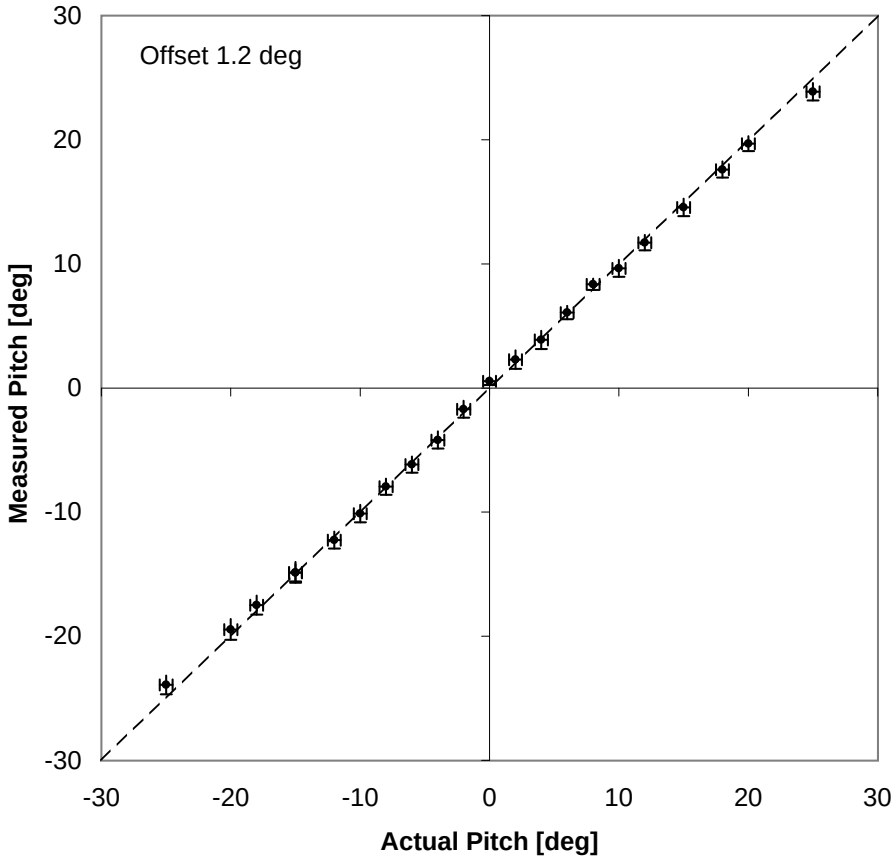

Figure 9.20: Calibration chart obtained by clamping the blade at known angles. Vertical error bars are ±1 standard deviation calculated for the revolution. Horizontal error bars are ±0.5°. A zero offset of 1.2° has been added to all points.

Figure 9.21 shows results for the turbine in operation. The blade is swinging from positive to negative pitch limits (approximately ±20°) at this speed. The azimuth angle is measured anti-clockwise (viewed from below) from the upwind direction. This is estimated from the image by manually setting a line to coincide with the cross-tunnel edges on the turbine frame.

The accuracy of the calculated pitch angle variation using the above method is limited by a number of factors. These are listed below:

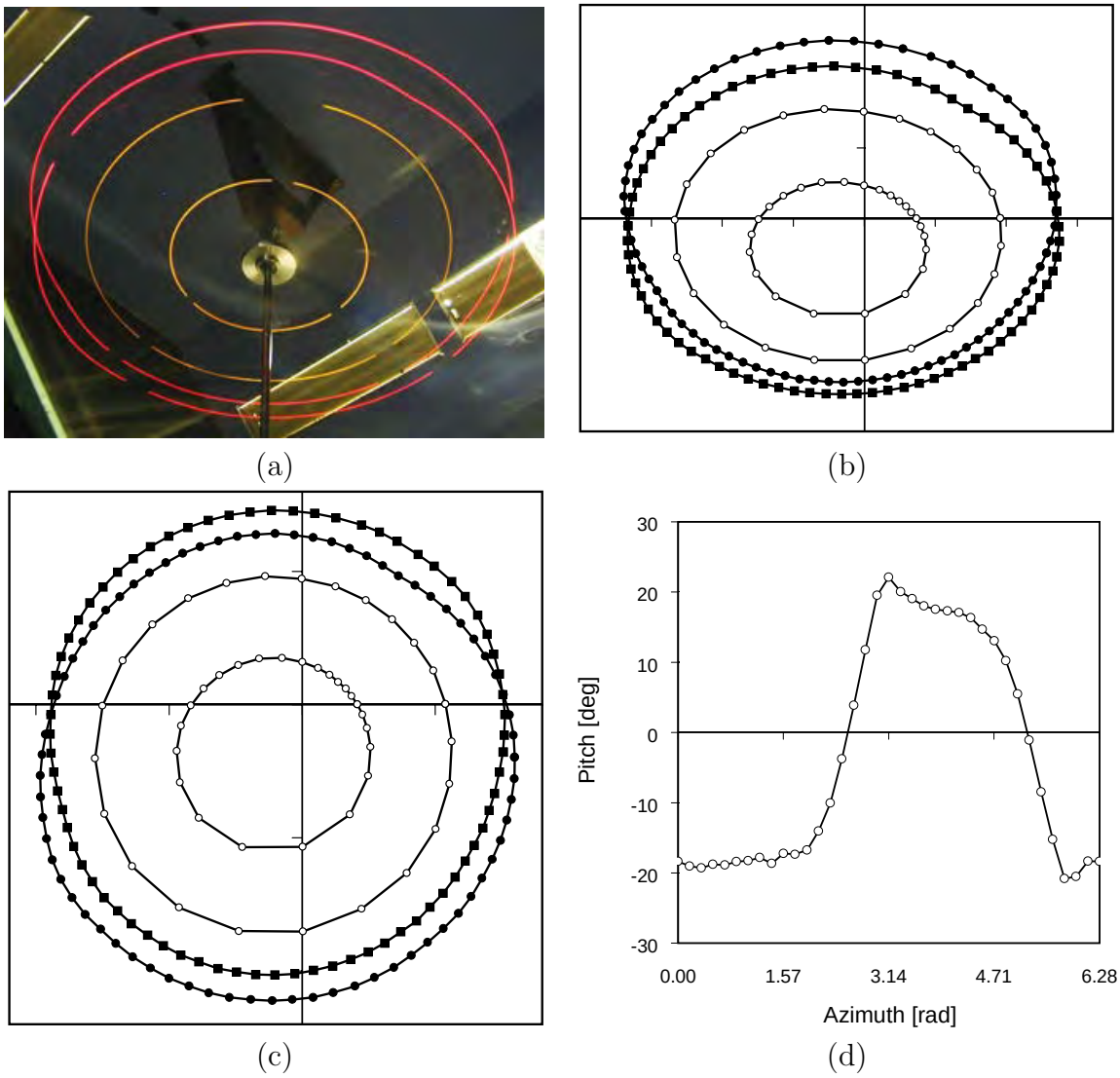

Figure 9.21: Blade pitch measurement results for turbine in operation at approximately 30 rpm and wind speed 7 m/s. The digital image (a) is sampled to obtain a discrete number of points (b). The inner reference ellipses are used to calculate projection of the outer samples back onto the LED plane in space (c). The resulting pitch angle pattern is shown in (d). Here the blade is just hitting its pitch limits at $\pm 20°$.

- Lens distortion and location of the principal point in the image. Lens distortion may result in error, however the calculated pitch angle is relatively insensitive to distortion as it is based on the separation between the LED traces in the same part if the image, rather than the absolute position relative to the principal point. The two traces are likely to be locally offset by a similar amount. For similar reasons, the pitch results are also quite insensitive to the exact location of the principal point in the image. In this case the principal point was assumed to be at the centre of the frame, however deviations of up to 50 pixels resulted in maximum changes in calculated pitch of less than 0.25°. Greater accuracy may be obtained by use of a calibrated camera, however even without this, results appear to be sufficiently accurate for many uses.
- LED traces not coplanar. Any out-of-plane errors for either of the blade LEDs or a reference LED will result in errors in the object space coordinates calculated. These can be corrected for if the out-of-plane distance can be measured by projecting image points back to the appropriate Z_2 plane. If one of the LEDs is slightly out-of-plane, its trajectory is effectively shifted 'vertically' in the image, and if no correction is made, an error in the calculated pitch angle that varies approximately sinusoidally with azimuth results.

  The magnitude of this error was estimated by generating trace images for zero pitch, but with one LED 5 mm out-of-plane. Then traces were then analysed with no out-of-plane correction. It was found that the calculated pitch had a mean of $-0.4°$ with amplitude 0.8°. This is a reasonably small error for quite a large out-of-plane distance for the present set up.

- Fitting of ellipses to reference trace sample points. The minimisation of algebraic distance ellipse fitting method is known to be biased, unlike a true geometric distance minimisation method. However if care is taken to ensure the sample points are positioned at accurately, the error involved here with regularly spaced samples on a complete ellipse should be small.
- Estimation of the perspective transformation parameters from the reference ellipses. The optimisation method used to find the 'best' values of viewing parameters to fit the reference ellipses are sensitive to the measured radii of these trajectories and the quality of the ellipse fitting process. However the accuracy of the calculated camera position can be checked by generating predicted images of the reference circles and measuring the goodness of fit to the image sample points.
- Overlap of blade LED traces. Small pitch angles where the leading and trailing LEDs produce traces on the image that are close to each other and sometimes overlapping would be better measured using LED's of different colour. This was tried initially but it was found that colours other than red did not record as well in the digital image and produced difficulty for trace detection.
- Smearing of traces. Another source of uncertainty is the 'smearing' of LED traces over several revolutions being recorded in a single exposure. For example a 2 second exposure at 180 rpm records 6 revolutions. Small fluctuations in the LED paths visible to the naked eye were not recorded by the digital camera, but must have caused the recorded traces to be wider and less distinct. To some extent however the uncertainty produced by this effect does

directly reflect actual uncertainty in the pitch of the blade because the traces are 'average' paths for the several revolutions recorded during the exposure.

- Refraction through wind tunnel window. All images were taken through the Perspex window in the wind tunnel test section. Refraction of light through the window may have contributed to distortion of the digital image.

By quantifying and minimising the above sources of error, the method has been demonstrated to be sufficiently accurate to quantify the pitching response of the turbine and gain insight into its performance characteristics.

9.5 Summary

A prototype turbine was designed and constructed for testing in the wind tunnel. The turbine was designed to investigate the potential of the new design concepts described in Chapter 3.

A design for the blades, which are subjected to large bending loads in operation, was chosen through extensive theoretical analysis.

Instrumentation to measure the shaft torque and speed of the turbine was incorporated. In addition, a new photogrammetric method of measuring the blade pitch angle response pattern was conceived and developed.

Results of wind tunnel testing and comparison with theoretical results are presented in Chapter 10.

Chapter 10

Wind Tunnel Test Results

The prototype turbine described in Chapter 9 was tested in the wind tunnel at UNSW with different designs of blade connecting components.

10.1 Rig Design Modifications

10.1.1 Pivot joint friction

Initially friction in the blade connections hampered starting performance of the turbine. In order to reduce the friction, the bearing surfaces on which the weight of the blades was taken were covered with plastic sheet to lower the coefficient of friction. The plastic surfaces were then lubricated using first WD40 then a silicone spray, however the moment required to initiate rotation (measured using a spring balance) was still at least 0.8 Nm.

In order to reduce the friction further, the upper arms were modified so that the weight of the blade was taken on a 6 mm brass screw head as the pivot point for the blade. The upper turbine arms were given an initial upward angular displacement using shims at the hub to offset the deflection under the weight of the blade. This allowed the blade weight to be taken entirely at the upper arm, with only the lightest contact remaining on the bearing surfaces at the lower arm. This modification reduced the friction in the pivot joint by an order of magnitude.

Problems were encountered with this arrangement once greater turbine speeds were attained. The increasing centrifugal load and the movement of the upper,

load-bearing, arms towards horizontal would cause the elastomeric component at the lower end of the blade to ride up out of its housing. The blade would then jam and pitching would cease.

In order to avoid this, a second load-bearing pivot point was installed at the lower arm, so that the weight of the blade was shared. These modifications greatly reduced the friction in the blade connection.

10.1.2 Brake friction

Even when the brake was released, the friction of the pads on the brake disc produced an appreciable amount of residual torque, which had to be overcome by the turbine. The minimum torque varied between 0.35 Nm and 1.5 Nm at different azimuthal positions, producing a cyclic average of approximately 0.8 Nm. The cyclical variation was due to misalignment of the brake disc on the shaft, causing periodic binding between the brake pads. The cyclical average figure also varied from run to run as braking caused movement of the calliper with respect to the disc.

All of the early trials of the turbine suffered from excessive friction torque, hampering attempts to achieve self-starting. The problem was addressed by grinding the brake pads to chamfer the edges, first in the tangential direction and then also in the radial direction. This reduced the area of the contact patch between pad and disc and so reduced the tendency to bind when the disc was not in correct alignment. This reduced the cyclical average brake friction to approximately 0.15 Nm.

The brake calliper used was a rear motorcycle brake. While the residual friction associated with it is of no consequence on a bike, the lack of springs to completely

release the brake was a significant problem for the turbine. Ultimately, the motorbike brake was replaced with one for a bicycle. This ensured that the brake pads were not in contact with the disc when the brake was not applied.

10.1.3 Parasitic drag

Parasitic drag was found to be more significant than was anticipated. While the radial arms themselves were produced with a streamlined profile, the fittings at the outer ends produced considerable drag. It was intended to provide fairings for this part of the rotor, however it was found that it was very difficult to reduce the drag while still allowing unrestricted movement of the blade and access to the connections.

Still air tests were conducted to estimate the magnitudes of aerodynamic drag and brake friction. The deceleration of the turbine in still air at the end of a wind tunnel run was used to calculate the torque arising from residual brake pad friction and rolling element bearing friction. The values of aerodynamic drag and dry friction coefficients of retarding torque were then estimated by numerically differentiating the speed data, as described in Appendix C.

10.2 Experimental Procedure

The turbine was allowed to accelerate from rest without the brake applied until a steady state speed was reached. In general, two different wind speeds were used: approximately 5.7 m/s and 7.1 m/s, corresponding to dynamic pressures measured at the pitot static tube of 2 mmH_2O and 3 mmH_2O respectively.

In general the turbine performance was assessed by allowing it to accelerate under no-load conditions and calculating the torque from the acceleration as described in Section 9.4.1.

The entire wind tunnel testing process was characterised by significant variation in turbine performance under nominally identical conditions. The sensitivity of performance to the blade pitch response meant that small changes in lubrication or alignment of parts could have a significant effect on the measured output.

10.3 Results

10.3.1 Fixed blades

For reference the turbine was tested with the blades fixed in the zero-pitch position, as a standard Darrieus turbine. The turbine did not operate at all, reaching a runaway speed of only approximately 10 rpm at a wind speed of 7 m/s. Since no external drive was included it was not possible to accelerate the turbine to a speed at which the turbine may have been able to operate with fixed blades.

10.3.2 Type A component

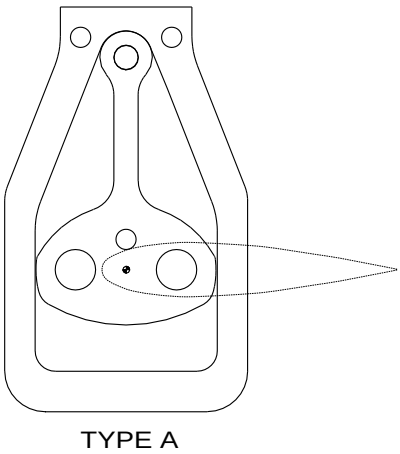

Figure 10.1: Type A geometry

Initial testing was conducted with the Type A geometry elastomeric pieces (see Figure 10.1). It was quickly apparent that the pieces were too stiff in torsion and did not allow adequate pitching. Under no load, the turbine reached a steady state speed of only 25 rpm at a wind speed of 7.1 m/s, a TSR of only 0.32.

In order to reduce the stiffness of the pieces, the stems of the elastomeric components were modified to reduce their cross sectional area. However little improvement was achieved. The maximum TSR at 7.0 m/s increased only to 0.41.

10.3.3 Type B component

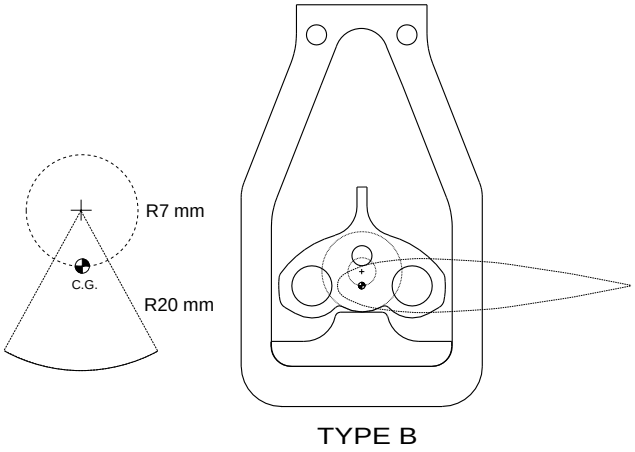

Figure 10.2: Type B geometry

The Type B geometry shown in Figure 10.2 was tested. Despite the much smaller cross sectional area of the flexible stem compared to the Type A geometry, the harder material made the component still too stiff in torsion. Insufficient pitch amplitude for starting resulted. Again, the turbine failed to exceed TSR 0.4 under no load.

It was therefore decided to test only the rolling profile portion of the Type B geometry components by removing the flexible stems. The restoring moment was then supplied only by inertial forces. This arrangement proved more successful. The blade was able to pitch easily at start up, producing significant torque.

At a wind speed of 5.7 m/s, the turbine initially failed to accelerate beyond approximately 20 rpm. At the higher wind speed, a similar steady-state velocity was initially attained at approximately 30 rpm. These speeds correspond to tip speed ratios of approximately 0.3 and 0.4 respectively.

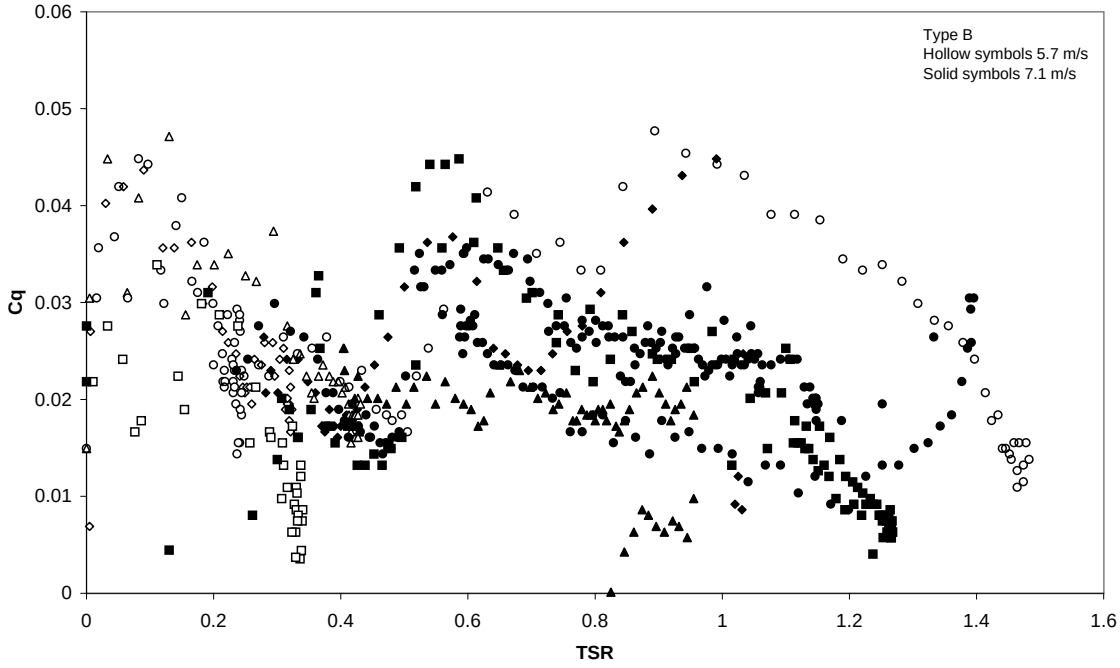

Figure 10.3: Measured torque coefficient versus tip speed ratio for the Type B purely inertial geometry.

Efforts to reduce the friction and sticking in the blade connections and residual drag in the brake calliper allowed the turbine to accelerate to higher speeds. However the turbine was still not able to accelerate beyond a tip speed ratio of approximately 1.5. Measured torque coefficient values for this geometry are presented in Figure 10.3. The torque coefficient values were calculated using Equation 9.1. Different symbols are used for separate test runs. Tests were conducted at two different wind speeds: 5.7 m/s and 7.1 m/s.

Significant variation in the results is evident from run to run, especially in the most successful run in which a maximum tip speed ratio of 1.5 was attained. Despite this variation, all runs show a high starting torque with a trough around TSR 0.4-0.5, a peak around TSR 0.6 and then a steady decline in torque towards the maximum speed.

Initial testing with this arrangement produced vigorous pitching of the blades at start up, but the blades were prone to becoming jammed at the extremes of their range due to the force with which they hit the limits. This problem was addressed using modified elastomeric components, where the flexible stem part was used to cushion the stops (see Figure 10.4).

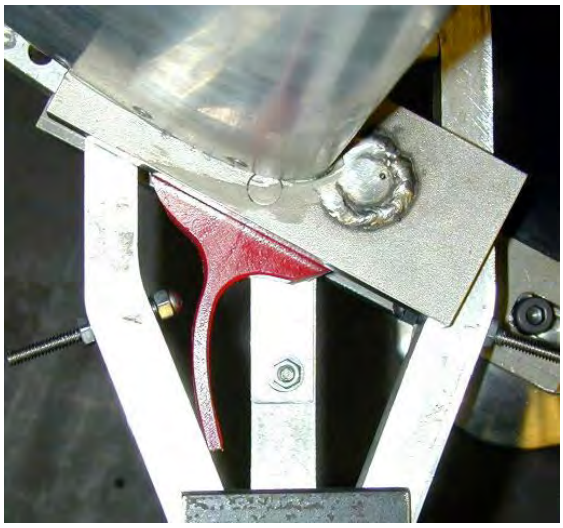

Figure 10.4: Use of the flexible stem to provide 'cushioned' pitch limits

This modification resulted in slightly improved starting performance, as well as an increase in the runaway speed to approximately TSR 1.6 (see Figure 10.5).

It was thought that friction and resistance to blade pitching was still the main problem preventing the turbine from reaching higher speeds, despite the fact that minimal resistance was detectable when the turbine was stopped. The weight of the blade was supported entirely at the upper arm and the lower arm was used only to locate the blade horizontally. Increasing rotational speed resulted in a reduction in the vertical deflection of the weight-bearing arm, causing an increase in the distance between the arms and a tendency for the blade to jump out of its housing. To avoid this a second pivot point was fitted to the lower arm so that the weight of the blade could be shared. This arrangement had the desired effect and

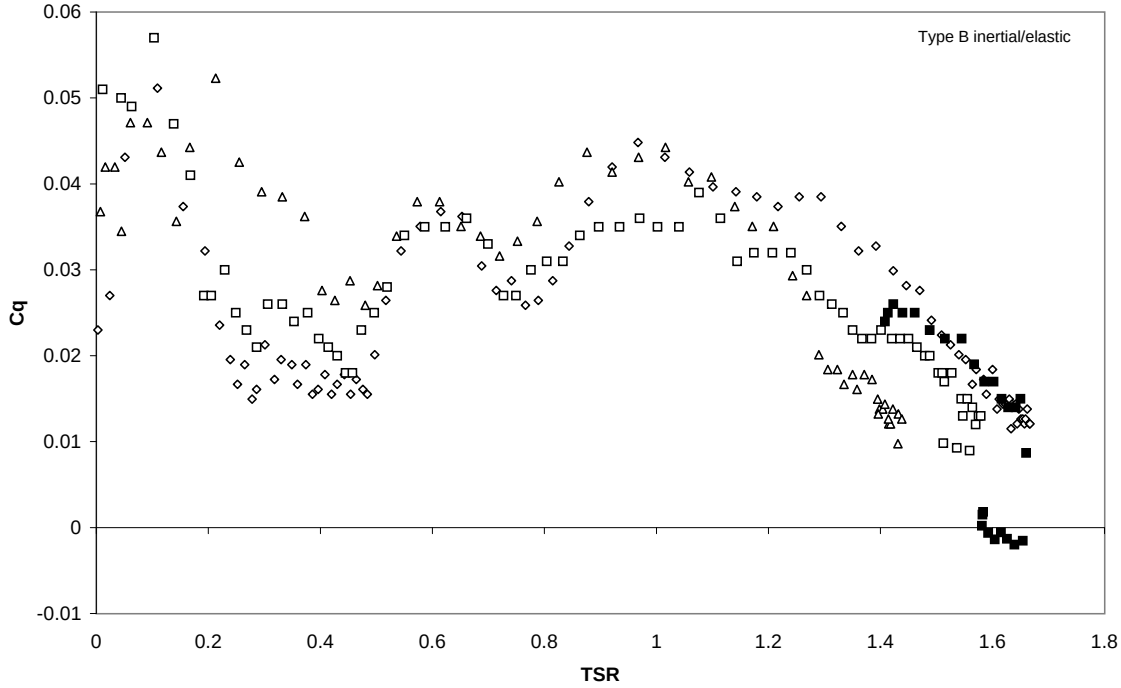

Figure 10.5: Measured torque coefficient versus tip speed ratio for the Type B with flexible stem

reduced misalignment and sticking of the blade at speed. Results of this improved arrangement are shown in Figure 10.6.

The logged data for the most successful run and the corresponding power coefficient curve is shown in Figure 10.7. The maximum power coefficient achieved was approximately 0.18 at a tip speed ratio of 2.9. There is a marked dip in output between tip speed ratios 1.6 and 1.9. Once the turbine emerged from this trough it accelerated rapidly up to a tip speed ratio of 3.2. At this point a load was applied to control the speed of the turbine and to attempt to extract sustained power from the shaft via the brake. However excessive load caused the turbine to decelerate rapidly.

The trough in torque around TSR 1.6-1.7 was repeatedly observed in these tests. True self-starting, with the turbine accelerating in a constant wind to a tip speed ratio above 2.5, was achieved on three occasions. However in subsequent

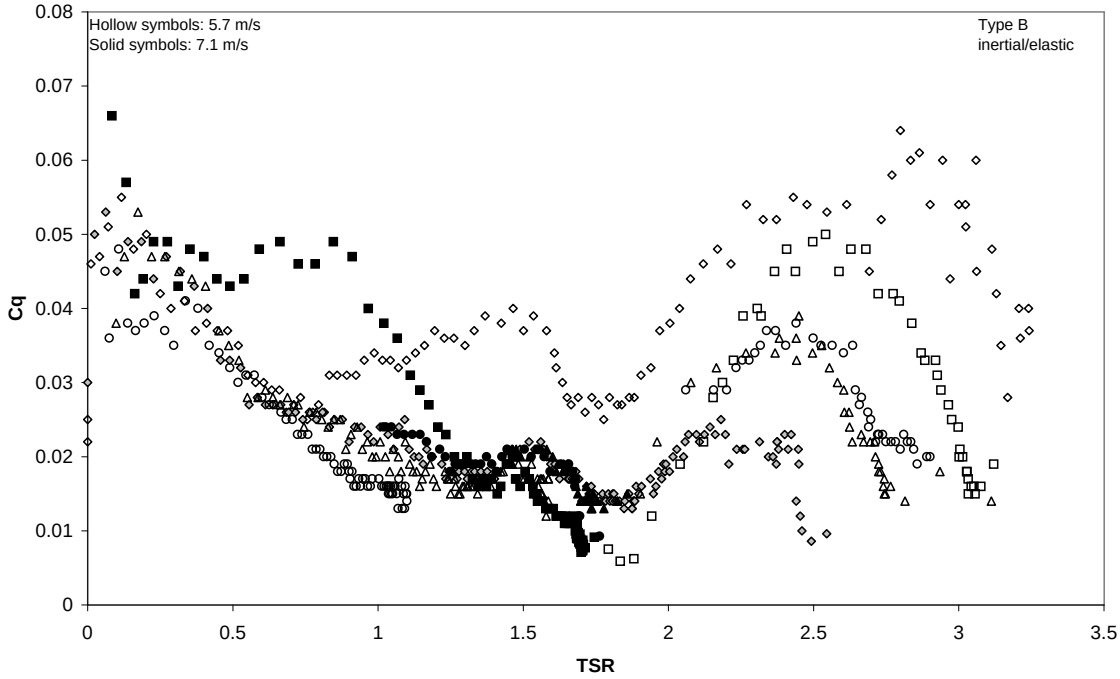

Figure 10.6: Torque results for the Type B polyurethane component with flexible stem and upper and lower pivot points.

tests the turbine failed to accelerate of its own accord past the trough in the torque curve at TSR 1.7. If the wind speed were increased to above 7 m/s until the steady-state speed corresponding to this TSR had been reached, then dropped back to 5.7 m/s to elevate the TSR, then the turbine would accelerate to a maximum tip speed ratio above 2.5. However this does not constitute self-starting as such a fluke of ambient wind conditions cannot be relied upon.

The reason for variation in performance is not known. It was suspected at the time that problems with friction and jamming of the blades caused by vertical movement of the arms at speed was still responsible. However extensive efforts to improve alignment and prevent interference were not able to repeat the initial successful results.

It was also suspected that the amplitude of the pitch response that was being observed using the LEDs mounted on the blade was diminishing too rapidly with

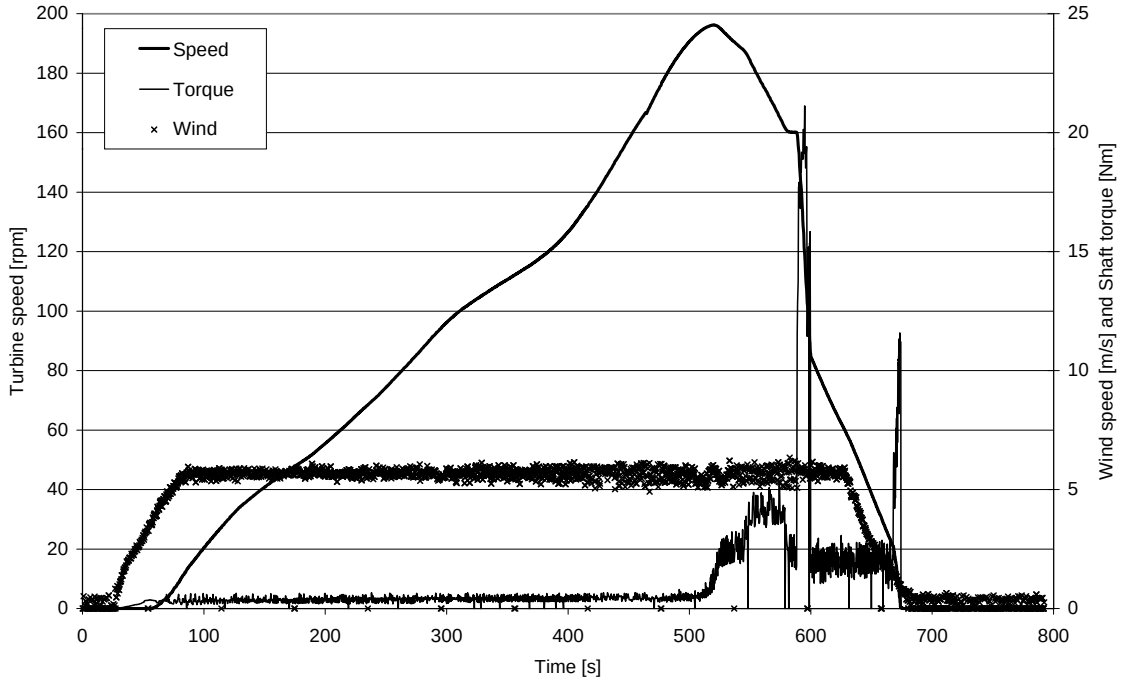

(a)

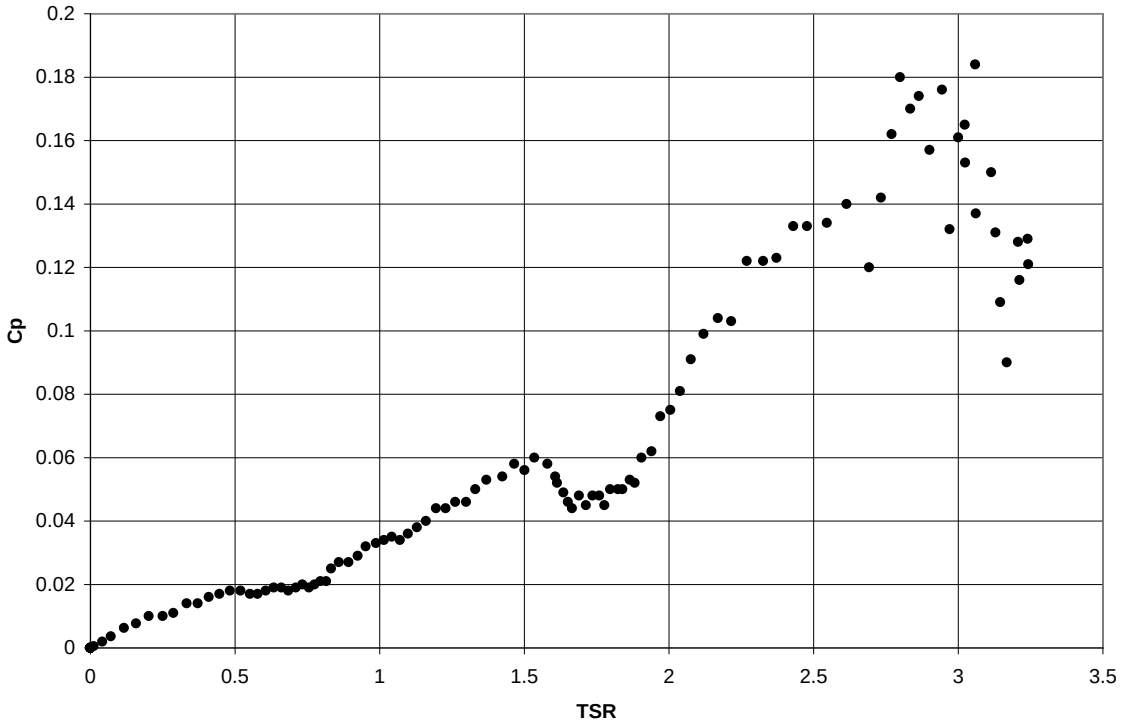

(b)

Figure 10.7: Logged speed, torque and wind velocity data for a run of the Type B inertial/elastic geometry (a). The corresponding power coefficient curve (b).

increasing speed. Blade pitching was observed to effectively cease at the threshold tip speed ratio of approximately 1.7 at which the turbine was stalling. This was not predicted by the mathematical models. It was thought that the pitch response may be reduced because of the compressibility of the polyurethane rolling profile, resulting in rolling resistance.

Accordingly, new profile components were manufactured from High Density Polyethylene (HDPE). The parts were NC milled to the same profile as the original moulded polyurethane components. These components were very much harder than the polyurethane parts. The original 'pillar' components on which the profile rolled, which were also moulded in polyurethane, were retained.

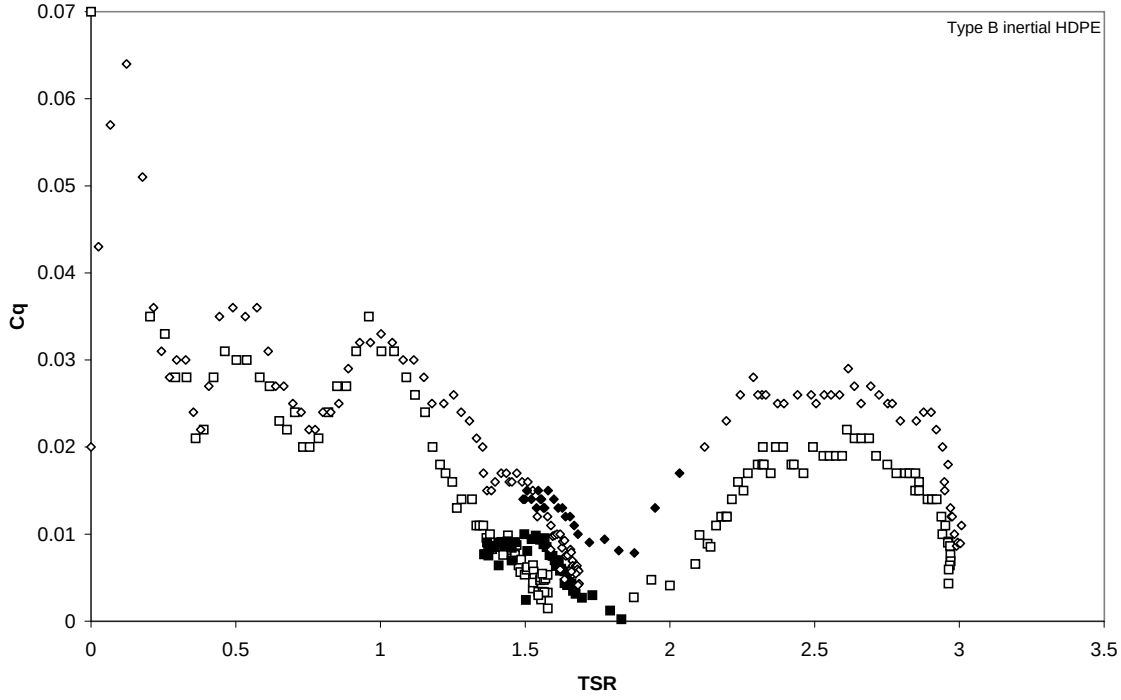

Figure 10.8: Torque results for the Type B High Density Polyethylene component.

Testing of the turbine with these components however did not yield radically different results. The results are shown in Figure 10.8. The trough in the torque curve between approximately TSR 1.5 and 1.7 was slightly negative, preventing

the turbine from accelerating up to running speed unassisted. However if the wind speed were temporarily increased to accelerate the turbine, then dropped back to 'leapfrog' the negative torque zone, the turbine would then accelerate again to a steady-state no-load TSR of 3.0.

The pitch response patterns for one of the turbine blades were measured using the technique described in Section 9.4.3. The variation of pitch response with tip speed ratio for one run is shown in Figure 10.9 for two different components. The flexible stem results in less 'dwell' at high pitch angles at low tip speed ratios (a) than is evident for the HDPE component (b). At higher tip speed ratios however there is little difference between the two sets of responses.

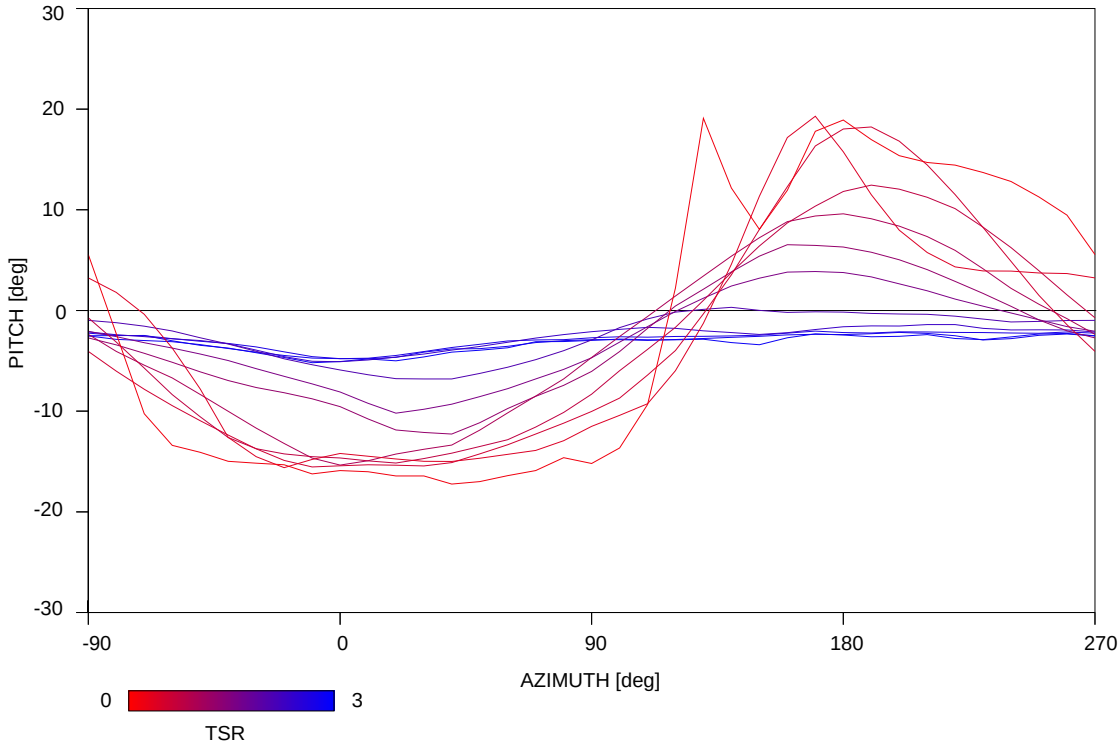

(a) Type B polyurethane geometry with flexible stem and upper and lower pivot points.

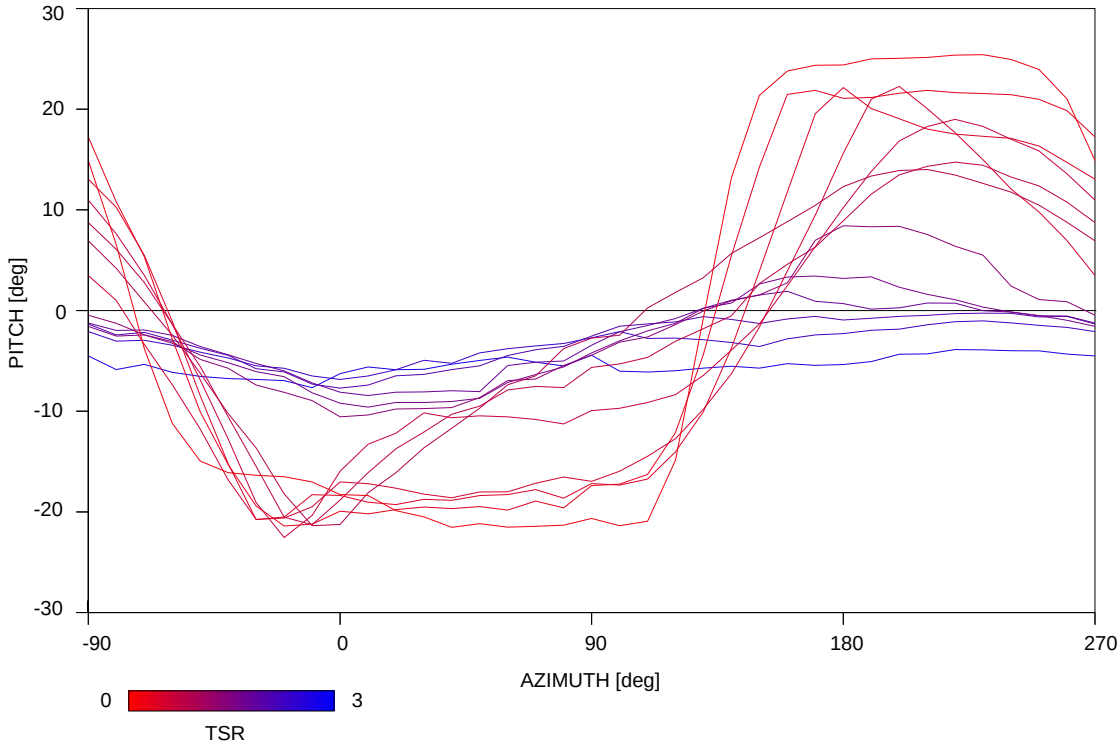

(b) Type B HDPE components.

Figure 10.9: Measured blade pitch responses for two blade mounting geometries.

It was felt that the pitch response amplitude was decreasing too rapidly with turbine speed and that performance would be improved by reducing the restoring moment applied to the blades. Accordingly, the HDPE components were modified to reduce the radius of curvature from 20 mm to 16 mm. This reduced the centre of gravity radius R_{cg} from 7 mm to 3 mm, while maintaining the y_0 offset at 13 mm (see Figure 10.10). The restoring moment should then be reduced to 3/7 of its initial value. According to the predictions of the momentum theory mathematical model, this level of torsional stiffness should be too low for the turbine to operate. The frequency ratio calculated by Equation 7.1 should be greater than one and the pitch response therefore out of phase with the variation in incidence at the blade.

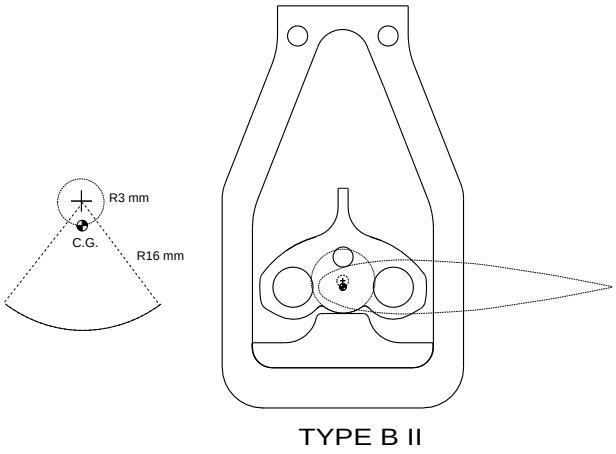

Figure 10.10: Type B II geometry

The performance of the turbine with the modified components (designated Type B II) was however not greatly different from that with the original Type B components. The torque coefficient data is shown in Figure 10.11(a), page 262. The measured pitch response is shown in Figure 10.11(b).

In a further attempt to increase the pitch response amplitude, another set of rolling profile components were manufactured from High Density Polyethylene.

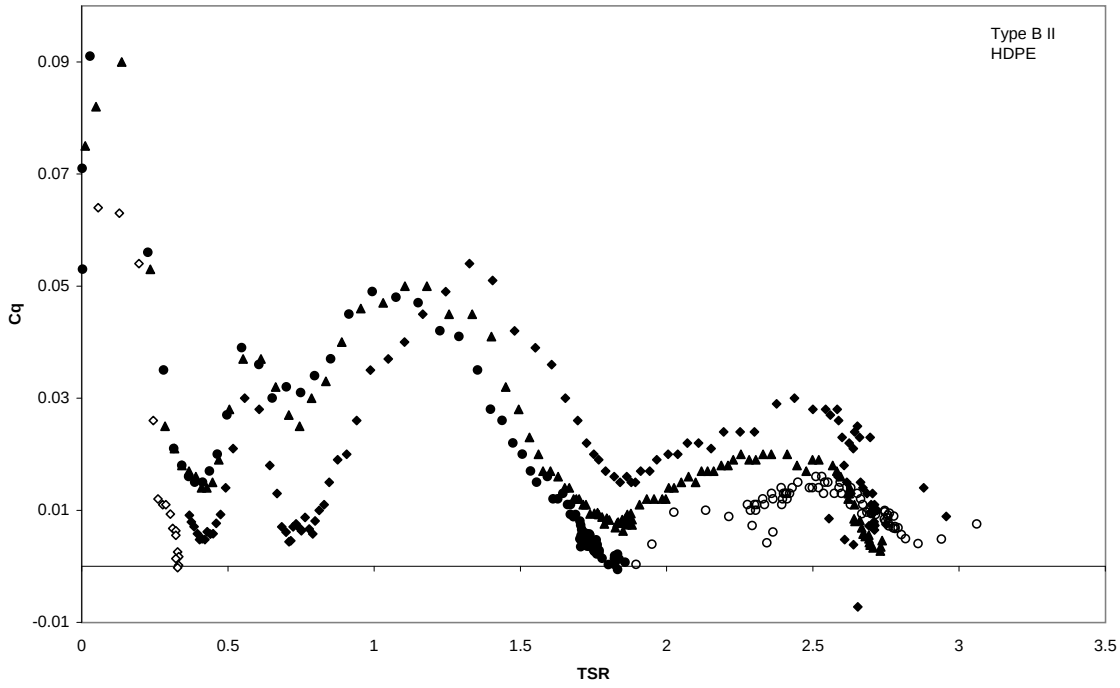

(a) Torque coefficient.

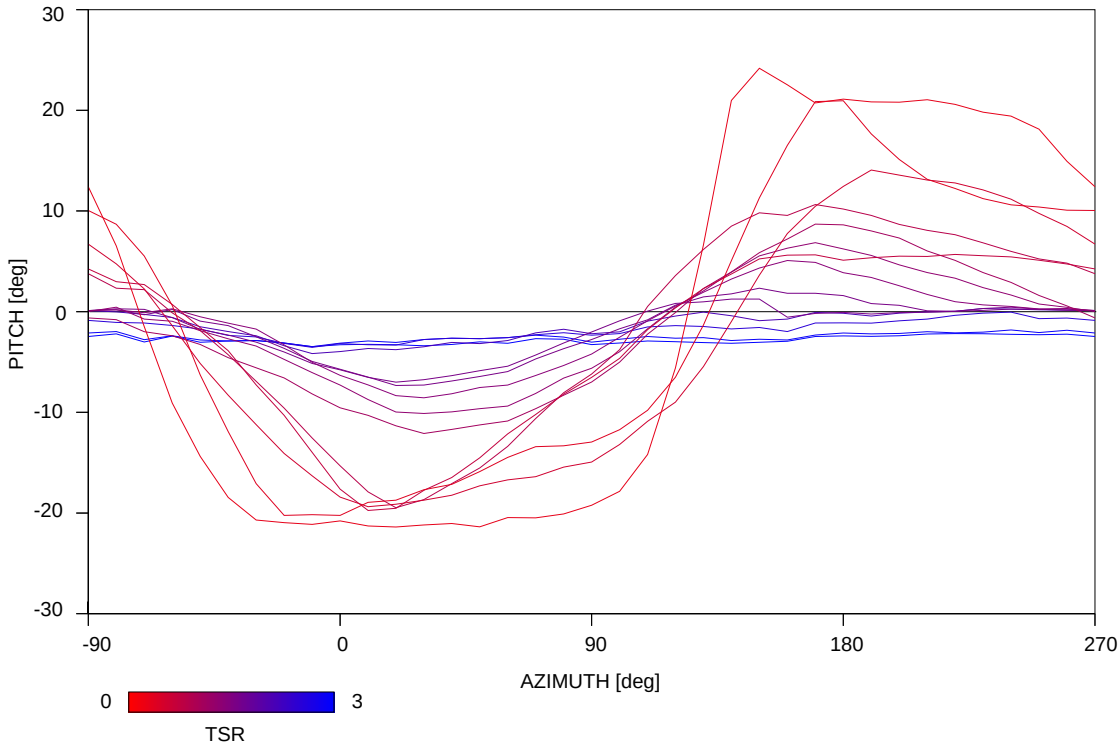

(b) Measured pitch response.

Figure 10.11: Torque and pitch results for the Type B II modified geometry.

In this geometry, labelled Type B III and shown in Figure 10.12, the radius of curvature over a range if $\pm 12°$ either side of the 'nose' was 14 mm, while outside this range the radius was 16 mm. This geometry produced a centre of gravity offset of just 1 mm at the nose. It was desired to test whether the concept of tailoring the profile could result in different pitch response behaviour at different tip speed ratios.

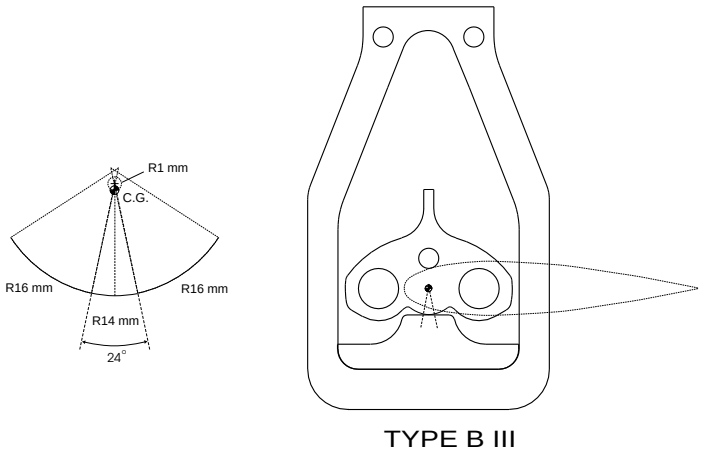

Figure 10.12: Type B III geometry

The torque coefficient results for this geometry are shown in Figure 10.13(a) and the measured pitch response is shown in Figure 10.14(a). The pitch response exhibits characteristics of a reduced restoring moment: the amplitude is greater at a given tip speed ratio than for the Type B and Type B II geometries; also the phase lag of the response is greater, indicating the blade is operating closer to its natural frequency. The turbine however did not progress beyond tip speed ratio 1.7.

Springs were then fitted to the blades to supplement the inertial restoring moment, to see how this would affect performance. The aim was to increase the torsional stiffness at low tip speed ratios, while allowing greater pitching at higher speeds. As the added springs acted independently of centrifugal force, they are

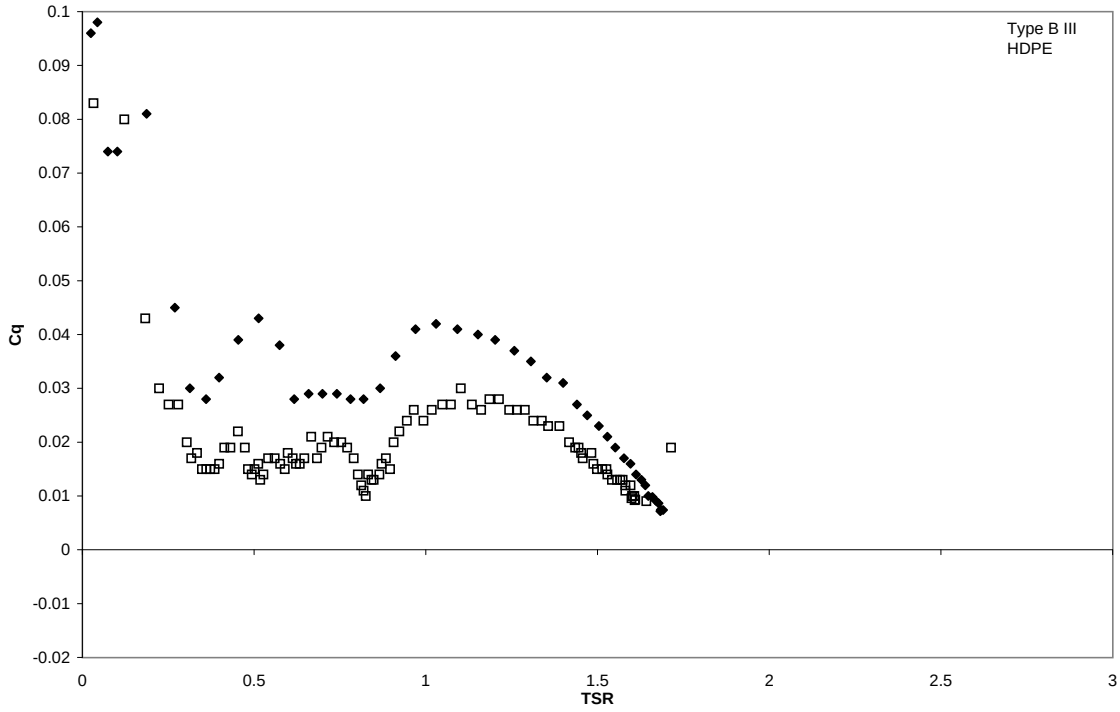

(a) Torque coefficient results

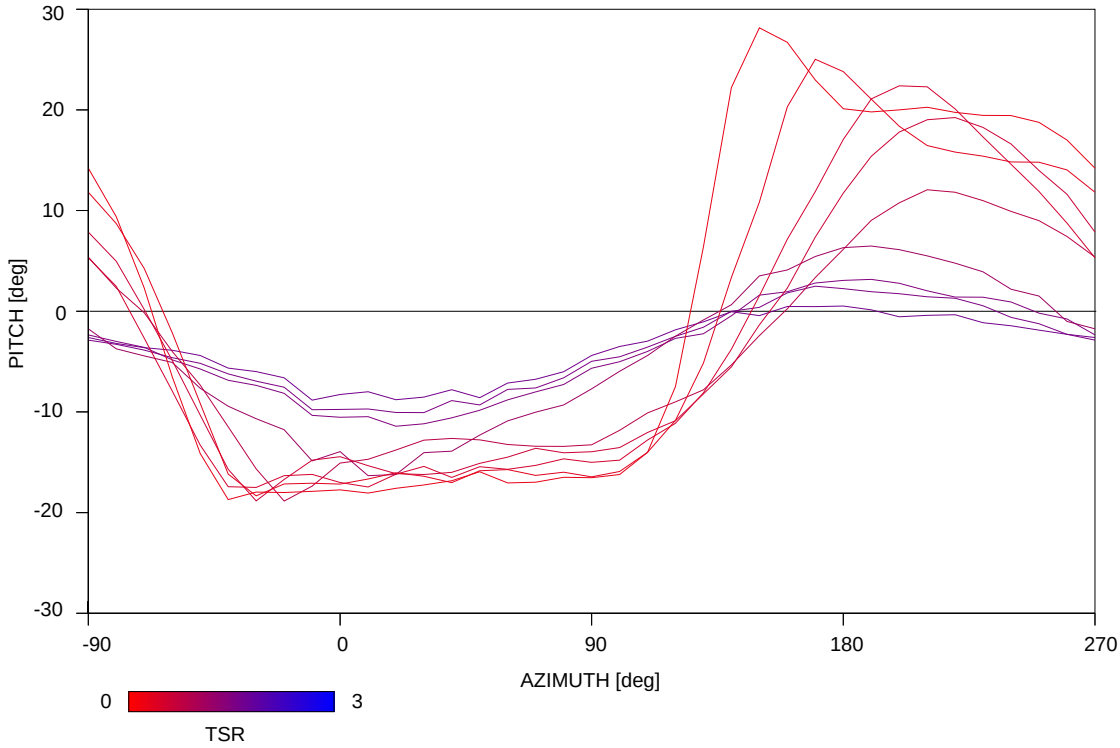

(b) Measured pitch response

Figure 10.13: Results for the Type B III geometry.

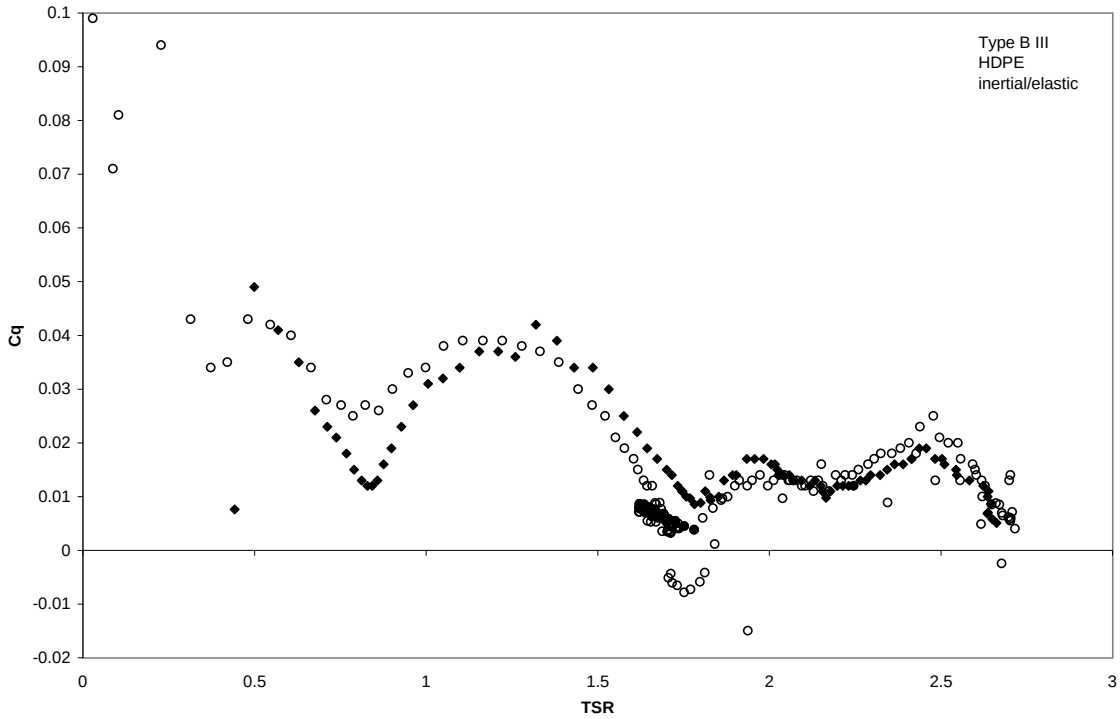

(a) Torque coefficient results

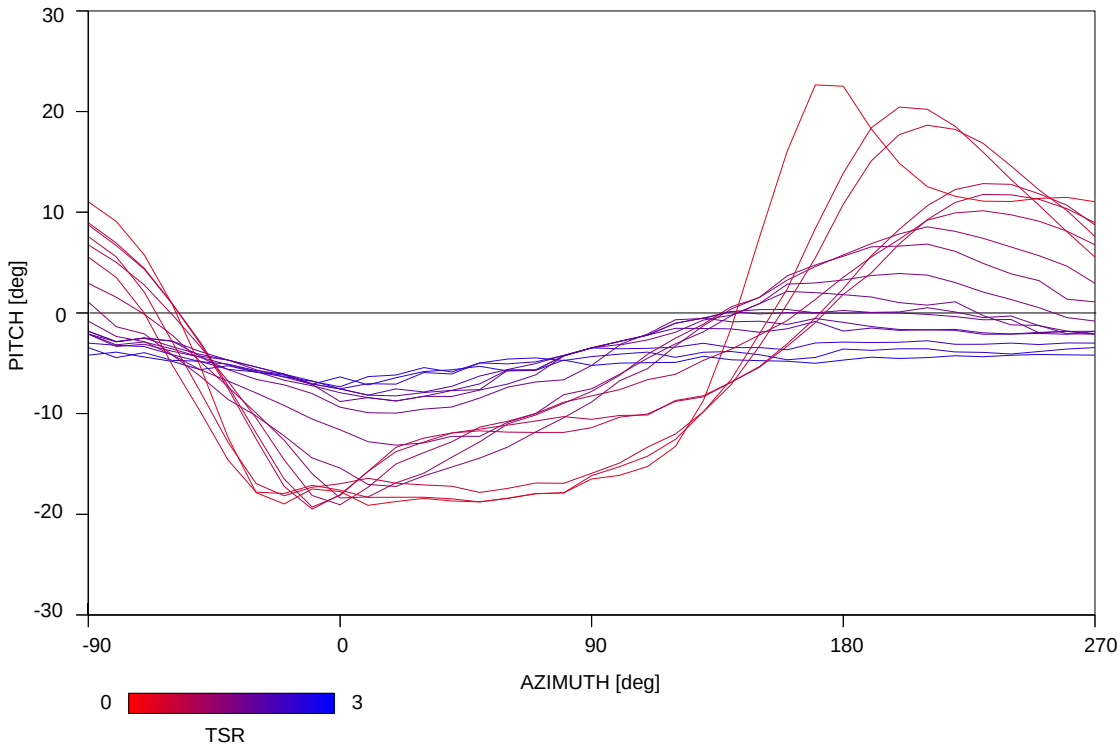

(b) Measured pitch response

Figure 10.14: Results the Type B III modified geometry with additional spring.

able to add a constant amount of stiffness that is significant at low speeds but becomes insignificant as the inertial component restoring moment increases.

The results are shown in Figures 10.13(b) and 10.14(b). This addition allowed the turbine to properly self-start on its initial test run, however subsequent runs failed to accelerate beyond the torque trough at TSR 1.8 without increasing then dropping the wind speed to jump the negative zone. Once above TSR 2, the turbine accelerated to a runaway speed of approximately TSR 2.7.

10.3.4 Type C geometry

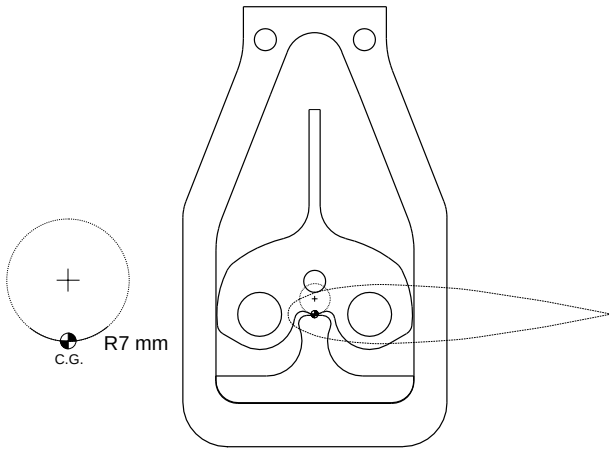

Figure 10.15: Type C geometry

Testing of the turbine with the Type C geometry was expected to yield similar performance to that obtained with the Type B geometry. The Type C component also had a circular arc rolling profile, with the centre of mass at a radius of 7 mm, as shown in Figure 10.15. The y_0 value was in this case zero.

As for the Type B geometry, the components in their original form were too stiff due to the elastic portion of the parts. Accordingly, as before, flexible stems of the components were cut and allowed to act as cushions on the pitch limits of the blade. In this case, the flexible stem made contact with the side of the housing at a pitch angle of approximately 14°, with a pitch limit of 28°.

Testing produced good low speed performance, but the turbine failed to accelerate beyond a tip speed ratio of 1.8. Significantly higher torque was produced in this speed range than for the Type B geometry. Torque coefficient results are plotted in Figure 10.16(a). For this geometry the results were relatively consistent, with maximum torque occurring at start-up, a dip in torque at TSR 0.5

The measured pitch responses for this geometry are shown in Figure 10.16(b).

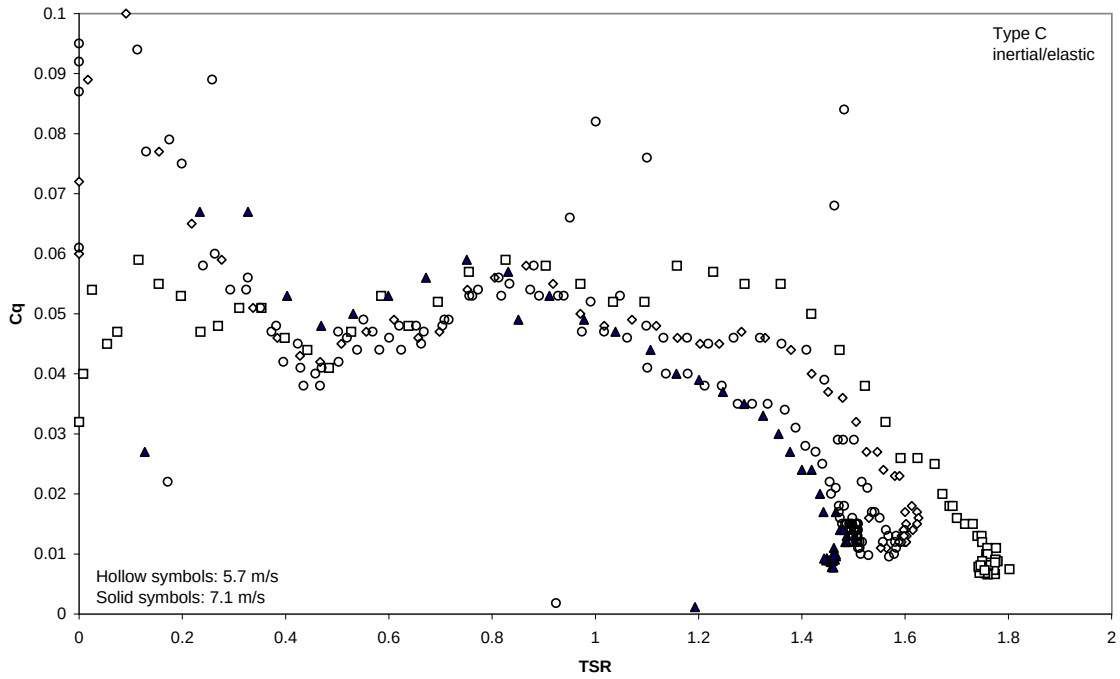

(a) Torque coefficient results

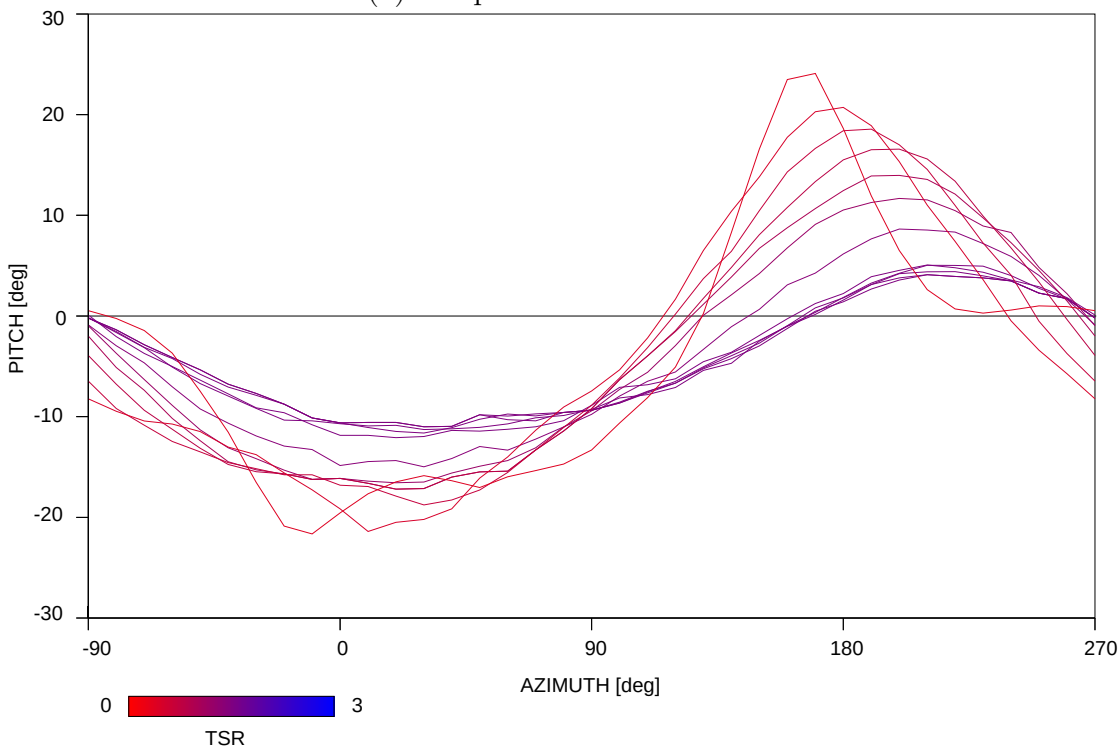

(b) Measured pitch response

Figure 10.16: Torque coefficient data and measured pitch response for the Type C geometry. Different symbols are used for separate test runs.

10.4 Comparison with Theoretical Results

The performance of the prototype turbine was predicted using both the Double Multiple Streamtube (DMS) model and the vortex model.

The Double Multiple Streamtube model by its nature predicts steady-state performance. It is therefore not strictly applicable to the prediction of performance of the turbine while accelerating. Neither the blade pitch response nor the unsteady wake can be assumed to be the same as those under steady conditions at a given tip speed ratio. Nevertheless, where acceleration is small the difference may be minimal and so the results are presented here for comparison. The vortex model on the other hand is designed to deal with unsteady behaviour.

The parameters used for the theoretical predictions are shown in Table 10.1.

Parameter	*Value*
Radius	0.87 m
Height	1.3 m
Blades	3
Chord	150 mm
Blade mass	7.36 kg
Blade moment of inertia	0.035 kgm^2
R_{ac}	20.5 mm
Damping coefficient	0.015 $\frac{\text{Nm}}{\text{rad/s}}$
Friction coefficient	0.0002

Table 10.1: Prototype turbine parameters

The friction coefficient is defined as the ratio of the frictional moment on the blade to the radial reaction at the blade connection.

The predicted performance of the turbine at a wind speed of 7 m/s with the Type B and Type C geometry rolling profile components under ideal conditions is shown in Figure 10.17. Here parasitic drag and blade friction have been set to zero.

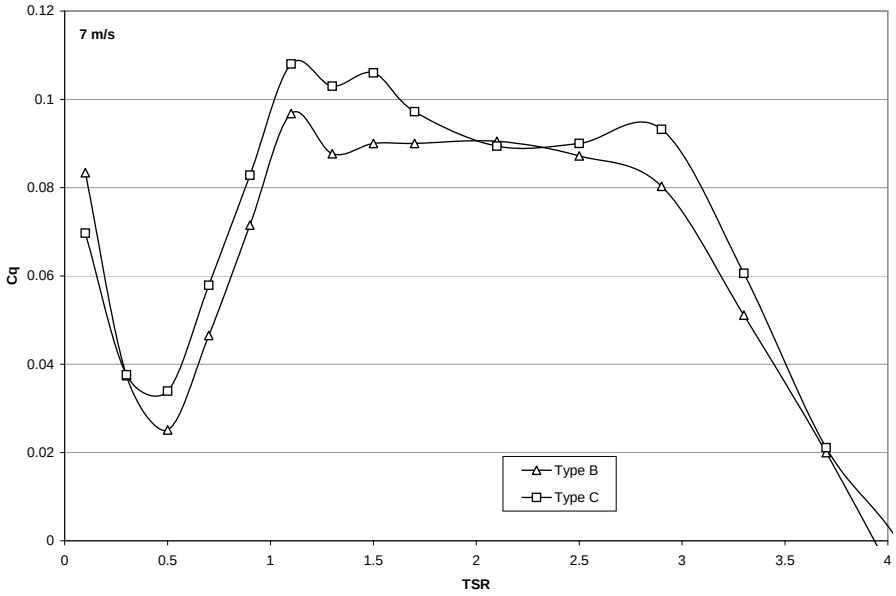

(a) Torque coefficient

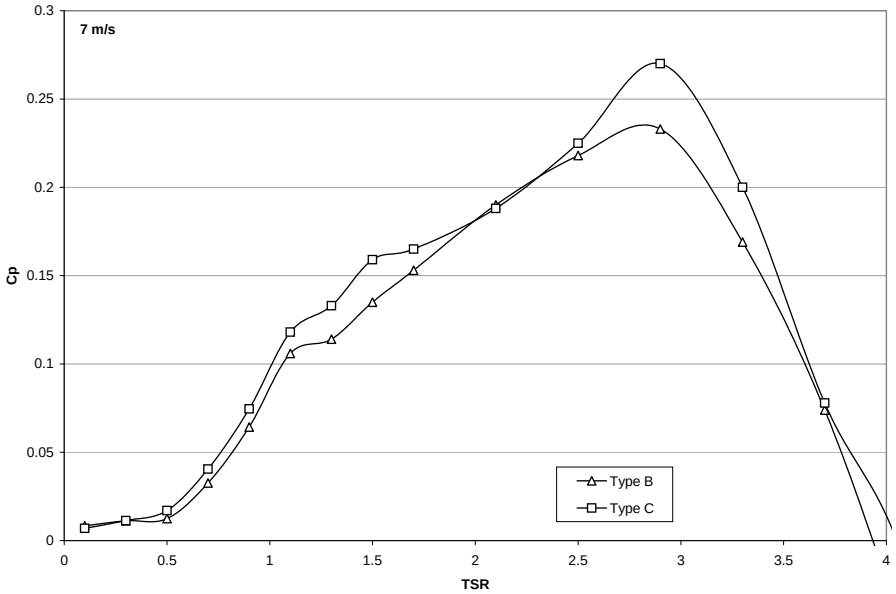

(b) Power coefficient

Figure 10.17: Torque and power coefficient predicted by the Double Multiple Streamtube (DMS) mathematical model under ideal conditions (ie no parasitic drag, no blade friction)

10.4.1 Type B component

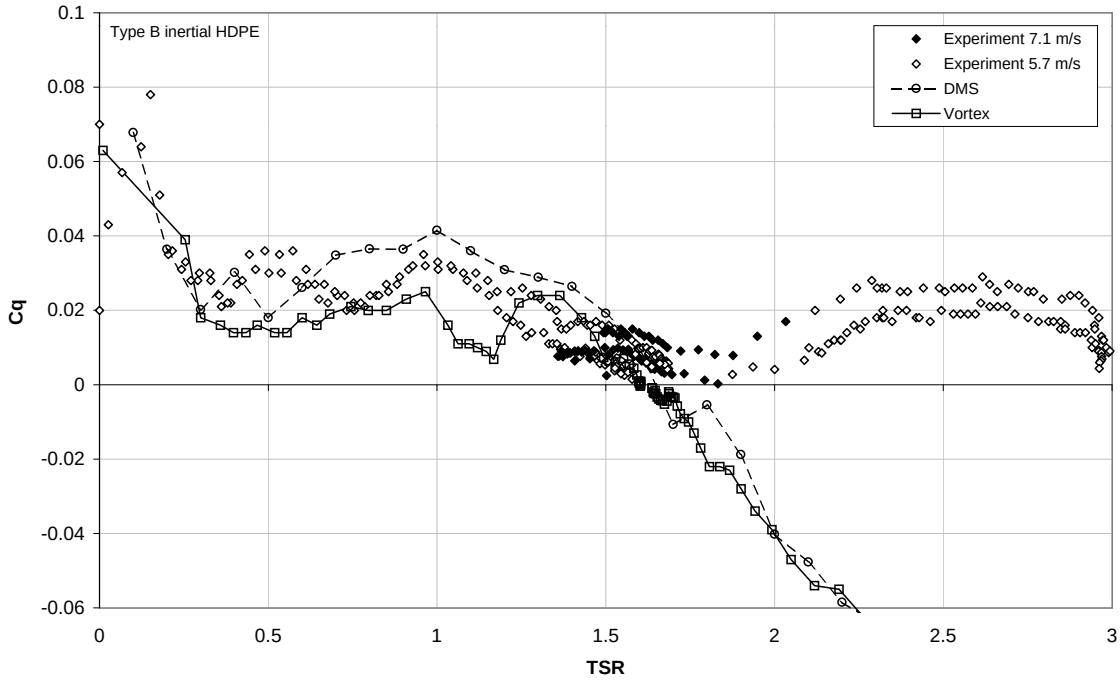

Figure 10.18: Torque coefficient predicted by the Double Multiple Streamtube (DMS) and vortex mathematical models, compared with experimental data

The DMS results are shown in Figure 10.18. The predicted values are net torque, parasitic drag and bearing friction, as estimated from turbine run-down tests (see Appendix C), have been subtracted.

Agreement between experimental and theoretical results from both models is reasonable for tip speed ratios less than 1.7. Both predict a high starting torque, dropping to a local minimum at approximately TSR 0.5. Both models predict a recovery of torque, with a local maximum at TSR 1.0, then a decline to zero torque at approximately TSR 1.7. These predictions match the general trends of the experimental data. The DMS model slightly overpredicts the torque, while the vortex model predicts a dip in torque between TSR 1.1 and 1.2 that is not evident in the measured data.

The main discrepancy between theoretical and experimental results is for tip speed ratios greater than 1.7. Both mathematical models predict a steady progression to increasingly large negative values. By contrast, the turbine exhibited a tendency to dip to zero torque at approximately TSR 1.7, but was able to produce positive torque for TSRs between 2 and 3.

To gain insight into the cause of this discrepancy, the pitch response for one of the experimental runs was compared with theoretical predictions. These results are presented in Figures 10.19, 10.20 and 10.21.

The predicted pitch responses for the DMS and vortex models are very similar for each tip speed ratio, despite the fact that the DMS model predicts the steady-state pattern while the vortex model predicts what is a transient pattern for the single revolution closest to the tip speed ratio of the measured pattern.

These predictions are made with the values of the damping coefficient and friction coefficient adjusted to best match the measured values. In the absence of damping and friction in the blade connection, the predicted pitch response is greater in amplitude than the measured response at almost all speeds. Only with the addition of friction does the blade settle to virtually zero amplitude at TSR 3.0, as was measured. It is clear that if the damping and friction are adjusted to match the measured pitch amplitude, the phase of the response changes. For all tip speed ratios shown in Figures 10.19, 10.20 and 10.21 the predicted pitch response lags the measured pitch response by approximately 30° to 40°. The shape of the predicted pitch response is otherwise fairly similar to the measured response. The predicted amplitude is slightly greater than the measured amplitude at most tip speed ratios. The asymmetry in the pitch response is slightly underpredicted. At

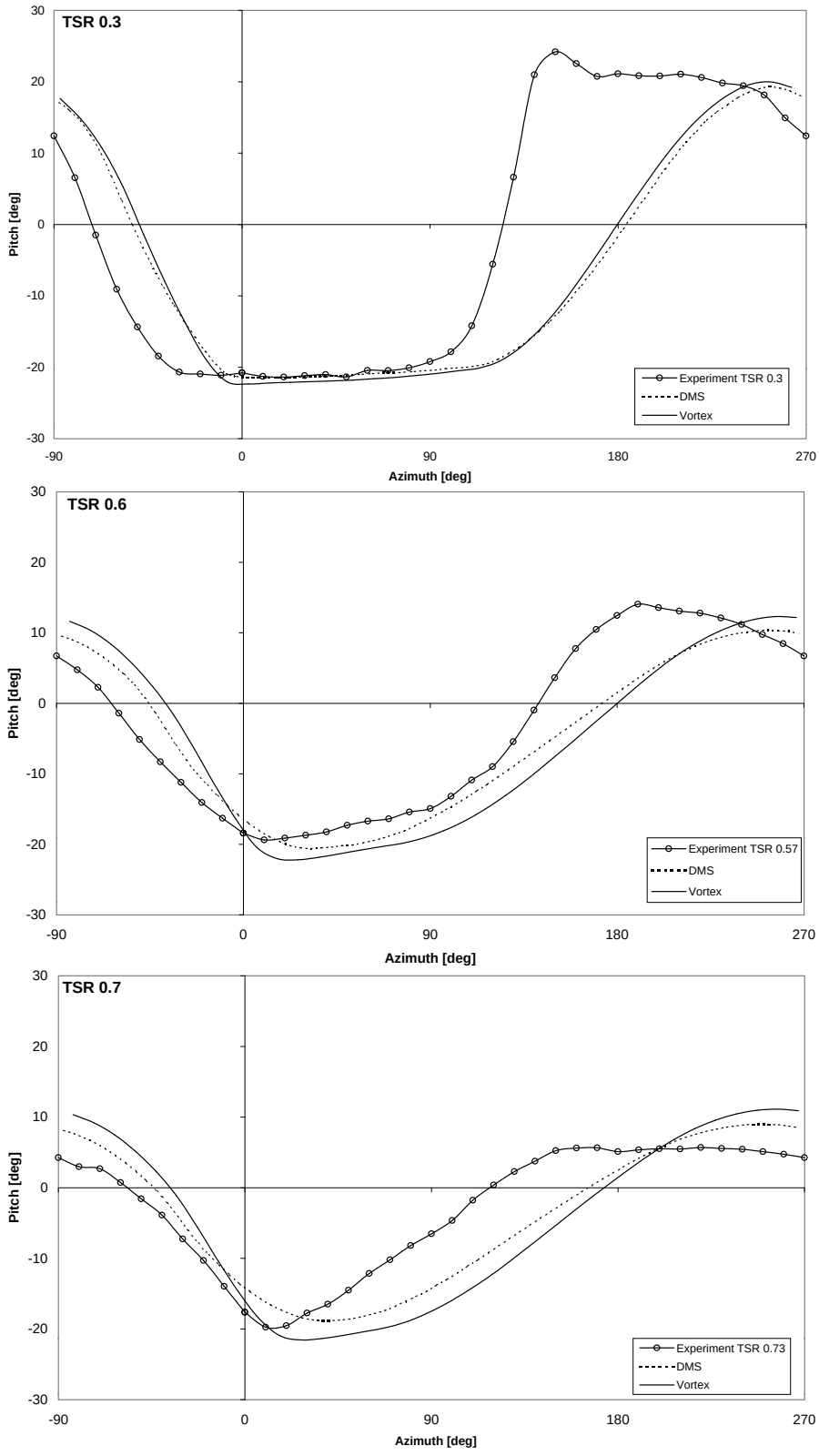

Figure 10.19: Measured and predicted pitch responses, Type B, TSR 0.3 - 0.7

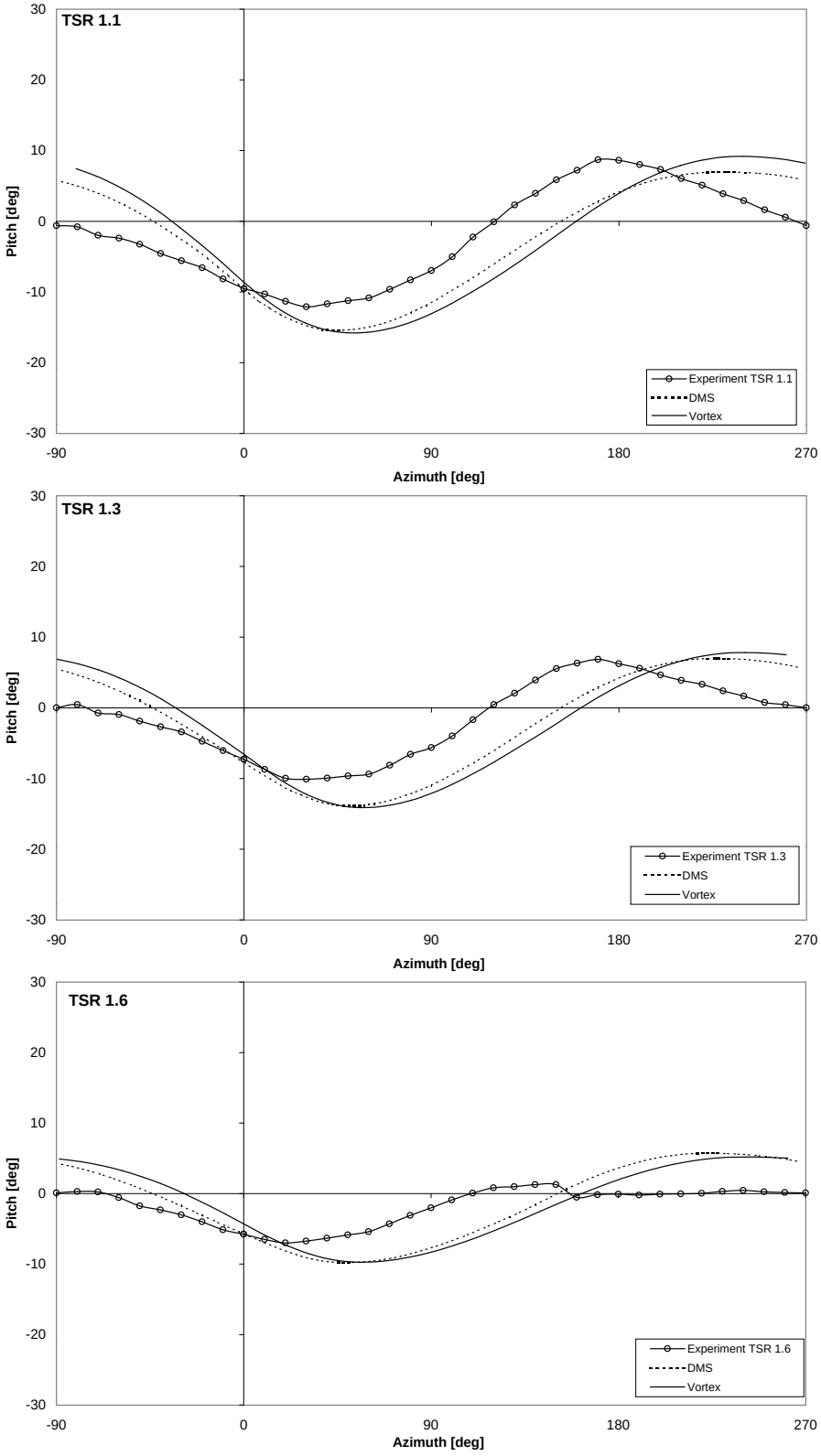

Figure 10.20: Measured and predicted pitch responses, Type B, TSR 1.1 - 1.6

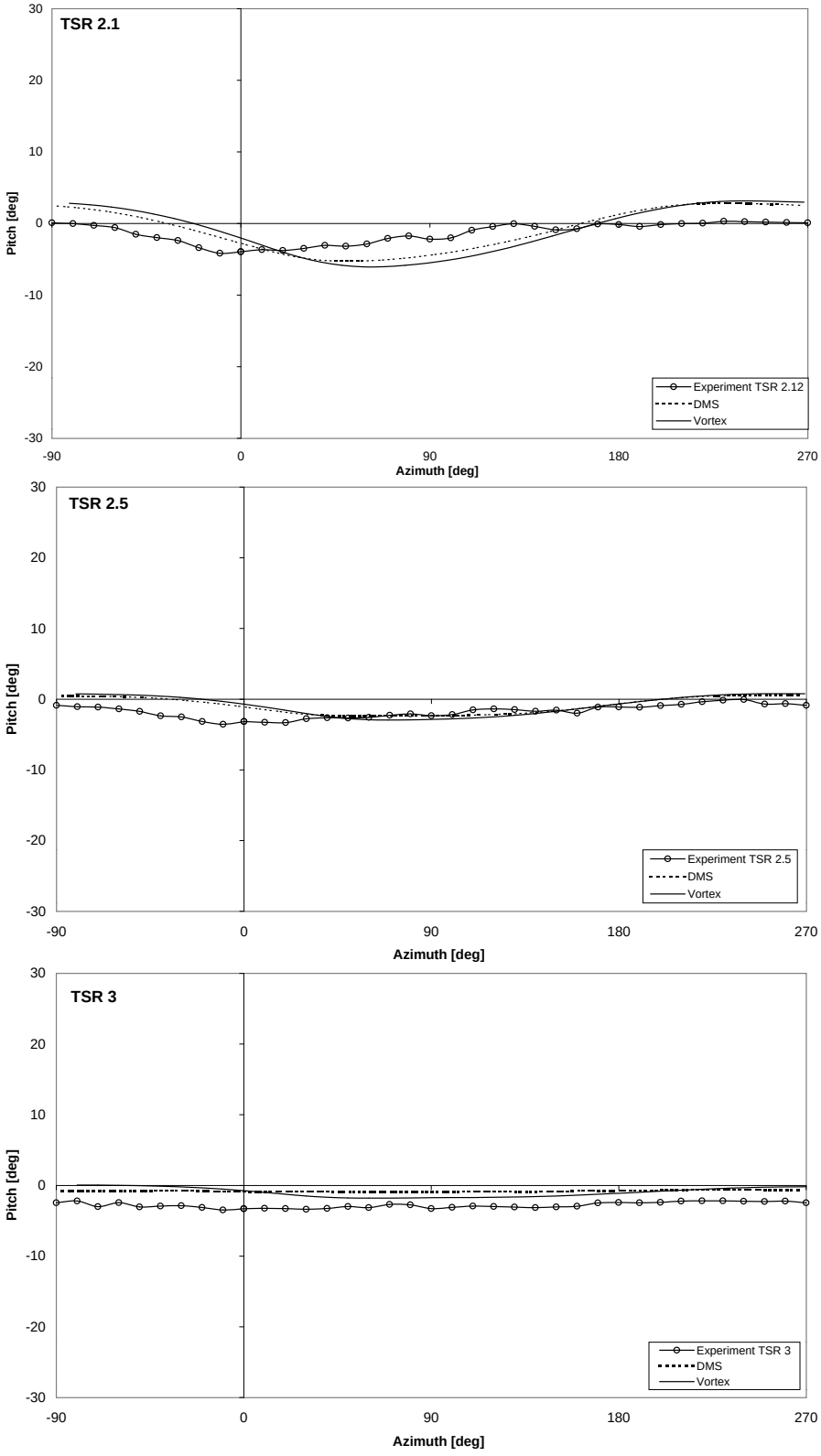

Figure 10.21: Measured and predicted pitch responses, Type B, TSR 2.1 - 3.0

TSR 3, the blade was observed to settle to an almost constant pitch of approximately -3°, while the momentum and vortex models predict an almost constant pitch of approximately -1°.

10.4.2 Type B II geometry

The theoretical results for the Type B II geometry predict that the restoring moment produced by this geometry should be too small. The frequency ratio for the blades should be greater than one, resulting in pitch response out of phase with the natural angle of incidence variation and negative torque for tip speed ratios greater than approximately 0.4. Below this speed the pitch stops limit the phase lag and result in positive torque at start up. Figure 10.22 shows the comparison between theoretical and experimental results for torque coefficient for this geometry. It is evident that agreement is good for tip speed ratios up to 0.4. At this speed the torque is almost zero. While in the wind tunnel the torque recovered at higher speeds and a maximum tip speed ratio of three was reached, both the mathematical models predict increasingly large negative torque.

The pitch responses shown in Figures 10.23 to 10.25 (pages 278 to 280) show the large phase difference, at times more than 90°, between the measured and predicted patterns, especially above TSR 0.4. It is the large phase lag of predicted pitch response that produces the negative predicted torque. The measured response however exhibits a much smaller lag angle. This phase difference suggests a greater than predicted restoring moment acting in the experimental rig. To test this hypothesis, the simulations were repeated with an additional restoring moment added to the inertial moment supplied by the rolling profile. The best agreement with the measured pitch responses was found by setting the additional moment proportional to centrifugal force at 0.006 (Nm/rad)/N. The new responses are

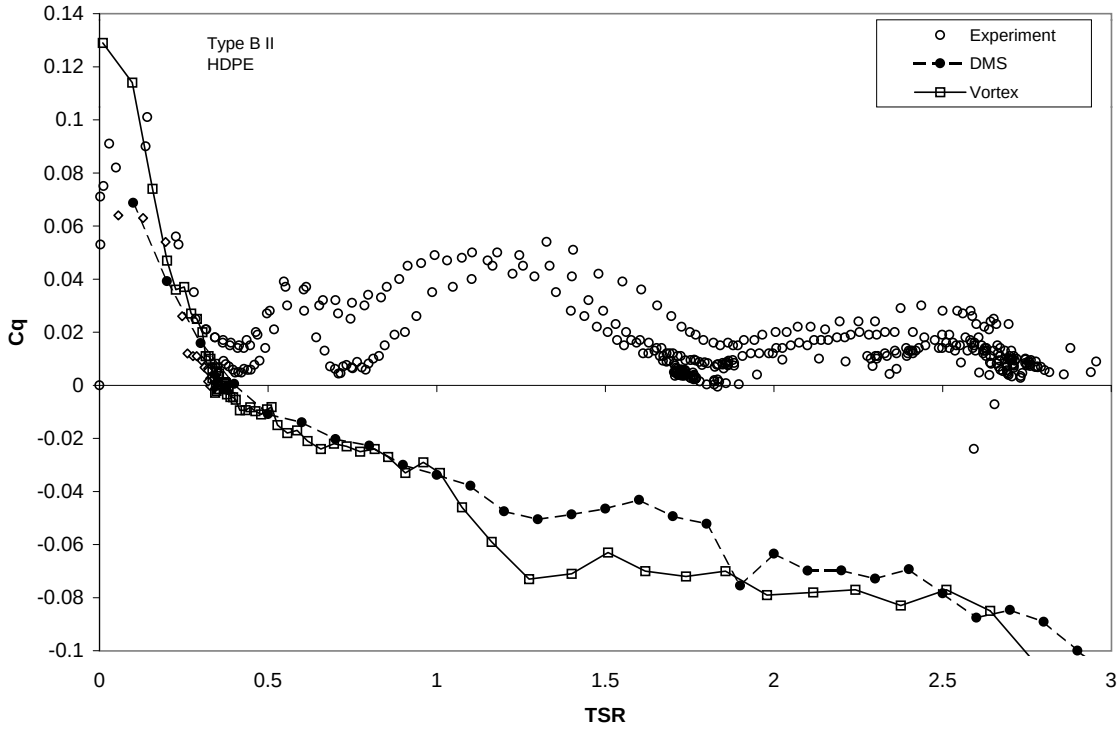

Figure 10.22: Measured and predicted torque coefficient, Type B II geometry

shown in Figures 10.26 and 10.27 (pages 281 to 282). The reduced phase angle is evident.

The predicted torque coefficient with this additional spring moment is shown in Figure 10.28 (page 283). The agreement with experimental data is improved, though the torque above TSR 1.7 is still negative.

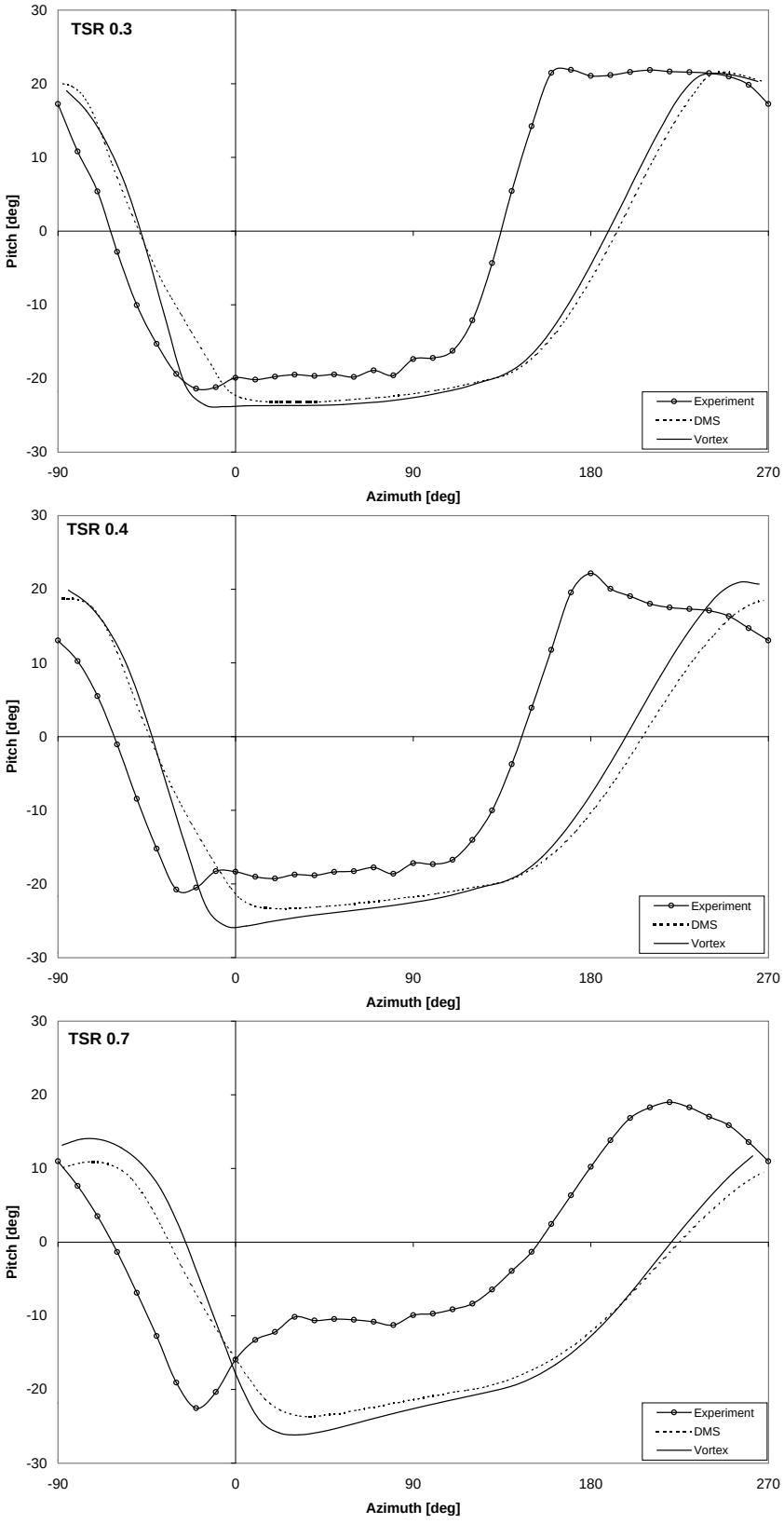

Figure 10.23: Measured and predicted pitch responses, Type B II, TSR 0.3 - 0.7

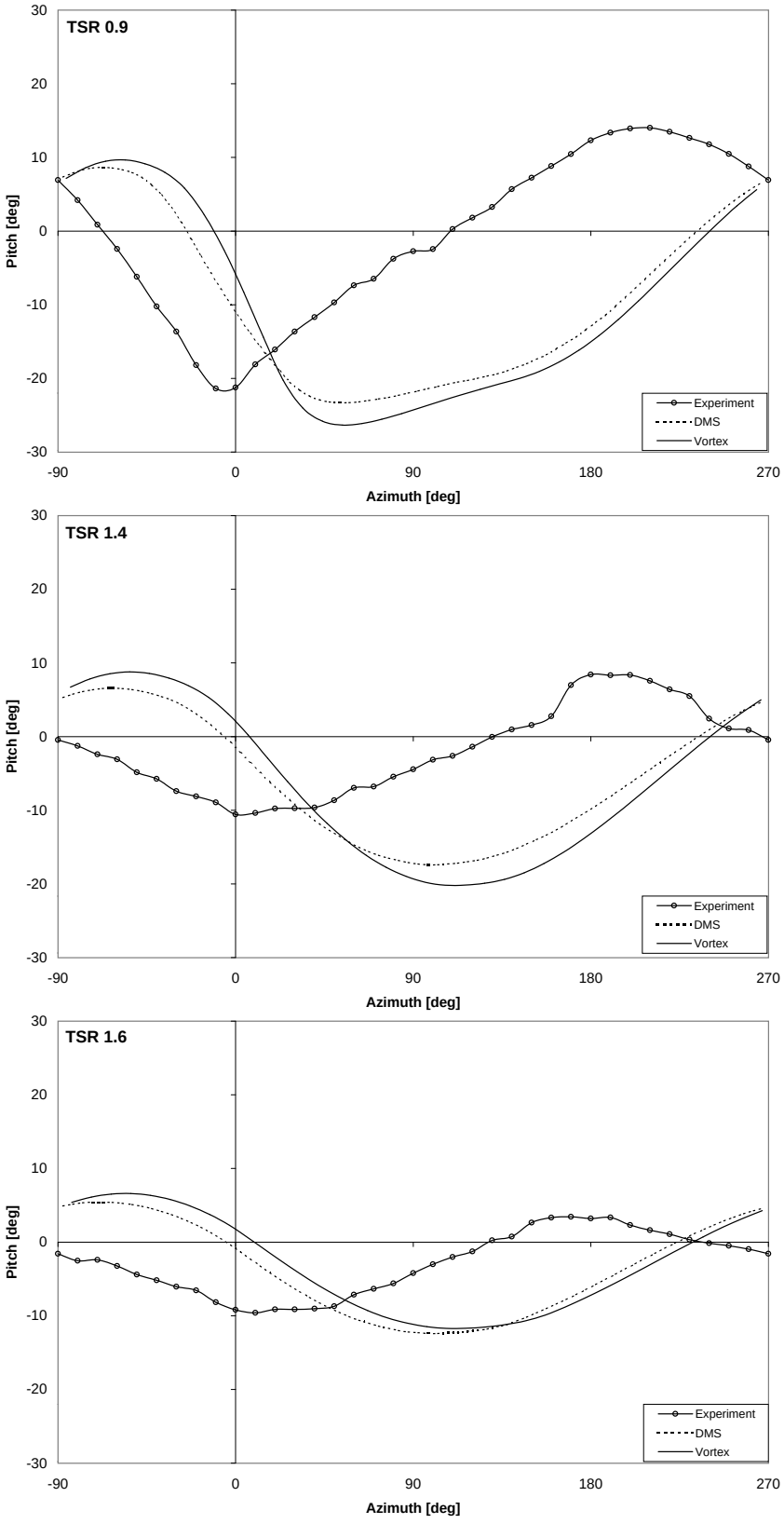

Figure 10.24: Measured and predicted pitch responses, Type B II, TSR 0.9 - 1.6

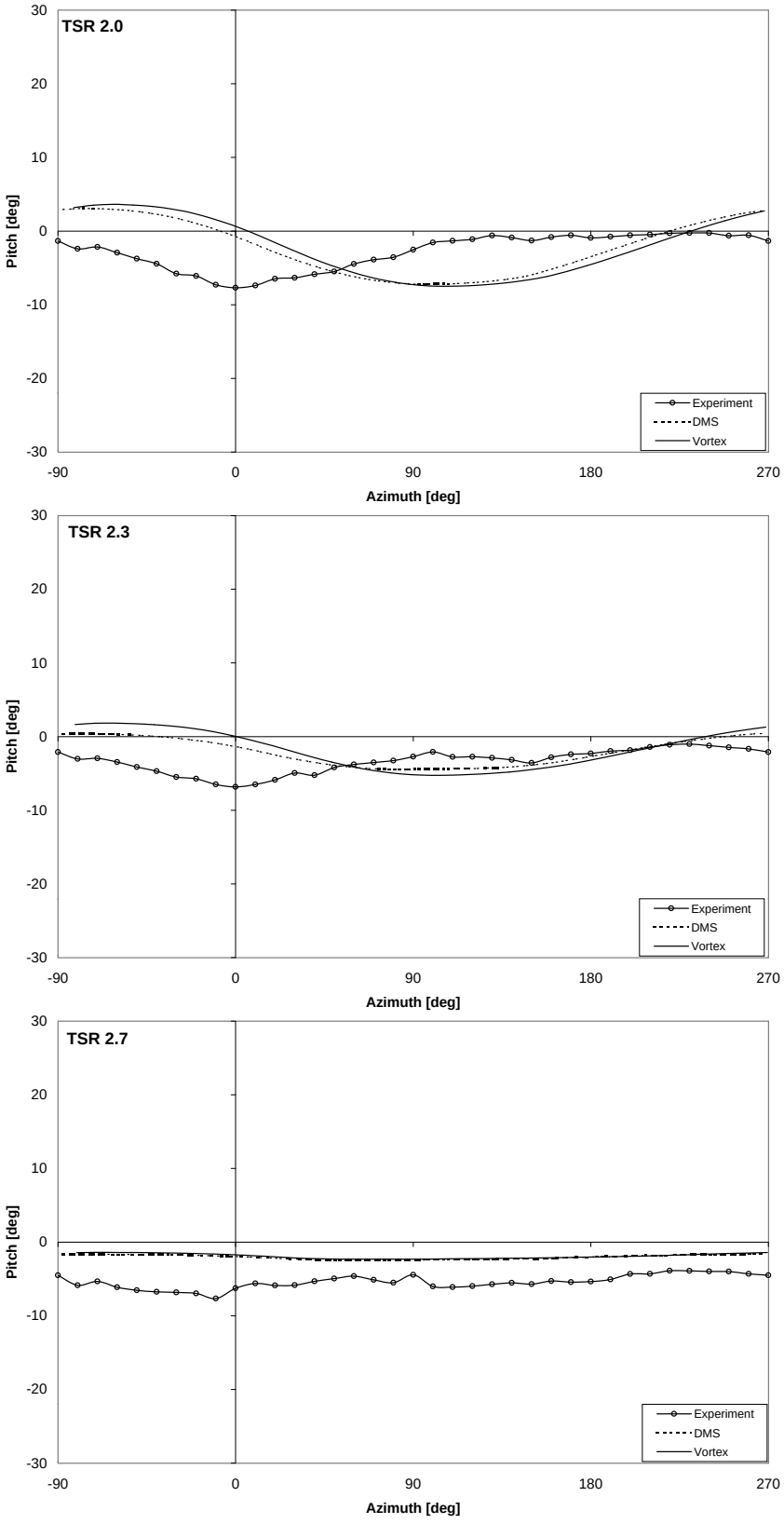

Figure 10.25: Measured and predicted pitch responses, Type B II, TSR 2.0 - 2.7

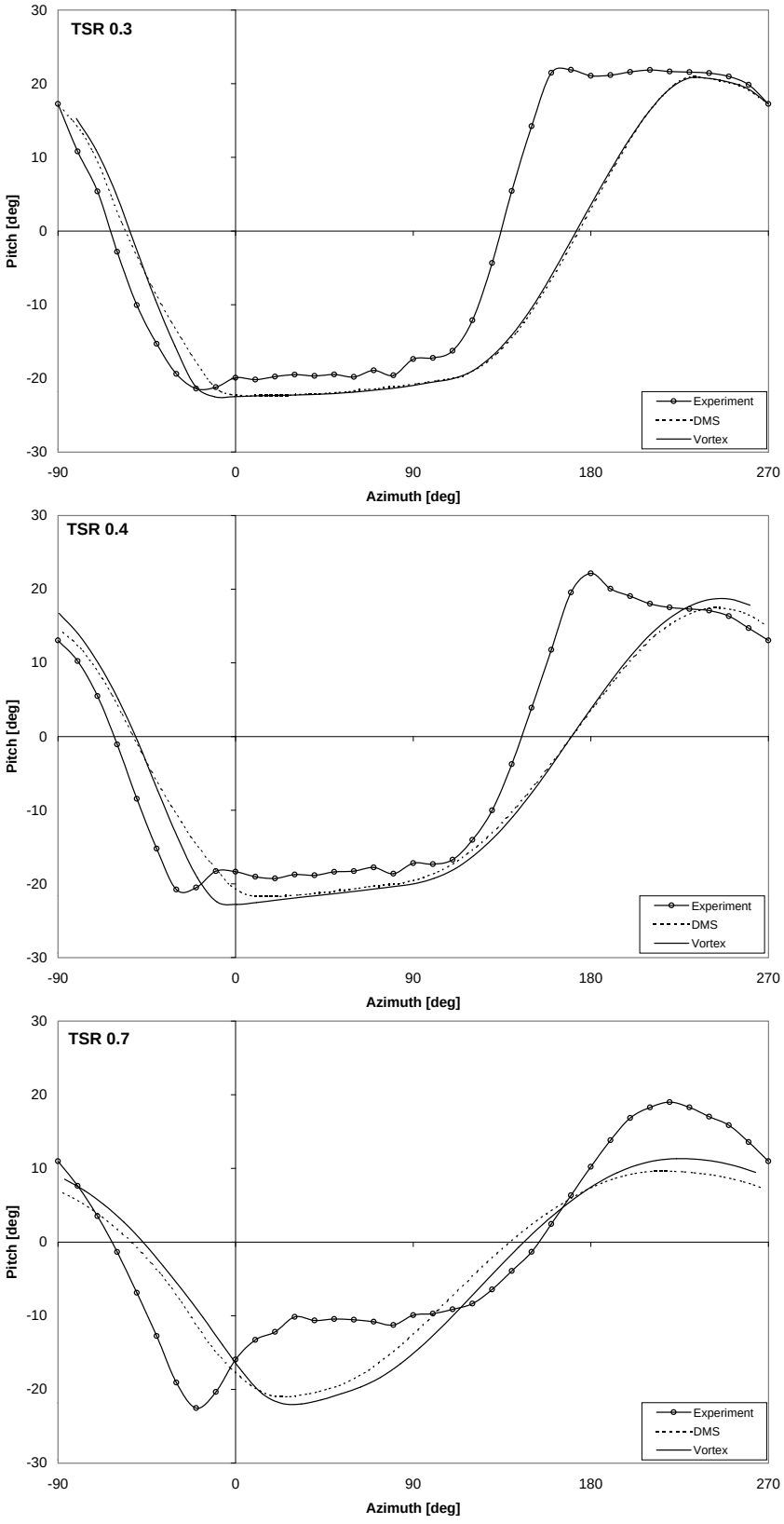

Figure 10.26: Measured pitch responses for the Type B II geometry compared with predicted pitch responses for Type B II with additional spring; TSR 0.3 - 0.7

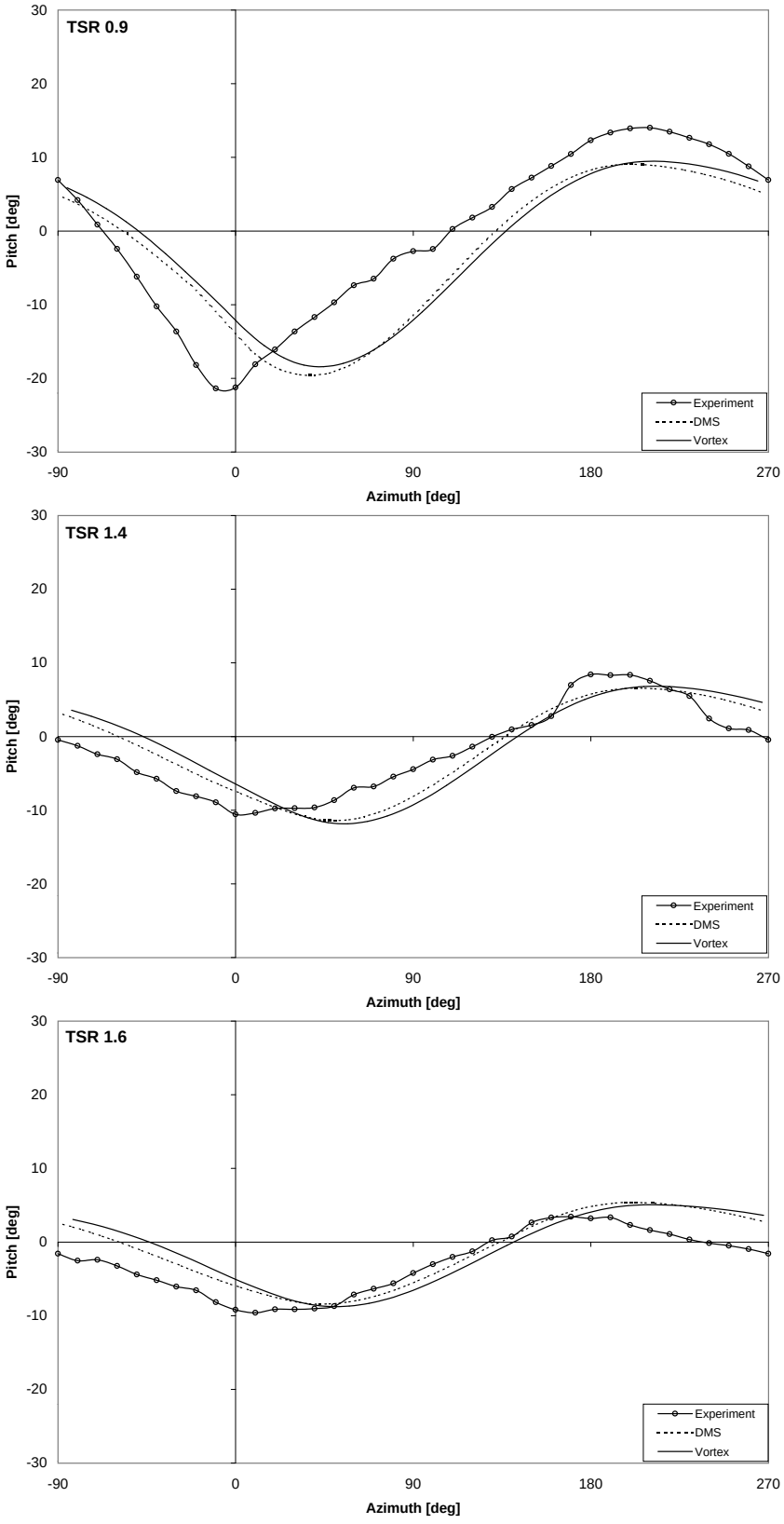

Figure 10.27: Measured pitch responses for the Type B II geometry compared with predicted pitch responses for Type B II with additional spring; TSR 0.9 - 1.6.

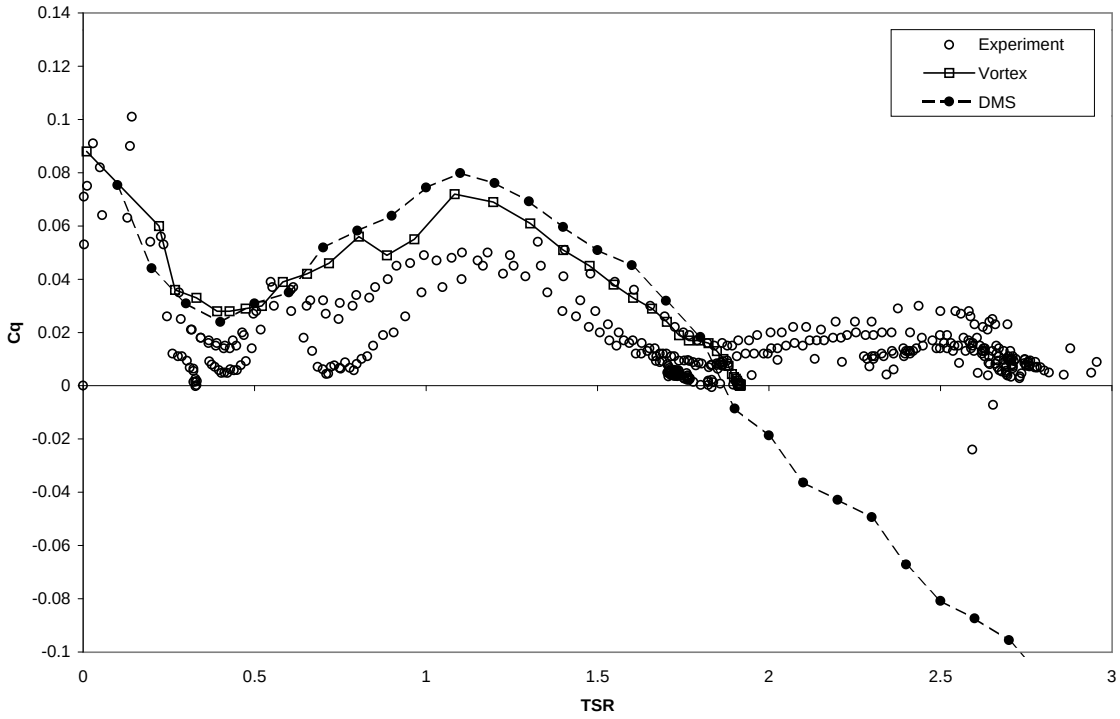

Figure 10.28: Measured torque coefficient for the Type B II geometry compared with predicted torque for Type B II with additional spring

If the same additional spring restoring moment is applied to the simulations for the original Type B geometry, the agreement between measured and predicted pitch response patterns similarly improves, as shown in Figures 10.29, 10.30 and 10.31 (pages 284 to 286). The predicted torque, shown in Figure 10.32 (page 287), however now over-estimates the actual torque, up to TSR 2 where the torque becomes negative.

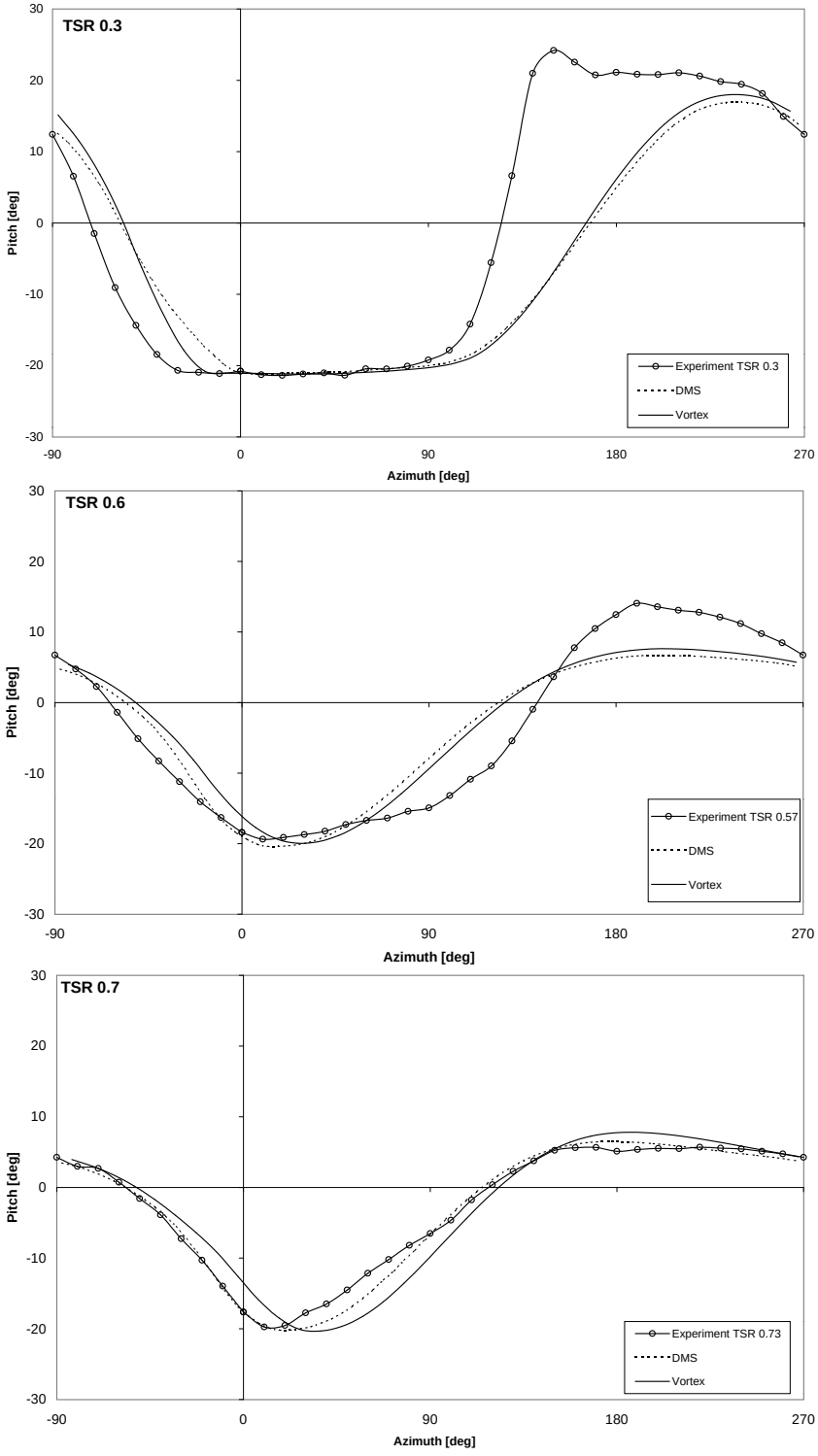

Figure 10.29: Measured pitch responses for the Type B geometry compared with predicted pitch responses for Type B with additional spring; TSR 0.3 - 0.7

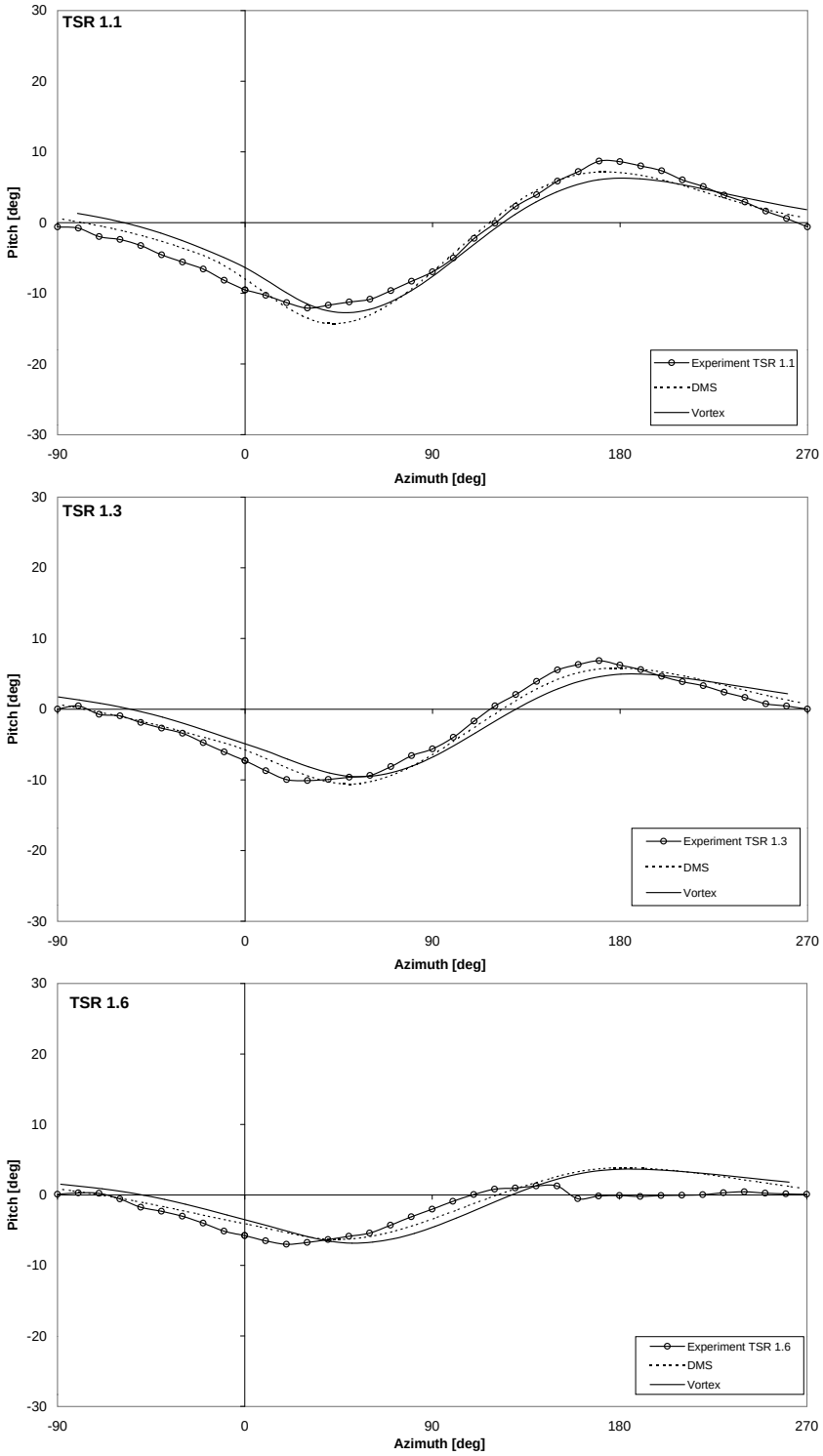

Figure 10.30: Measured pitch responses for the Type B geometry compared with predicted pitch responses for Type B with additional spring; TSR 1.1 - 1.6.

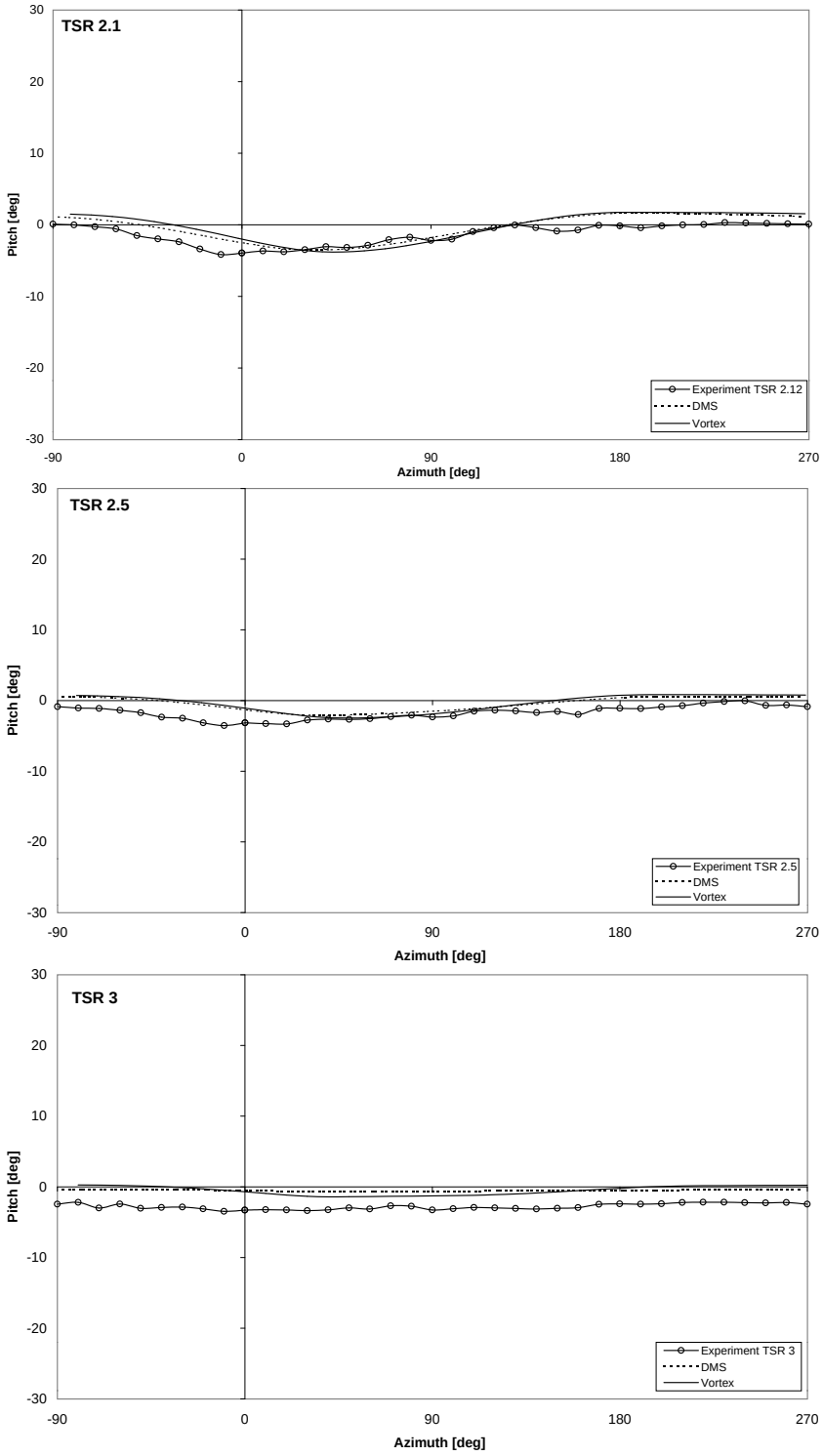

Figure 10.31: Measured pitch responses for the Type B geometry compared with predicted pitch responses for Type B with additional spring; TSR 2.1 - 3.0.

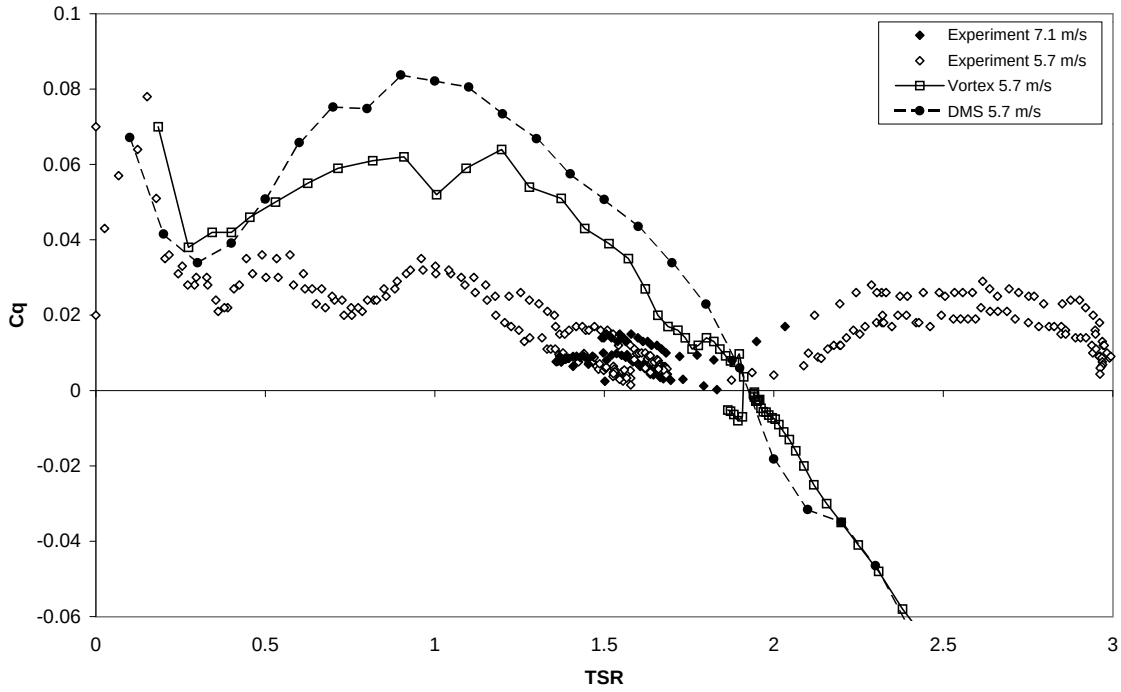

Figure 10.32: Measured torque coefficient for the Type B geometry compared with predicted torque for Type B with additional spring

10.4.3 Type C component

Comparison between predicted and measured torque coefficients for the Type C geometry is shown in Figure 10.33. Both the DMS and vortex model predictions follow the general trend of the experimental data and predict the maximum tip speed ratio fairly well.

The predicted and measured pitch response patterns for a range of tip speed ratios is shown in Figures 10.34 and 10.35 (pages 289 and 290). Unlike the results for the Type B and Type B II geometries, there is no significant phase difference between the predicted and measured pitch responses. This suggests there is no significant additional restoring moment acting that is not included in the mathematical models.

The vortex model predicted torque exhibits oscillations in the range TSR 0.7 - TSR 1.1. The exact location and magnitude of the peaks and troughs in the

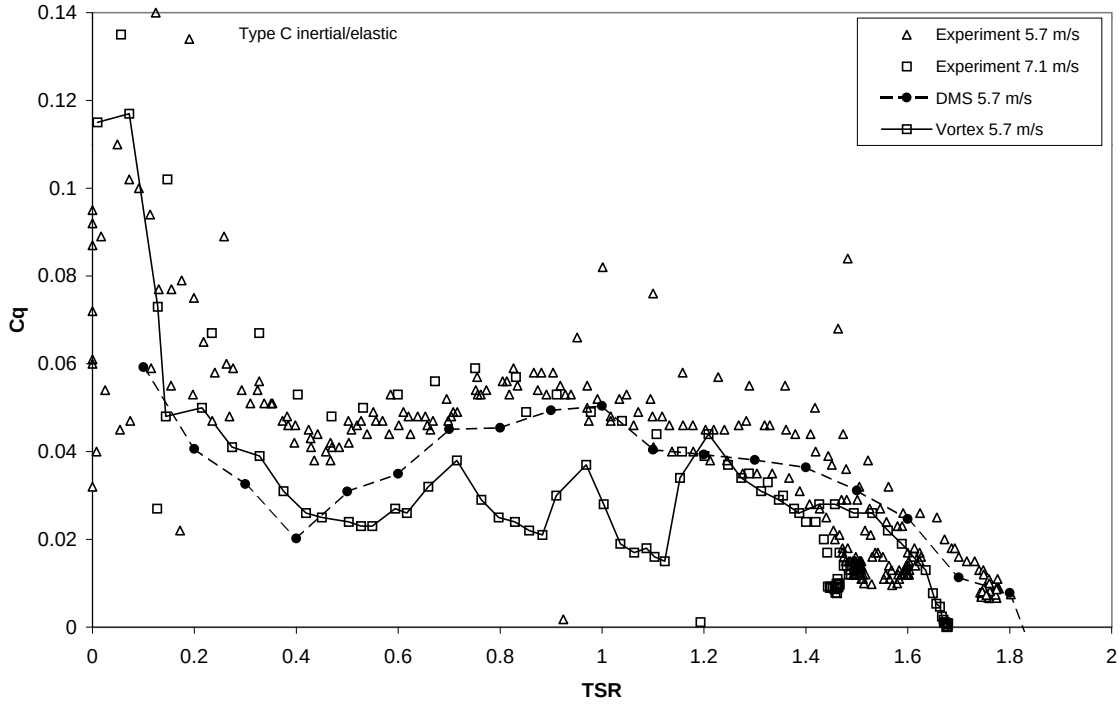

Figure 10.33: Measured and predicted torque coefficient, Type C geometry

torque curve in this region are dependent on the initial conditions set for the run. To illustrate this, two runs were conducted with an initial velocity corresponding to a tip speed ratio of 0.01. In one run, the blades were given an initial pitch of zero degrees and for the other they were all set to $+14°$. The predicted speed-time histories and corresponding torque coefficient curves are shown in Figure 10.36. It is evident that the initial conditions affect the output of the turbine throughout the run, even producing different final speeds after 250 seconds of simulated time. While the general nature of the torque coefficient curves are the same, the exact locations of the various peaks, corresponding to 'spurts' in the speed histories, are different. This indicates that for the accelerating turbine the pitch response at a given speed is transient and may result in appreciably different torques from those produced under different unsteady conditions or at steady-state at that speed.

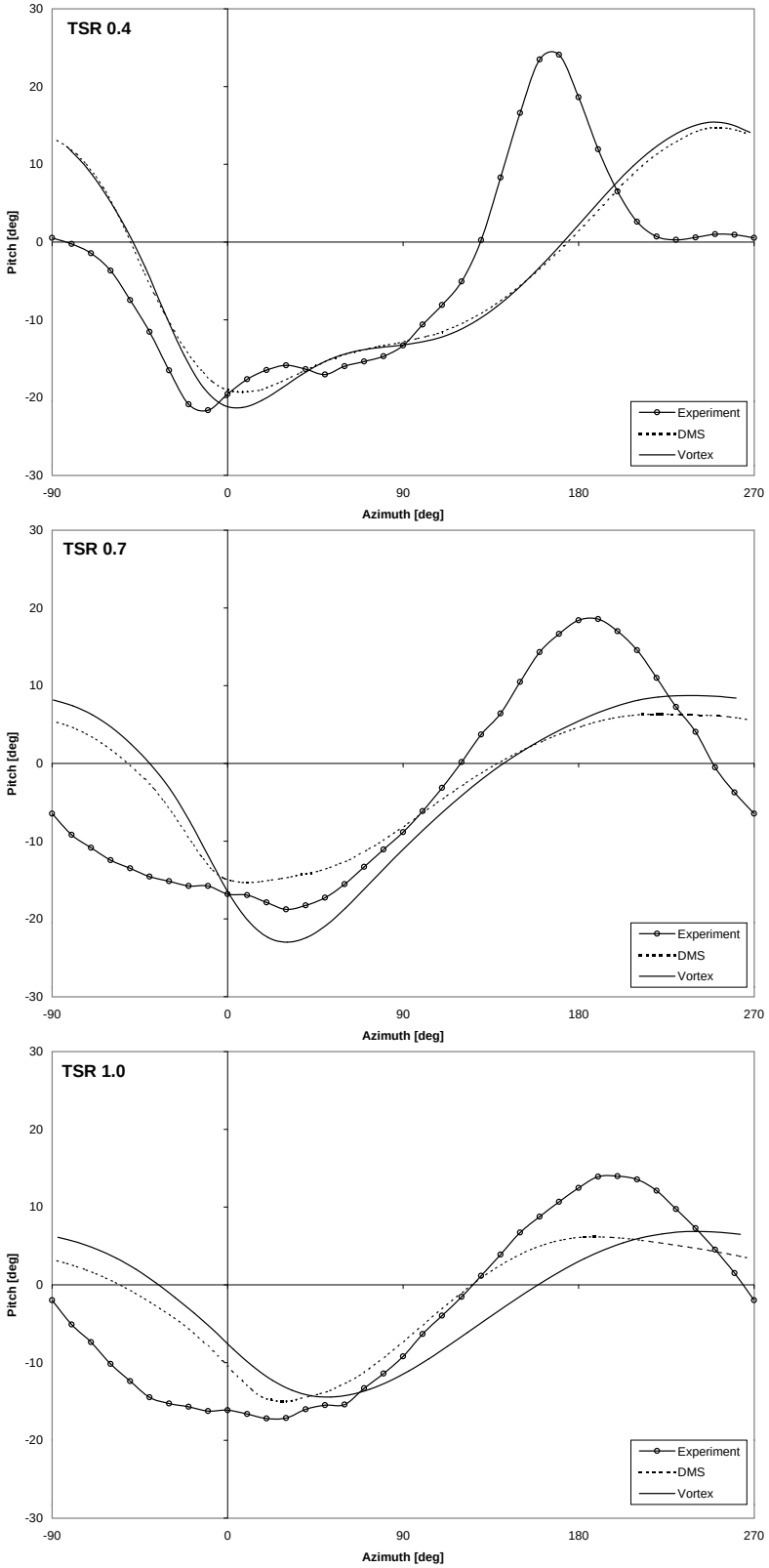

Figure 10.34: Measured and predicted pitch responses, Type C, TSR 0.4 - 1.0

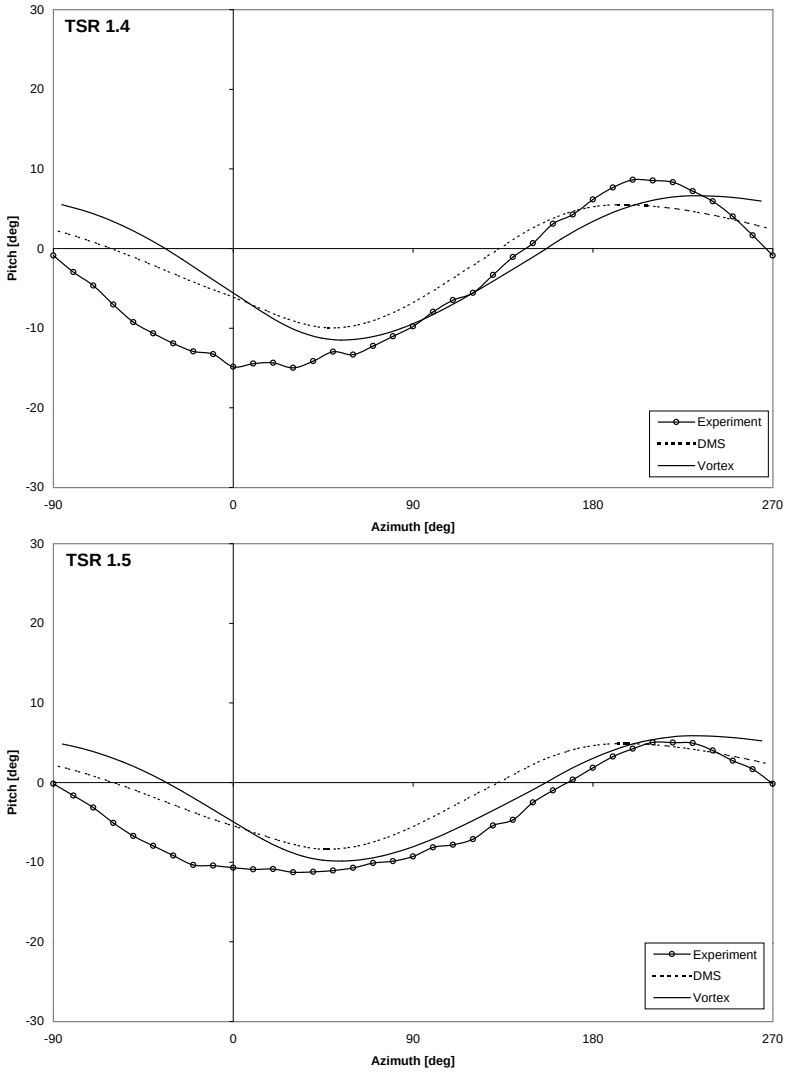

Figure 10.35: Measured and predicted pitch responses, Type C, TSR 1.4 - 1.5

10.4.4 Discussion

Friction

For all the Type B geometries the blades settled to a fixed, non-zero pitch at a tip speed ratio less than three. Initial modelling predicted significant pitch amplitude at this speed. The discrepancy must be attributed to friction. Friction in the blade connections was not initially included in the mathematical models as it was expected to have negligible effect. For the rolling profile design concept there is not supposed to be any sliding contact, except between the pivot point and

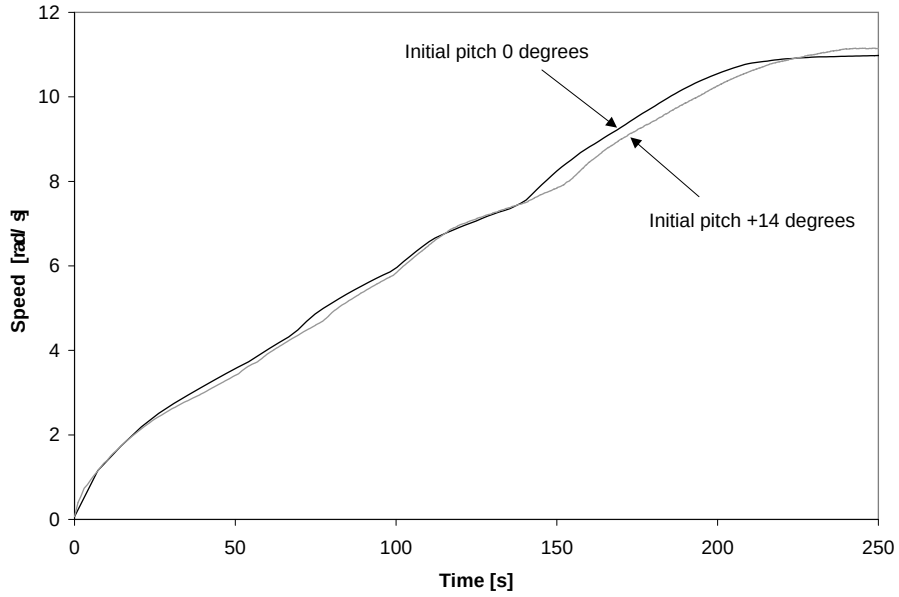

(a)

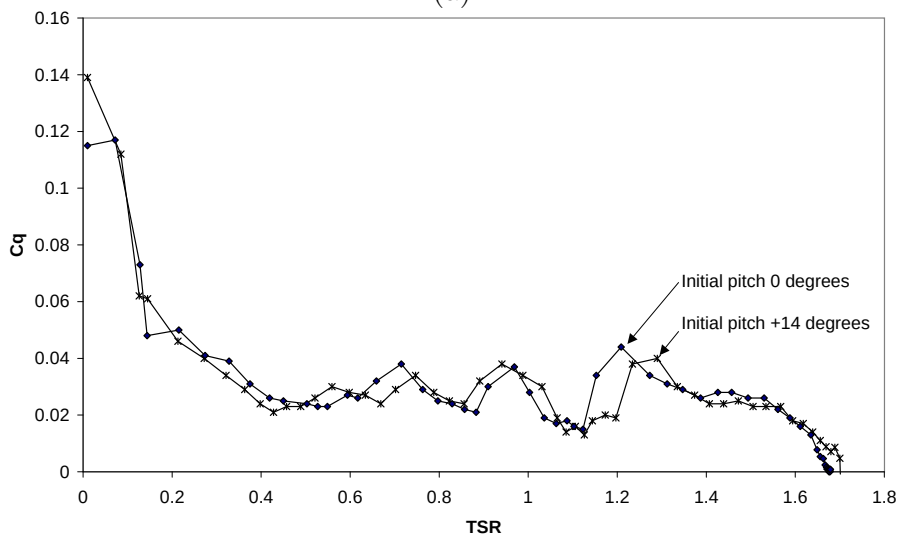

(b)

Figure 10.36: Comparison of the speed-time histories (a) and corresponding torque coefficient-TSR curves (b) for the Type C geometry component with two different initial conditions.

its bearing surface. Since this contact had to transmit only the weight of the blade due to gravity rather than its centrifugal weight, and because vibration was expected to reduce resistance under operating conditions, friction at this point was not expected to be high.

The pitch response patterns measured during operation however indicate appreciable friction that is proportional to centrifugal load. This must be due to rolling resistance caused by deformation of the rolling profile component and the surface on which it rolls. This deformation produces a finite area contact patch and moves the location of the resultant normal contact force forward (in the direction of motion). There is then effectively an additional moment retarding the rolling motion. The magnitude of this resistance is dependent on the geometry and material properties of the two components. The initial rolling profile components were manufactured in polyurethane in order to incorporate an elastic restoring moment through the flexibility of the material. However this flexibility would have resulted in increased contact patch deformation and increased rolling resistance. This point was realised during testing and replacement parts manufactured in much harder High Density Polyethylene. The polyurethane mating components however were retained and little change was measured in the pitching behaviour.

In order to reduce such resistance both the rolling profile component and the mating part should be manufactured in a harder material, possibly steel. The wearing properties of the two materials must be considered. Wear resistance was a factor in the selection of polyurethane as the original material.

Some aspects of the turbine performance cannot be attributed to friction. The fact that the Type B II and Type B III geometry components produced success-

ful operation of the turbine when both mathematical models predicted that they should not work indicates a stronger than expected restoring moment.

Increased restoring moment could result if the centre of mass of the blade assembly were displaced radially outwards. This would increase the centrifugal restoring moment at any pitch angle.

The mathematical models produce the best agreement with measured pitch patterns when an additional spring of stiffness 0.006 Nm/rad/N centrifugal force is added. For small angles this is equivalent to a mass centre offset of 6 mm. A check of the balance of the blades however ruled out a balance error of the magnitude needed to explain the discrepancy. In addition, the fact that very little 'additional' restoring moment was evident for the smaller radius Type C geometry suggests that there was no significant balance error.

It is possible that deformation of the components does alter the contact between them in such a way as to produce not just resistance to movement but actually a resistance to displacement, even with the use of HDPE. The experimental results presented in Section 3.4 indicated a rise in the torsional stiffness of both the Type B and Type C polyurethane components for radial loads greater than 750 N. For a blade mass of 7.36 kg and turbine radius of 870 mm, this force corresponds to a turbine speed of approximately 15 rad/s, or 146 rpm. While the increase in the torsional stiffness on the turbine was modelled as increasing linearly with centrifugal force, it is possible that the effect becomes increasingly non-linear as speed increases. In order to minimise this effect metal components could be used.

It is evident also that the measured pitch response exhibits an offset in mean pitch angle. This offset is matched by an asymmetry in the predicted pitch response. At low tip speed ratios this is a result of the asymmetry in the pattern

of incidence angle variation. The incident wind swings around the trailing edge of the blade as it travels downwind much more rapidly than it travels around the leading edge as it travels upwind. To take a sailing analogy, the angle of attack changes much faster as the blade 'gybes' than it does as it 'tacks'. This results in a more gradual motion of the blade from its positive limit to the negative limit than in the reverse direction.

As tip speed ratio increases, the deceleration of the flow through the turbine becomes more pronounced. For a high solidity turbine like that tested here, most of the deceleration occurs at the upwind half of the blades' orbit. By the time the flow reaches the blades in the downwind half, most of its energy has already been extracted. This results in smaller angles of attack on the downwind pass than on the upwind pass. The positive pitch excursion that occurs in the downwind pass can then be expected to be smaller than the negative angle excursion on the upwind pass. This effect should become more pronounced as tip speed ratio increases.

This effect however cannot explain a constant negative pitch offset being maintained with virtually zero pitch amplitude. The decelerated flow experienced by the blades in the downwind pass only reduces the disturbing aerodynamic moment. If the inertial restoring moment is moving the blade towards zero pitch, then the pitch should approach zero, not adopt a constant negative value.

The only factor that would produce a constant negative pitch offset is the aerodynamic force on the blade that is pivoted about a point forward of its aerodynamic centre. The zero pitch line is defined as being perpendicular to the radius through the pivot axis. Here the quarter chord point of the blade is 20.5 mm aft of the pivot axis. At zero pitch there is therefore a some negative angle of attack

experienced at the aerodynamic centre. This would cause the blade to adopt some small negative pitch angle to find the orientation of least resistance as the turbine spins, even in still air. In addition, the curvature of the flow experienced by a blade moving in a circular path causes further negative deflection of the blade. The observed decrease in the pitch offset with decreasing turbine speed as the turbine decelerates from speed in still air is in keeping with the idea that these effects contribute to the offset.

Both of these effects are handled in the mathematical models. The calculated angle of attack takes into account the distance between the pivot axis and the aerodynamic centre and the flow curvature method of Migliore (1984) modifies the effective angle of attack. The inclusion of friction in the model successfully reproduces the settling to an almost constant negative pitch angle at high tip speed ratios, albeit of a smaller magnitude than was measured.

Blockage

The other major area of discrepancy between predicted and experimental performance was for tip speed ratios greater than 1.7. While the mathematical models predict negative torque at these speeds, positive torque was produced experimentally. The mathematical models predict positive 'gross' torque, but when parasitic drag is subtracted, the net torque is negative.

The reason for this discrepancy is not known. The quality of agreement at lower tip speed ratios is reasonable. It is possible that the effects of blockage in the wind tunnel contribute to this difference. The constraints of the tunnel walls may force the flow velocity to be higher than would be the case in the open, especially in the downwind half of the turbine.

Grylls et al. (1978) however attributed a lower than predicted maximum torque to blockage effects. They tested a 'cycloturbine', with a cam driving a preset schedule of pitch variation, in a wind tunnel and measured the power coefficient using a dynamometer. They measured a maximum power coefficient of approximately 0.2. This was lower than their predicted value of more than 0.3. They speculated that the discrepancy may be due to the wind tunnel walls preventing the full expansion of the wake that would occur under free conditions. Their turbine had a diameter of 2.4 m and a height of 1.6 m. The wind tunnel test section measured 10 ft x 12 ft (3.05 m x 3.66 m), giving a blockage of approximately 34%. Grylls et al. state that:

> "It is believed that the wake of the rotor is unable to expand any further than the size corresponding to a 20% power extraction...
>
> Our experience ... suggests that blockage does not give an increased speed at the rotor, but rather higher speed in the wake than anticipated."

The maximum Cp recorded by Kirke (1998) for the 2 m diameter turbine he tested in the wind tunnel was approximately 0.22. Bayly (1981) recorded a maximum Cp of approximately 0.36 for a 508 mm diameter model turbine tested in the wind tunnel, however this was of the open-jet type where blockage does not occur.

The effect of blockage is likely to be even more significant in the present case due to the short length of the working section. At a distance of approximately one turbine diameter downstream of the turbine axis, the air enters a 10:1 contraction, further inhibiting the natural expansion of the wake.

Sheldahl (1981) compared the performance of a 2 metre diameter troposkien Darrieus turbine measured in the wind tunnel and in the field. He found good agreement for the maximum power coefficient, with slightly higher efficiency measured in the field than in the wind tunnel for tip speed ratios greater than that at which peak efficiency occurred. Sheldahl was not able to conclude if the difference was due to the blockage correction factor used for the wind tunnel results (Sheldahl, 1976) or whether the difference was real. The wind tunnel test section measured 4.6 m x 6.1 m, giving a ratio of turbine swept area to tunnel cross-sectional area of 0.092. In the present work, the test section area is 7.46 m^2 and the turbine swept area is 2.09 m^2, making the corresponding ratio 0.28. The much greater value makes it impossible to rely on Sheldahl's work to determine the significance of blockage in this case.

The only way to tell how the performance of the turbine in the wind tunnel differs from that in the open would be to conduct outdoor tests. Field testing however brings its own problems, particularly the inevitable turbulence of the wind, which would make direct comparison with wind tunnel results difficult. The estimation of the effect of wind tunnel blockage on the performance of passive variable-pitch turbines is particularly difficult, given the sensitivity of the pitch response and the measured torque to the variation of flow velocity across and through the turbine.

However significant the effect of blockage, its influence should be smaller at low tip speed ratios where the deceleration of the flow is small. This is the operating region of interest in the present study.

10.5 Conclusion

10.5.1 Performance of turbine

The turbine was able to generate torque at low tip speed ratios using a number of components embodying the rolling profile design concept. Virtually no starting torque was produced with the blades fixed. The turbine was demonstrated to be self-starting, however variability in performance was observed. It appears that the compressibility of the rolling profile components affected the pitching behaviour of the blades and the performance of the turbine as a whole.

The potential of the elastomeric pitch control concept was not demonstrated by use of the particular geometry tested. The components tested proved to be excessively stiff and did not allow sufficient pitching to occur at start up. Further testing using different geometries is required.

Aerodynamic drag was higher than was anticipated and significantly affected the measured performance of the turbine. On the basis of run-down tests conducted to measure resistance, at design speeds most of the torque produced by the blades was lost in overcoming aerodynamic drag on the radial arms and blade fittings. While this is an inherent disadvantage of straight-bladed vertical axis wind turbines, in hindsight insufficient design attention was given to this problem in this case. Even a modest reduction in drag would result in a significant percentage increase in the peak efficiency measured here.

The size of the turbine relative to the test section is suspected to have had a significant effect on performance at higher tip speed ratios. Restriction of the natural expansion of the wake may be responsible for the discrepancy between predicted and measured performance at tip speed ratios greater than approximately 1.7.

10.5.2 Development of pitch measurement technique

A photogrammetric method was developed to allow measurement of the pitch response pattern of one of the turbine blades in operation. This allowed comparison with the pitch patterns predicted by the mathematical models. The technique proved invaluable in providing insight into the behaviour of the passive variable-pitch mechanisms.

10.5.3 Performance of mathematical models

In general the momentum and vortex models produced similar results, with similar levels of agreement with experimental data. Uncertainty surrounding the true kinematics of the blade connections and the effects of the wind tunnel on the aerodynamics makes comparison of theoretical and experimental results difficult. Three-dimensional effects, which are neglected in these two-dimensional analyses, may also play an important role in the turbine's aerodynamics.

The vortex model predicted slightly lower torque than the momentum model for virtually all cases. This should be expected, as the momentum model predicts the steady-state performance at each speed, while the vortex model models the more realistic case of the accelerating turbine, where the blades do not always have time to approach the steady-state response pattern.

The vortex model results also exhibited some degree of variability in the same manner as the experimental results. The location and magnitude of peaks and troughs in the torque curve (corresponding to spurts and plateaus in the speed history) were dependent on the exact initial conditions for the run. Both the initial turbine speed and even initial blade pitch angles were found to effect the predicted performance for the entire run. Similar variability of performance under nominally identical conditions was continually observed in the wind tunnel. At

the time this was attributed to variation in friction, alignment and resistance to pitching. It seems that to some degree such variation reflects the complexity of the system and the sensitivity of performance to small disturbances.

This sensitivity made both physical testing and mathematical modelling difficult. Ultimately the quantity of interest for a wind turbine is the average energy capture over a long period in a real wind. Not only is the task of isolating a test system from disturbances in order to distill its 'ideal' performance characteristic difficult, it is also not straightforward to use this ideal characteristic to predict its performance in the 'real world', where disturbances dominate. While the vortex model is conceptually more appealing on these grounds, as it is able to simulate directly the unsteady performance of the turbine, its results have not in general proven to be in better agreement with experiments. Consequently the momentum theory mathematical model may be viewed as delivering greater 'value-for-effort' than the vortex model, whose complexity and order-of-magnitude greater expense do not in general yield commensurate gains in accuracy.

Chapter 11

Conclusion

Darrieus turbines with fixed blades are characterised by low or even negative torque at tip speed ratios below that at which they are designed to run (greater than approximately three). This feature prevents or greatly inhibits the ability of such turbines to self-start. It also significantly affects total energy capture in a turbulent wind. The use of passive variable-pitch blade mechanisms to improve this aspect of performance of straight-bladed vertical axis wind turbines is the subject of this thesis. A momentum theory mathematical model and a vortex theory mathematical model have been developed as part of this work to predict the performance of different designs of passive variable-pitch turbine. Wind tunnel testing of a prototype turbine featuring two new design concepts has also been undertaken.

Evaluation of existing designs

A review of existing passive variable-pitch vertical axis wind turbine designs has been performed. The provision of some form of 'restoring moment' acting independently on each blade is a common feature of almost all the design concepts found in the literature. This moment may be produced by elastic means or by the inertial loads on the blade. Insight into the operation of passive variable-pitch turbines and a basis for systematic selection of design parameter values has been gained through use of Pro/MECHANICA and the momentum model. It is concluded that greatest torque at all tip speed ratios is achieved if the magnitude of

this restoring moment increases with the square of turbine speed. Inertial-type designs inherently produce such a moment.

A theoretical basis for the selection of parameters governing the strength of the restoring moment has been developed. Treatment of the pitching blade as a spring/mass/damper system excited by a harmonic driving force indicates that the natural frequency is a function of turbine speed and that the frequency ratio is therefore a constant function of design parameters. This ratio must be less than one to ensure that the blade motion is not too far out of phase with the aerodynamic driving force and that positive torque is produced.

Potential of new designs

Elastomeric blade mounting component concept - A design concept featuring elastomeric blade mounting components has been proposed. The aim is to produce an elastic restoring moment on the blades that increases with centrifugal load.

The turbine using the particular design of flexible elastomeric components tested in the wind tunnel did not perform well. The combination of geometry and material that was chosen proved to be excessively stiff in torsion, preventing the blade from pitching sufficiently. A different geometry could be selected to reduce this stiffness, however it is likely that the tensile stiffness of the component would then be reduced. It appears that it would be difficult to find a suitable compromise between these two constraints.

A further potential difficulty is that if an appropriate combination of part geometry and material properties could be found to produce the desired relationship between torsional stiffness and radial force, the properties of the material may

change with time. This may result from fatigue, moisture absorption or temperature. Given the sensitivity of blade pitch response and turbine performance to the torsional stiffness of the blade connection, this may prove to be a significant issue.

Rolling profile concept - A design concept that produces restoring moment from inertial loads using a component in rolling contact with the rotor has been proposed. Mathematical modelling, using both the momentum and vortex mathematical models has indicated the potential of the concept. The design allows greater control over restoring moment than is available with other inertial type passive variable-pitch designs. It also reduces the mass moment of inertia of the blades, allowing smaller aerodynamic moment arms to be used and producing faster blade response.

Wind tunnel testing of a prototype turbine has been conducted and the rolling profile concept was demonstrated to enable self-starting. Further refinement of the design is required to reduce the effects of friction and parasitic drag. The compressibility of the components used for testing is thought to have affected performance significantly.

The 'pendulum' design of Sicard (1977) and Kentfield (1978) is probably the simplest design of passive variable-pitch VAWT and its predicted performance is not greatly different from that of the rolling profile concept. The conceptual advantages of the new design - of reduced blade mass moment of inertia and greater control over restoring moment - will be of little value if the turbine is significantly less reliable or more expensive. Further development of the detailed design is required before the concept can be judged as successful.

Development of a blade pitch response measurement technique

A significant part of the present thesis has been the development of a technique for the measurement of the pattern of blade pitch angle variation when the turbine is in operation. A photogrammetric technique using long exposures to record the trajectories of light emitting diodes mounted on one of the blades was adopted. A computer program has been written to extract the pitch angle history from the digital camera images. This method has been used successfully to measure the pitch response patterns of the prototype turbine operating in the wind tunnel.

Performance of mathematical models

Each of the mathematical models was able to produce results that are in general agreement with torque coefficient data measured from the wind tunnel experiments with the prototype turbine. The difference in results from the two models is surprisingly small given the different approaches to calculation of the velocity field. Both models failed to reproduce the higher tip speed ratio performance observed for a number of variations of the rolling profile design, potentially due to the effect of blockage. The pitch response patterns produced by both models were reasonably close to those measured over a range of tip speed ratios once adjustments to friction and restoring moment values had been made.

The difference in performance predicted by the momentum and vortex models was not great, despite the greater complexity of the vortex model. It is concluded that for general design analysis and parameter selection the faster momentum model is adequate. The much greater computational expense of the vortex model appears only to be justified for the study of turbulent wind performance, which momentum methods cannot handle.

Turbulent wind performance

The vortex model has been used to simulate turbulent wind performance of a number of passive variable-pitch turbines. The results indicate that significant reductions in average efficiency occur in unsteady conditions. Well-designed passive variable-pitch turbines are predicted to suffer losses in efficiency of around 10% in typical wind conditions. A standard Darrieus turbine is predicted to lose approximately 28% of its steady-state efficiency. The results indicate the importance of a 'flat' turbine power coefficient curve and the ability of passive variable-pitch turbines to achieve this. Rotor and blade mass moment of inertia also influence turbulent wind efficiency, though to a lesser extent. The results indicate that a major advantage of variable-pitch turbines is improved total energy capture, not just self-starting ability.

11.1 Summary of Research outcomes

The key outcomes of the research are:

- Development and wind tunnel testing of two new design concepts for passive variable-pitch turbines. These are the use of a specially designed elastomeric component to produce a connection whose torsional stiffness increases with centrifugal force; and the use of a rolling profile component whose shape determines the relationship between pitch angle and the restoring moment arising from inertial force. Refer to Chapters 3 and 10.
- Extension of the Double Multiple Streamtube type mathematical model to include the full inertia effects of pitching blades, as well as different passive variable-pitch designs. Refer to Chapter 5.

- Development of a free vortex wake mathematical model for passive variable-pitch Darrieus turbines, allowing modelling of unsteady performance. Refer to Chapter 6.
- Development of a parameter selection strategy for passive variable-pitch turbines based on a frequency response analysis of the blade pitching. Refer to Chapter 7.
- Investigation of the turbulent wind performance of VAWTs, indicating the ability of passive variable-pitch turbines to achieve significantly greater average efficiency than the corresponding fixed-bladed turbine. Refer to Chapter 8.
- Development of a simple, non-invasive method for measuring the blade pitch response of a turbine in operation in the wind tunnel. Refer to Section 9.4.3.
- Modification of the semi-empirical MIT dynamic stall method to allow it to be used in the modelling of the starting performance of Darrieus turbines. Refer to Section 5.1 and Appendix B.

11.2 Conclusion and Recommendations for Further Work

This thesis has identified a logical basis for the design and selection of key parameters for passive variable-pitch vertical axis wind turbines. This knowledge enables specious ideas to be identified amongst the variety of possible design concepts and provides guidance for blind trial and error optimisation processes. A range of design paths remain open for passive variable-pitch turbines and the question of which, or if any, of these can lead to an economical and reliable self-starting VAWT remains to be answered. The most critical hurdles may lie in the detailed design and materials selection to produce a simple, economical, reliable machine with adequate fatigue life. Before these issues are tackled however a sound design concept

must be selected and confidence must exist that the effect of different parameter selections on performance can be adequately predicted. Continued development of mathematical models and experimental validation is therefore required. A number of specific areas warrant further attention:

- The greatest area of weakness of all mathematical models of Darrieus turbines is the prediction of unsteady aerodynamic forces, including dynamic stall. The complexity of the phenomenon places upper limits on the ability of semi-empirical techniques to accurately predict unsteady forces by modifying static lift, drag and pitching moment coefficients. While greater accuracy may be obtained by using computational fluid dynamics techniques, greater computing power will be required to make their use practical.
- Further testing of a passive variable-pitch turbine using metal rolling profile components is needed to further assess the potential of this concept.
- Outdoor testing of this turbine is needed to assess the effect of constraint of the turbine wake in the wind tunnel.

Such work may ultimately allow passive variable-pitch vertical axis wind turbines to be widely used as a decentralised, renewable and economical energy source.

References

AGO (2002). Renewable Energy Overview 2002. Australian Greenhouse Office.

Allet, A., S. Halle, and I. Paraschivoiu (1999). Numerical Simulation Of Dynamic Stall Around An Airfoil In Darrieus Motion. *Journal of Solar Energy Engineering 121*(1), 69–76.

AWEA (2001). Global Wind Energy Market Report 2001. American Wind Energy Association publication.

AWEA (2002a). Global Wind Energy Market Report 2002. American Wind Energy Association.

AWEA (2002b). U.S. wind energy industry doubles capacity in 2001. American Wind Energy Association News Release.

Azim, R. A. (2001). Investigation of an Elastomeric Mount for a Vertical Axis Wind Turbine. Master's thesis, University of NSW.

Baker, G. (1979). The Cloud In Cell Technique Applied To The Roll Up Of Vortex Sheets. *Journal of Comutational Physics 31*, 76–95.

Bayly, D. (1981). The Cyclobrid Wind Turbine: Theory, Design and Experimental Results. Master's thesis, University of Calgary.

Bayly, D. and J. Kentfield (1981). A Vertical Axis Cycligiro Type Wind-Turbine With Freely-Hinged Blades. In *Proceedings of the Intersociety Energy Conversion Conference*, Volume II, pp. 2053.

Brenneman, B. (1983). Transverse axis fluid turbine. United States Patent 4,415,312.

Cameron, J. (1978). Vertical axis wind turbine. Canadian Patent CA1045038.

Cardona, J. (1984). Flow Curvature And Dynamic Stall Simulated with an Aerodynamic Free-Vortex Model for VAWT. *Wind Engineering 18*(3), 135–143.

CEC (1995). Wind Performance Report Summary 1995. California Energy Commission.

CEC (1999). Wind Performance Report Summary 1996-1999. California Energy Commission.

CEC (2001). Annual Project Activity Report to the Legislature 2001. California Energy Commission.

Cook, R. (1995). *Finite Element Modelling for Stress Analysis*. John Wiley.

Daley, D. and E. Jumper (1984). Experimental Investigation Of Dynamic Stall For A Pitching Airfoil. *Journal of Aircraft 21*(10 (Oct 1984)), 831–832.

Darrieus, G. (1931). Turbine having its rotating shaft transverse to the flow of the current. United States Patent 1,835,018.

Dawson, A. (2000). Blade Design for a Vertical Axis Wind Turbine. Undergraduate Thesis, School of Mechanical and Manufacturing Engineering, University of NSW.

de Vahl Davis, G. (1991). *Numerical methods in engineering and science*. Chapman and Hall.

Dodge, D. (2001). An Illustrated History of Wind Power Development. Online 31/10/02 http://telosnet.com/wind/index.html.

Drees, H. (1978). The Cycloturbine And Its Potential For Broad Application. In *2nd International Symposium on Wind Energy Systems Oct 3-6 1978*, Volume 2, pp. E–7.

Drees, H. (1979). Self-starting windmill energy conversion system. United States Patent 4,180,367.

EERE (2001). EREC Reference Briefs: Contribution of Renewable Energy to the United States Energy Supply. Online 23-10-2002 at http://www.eren.doe.gov/consumerinfo/refbriefs/da8.html. US DOE Office of Energy Efficiency and Renewable Energy.

EIA (2002). International Energy Outlook 2002 Renewables. Energy Information Agency publication.

ESDU (2001). Characteristics of atmospheric turbulence near the ground - Part II: single point data for strong winds (neutral atmosphere). Wind Engineering series, Vol. 1a, Data Item 85020. Engineering Sciences Data Unit.

Evans, F. (1978). Practical Considerations In The Design Of A Vertical Axis Windmill. In *2nd International Symposium on Wind Energy Conversion Systems, Amsterdam, Oct 1978*, Volume 2, pp. Z56.

EWEA (2000). Wind Directions. 36739. European Wind Energy Association publication.

EWEA (2002). Another Record Year for European Wind Power. European Wind Energy Association publication.

Fanucci, J. and R. Walters (1976). Innovative Wind Machines: The Theoretical Performances of a Vertical Axis Wind Turbine. In *Proc. Of the VAWT Technology Workshop, Sandia Lab. Report SAND 76-5586, pp III-61-93.*

Fink, P. T. and W. K. Soh (1978). New Approach To Roll-Up Calculations Of Vortex Sheets. *Proc R Soc London Ser A 362*(1709), 195–209.

Fitzgibbon, A., M. Pilu, and R. Fisher (1999). Direct least-square fitting of Ellipses. In *IEEE PAMI , June 1999.*

Francis, M. and J. Keesee (1985). Airfoil Dynamic Stall Performance With Large-Amplitude Motions. *AIAA-Journal. v. 23 Nov. '85 p. 1653-9 23*(31352), 1653–1659.

Fung, Y. (1955). *An Introduction To The Theory Of Aeroelasticity*. John Wiley & Sons, NY.

Glauert, H. (1926). The Analysis of Experimental Results in the Windmill Brake and Vortex Ring States of an Airscrew. Technical Report R&M No. 1026 AE 222, London: Aeronautical Research Committee.

Gormont, R. (1973). A Mathematical Model of Unsteady Aerodynamics and Radial Flow for Applications to Helicopters. Technical Report DAAJO2-71-C-0045, May 1973, US Army Air Mobility Research & Development Lab. Vertol Div.

Gracey, M., F. Coton, and R. Galbraith (1997). On The Prediction Of Aerofoil Unsteady Stall Criticality. *The Aeronautical Journal Aug/Sep 1997*, 331–334.

Gracey, M., A. Niven, F. Coton, R. Galbraith, and D. Jiang (1996). Correlation Indicating Incipient Dynamic Stall. *Aeronautical Journal 100*(997), 305–311.

Grylls, W., B. Dale, and P. Sarr (1978). A Theoretical And Experimental Investigation Into The Variable Pitch Vertical Axis Wind Turbine. In *2nd International Symposium on Wind Energy Systems Oct 3-6 1978*, Volume 2, pp. E–9.

Halir, R. and J. Flusser (1998). Numerically Stable Direct Least Squares Fitting Of Ellipses. In *Proc. 6th International Conference in Central Europe on Computer Graphics and Visualization. WSCG '98, CZ, Plzen, Czech Republic*, pp. 125–132.

Hansen, A. (1995). Aerodynamic Damping Of Blade Flap Motions At High Angles Of Attack. *Journal of Solar Energy Engineering 117*(3), 194–199.

Hansen, A., C. Butterfied, and X. Cui (1990). Yaw loads and motions of a horizontal axis wind turbine. *Journal of Solar Energy Engineering 112*(4), 310–314.

IEA (1999). Evolving Renewable Energy Market. International Energy Agency publication.

IEA (2001a). Key World Energy Statistics 2001. International Energy Agency publication.

IEA (2001b). Wind Energy Annual Report 2001 Australia. International Energy Agency publication.

Jiang, D., F. Coton, and M. R. Galbraith (1991). Fixed Wake Vortex Model For Vertical Axis Wind Turbines Including Unsteady Aerodynamics. *Wind Engineering 15*(6), 348–360.

Johnson, W. (1970, May). The Response and Airloading of Helicopter Rotor Blades due to Dynamic Stall. Technical Report TR 130-1, MIT Aeroelastic and Structures Research Lab.

Kentfield, J. (1978). A Hybrid Cyclogiro-Darrieus Rotor Wind Turbine. In *Proc. 1st Brazilian Energy Congress, Rio de Janiero 1978*, Volume B, pp. 4448–463.

Kirke, B. (1998). *Evaluation Of Self-Starting Vertical Axis Wind Turbines For Stand-Alone Applications*. Ph. D. thesis, Griffith University.

Kirke, B. and L. Lazauskas (1987). A Novel Variable Pitch Vertical Axis Wind Turbine. In *The Annual Conference and AGM of ANZSES, ANU 26-28 Nov 1987*, pp. 67–76.

Kirke, B. and L. Lazauskas (1991). Enhancing The Performance Of A Vertical Axis Wind Turbine Using A Simple Variable Pitch System. *Wind Engineering 15*(4), 187–195.

Kirke, B. and L. Lazauskas (1992). Performance Optimisation Of A Self-Acting Variable Pitch Vertical Axis Wind Turbine. *Wind Engineering 16*(1), 10–26.

Kirke, B. and L. Lazauskas (1993). Experimental Verification af a Mathematical Model For Predicting The Performance of a Self-Acting Vertical Axis Wind Turbine. *Wind Engineering 17*(2), 58–66.

Klimas, P. (1982). Darrieus Rotor Aerodynamics. *Journal of Solar Energy Engineering 104*, 102–105.

Krasny, R. (1987). Computation of Vortex Roll-Up in the Trefftz Plane. *Journal of Fluid Mechanics 184*, 123–155.

Laneville, A. and P. Vittecoq (1986). Dynamic Stall; The Case Of The Vertical Axis Wind Turbine. *Journal of Solar Energy Engineering 108*, 140–145.

Larsen, H. (1975). Summary Of Vortex Theory Of The Cycogiro. In *Proc. 2nd national Conference on Wind Engineering Research, June 22-25 1975*, pp. V–8–1.

Lazauskas, L. (1992). Three Pitch Control Systems For Vertical Axis Aind Turbine Compared. *Wind Engineering 16*(5), 269–276.

Lazauskas, L. (2002). Maths dept, Adelaide University website, Online 19-9-2002 at http://www.maths.adelaide.edu.au/Applied/llazausk/aero/foil/foil.htm.

Leigh, G. (1980). A Concept for Automatic Blade Pitch for a Darrieus Vertical Axis Wind Turbine. In *Proc. of 2nd WEIS Conference, Dec. 1980*.

Leishman, J. (2002). Challenges in modelling the unsteady aerodynamics of wind turbines. AIAA 2002-0037, 21st ASME Wind Energy Symposium.

Leishman, J. and T. Beddoes (1986). A Generalized Model for Unsteady Airfoil Behaviour and Dynamic Stall Using the Indicial Method. In *Proc. Of the 42nd Annual Forum of the American Helicopter Society*.

Leishman, J. and T. Beddoes (1989). A Semi-Empirical Model for Dynamic Stall. *Journal of the American Helicopter Society 34*(3), 3–17.

Liljegren, L. (1984). Vertical axis wind turbine. United States Patent 4,430,044.

Lorber, P. and F. Carta (1988). Airfoil Dynamic Stall At Constant Pitch Rate And High Reynolds Number. *Journal of Aircraft 25*(6), 548–556.

Major, S. and I. Paraschivoiu (1992). Indicial Method Calculating Dynamic Stall On A Vertical Axis Wind Turbine. *Journal of Propulsion 8*(4 Jul-Aug 1992), 909–911.

Marie, J. (1984). Moving blades for automatically starting up panemones of the Darrieus type. French Patent FR2541733.

Martin, M. (1989). Wind-energy converter. United States Patent 4,799,860.

McConnell, R. (1979). Giromill Overview. In *Wind Energy Innovative Systems Conference, Colorado May 23-25 1979*.

McFarland, R. and K. Duisenberg (1995). Simulation of Rotor Blade Element Turbulence. Technical Report Technical Memorandum 108862, NASA.

Meikle, P. (1993). A Family of Novel Vertical Axis Wind Turbines. *Uni. Of Melbourne*.

Migliore, P. (1984). Straight-Bladed Darrieus Wind Turbines - A Protagonists View. In *Intersociety Energy Conversion Engineering Conference 1984*, Volume 4, pp. 2326–2332.

Milne-Thomson, L. (1968). *Theoretical Hydrodynamics*. MacMillan & Co.

Moore, D. (1981). On The Point Vortex Method. *Siam Journal On Scientific And Statistical Computing 2*(1), 65–84.

Nattuvetty, V. and W. Gunkel (1982). Theoretical Performance of a Straight-Bladed Cycloturbine Under Four Different Operating Conditions. *Wind Engineering 6*(3), 110–130.

Niven, A. and R. Galbraith (1997). Modelling Dynamic Stall Vortex Inception At Low Mach Numbers. *Aeronautical Journal 101*(1002), 67–76.

Noll, R. and N. Ham (1982). Effects Of Dynamic Stall On Swecs. *Journal of Solar Energy Engineering 104*, 96–101.

Paraschivioiu, I., P. Desy, and C. Masson (1988). Blade Tip, Finite Aspect Ratio And Dynamic Stall Effects On The Darrieus Rotor. *Journal of Propulsion 4*(1), 73–80.

Paraschivoiu, I. (1981). Aerodynamic Loads and Performance of the Darrieus Rotor. *Journal of Energy 6*(Nov-Dec), 406–421.

Paraschivoiu, I. (1983). Predicted And Experimental Aerodynamic Forces On The Darrieus Rotor. *Journal of Energy 7*(Nov-Dec), 610–615.

Paraschivoiu, I. and A. Allet (1988). Aerodynamic Analysis Of The Darrieus Wind Turbines Including Dynamic Stall Effects. *Journal of Propulsion 4*(5), 472–477.

Paul, B. (1979). *Kinematics And Dynamics Of Planar Machinery*. Prentice Hall.

Pawsey, N. and A. Barratt (1999). Evaluation Of A Variable-Pitch Vertical Axis Wind Turbine. *Wind Engineering 23*(1), 23–30.

Pesmajoglou, S. and J. Graham (2000). Prediction of aerodynamic forces on horizontal axis wind turbines in free yaw and turbulence. *Journal of Wind Engineering and Industrial Aerodynamics 86*, 1–14.

Petot, D. (1989). Differential equation modellling of dynamic stall. *Rech. Aerosp. 5*.

Ponta, F. and P. Jacovkis (2001). A Vortex Model for Darrieus Turbine Using Finite Element Techniques. *Renewable Energy 24*, 1–18.

Rosen, A. and Y. Sheinman (1994). The Average Output Power Of A Wind Turbine In A Turbulent Wind. *Journal of Wind Engineering and Industrial Aerodynamics 51*(3), 287–302.

Sandia National Laboratories (1987). Vertical Axis Wind Turbines – The History of the DOE Program. Online 13-5-02 http://www.sandia.gov/Renewable_Energy/wind_energy/images/VAWThist.doc.

Sharp, P. (1982). Wind or fluid current turbine. United States Patent 4,334,823.

Sharpe, D. J. (1990). Wind Turbine Aerodynamics. In L. Freris (Ed.), *Wind Energy Conversion Systems*, pp. 54–118. Prentice Hall.

Sheldahl, R. (1976). Wind tunnel performance data for the Darrieus wind turbine with NACA 0012 blades. Technical Report SAND76-0130, Sandia National Laboratories.

Sheldahl, R. (1981). Comparison of Field and Wind Tunnel Darrieus Wind Turbine Data. Technical Report SAND80-2469, Sandia National Laboratories.

Sheldahl, R. and P. Klimas (1981). Aerodynamic Characteristics of Seven Symmetrical Airfoil Sections Through 180 Degrees for Use in Aerodynamic Analyses of Vertical Axis Wind Turbines. Technical Report SAND80-2114, Sandia National Laboratories.

Sicard, C. (1977). Fluid current turbine. United States Patent 4,048,947.

South, P. and R. Rangi (1973). The Performance and Economics of the Vertical Axis Wind Turbine Developed at the National Research Council, Ottawa, Canada. In *Proceedings of the 1973 Annual Meeting of the Pacific Northwest Region of the American Soc. of Agricultural Engineers, Calgary.*

Stoddard, F. (1976). Momentum Theory and Flow State for Windmills. *Wind Technology Journal 1*(1), 3–9.

Strickland, J. (1975). The Darrieus turbine: A Performance Prediction Model Using Multiple Streamtubes. Technical Report SAND75-041, Sandia National Laboratories.

Strickland, J. and G. Graham (1986). Dynamic Stall Inception Correlation For Airfoils Undergoing Constant Pitch Rate Motions. *AIAA Journal 24*(4), 678–680.

Strickland, J., B. Webster, and T. Nguyen (1979). Vortex Model Of The Darrieus Turbine: An Analytical And Experimental Study. *Journal Of Fluids Engineering 101*, 500–505.

Strickland, J., B. Webster, and T. Nguyen (1980). A Vortex Model Of The Darrieus Turbine: An Analytical And Experimental Study. Technical Report SAND79-7058*, Sandia National Laboratories.

Strickland, J., B. Webster, and T. Nguyen (1981). A Vortex Model Of The Darrieus Turbine: An Analytical And Experimental Study. Technical Report SAND81-7017*, Sandia National Laboratories.

Templin, R. (1974, June). Aerodynamic Performance Theory for the NRC Vertical-Axis Wind Turbine. Technical Report National Aeronautical Establishment Laboratory Technical Report LTR-LA-160, National Research Council, Canada.

Theodorsen, T. (1935). General Theory of Aerodynamic Instability and the Mechanism of Flutter. Technical Report 496, NACA.

Thomson, W. (1993). *Theory of Vibration with Applications, 4th Ed.* Chapman & Hall.

Vandenberghe, D. and E. Dick (1986). A Theoretical And Experimental Investigation Into The Straight Bladed Vertical Axis Wind Turbine With Second Order Harmonic Pitch Control. *Wind Engineering 10*(3), 122–138.

Verastegui, R. (1996). Cross-wind-axis wind turbine. United States Patent 5,518,367.

Vincze, M. (2001). Robust Tracking Of Ellipses At Frame Rate. *Pattern Recognition 34*, 487–498.

Von Karman, T. and W. Sears (1938). Airfoil Theory For Non-Uniform Motion. *Journal of the Aeronautical Sciences 5*(10), 379–389.

Wickens, R. (1985). Aerodynamic Characteristics Of An Oscillating Airfoil. In *Intersol 85, Proceedings of the Ninth Biennial Congress of the International Solar Energy Society*, pp. 1989–1998.

Wilson, R. and P. Lissaman (1974). Applied Aerodynamics of Wind Powered Machines. Technical Report NSF-RA-N-74-113, Oregon State University.

Wilson, R., P. Lissaman, M. James, and W. McKie (1983). Aerodynamic Loads On A Darrieus Rotor Blade. *Journal of Fluids Engineering 105*(1), 53–58.

Wilson, R. E. (1978). Vortex Sheet Analysis Of The Giromill. *Journal Of Fluids Engineering 100*(3), 340–342.

Wilson, R. E. and S. N. Walker (1983). Fixed Wake Theory For Vertical Axis Wind Turbines. *Journal of Fluids Engineering 105*(4), 389–393.

Zheng, Y. (1984). Vertical axis windmill. United States Patent 4,435,124.

Appendix A

Turbine Kinematics

The various designs of passive variable-pitch turbine examined are distinguished by the specific kinematics of the blade motion.

In order to generate the velocity and acceleration coefficients required for the Lagrangian equation of motion for the turbine described in Section 6.6, the kinematic relationships reflecting the specific turbine mechanism are required. The velocity and acceleration coefficients relate the generalised coordinates for the system (the rotor position and the pitch angle of each blade) to the x-y ground-based Cartesian coordinate system, defined such that the y-axis points into the mean free wind.

The position of the rotor is always directly represented by the q_0 generalised coordinate. The motion of the mass centres of the blades is dependent on the specific turbine design. The first step is to express velocities and accelerations of the blade mass centre in a Cartesian coordinate system fixed to the rotor.

Referring to Figure A.1, the ρ-τ coordinate system rotates with the rotor, has its origin at radius R from the rotor axis and marks radial and tangential directions. The general velocity and acceleration components of the mass centre of the blade assembly are shown.

The acceleration includes components due to the rotation and acceleration of the coordinate system, as well as the Coriolis acceleration, normal to the direction

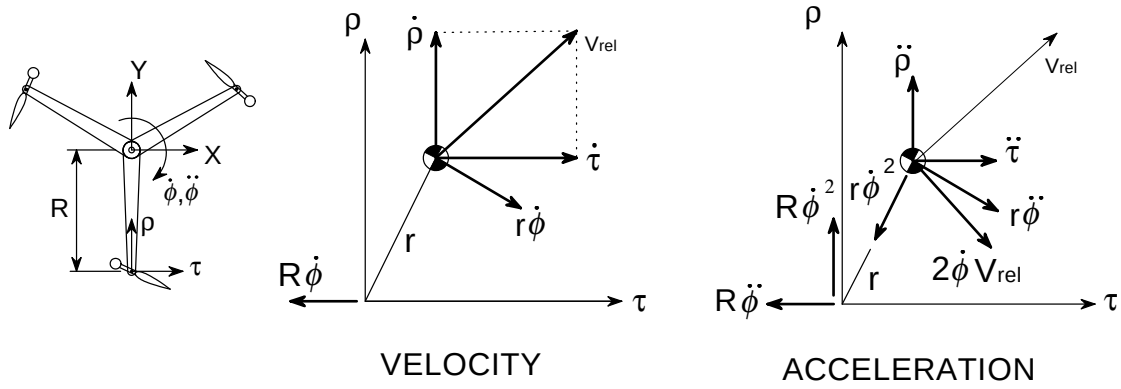

Figure A.1: Kinematics of the blade mass centre

of relative velocity.

The absolute velocities and accelerations of the blades are then found in the X-Y coordinate system shown in Figure A.1. Using the velocity components illustrated and noting that the rotor position is labelled ϕ, the absolute velocities are:

$$\dot{X} = (\tau\dot{\phi} - \dot{\rho})\sin\phi + ((R-\rho)\dot{\phi} - \dot{\tau})\cos\phi \tag{A.1}$$

$$\dot{Y} = (\tau\dot{\phi} - \dot{\rho})\cos\phi - ((R-\rho)\dot{\phi} - \dot{\tau})\sin\phi \tag{A.2}$$

$$\dot{\alpha} = \dot{\phi} + \dot{\theta} \tag{A.3}$$

The absolute acceleration components are:

$$\begin{aligned}\ddot{X} &= \{(R-\rho)\ddot{\phi} - \ddot{\tau} - 2\dot{\rho}\dot{\phi} + \tau\dot{\phi}^2\}\cos\phi \\ &\quad + \{\tau\ddot{\phi} - \ddot{\rho} + 2\dot{\tau}\dot{\phi} - (R-\rho)\dot{\phi}^2\}\sin\phi \end{aligned}\tag{A.4}$$

$$\begin{aligned}\ddot{Y} &= \{\tau\ddot{\phi} - \ddot{\rho} + 2\dot{\tau}\dot{\phi} - (R-\rho)\dot{\phi}^2\}\cos\phi \\ &\quad - \{(R-\rho)\ddot{\phi} - \ddot{\tau} - 2\dot{\rho}\dot{\phi} + \tau\dot{\phi}^2\}\sin\phi \end{aligned}\tag{A.5}$$

$$\ddot{\alpha} = \ddot{\phi} + \ddot{\theta} \tag{A.6}$$

The quantities $\dot{\rho}$, $\dot{\tau}$, $\ddot{\rho}$, $\ddot{\tau}$ must be determined as functions of the pitch angle θ for the specific turbine design.

The above kinematic relations are used to generate the velocity and acceleration coefficients used in the Lagrangian dynamics part of the free vortex model. The X and Y direction coefficients are dependent on the kinematics of the specific blade suspension design. The angular coefficients however are fixed by the definition of the generalised coordinates. The only non-zero angular coefficients are:

$$\begin{aligned} \Omega_{i0} &= 1 \\ \Omega_{ii} &= 1 \end{aligned} \tag{A.7}$$

They are also used calculate the reactions at the rolling contact point for each blade, once the external forces and moments and the velocities and accelerations have been calculated. This is done by a kineto-static analysis of each blade - effectively creating a free body diagram of the blade and using d'Alembert's principle to find the reaction forces.

A.1 Pendulum Kinematics

For the pendulum inertial pitch control design, the mass centre of the blade moves in a circular arc centred on the origin of the ρ-τ coordinate system. As a function

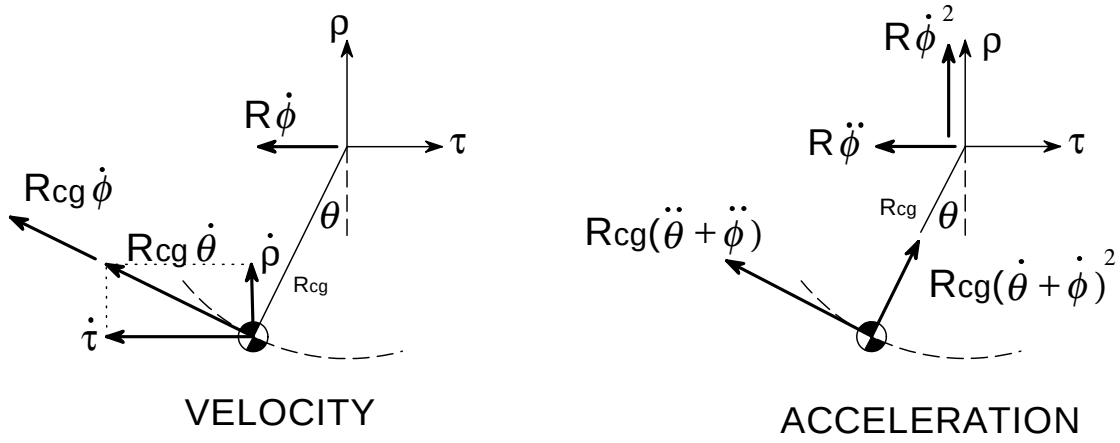

Figure A.2: Kinematics of the blade mass centre for the 'pendulum' type design

of pitch angle, it may be verified that:

$$\tau = -R_{cg}\sin\theta \tag{A.8}$$

$$\rho = -R_{cg}\cos\theta \tag{A.9}$$

$$\dot{\tau} = -R_{cg}\dot{\theta}\cos\theta \tag{A.10}$$

$$\dot{\rho} = R_{cg}\dot{\theta}\sin\theta \tag{A.11}$$

$$\ddot{\tau} = R_{cg}(\dot{\theta}^2\sin\theta - \ddot{\theta}\cos\theta) \tag{A.12}$$

$$\ddot{\rho} = R_{cg}(\dot{\theta}^2\cos\theta + \ddot{\theta}\sin\theta) \tag{A.13}$$

R_{cg} is the 'length' of the pendulum - the distance from the pivot axis to the mass centre of the blade.

For the momentum theory model, where the turbine speed is pre-determined, the pitching acceleration of the blade is calculated using d'Alembert's principle. It may be verified that

$$\ddot{\theta} = \frac{\sum M - R_{cg}\sin\theta mR\ \dot{\phi}^2 - \{(I + mR_{cg}^2) + mR_{cg}R\cos\theta\}\ \ddot{\phi}}{I + mR_{cg}^2} \tag{A.14}$$

where $\sum M$ is the total external moment acting on the blade about the mass centre in the direction of positive θ; I is the polar mass moment of inertia of the blade assembly about the mass centre. For the constant speed case, $\ddot{\phi}$ is zero and so the final term in the numerator drops out.

For the whole mechanism treatment used in the free vortex model, the velocity and acceleration coefficients used by Paul (1979) are required. In this case, substituting the above into Equations (A.1) and (A.2) and simplifying we get :

$$\begin{aligned} \dot{X} &= \{R_{cg}\cos(\theta+\phi) + R\cos\phi\}\,\dot{\phi} + \\ &\quad \{R_{cg}\cos(\theta+\phi)\}\,\dot{\theta} \qquad \text{(A.15)} \\ \dot{Y} &= \{-R\sin(\phi) - R_{cg}\sin(\phi+\theta)\}\,\dot{\phi} + \\ &\quad \{-R_{cg}\sin(\phi+\theta)\}\,\dot{\theta} \qquad \text{(A.16)} \end{aligned}$$

(A.17)

Equations (A.4) and (A.5) become:

$$\begin{aligned} \ddot{X} &= -\{R_{cg}\sin\theta(\dot{\theta}+\dot{\phi})^2 - R_{cg}\cos\theta(\ddot{\theta}+\ddot{\phi}) - R\ddot{\phi}\}\,\cos\phi \\ &\quad -\{R_{cg}\cos\theta(\dot{\theta}+\dot{\phi})^2 + R_{cg}\sin\theta(\ddot{\theta}+\ddot{\phi}) + R\dot{\phi}^2\}\,\sin\phi \qquad \text{(A.18)} \\ \ddot{Y} &= \{R_{cg}\sin\theta(\dot{\theta}+\dot{\phi})^2 - R_{cg}\cos\theta(\ddot{\theta}+\ddot{\phi}) - R\ddot{\phi}\}\,\sin\phi \\ &\quad -\{R_{cg}\cos\theta(\dot{\theta}+\dot{\phi})^2 + R_{cg}\sin\theta(\ddot{\theta}+\ddot{\phi}) + R\dot{\phi}^2\}\,\cos\phi \qquad \text{(A.19)} \end{aligned}$$

In order to extract the acceleration coefficients used by Paul (1979), Equations (A.37) and(A.38) need to be reformulated to extract terms proportional to the

generalised coordinate accelerations:

$$\begin{aligned}
\ddot{X} &= \{R_{cg}\cos(\theta+\phi) + R\cos\phi\}\,\ddot{\phi} + \\
&\quad \{R_{cg}\cos(\theta+\phi)\}\,\ddot{\theta} \\
&\quad -R_{cg}(\dot{\phi}+\dot{\theta})^2\sin(\phi+\theta) - R\,\dot{\phi}^2\sin\phi \qquad \text{(A.20)} \\
\ddot{Y} &= \{-R\sin(\phi) - R_{cg}\sin(\phi+\theta)\}\,\ddot{\phi} + \\
&\quad \{-R_{cg}\sin(\phi+\theta)\}\,\ddot{\theta} \\
&\quad -R_{cg}(\dot{\phi}+\dot{\theta})^2\cos(\phi+\theta) - R\,\dot{\phi}^2\cos\phi \qquad \text{(A.21)}
\end{aligned}$$

The non-zero velocity coefficients for blade i are then:

$$\begin{aligned}
U_{i0} &= R\cos\phi + R_{cg}\cos(\phi+\theta) \\
U_{ii} &= R_{cg}\cos(\phi+\theta) \\
V_{i0} &= -R\sin(\phi) - R_{cg}\sin(\phi+\theta) \\
V_{ii} &= -R_{cg}\sin(\phi+\theta) \qquad \text{(A.22)}
\end{aligned}$$

Equations (A.20) and (A.21) can then be seen to be:

$$\begin{aligned}
\ddot{X} &= U_{ii}\,\ddot{\theta} + U_{i0}\,\ddot{\phi} + U' \\
\ddot{Y} &= V_{ii}\,\ddot{\theta} + V_{i0}\,\ddot{\phi} + V' \qquad \text{(A.23)}
\end{aligned}$$

where the acceleration coefficients, which contain centripetal and Coriolis acceleration components, are:

$$\begin{aligned} U' &= -R_{cg}(\dot{\phi}+\dot{\theta})^2 \sin(\phi+\theta) - R\,\dot{\phi}^2 \sin\phi \\ V' &= -R_{cg}(\dot{\phi}+\dot{\theta})^2 \cos(\phi+\theta) - R\,\dot{\phi}^2 \cos\phi \end{aligned}$$

A.2 Rolling Profile Kinematics

The derivation of the rolling profile shape for a desired moment-angle relationship is described in Section 3.3.

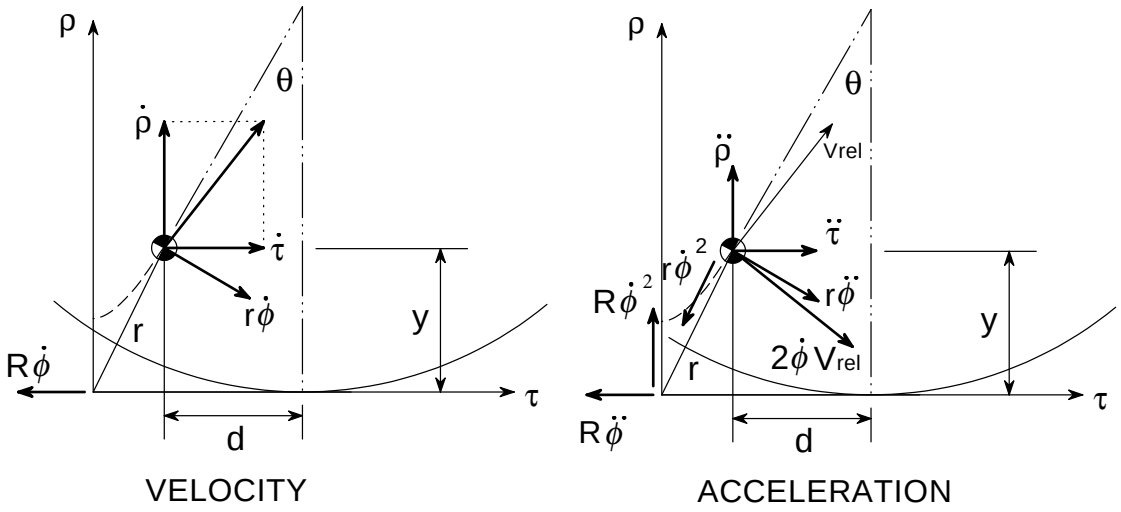

Figure A.3: Kinematics of the rolling profile design concept

The radial coordinate ρ is equal to the dimension y. According to Equation (3.4) on page 60, y is defined in terms of the specified relationship between d and θ:

$$\frac{\partial y}{\partial \theta} = d(\theta) \tag{A.24}$$

giving:

$$y = \rho = \int d\,\mathrm{d}\theta + y_0 \tag{A.25}$$

The τ coordinate is found by assuming no-slip rolling contact. Then τ is the arc length from the initial contact point to the current contact point minus the offset d. Labelling the arc length coordinate between the initial position ($\theta = 0$) and the contact point corresponding to pitch angle θ as s:

$$\tau = s - d \tag{A.26}$$

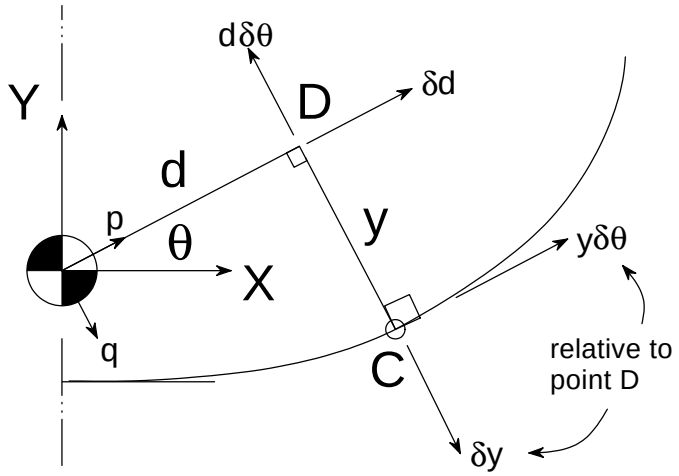

Figure A.4: Rolling profile coordinate system, showing the infinitesimal displacements of a point C at (d, y, θ) in terms of infinitesimal changes in the coordinates.

Figure A.4 shows the infinitesimal displacements of a point C in terms of infinitesimal changes in the coordinates d, y and θ. It can be seen that:

$$\delta s = \delta d + y\,\delta\theta \tag{A.27}$$

Accordingly,

$$\begin{aligned} s &= \int_0^\theta \left(\frac{\mathrm{d}d}{\mathrm{d}\Theta} + y \frac{\mathrm{d}\Theta}{\mathrm{d}\Theta} \right) \mathrm{d}\Theta \\ &= d + \int_0^\theta y \, \mathrm{d}\Theta \end{aligned} \tag{A.28}$$

From Equations (A.26) and (A.28),

$$\tau = \int_0^\theta y \, \mathrm{d}\Theta \tag{A.29}$$

The relative velocities are then obtained by differentiation. From Equation(A.29):

$$\dot{\tau} = \frac{\mathrm{d}\tau}{\mathrm{d}\theta} \frac{\mathrm{d}\theta}{\mathrm{d}t} = y\dot{\theta} \tag{A.30}$$

and from Equation (A.25):

$$\dot{\rho} = \frac{\mathrm{d}\rho}{\mathrm{d}\theta} \frac{\mathrm{d}\theta}{\mathrm{d}t} = d\dot{\theta} \tag{A.31}$$

Differentiating again to obtain accelerations:

$$\begin{aligned} \ddot{\tau} &= \frac{\mathrm{d}^2\tau}{\mathrm{d}\theta^2} \dot{\theta}^2 + \frac{\mathrm{d}\tau}{\mathrm{d}\theta} \ddot{\theta} \\ &= d\,\dot{\theta}^2 + y\,\ddot{\theta} \end{aligned} \tag{A.32}$$

and

$$\begin{aligned} \ddot{\rho} &= \frac{\mathrm{d}^2\rho}{\mathrm{d}\theta^2} \dot{\theta}^2 + \frac{\mathrm{d}\rho}{\mathrm{d}\theta} \ddot{\theta} \\ &= \frac{\mathrm{d}d}{\mathrm{d}\theta} \dot{\theta}^2 + d\,\ddot{\theta} \end{aligned} \tag{A.33}$$

For the single-degree-of-freedom treatment used in the momentum model, the pitching acceleration is found for the instantaneous values of the pitch and pitching velocity θ and $\dot{\theta}$ and the turbine speed and acceleration $\dot{\phi}$ and $\ddot{\phi}$. It may be verified using Figure A.3 that

$$\ddot{\theta} = \frac{\sum M - [I - m\{\tau d + \rho(R-\rho)\}]\,\ddot{\phi} - mA}{I + m(d^2+\rho^2)} \tag{A.34}$$

where

$$\begin{aligned} \sum M &= M + F_\rho d + F_\tau \rho \\ A &= \left[d(\rho + \frac{\mathrm{d}d}{\mathrm{d}\theta})\dot{\theta}^2 - \{\tau\rho - d(R-\rho)\}\dot{\phi}^2 \right] \end{aligned}$$

As in Section A.1, M is the external moment about the mass centre. F_ρ and F_τ are the radial and tangential components of the external aerodynamic force on the blade.

In this case, Equations (A.1) and (A.2) become:

$$\dot{X} = (-\rho\cos\phi - d\sin\phi)\,\dot{\theta} + ((R-\rho)\cos\phi + \tau\sin\phi)\,\dot{\phi} \tag{A.35}$$

$$\dot{Y} = (\rho\sin\phi - d\cos\phi)\,\dot{\theta} + ((\rho-R)\sin\phi + \tau\cos\phi)\,\dot{\phi} \tag{A.36}$$

Equations (A.4) and (A.5) become:

$$\begin{aligned} \ddot{X} &= \{(R-\rho)\ddot{\phi} - (d\dot{\theta}^2 + \rho\ddot{\theta}) - 2d\dot{\theta}\dot{\phi} - \tau\dot{\phi}^2\}\cos\phi \\ &\quad + \{\tau\ddot{\phi} - (\frac{\mathrm{d}d}{\mathrm{d}\theta}\,\dot{\theta}^2 + d\ddot{\theta}) + 2\dot{\tau}\dot{\phi} - (R-\rho)\dot{\phi}^2\}\sin\phi \qquad \text{(A.37)} \\ \ddot{Y} &= \{\tau\ddot{\phi} - (\frac{\mathrm{d}d}{\mathrm{d}\theta}\,\dot{\theta}^2 + d\ddot{\theta}) + 2\dot{\tau}\dot{\phi} - (R-\rho)\dot{\phi}^2\}\cos\phi \\ &\quad - \{(R-\rho)\ddot{\phi} - (d\dot{\theta}^2 + \rho\ddot{\theta}) - 2d\dot{\theta}\dot{\phi} - \tau\dot{\phi}^2\}\sin\phi \qquad \text{(A.38)} \end{aligned}$$

In order to extract the acceleration coefficients used by Paul (1979), Equations (A.37) and(A.38) need to be reformulated to extract terms proportional to the generalised coordinate accelerations:

$$\begin{aligned}
\ddot{X} &= (-\rho\cos\phi - d\sin\phi)\,\ddot{\theta} + ((R-\rho)\cos\phi + \tau\sin\phi)\,\ddot{\phi} \\
&\quad + (-d\cos\phi - \frac{\mathrm{d}d}{\mathrm{d}\theta}\sin\phi)\,\dot{\theta}^2 + (-2d\cos\phi + 2\rho\sin\phi)\,\dot{\phi}\dot{\theta} \\
&\quad + \{(\rho - R)\sin\phi + \tau\cos\phi\}\,\dot{\phi}^2 \qquad \text{(A.39)} \\
\ddot{Y} &= (\rho\sin\phi - d\cos\phi)\,\ddot{\theta} + ((\rho - R)\sin\phi + \tau\cos\phi)\,\ddot{\phi} \\
&\quad + (d\sin\phi - \frac{\mathrm{d}d}{\mathrm{d}\theta}\cos\phi)\,\dot{\theta}^2 + (2d\sin\phi + 2\rho\cos\phi)\,\dot{\phi}\dot{\theta} \\
&\quad + \{(\rho - R)\cos\phi - \tau\sin\phi\}\,\dot{\phi}^2 \qquad \text{(A.40)}
\end{aligned}$$

The non-zero velocity coefficients for blade i are then:

$$\begin{aligned}
U_{i0} &= (R-\rho)\cos\phi + \tau\sin\phi \\
U_{ii} &= -\rho\cos\phi - d\sin\phi \\
V_{i0} &= (\rho - R)\sin\phi + \tau\cos\phi \\
V_{ii} &= \rho\sin\phi - d\cos\phi \qquad \text{(A.41)}
\end{aligned}$$

Equations (A.39) and (A.40) can then be seen to be:

$$\begin{aligned}
\ddot{X} &= U_{ii}\,\ddot{\theta} + U_{i0}\,\ddot{\phi} + U' \\
\ddot{Y} &= V_{ii}\,\ddot{\theta} + V_{i0}\,\ddot{\phi} + V' \qquad \text{(A.42)}
\end{aligned}$$

where the acceleration coefficients are:

$$\begin{aligned} U' &= (-d\cos\phi - \frac{\mathrm{d}d}{\mathrm{d}\theta}\sin\phi)\,\dot{\theta}^2 + (-2d\cos\phi + 2\rho\sin\phi)\,\dot{\phi}\dot{\theta} \\ &\quad + \{(\rho - R)\sin\phi + \tau\cos\phi\}\,\dot{\phi}^2 \\ V' &= (d\sin\phi - \frac{\mathrm{d}d}{\mathrm{d}\theta}\cos\phi)\,\dot{\theta}^2 + (2d\sin\phi + 2\rho\cos\phi)\,\dot{\phi}\dot{\theta} \\ &\quad + \{(\rho - R)\cos\phi - \tau\sin\phi\}\,\dot{\phi}^2 \end{aligned} \tag{A.43}$$

If the specified relationship between d and θ is analytic, differentiable and integrable, then the positions, velocities and accelerations derived above may be found analytically.

For example, for a simple circular profile or radius R_p and centre of gravity located at radius R_{cg} from the centre of curvature, $d = R_{cg}\sin\theta$ and $y = R_p - R_{cg}\cos\theta$. We then get:

$$\begin{aligned} \tau &= \int_0^\theta y\ \mathrm{d}\Theta = R_p\theta - q\sin\theta \\ \rho &= y = R_p - R_{cg}\cos\theta \\ \dot{\tau} &= y\dot{\theta} = (R_p - R_{cg}\cos\theta)\dot{\theta} \\ \dot{\rho} &= d\dot{\theta} = (R_{cg}\sin\theta)\dot{\theta} \\ \ddot{\tau} &= d\,\dot{\theta}^2 + y\,\ddot{\theta} = (R_{cg}\sin\theta)\dot{\theta}^2 + R_p - (R_{cg}\cos\theta)\ddot{\theta} \\ \ddot{\rho} &= \frac{\mathrm{d}d}{\mathrm{d}\theta}\,\dot{\theta}^2 + d\,\ddot{\theta} = (R_{cg}\cos\theta)\dot{\theta}^2 + (R_{cg}\sin\theta)\ddot{\theta} \end{aligned}$$

If d is not defined analytically, then the above quantities must be determined numerically. Note that it may be defined in a piecewise analytical fashion also.

Equation A.34, giving the pitching acceleration for known position, velocity and rotor acceleration, becomes

$$\ddot{\theta} = \frac{\sum M - \left[I - m\{RR_p - R_{cg}^2 - R_p^2 + R_p\theta R_{cg}\sin\theta - (R-2R_p)R_{cg}\cos\theta\}\right]\ddot{\phi} - mA}{I + m(R_{cg}^2 + R_p^2 - 2RR_{cg}\cos\theta)} \tag{A.44}$$

where

$$\begin{aligned} \sum M &= M + F_\rho(R_{cg}\sin\theta) + F_\tau(R_p - R_{cg}\cos\theta) \\ A &= \left[(R_pR_{cg}\sin\theta)\dot{\theta}^2 - \{R_p^2\theta - R_p\theta R_{cg}\cos\theta - RR_{cg}\sin\theta\}\dot{\phi}^2\right] \end{aligned}$$

Note that if R_p is set to zero, the situation reverts to that for a pendulum of length R_{cg}. It may be checked that Equation A.44 reverts to Equation A.14.

A.3 Kinematics of the Kirke-Lazuaskas Design

In the Kirke-Lazauskas design (Kirke and Lazauskas, 1992; Kirke, 1998), a separate stabiliser mass that is free to slide radially along the support arm provides the restoring moment. Unlike other designs, the magnitude of the restoring moment is independent of the pitch angle, and depends only on the offset between pivot axis and the point of contact between stabiliser mass and blade (labelled a_f and a_r in Figure A.5. The design allows the restoring moment to be different for positive and negative pitch angles.

Referring to Figure A.6, the restoring moment M_r is given by

$$\begin{aligned} M_r &= m_s\{\ddot{\rho} + (R-\rho)\dot{\phi}^2\}\ a_f \qquad \text{for} \quad \theta > 0 \\ &= -m_s\{\ddot{\rho} + (R-\rho)\dot{\phi}^2\}\ a_r \qquad \text{for} \quad \theta < 0 \end{aligned} \tag{A.45}$$

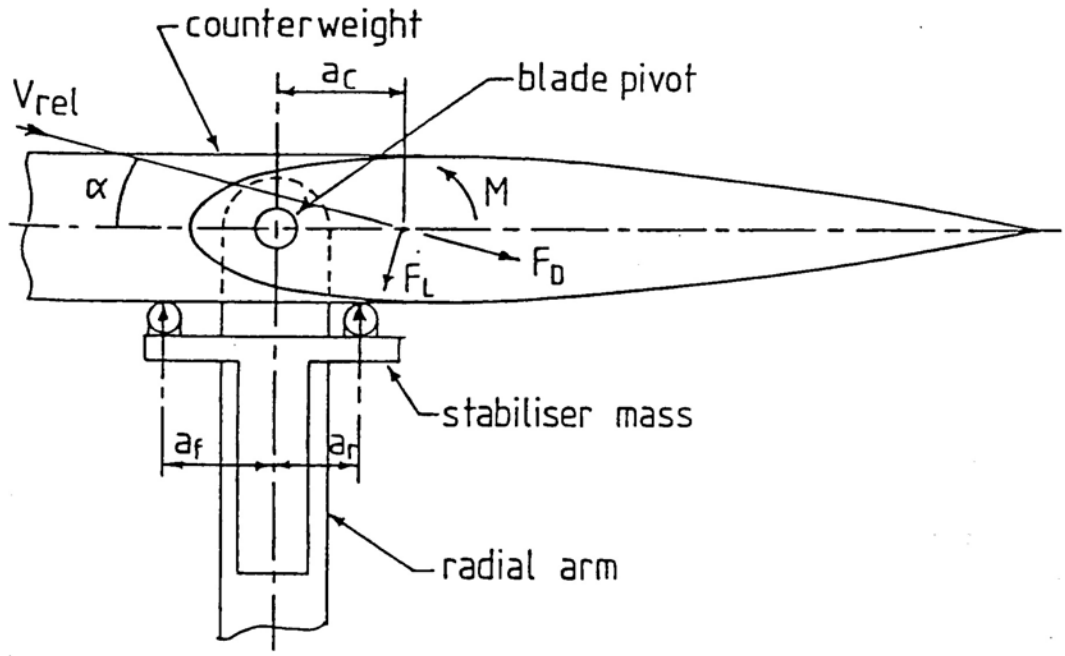

Figure A.5: Key parameters of the Kirke-Lazauskas design (reproduced from Kirke, 1998)

where m_s is the mass of the stabiliser, R is the turbine radius and ρ is the radial offset of the stabiliser centre of mass from the ρ-τ coordinate system at radius R.

Noting that

$$\begin{aligned} \rho &= a_f \tan\theta \qquad \text{for} \quad \theta > 0 \\ &= -a_r \tan\theta \qquad \text{for} \quad \theta < 0 \end{aligned} \tag{A.46}$$

$$\begin{aligned} \dot{\rho} &= a_f \sec^2\theta \qquad \text{for} \quad \theta > 0 \\ &= -a_r \sec^2\theta \qquad \text{for} \quad \theta < 0 \end{aligned} \tag{A.47}$$

$$\begin{aligned} \ddot{\rho} &= a_f \sec^2\theta(2\tan\theta\,\dot{\theta}^2 + \ddot{\theta}) \qquad \text{for} \quad \theta > 0 \\ &= -a_r \sec^2\theta(2\tan\theta\,\dot{\theta}^2 + \ddot{\theta}) \qquad \text{for} \quad \theta < 0 \end{aligned} \tag{A.48}$$

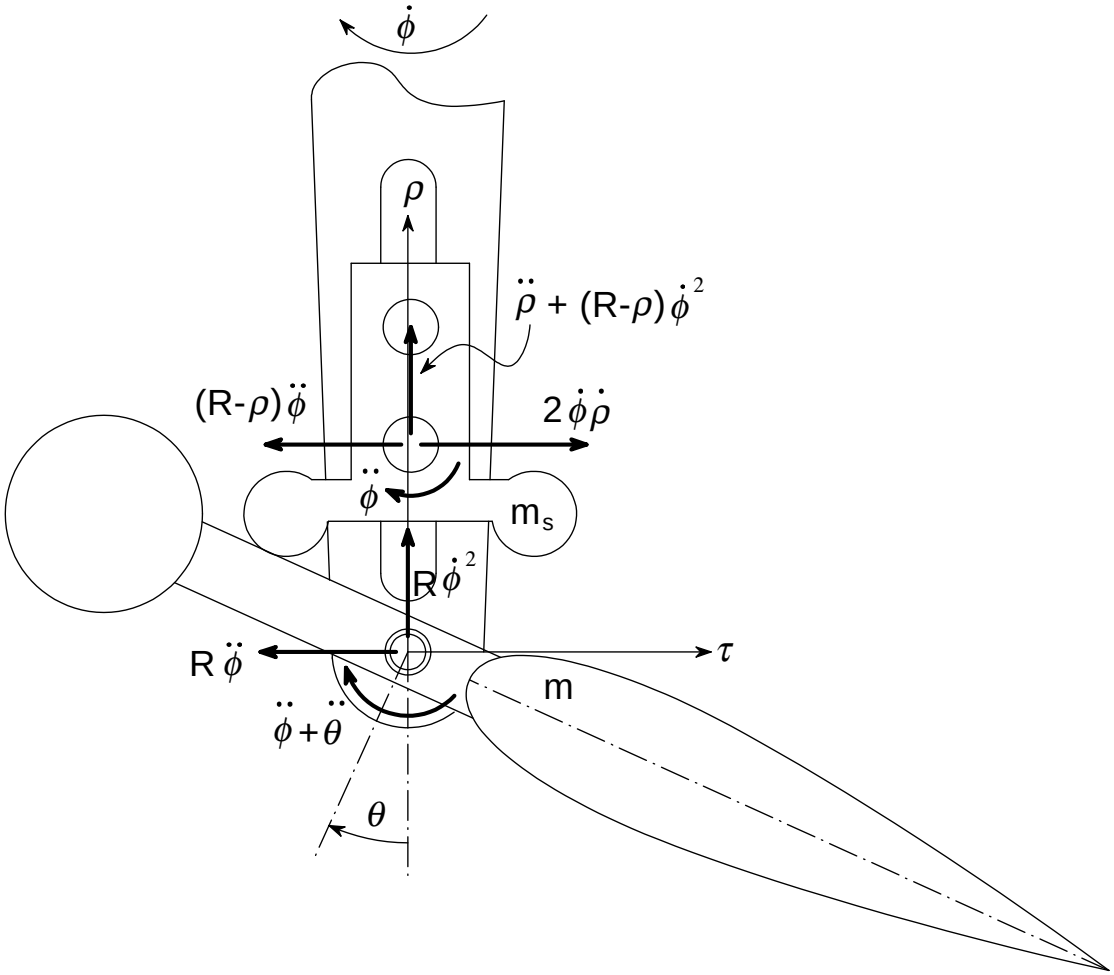

Figure A.6: Acceleration components of the blade and stabiliser mass for the Kirke-Lazauskas design (Kirke, 1998)

Equation (A.49) becomes

$$\begin{aligned} M_r &= m_s\{a_f \sec^2\theta(2\tan(\theta)\,\dot{\theta}^2 + \ddot{\theta}) + (R - a_f\tan\theta)\dot{\phi}^2\}\; a_f \;\text{ for } \theta > 0 \\ &= -m_s\{-a_r \sec^2\theta(2\tan(\theta)\,\dot{\theta}^2 + \ddot{\theta}) + (R + a_r\tan\theta)\dot{\phi}^2\}\; a_r \;\text{ for } \theta < 0 \end{aligned} \tag{A.49}$$

Using d'Alembert's principle, the pitching acceleration is found to be:

$$\ddot{\theta} = \frac{\sum M - M_r - \ddot{\phi}}{I}$$

which becomes:

$$\begin{aligned}\ddot{\theta} &= \frac{\sum M - m_s\{a_f \sec^2\theta(2\tan(\theta)\,\dot{\theta}^2) + (R - a_f\tan\theta)\dot{\phi}^2\}\; a_f - \ddot{\phi}}{I + m_s(a_f\sec\theta)^2} \quad \text{for } \theta > 0 \\ &= \frac{\sum M + m_s\{-a_r \sec^2\theta(2\tan(\theta)\,\dot{\theta}^2) + (R + a_r\tan\theta)\dot{\phi}^2\}\; a_r - \ddot{\phi}}{I + m_s(a_r\sec\theta)^2} \quad \text{for } \theta < 0\end{aligned} \tag{A.50}$$

where $\sum M$ is the total aerodynamic moment about the pivot axis and I is the polar mass moment of inertia about the pivot axis.

Note that there is a step change in the restoring moment across $\theta = 0$. When $\theta = 0$, the restoring moment may vary to match the disturbing aerodynamic moment up to a magnitude equal to that given by Equation A.49.

It is very difficult to properly model the motion of the blade pitching through $\theta = 0$. Because the stabilising mass is asked to change directions instantaneously, the real force will be determined by the compressibility and damping of the contact regions. This complexity is neglected in the present analysis.

It should also be noted that the radial movement of the stabiliser mass results in inertial moment and tangential reactions on the rotor. From Figure A.6 it may be seen that the tangential reaction, decelerating the rotor, is given by:

$$\begin{aligned}R_\tau &= m_s\{(R-\rho)\ddot{\phi} - 2\dot{\phi}\dot{\rho}\} \\ &= m_s\{(R - a_f\tan\theta)\ddot{\phi} - 2\dot{\phi}\dot{\theta}a_f\sec^2\theta\} \quad \text{for } \theta > 0 \\ &= m_s\{(R + a_r\tan\theta)\ddot{\phi} + 2\dot{\phi}\dot{\theta}a_r\sec^2\theta\} \quad \text{for } \theta < 0\end{aligned}$$

The inertial moment reaction, also decelerating the rotor, is:

$$\begin{aligned} M_{reac} &= I_s\ddot{\phi} - m_s\{a_f \sec^2\theta(2\tan(\theta)\,\dot{\theta}^2 + \ddot{\theta}) + (R - a_f\tan\theta)\dot{\phi}^2\} \quad \text{for } \theta > 0 \\ &= I_s\ddot{\phi} + m_s\{-a_r \sec^2\theta(2\tan(\theta)\,\dot{\theta}^2 + \ddot{\theta}) + (R + a_r\tan\theta)\dot{\phi}^2\} \quad \text{for } \theta < 0 \end{aligned} \tag{A.51}$$

These reactions affect the instantaneous turbine torque, just as inertial reactions affect the torque for the pendulum and rolling contact designs.

A.4 Comparison of Blade Responsiveness for Different Designs

The three designs analysed above all rely on inertial forces to produce the restoring moment on the blade. For the same blade and counterweight, each design results in a different 'effective moment of inertia' for the blade assembly, resulting in different dynamic response to aerodynamic driving forces.

Compare the expressions for the pitching acceleration given a values of external driving moment, blade position and velocity and turbine velocity and acceleration, for the three designs:

$$\ddot{\theta} = \frac{F_t R_{cg} + M - R_{cg}\sin\theta m R\ \dot{\phi}^2 - \{(I + mR_{cg}^2) + mR_{cg}R\cos\theta\}\ \ddot{\phi}}{I + mR_{cg}^2}$$

for the pendulum type (A.14)

$$\ddot{\theta} = \frac{\sum M - [I - m\{\tau d + \rho(R - \rho)\}]\,\ddot{\phi} - mA}{I + m(d^2 + \rho^2)}$$

for the rolling profile (A.34)

$$\ddot{\theta} = \frac{\sum M - m_s\{a_f \sec^2\theta(2\tan(\theta)\,\dot{\theta}^2) + (R - a_f\tan\theta)\dot{\phi}^2\}\ a_f - \ddot{\phi}}{I + m_s(a_f\sec\theta)^2} \quad \text{for } \theta > 0$$

for the Kirke-Lazauskas design (A.50)

The denominators of the three expressions may be regarded as the effective mass moments of inertia for the three designs. The pendulum type is simply the moment of inertia about the pivot axis using the translation of axes theorem.

For the rolling profile, the relevant moment of inertia is that about the contact point. The moment of inertia therefore changes with the pitch angle, and is minimum at zero.

For the Kirke-Lazauskas design, the effective moment of inertia also changes with pitch angle, and may be seen to be that equivalent to lumping the stabiliser mass at the contact point.

Appendix B

Dynamic Stall Models

Details of the Boeing-Vertol dynamic stall method, including modifications suggested by Cardona (1984), and the MIT model as modified by Noll and Ham (1982) are given below.

B.1 Boeing-Vertol (Gormont) Dynamic Stall Model

The Boeing-Vertol method is not a full unsteady aerodynamics model as it does not modify the aerodynamic forces on an aerofoil pitching at angles below static stall. It models the delayed stall and increased lift observed in pitching aerofoil experiments. Delayed stall is handled by using static lift, drag and moment coefficient look-up tables with a modified angle of attack. The empirical angle of attack modification is derived from wind tunnel data on oscillating aerofoils. The modified angle of attack is a function of the square root of a dimensionless pitch rate parameter:

$$\alpha_m = \alpha_B - \gamma K_1 \left(\frac{c\dot{\alpha}_B}{2W} \right)^{1/2} \text{sign}(\dot{\alpha}_B) \tag{B.1}$$

where α_m is the modified angle, α_B is the geometric angle of attack, c is the blade chord, W is the relative flow velocity.

The drag and moment coefficients based on this modified angle of attack are found directly from the static look-up table, while the lift coefficient is increased

by a factor proportional to the angle of attack modification:

$$\begin{aligned} C_L &= C_L(\alpha_m)\left(\frac{\alpha_m}{\alpha_B - \alpha_0}\right) \\ C_D &= C_D(\alpha_m) \\ C_M &= C_M(\alpha_m) \end{aligned} \tag{B.2}$$

where α_0 is the angle of attack at which lift is zero (0° for a symmetrical section).

The gamma functions are also empirically derived and are functions of the blade thickness to chord ratio.

$$\begin{aligned} \gamma_L &= 1.4 - 6\left(0.06 - \frac{t}{c}\right) \\ \gamma_D &= 1 - 2.5\left(0.06 - \frac{t}{c}\right) \\ \gamma_M &= \gamma_D \end{aligned} \tag{B.3}$$

K_1 changes with the sign of the rate of change of angle of attack and is specified as 1.0 when a is increasing in magnitude and 0.5 when it is decreasing in magnitude.

Paraschivoiu and Allet (1988) state that the model is especially applicable to thin aerofoils (t/c $< 12\%$) and is not suited to deep stall ($\alpha > \alpha_{\text{static stall}} + 5°$).

Strickland et al. (1981) applied the model when the angle of attack exceeds the static stall angle or when the angle is decreasing having been above stall. This models the hysteresis observed oscillating aerofoil experiments.

B.2 MIT Dynamic Stall Model

The MIT dynamic stall model similarly does not deal with dynamic effects in the attached flow case, only with the delay of stall under dynamic conditions. In the

version modified by Noll and Ham (1982) the angle at which dynamic stall occurs is found using the Boeing-Vertol empirical relation:

$$\alpha_{DS} = \alpha_{SS} + \gamma \left| \frac{c\dot{\alpha}}{2W} \right|^{1/2} \tag{B.4}$$

Noll and Ham show the experimentally derived value of γ for a NACA0012 aerofoil as being 1.6 radians. While the geometric angle of attack is less than the static stall angle, the static coefficients are used for lift, drag and pitching moment.

If the angle of attack exceeds the static stall angle but is still less than the dynamic stall angle, the drag and moment coefficients are selected from the static coefficient look-up tables, while the lift is estimated by

$$C_L = a_s \sin \alpha \tag{B.5}$$

where a_s is the lift curve slope at static stall. This allows the lift to continue to increase, while the drag and moment increase as for static stall.

When the geometric angle of attack reaches the dynamic stall angle the dynamic stall vortex is assumed to be released from the leading edge. It then convects rearward over the upper surface of the aerofoil, continuing to build in strength as it does. Consequently the lift continues to increase and the centre of pressure moves aft, contributing to nose-down pitching moment. The maximum lift and moment coefficients are calculated based on an instantaneous pitch rate parameter

from an empirically derived relation:

$$\begin{aligned} C_{Lmax} &= 1.0 + 40.0\left|\frac{c\dot{\alpha}}{W}\right| \quad \text{if} \quad 0 \leq \left|\frac{c\dot{\alpha}}{W}\right| \leq 0.05 \\ &= 3.0 \quad \text{otherwise} \end{aligned} \tag{B.6}$$

$$\begin{aligned} C_{Mmax} &= -0.15 \quad \text{if} \quad 0 \leq \left|\frac{c\dot{\alpha}}{W}\right| \leq 0.02 \\ &= -0.15 - 21.0\left(\left|\frac{c\dot{\alpha}}{W}\right| - 0.02\right) \quad \text{if} \quad 0.02 < \left|\frac{c\dot{\alpha}}{W}\right| \leq 0.05 \\ &= -0.78 \quad \text{otherwise} \end{aligned} \tag{B.7}$$

The lift coefficient continues to be calculated from Equation B.5 until it reaches the maximum value. It is assumed that the maximum lift occurs when the dynamic stall vortex reaches the midchord, while the maximum pitching moment occurs when it reaches the 3/4 chord position. Pitching moment about the quarter chord in this region is calculated on the basis of the position of the centre of pressure.

$$C_M = -C_N(X_{CP} - 0.25) \tag{B.8}$$

where X_{CP} is the distance (in chords) of the centre of pressure from the leading edge. The rearward velocity of the centre of pressure is assumed to be constant, and the position, prior to reaching C_{Lmax}, is given by:

$$X_{CP} = (t - t_{DS})\frac{V}{4c} + 0.25 \tag{B.9}$$

and subsequent to reaching C_{Lmax} by:

$$X_{CP} = (t - t_L)(0.75 - X_{CPL})\frac{2V}{c} + X_{CPL} \tag{B.10}$$

Once the lift and moment coefficients reach their pre-determined maximum values, according to the MIT model they are held at this level until the peak angle of attack is reached. Only after this point do the lift and moment begin to decay exponentially back to the static stall values.

$$C_L = (C_{Lmax} - C_{LSS})e^{-(\psi-\psi_0)2R/c} + C_{LSS} \quad \text{(B.11)}$$

$$C_M = (C_{Mmax} - C_{MSS})e^{-(\psi-\psi_0)2R/2.5c} + C_{MSS} \quad \text{(B.12)}$$

where time has been expressed in terms of the azimuth angle specifically for Darrieus turbines. ψ is the current azimuth and ψ_0 is the azimuth at the start of decay.

This part of the model is problematic. Derived from oscillating aerofoil wind tunnel test data and developed for helicopter applications, it is not suitable for studying the low speed performance Darrieus turbines in this form. At low tip speed ratios the amplitude of the angle of attack oscillations may be very large (up to 90°) and it is not plausible that this peak lift and moment would be maintained for so long after the inception of dynamic stall. Worse, at tips speed ratios less than one, the angle of attack does not oscillate but continuously decreases, the relative wind orbiting the blade with each revolution of the rotor.

Thus some alternative criterion is required for the commencement of the decay of lift. The passage of the dynamic stall vortex beyond the trailing edge of the aerofoil would seem to be a reasonable criterion, as this is used in the indicial Beddoes-Leishman model. Since it has already been assumed that the velocity of the vortex is constant and that the maximum lift occurs when it reaches the midchord, the time of arrival at the trailing edge is simply twice the time after

the start of dynamic stall to the attainment of maximum lift. At this point decay begins, whether or not the peak angle of attack has been reached.

The decay of lift and moment coefficients towards the static stall values is also not compatible with a monotonic increase in the magnitude of angle of attack. Accordingly, the coefficients are made to decay towards the static value at the current angle of attack. That is:

$$C_L = [C_{Lmax} - C_{Lstatic}(\alpha)]\ e^{-(\psi-\psi_0)2R/c} + C_{Lstatic}(\alpha) \quad \text{(B.13)}$$

$$C_M = [C_{Mmax} - C_{Mstatic}(\alpha)]\ e^{-(\psi-\psi_0)2R/2.5c} + C_{Mstatic}(\alpha) \quad \text{(B.14)}$$

In this way, as the blade continues into deep stall, the lift and moment coefficients approach the static values at high angles of attack, effectively 'turning off' the dynamic stall model.

If angle of attack starts to decrease before peak lift is attained, decay begins immediately from the currently attained lift and moment values.

The exponential decay continues until the angle of attack drops to below the static stall angle once more and attached flow is assumed to resume. Paraschivoiu and Allet (1988) claim that the MIT model fails to predict the delayed reattachment of flow, to angles well below static stall, that is observed in experiments.

Above the dynamic stall angle and during the exponential decay of coefficients, Noll and Ham calculate the drag by

$$C_D = C_L \tan\alpha \quad \text{(B.15)}$$

The problem with this relation is that while it produces plausible values for the drag coefficient, for a blade at zero-pitch on a Darrieus turbine, the tangential

component of the aerodynamic force is identically zero. This is not in agreement with experimental results (for example Strickland et al. (1981) and Paraschivoiu (1983) - refer to Section 6.4).

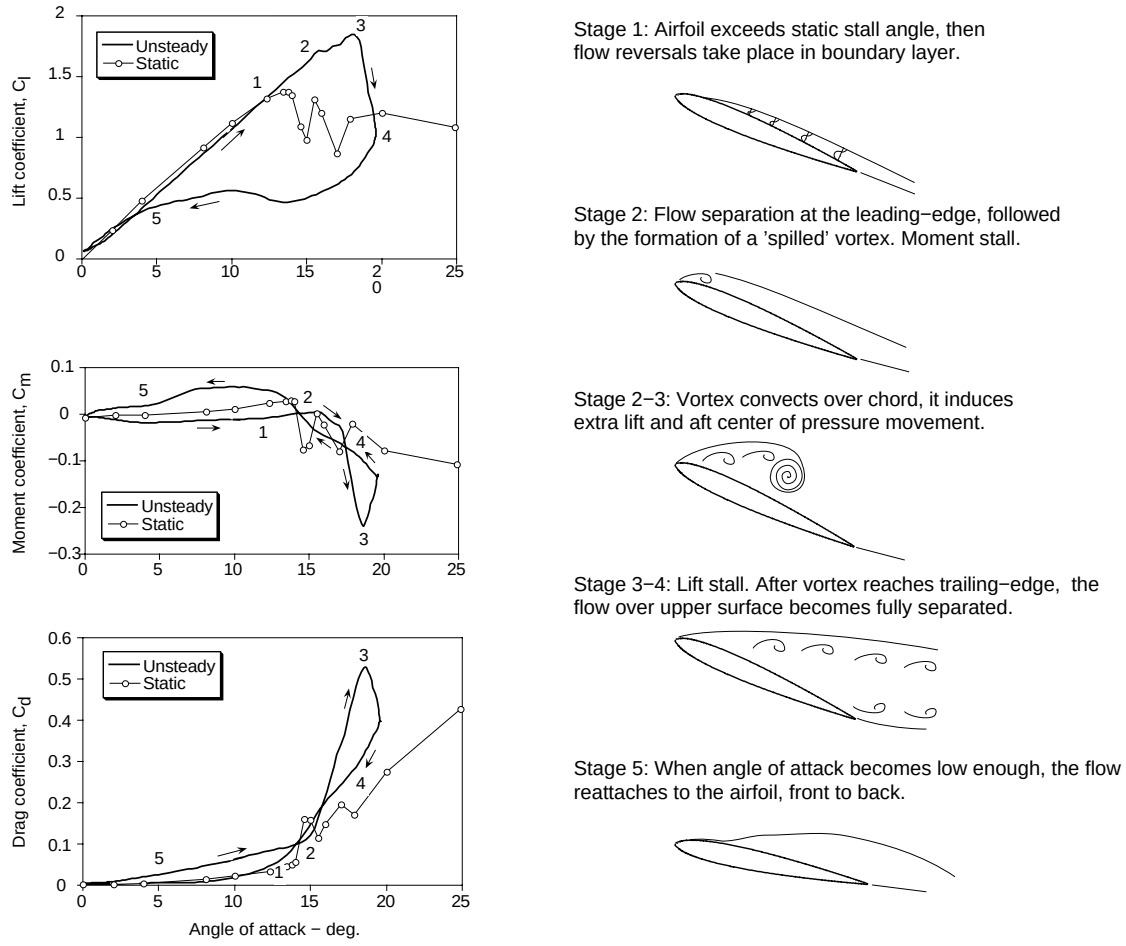

Figure B.1: Schematic showing the features of the dynamic stall process. Reproduced from Leishman (2002)

Referring to the characterisation of the dynamic stall process given by Leishman (2002) (see Figure B.1), the drag coefficient increases rapidly under dynamic conditions as the angle of attack increases beyond the static stall angle and the linear region of the lift curve is extended. The peak drag coefficient and peak lift occur close to the peak angle of attack for an oscillating aerofoil, before both coefficients drop rapidly, in the region governed by the exponential decay in the

MIT model. These features are confirmed by the experimental work of Laneville and Vittecoq (1986) and of Lorber and Carta (1988).

Instead of using Equation B.15 therefore, the drag for the period after the dynamic stall angle (determined from Equation B.4) is reached but before lift coefficient decay begins is calculated here by:

$$C_D = C_D(\alpha)|\alpha/\alpha_{DS}| \tag{B.16}$$

The normal static increase in drag associated with angles of attack above static stall is exaggerated by scaling the static coefficient by the ratio of the current angle to the angle at which dynamic stall began.

Once the decay of the lift coefficient begins, the drag coefficient is linked to the lift coefficient using the expression:

$$C_D = C_{D\,static}(\alpha)|C_L/C_{L\,static}(\alpha)| \tag{B.17}$$

C_L is calculated using Equation B.11. The drag coefficient is thus naturally linked to the decay time constant for the lift coefficient and decays with it towards the static value at the current angle of attack.

While the above modifications to the MIT method are to some extent arbitrary in their specific form, they are consistent with the documented features of dynamic stall and address aspects of the model that are clearly inappropriate for application to the starting behaviour of Darrieus turbines. The modifications were settled on because they provided the best agreement with available experimental data on Darrieus blade forces. Validation against this data is discussed in Section 6.4.

Appendix C

Calculation of the prototype turbine drag coefficient

Calculations of the torque lost to bearing and brake friction and parasitic aerodynamic drag for the prototype turbine are presented.

Drag losses were estimated by measuring the decay of turbine speed in still air. As no motor was provided to accelerate the turbine, these measurements had to be conducted at the end of wind tunnel test runs by reducing the wind speed to zero and allowing the turbine to coast to rest. Data from five separate runs is shown in Figure C.1.

The total torque decelerating the turbine was estimated by calculating the deceleration by numerical differentiation. To reduce scatter in the results, the data was thinned, taking speed values every 5 seconds. A cubic spline was fitted through the values and the slopes at the data points used as the acceleration values. The acceleration was multiplied by the total moment of inertia of the turbine to give the torque. Torque is plotted as a function of speed for these five runs in Figure C.2.

A curve was then fitted through the torque-speed data. The curve fitting was function was chosen to be of the form

$$T = A\omega^2 + B \tag{C.1}$$

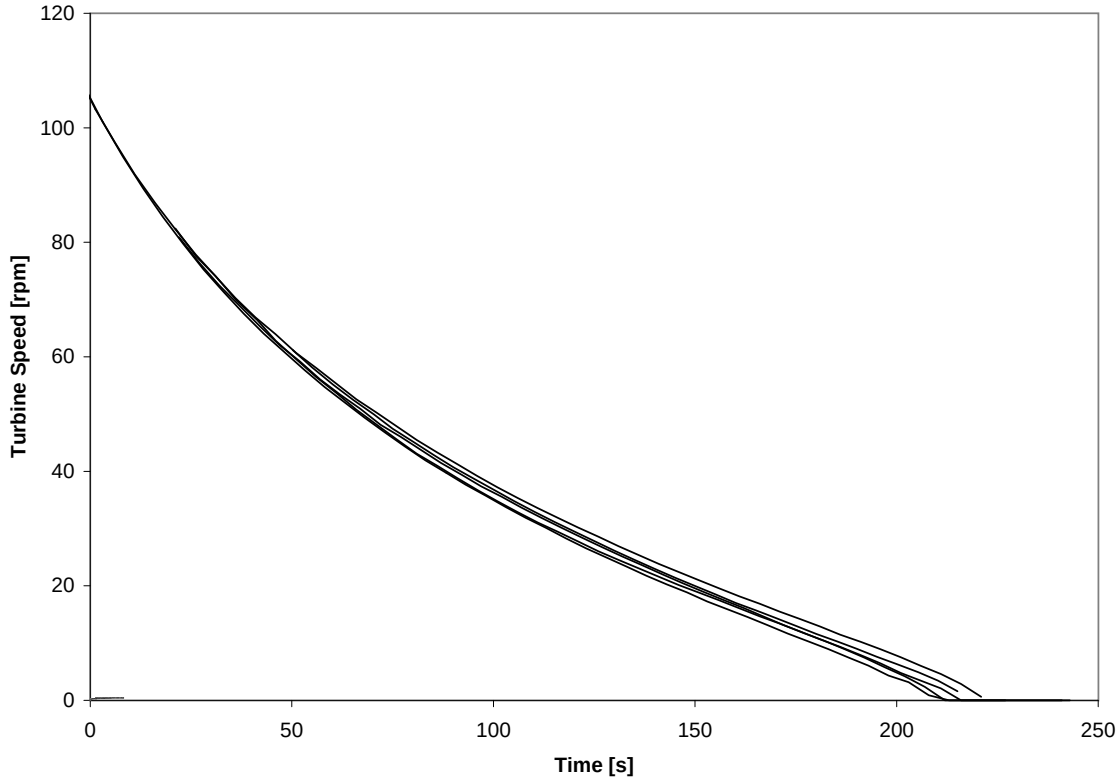

Figure C.1: Measured still air speed decay for five runs.

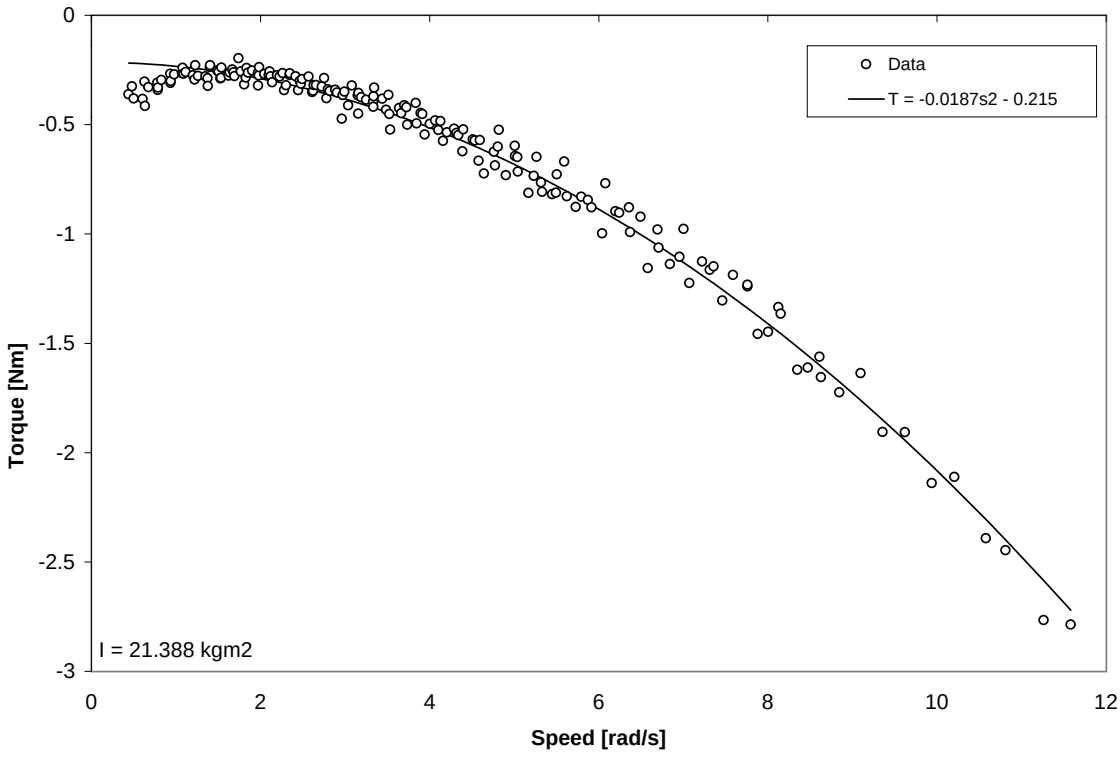

Figure C.2: Torque found by numerical differentiation.

This assumes that the total resistance is composed of aerodynamic drag, which is assumed proportional to the square of the turbine speed, and dry friction, which is independent of speed. The values of A and B for this data were found to be 0.0187 and 0.215 respectively. The curve provides a good fit to the data, except for speeds below approximately 1 rad/s, where the drag appears to increase slightly.

This measured drag includes that from the blades themselves, as well as the non-working parts of the turbine. For application to the mathematical models, the drag contributed by the blades was subtracted from the total, as this component is accounted for by the blade section drag coefficient data.

The still air drag due to the blades alone was calculated as:

$$T_{blades} = N_b \, \frac{1}{2} \, C_{d0} \, \rho \, L \, c \, R \, (R\omega)^2 \tag{C.2}$$

where N_b is the number of blades, C_{d0} is the zero incidence drag coefficient, ρ is the air density, L is the length of the blades, c is the blade chord, R is the turbine radius and ω is the turbine speed.

The blade drag coefficient is defined as:

$$\begin{aligned} A_{blades} &= T_{blade}/\omega^2 \\ &= N_b \, \frac{1}{2} \, C_{d0} \, \rho \, L \, c \, R^3 \\ &= 3 \text{ x } 0.5 \text{ x } 0.02 \text{ x } 1.2 \text{ x } 1.3 \text{ x } 0.15 \text{ x } 0.87^3 \\ &= 0.0046 \end{aligned} \tag{C.3}$$

This coefficient is subtracted from the total aerodynamic drag coefficient measured for the turbine above. In the momentum and vortex mathematical models,

a retarding torque calculated by

$$\begin{aligned} T_{drag} &= (A - A_{blades})\,\omega^2 + B \\ &= (0.0187 - 0.0046)\,\omega^2 + 0.215 \\ &= 0.0141\,\omega^2 + 0.215 \quad \text{Nm} \end{aligned} \tag{C.4}$$

is subtracted from the raw torque at turbine speed ω rad/s.

Appendix D

Aerofoil aerodynamic data

The following data was used for the NACA0018 profile used in the mathematical models. It was still available as at 3/10/2002 online at http://www.maths.adelaide.edu.au/Applied/llazausk/aero/foil/foil.htm. Lift and drag coefficient data is plotted in Figure D.1.

```
------------------------------------------------------------------------
AIRFOIL: NACA 0018
DATA: Lift Coefficients
------------------------------------------------------------------------
ORIGINAL SOURCE: Sheldahl, R. E. and Klimas, P. C., Aerodynamic
Characteristics of Seven Airfoil Sections Through
180 Degrees Angle of Attack for Use in Aerodynamic
Analysis of Vertical Axis Wind Turbines, SAND80-2114,
March 1981, Sandia National Laboratories, Albuquerque,
New Mexico.

NOTES: The data herein were synthesised from a combination of
experimental results and computer calculations.


The original report contains data for lower Reynolds numbers
than contained herein, but there are some anomalies, in
particular with CL at small angles of attack.


Data extended to 360 degrees of attack and glaring anomalies
corrected by L. Lazauskas. All deviations from the original
are due to L. Lazauskas.

Please refer to the original report for more details.
```

Lift Coefficient

	REYNOLDS NUMBER							
ALPHA	40000	80000	160000	360000	700000	1000000	2000000	5000000
0	0.0000	0.0000	0.0000	0.0000	0.0000	0.0000	0.0000	0.0000
1	0.0936	0.0889	0.1100	0.1100	0.1100	0.1100	0.1100	0.1100
2	0.1833	0.1935	0.2200	0.2200	0.2200	0.2200	0.2200	0.2200
3	0.2688	0.2924	0.3088	0.3300	0.3300	0.3300	0.3300	0.3300
4	0.3495	0.3880	0.4114	0.4400	0.4400	0.4400	0.4400	0.4400
5	0.4117	0.4753	0.5068	0.5240	0.5500	0.5500	0.5500	0.5500
6	0.4573	0.5615	0.5960	0.6228	0.6328	0.6600	0.6600	0.6600
7	0.4758	0.6224	0.6724	0.7100	0.7291	0.7362	0.7449	0.7700
8	0.4428	0.6589	0.7373	0.7879	0.8156	0.8256	0.8439	0.8538
9	0.3544	0.6606	0.7781	0.8526	0.8904	0.9067	0.9314	0.9525
10	0.2108	0.6248	0.7949	0.8983	0.9541	0.9751	1.0111	1.0404
11	0.1124	0.5531	0.7852	0.9249	0.9973	1.0284	1.0772	1.1211
12	0.0139	0.4408	0.7488	0.9279	1.0245	1.0664	1.1296	1.1884
13	0.0314	0.3332	0.6923	0.9104	1.0289	1.0804	1.1662	1.2430
14	0.0489	0.2256	0.6237	0.8803	1.0175	1.0793	1.1813	1.2808
15	0.0889	0.2142	0.5567	0.8405	0.9938	1.0624	1.1813	1.3004
16	0.1287	0.2027	0.4896	0.8007	0.9648	1.0402	1.1695	1.3067
17	0.1758	0.2315	0.4549	0.7663	0.9399	1.0181	1.1550	1.3038
18	0.2228	0.2603	0.4202	0.7319	0.9150	0.9959	1.1383	1.2960
19	0.2732	0.3038	0.4292	0.7158	0.9014	0.9833	1.1278	1.2853
20	0.3236	0.3472	0.4382	0.6997	0.8877	0.9707	1.1172	1.2768
21	0.3751	0.3951	0.4704	0.7024	0.8872	0.9702	1.1150	1.2741
22	0.4265	0.4430	0.5026	0.7050	0.8867	0.9696	1.1127	1.2714
25	0.5840	0.5963	0.6321	0.7724	0.9326	1.0107	1.1468	1.2925
30	0.8550	0.8550	0.8550	0.8550	0.8550	0.8550	0.8550	0.8550
35	0.9800	0.9800	0.9800	0.9800	0.9800	0.9800	0.9800	0.9800
40	1.0350	1.0350	1.0350	1.0350	1.0350	1.0350	1.0350	1.0350
45	1.0500	1.0500	1.0500	1.0500	1.0500	1.0500	1.0500	1.0500
50	1.0200	1.0200	1.0200	1.0200	1.0200	1.0200	1.0200	1.0200
55	0.9550	0.9550	0.9550	0.9550	0.9550	0.9550	0.9550	0.9550
60	0.8750	0.8750	0.8750	0.8750	0.8750	0.8750	0.8750	0.8750
65	0.7600	0.7600	0.7600	0.7600	0.7600	0.7600	0.7600	0.7600
70	0.6300	0.6300	0.6300	0.6300	0.6300	0.6300	0.6300	0.6300

75	0.5000	0.5000	0.5000	0.5000	0.5000	0.5000	0.5000	0.5000
80	0.3650	0.3650	0.3650	0.3650	0.3650	0.3650	0.3650	0.3650
85	0.2300	0.2300	0.2300	0.2300	0.2300	0.2300	0.2300	0.2300
90	0.0900	0.0900	0.0900	0.0900	0.0900	0.0900	0.0900	0.0900
95	-0.0500	-0.0500	-0.0500	-0.0500	-0.0500	-0.0500	-0.0500	-0.0500
100	-0.1850	-0.1850	-0.1850	-0.1850	-0.1850	-0.1850	-0.1850	-0.1850
105	-0.3200	-0.3200	-0.3200	-0.3200	-0.3200	-0.3200	-0.3200	-0.3200
110	-0.4500	-0.4500	-0.4500	-0.4500	-0.4500	-0.4500	-0.4500	-0.4500
115	-0.5750	-0.5750	-0.5750	-0.5750	-0.5750	-0.5750	-0.5750	-0.5750
120	-0.6700	-0.6700	-0.6700	-0.6700	-0.6700	-0.6700	-0.6700	-0.6700
125	-0.7600	-0.7600	-0.7600	-0.7600	-0.7600	-0.7600	-0.7600	-0.7600
130	-0.8500	-0.8500	-0.8500	-0.8500	-0.8500	-0.8500	-0.8500	-0.8500
135	-0.9300	-0.9300	-0.9300	-0.9300	-0.9300	-0.9300	-0.9300	-0.9300
140	-0.9800	-0.9800	-0.9800	-0.9800	-0.9800	-0.9800	-0.9800	-0.9800
145	-0.9000	-0.9000	-0.9000	-0.9000	-0.9000	-0.9000	-0.9000	-0.9000
150	-0.7700	-0.7700	-0.7700	-0.7700	-0.7700	-0.7700	-0.7700	-0.7700
155	-0.6700	-0.6700	-0.6700	-0.6700	-0.6700	-0.6700	-0.6700	-0.6700
160	-0.6350	-0.6350	-0.6350	-0.6350	-0.6350	-0.6350	-0.6350	-0.6350
165	-0.6800	-0.6800	-0.6800	-0.6800	-0.6800	-0.6800	-0.6800	-0.6800
170	-0.8500	-0.8500	-0.8500	-0.8500	-0.8500	-0.8500	-0.8500	-0.8500
175	-0.6600	-0.6600	-0.6600	-0.6600	-0.6600	-0.6600	-0.6600	-0.6600
180	0.0000	0.0000	0.0000	0.0000	0.0000	0.0000	0.0000	0.0000
185	0.6600	0.6600	0.6600	0.6600	0.6600	0.6600	0.6600	0.6600
190	0.8500	0.8500	0.8500	0.8500	0.8500	0.8500	0.8500	0.8500
195	0.6800	0.6800	0.6800	0.6800	0.6800	0.6800	0.6800	0.6800
200	0.6350	0.6350	0.6350	0.6350	0.6350	0.6350	0.6350	0.6350
205	0.6700	0.6700	0.6700	0.6700	0.6700	0.6700	0.6700	0.6700
210	0.7700	0.7700	0.7700	0.7700	0.7700	0.7700	0.7700	0.7700
215	0.9000	0.9000	0.9000	0.9000	0.9000	0.9000	0.9000	0.9000
220	0.9800	0.9800	0.9800	0.9800	0.9800	0.9800	0.9800	0.9800
225	0.9300	0.9300	0.9300	0.9300	0.9300	0.9300	0.9300	0.9300
230	0.8500	0.8500	0.8500	0.8500	0.8500	0.8500	0.8500	0.8500
235	0.7600	0.7600	0.7600	0.7600	0.7600	0.7600	0.7600	0.7600
240	0.6700	0.6700	0.6700	0.6700	0.6700	0.6700	0.6700	0.6700
245	0.5750	0.5750	0.5750	0.5750	0.5750	0.5750	0.5750	0.5750
250	0.4500	0.4500	0.4500	0.4500	0.4500	0.4500	0.4500	0.4500
255	0.3200	0.3200	0.3200	0.3200	0.3200	0.3200	0.3200	0.3200
260	0.1850	0.1850	0.1850	0.1850	0.1850	0.1850	0.1850	0.1850
265	0.0500	0.0500	0.0500	0.0500	0.0500	0.0500	0.0500	0.0500

```
270     -0.0900 -0.0900 -0.0900 -0.0900 -0.0900 -0.0900 -0.0900 -0.0900
275     -0.2300 -0.2300 -0.2300 -0.2300 -0.2300 -0.2300 -0.2300 -0.2300
280     -0.3650 -0.3650 -0.3650 -0.3650 -0.3650 -0.3650 -0.3650 -0.3650
285     -0.5000 -0.5000 -0.5000 -0.5000 -0.5000 -0.5000 -0.5000 -0.5000
290     -0.6300 -0.6300 -0.6300 -0.6300 -0.6300 -0.6300 -0.6300 -0.6300
295     -0.7600 -0.7600 -0.7600 -0.7600 -0.7600 -0.7600 -0.7600 -0.7600
300     -0.8750 -0.8750 -0.8750 -0.8750 -0.8750 -0.8750 -0.8750 -0.8750
305     -0.9550 -0.9550 -0.9550 -0.9550 -0.9550 -0.9550 -0.9550 -0.9550
310     -1.0200 -1.0200 -1.0200 -1.0200 -1.0200 -1.0200 -1.0200 -1.0200
315     -1.0500 -1.0500 -1.0500 -1.0500 -1.0500 -1.0500 -1.0500 -1.0500
320     -1.0350 -1.0350 -1.0350 -1.0350 -1.0350 -1.0350 -1.0350 -1.0350
325     -0.9800 -0.9800 -0.9800 -0.9800 -0.9800 -0.9800 -0.9800 -0.9800
330     -0.8550 -0.8550 -0.8550 -0.8550 -0.8550 -0.8550 -0.8550 -0.8550
335     -0.5840 -0.5963 -0.6321 -0.7724 -0.9326 -1.0107 -1.1468 -1.2925
338     -0.4265 -0.4430 -0.5026 -0.7050 -0.8867 -0.9696 -1.1127 -1.2714
339     -0.3751 -0.3951 -0.4704 -0.7024 -0.8872 -0.9702 -1.1150 -1.2741
340     -0.3236 -0.3472 -0.4382 -0.6997 -0.8877 -0.9707 -1.1172 -1.2768
341     -0.2732 -0.3038 -0.4292 -0.7158 -0.9014 -0.9833 -1.1278 -1.2853
342     -0.2228 -0.2603 -0.4202 -0.7319 -0.9150 -0.9959 -1.1383 -1.2960
343     -0.1758 -0.2315 -0.4549 -0.7663 -0.9399 -1.0181 -1.1550 -1.3038
344     -0.1287 -0.2027 -0.4896 -0.8007 -0.9648 -1.0402 -1.1695 -1.3067
345     -0.0889 -0.2142 -0.5567 -0.8405 -0.9938 -1.0624 -1.1813 -1.3004
346     -0.0489 -0.2256 -0.6237 -0.8803 -1.0175 -1.0793 -1.1813 -1.2808
347     -0.0314 -0.3332 -0.6923 -0.9104 -1.0289 -1.0804 -1.1662 -1.2430
348     -0.0139 -0.4408 -0.7488 -0.9279 -1.0245 -1.0664 -1.1296 -1.1884
349     -0.1124 -0.5531 -0.7852 -0.9249 -0.9973 -1.0284 -1.0772 -1.1211
350     -0.2108 -0.6248 -0.7949 -0.8983 -0.9541 -0.9751 -1.0111 -1.0404
351     -0.3544 -0.6606 -0.7781 -0.8526 -0.8904 -0.9067 -0.9314 -0.9525
352     -0.4428 -0.6589 -0.7373 -0.7879 -0.8156 -0.8256 -0.8439 -0.8538
353     -0.4758 -0.6224 -0.6724 -0.7100 -0.7291 -0.7362 -0.7449 -0.7700
354     -0.4573 -0.5615 -0.5960 -0.6228 -0.6328 -0.6600 -0.6600 -0.6600
355     -0.4117 -0.4753 -0.5068 -0.5240 -0.5500 -0.5500 -0.5500 -0.5500
356     -0.3495 -0.3880 -0.4114 -0.4400 -0.4400 -0.4400 -0.4400 -0.4400
357     -0.2688 -0.2924 -0.3088 -0.3300 -0.3300 -0.3300 -0.3300 -0.3300
358     -0.1833 -0.1935 -0.2200 -0.2200 -0.2200 -0.2200 -0.2200 -0.2200
359     -0.0936 -0.0889 -0.1100 -0.1100 -0.1100 -0.1100 -0.1100 -0.1100
-------------------------------------------------------------------------
```

AIRFOIL: NACA 0018

DATA: Drag Coefficients

ORIGINAL SOURCE: Sheldahl, R. E. and Klimas, P. C., Aerodynamic Characteristics of Seven Airfoil Sections Through 180 Degrees Angle of Attack for Use in Aerodynamic Analysis of Vertical Axis Wind Turbines, SAND80-2114, March 1981, Sandia National Laboratories, Albuquerque, New Mexico.

NOTES: The data herein were synthesised from a combination of experimental results and computer calculations.

The original report contains data for lower Reynolds numbers than contained herein, but there are some anomalies, in particular with CL at small angles of attack.

Data extended to 360 degrees of attack and glaring anomalies corrected by L. Lazauskas. All deviations from the original are due to L. Lazauskas.

Please refer to the original report for more details.

Drag Coefficient

	REYNOLDS NUMBER						
ALPHA	40000	80000	160000	360000	700000	1000000	2000000	5000000
0	0.0214	0.0162	0.0128	0.0101	0.0085	0.0082	0.0077	0.0073
1	0.0215	0.0163	0.0129	0.0102	0.0087	0.0082	0.0077	0.0073
2	0.0219	0.0167	0.0131	0.0104	0.0088	0.0083	0.0078	0.0075
3	0.0225	0.0172	0.0137	0.0107	0.0091	0.0086	0.0080	0.0077
4	0.0235	0.0181	0.0144	0.0112	0.0096	0.0089	0.0084	0.0079

5	0.0247	0.0192	0.0153	0.0121	0.0102	0.0095	0.0087	0.0083
6	0.0263	0.0206	0.0166	0.0132	0.0112	0.0102	0.0093	0.0087
7	0.0282	0.0223	0.0181	0.0145	0.0123	0.0115	0.0101	0.0093
8	0.0303	0.0242	0.0198	0.0159	0.0136	0.0126	0.0111	0.0100
9	0.0327	0.0264	0.0217	0.0176	0.0150	0.0139	0.0122	0.0108
10	0.0620	0.0288	0.0238	0.0194	0.0166	0.0154	0.0134	0.0117
11	0.0925	0.0315	0.0262	0.0213	0.0183	0.0170	0.0148	0.0128
12	0.1230	0.0800	0.0288	0.0235	0.0202	0.0187	0.0163	0.0140
13	0.1405	0.1190	0.0770	0.0259	0.0223	0.0206	0.0179	0.0153
14	0.1580	0.1580	0.1580	0.0940	0.0245	0.0227	0.0197	0.0168
15	0.1770	0.1770	0.1770	0.1450	0.1020	0.0251	0.0218	0.0185
16	0.1960	0.1960	0.1960	0.1960	0.1960	0.1080	0.0240	0.0203
17	0.2170	0.2170	0.2170	0.2170	0.2170	0.1730	0.1200	0.0223
18	0.2380	0.2380	0.2380	0.2380	0.2380	0.2380	0.2380	0.0244
19	0.2600	0.2600	0.2600	0.2600	0.2600	0.2600	0.2600	0.1400
20	0.2820	0.2820	0.2820	0.2820	0.2820	0.2820	0.2820	0.2820
21	0.3055	0.3055	0.3055	0.3055	0.3055	0.3055	0.3055	0.3055
22	0.3290	0.3290	0.3290	0.3290	0.3290	0.3290	0.3290	0.3290
25	0.4050	0.4050	0.4050	0.4050	0.4050	0.4050	0.4050	0.4050
30	0.5700	0.5700	0.5700	0.5700	0.5700	0.5700	0.5700	0.5700
35	0.7450	0.7450	0.7450	0.7450	0.7450	0.7450	0.7450	0.7450
40	0.9200	0.9200	0.9200	0.9200	0.9200	0.9200	0.9200	0.9200
45	1.0750	1.0750	1.0750	1.0750	1.0750	1.0750	1.0750	1.0750
50	1.2150	1.2150	1.2150	1.2150	1.2150	1.2150	1.2150	1.2150
55	1.3450	1.3450	1.3450	1.3450	1.3450	1.3450	1.3450	1.3450
60	1.4700	1.4700	1.4700	1.4700	1.4700	1.4700	1.4700	1.4700
65	1.5750	1.5750	1.5750	1.5750	1.5750	1.5750	1.5750	1.5750
70	1.6650	1.6650	1.6650	1.6650	1.6650	1.6650	1.6650	1.6650
75	1.7350	1.7350	1.7350	1.7350	1.7350	1.7350	1.7350	1.7350
80	1.7800	1.7800	1.7800	1.7800	1.7800	1.7800	1.7800	1.7800
85	1.8000	1.8000	1.8000	1.8000	1.8000	1.8000	1.8000	1.8000
90	1.8000	1.8000	1.8000	1.8000	1.8000	1.8000	1.8000	1.8000
95	1.7800	1.7800	1.7800	1.7800	1.7800	1.7800	1.7800	1.7800
100	1.7500	1.7500	1.7500	1.7500	1.7500	1.7500	1.7500	1.7500
105	1.7000	1.7000	1.7000	1.7000	1.7000	1.7000	1.7000	1.7000
110	1.6350	1.6350	1.6350	1.6350	1.6350	1.6350	1.6350	1.6350
115	1.5550	1.5550	1.5550	1.5550	1.5550	1.5550	1.5550	1.5550
120	1.4650	1.4650	1.4650	1.4650	1.4650	1.4650	1.4650	1.4650
125	1.3500	1.3500	1.3500	1.3500	1.3500	1.3500	1.3500	1.3500

130	1.2250	1.2250	1.2250	1.2250	1.2250	1.2250	1.2250	1.2250
135	1.0850	1.0850	1.0850	1.0850	1.0850	1.0850	1.0850	1.0850
140	0.9250	0.9250	0.9250	0.9250	0.9250	0.9250	0.9250	0.9250
145	0.7550	0.7550	0.7550	0.7550	0.7550	0.7550	0.7550	0.7550
150	0.5750	0.5750	0.5750	0.5750	0.5750	0.5750	0.5750	0.5750
155	0.4200	0.4200	0.4200	0.4200	0.4200	0.4200	0.4200	0.4200
160	0.3200	0.3200	0.3200	0.3200	0.3200	0.3200	0.3200	0.3200
165	0.2300	0.2300	0.2300	0.2300	0.2300	0.2300	0.2300	0.2300
170	0.1400	0.1400	0.1400	0.1400	0.1400	0.1400	0.1400	0.1400
175	0.0550	0.0550	0.0550	0.0550	0.0550	0.0550	0.0550	0.0550
180	0.0250	0.0250	0.0250	0.0250	0.0250	0.0250	0.0250	0.0250
185	0.0550	0.0550	0.0550	0.0550	0.0550	0.0550	0.0550	0.0550
190	0.1400	0.1400	0.1400	0.1400	0.1400	0.1400	0.1400	0.1400
195	0.2300	0.2300	0.2300	0.2300	0.2300	0.2300	0.2300	0.2300
200	0.3200	0.3200	0.3200	0.3200	0.3200	0.3200	0.3200	0.3200
205	0.4200	0.4200	0.4200	0.4200	0.4200	0.4200	0.4200	0.4200
210	0.5750	0.5750	0.5750	0.5750	0.5750	0.5750	0.5750	0.5750
215	0.7550	0.7550	0.7550	0.7550	0.7550	0.7550	0.7550	0.7550
220	0.9250	0.9250	0.9250	0.9250	0.9250	0.9250	0.9250	0.9250
225	1.0850	1.0850	1.0850	1.0850	1.0850	1.0850	1.0850	1.0850
230	1.2250	1.2250	1.2250	1.2250	1.2250	1.2250	1.2250	1.2250
235	1.3500	1.3500	1.3500	1.3500	1.3500	1.3500	1.3500	1.3500
240	1.4650	1.4650	1.4650	1.4650	1.4650	1.4650	1.4650	1.4650
245	1.5550	1.5550	1.5550	1.5550	1.5550	1.5550	1.5550	1.5550
250	1.6350	1.6350	1.6350	1.6350	1.6350	1.6350	1.6350	1.6350
255	1.7000	1.7000	1.7000	1.7000	1.7000	1.7000	1.7000	1.7000
260	1.7500	1.7500	1.7500	1.7500	1.7500	1.7500	1.7500	1.7500
265	1.7800	1.7800	1.7800	1.7800	1.7800	1.7800	1.7800	1.7800
270	1.8000	1.8000	1.8000	1.8000	1.8000	1.8000	1.8000	1.8000
275	1.8000	1.8000	1.8000	1.8000	1.8000	1.8000	1.8000	1.8000
280	1.7800	1.7800	1.7800	1.7800	1.7800	1.7800	1.7800	1.7800
285	1.7350	1.7350	1.7350	1.7350	1.7350	1.7350	1.7350	1.7350
290	1.6650	1.6650	1.6650	1.6650	1.6650	1.6650	1.6650	1.6650
295	1.5750	1.5750	1.5750	1.5750	1.5750	1.5750	1.5750	1.5750
300	1.4700	1.4700	1.4700	1.4700	1.4700	1.4700	1.4700	1.4700
305	1.3450	1.3450	1.3450	1.3450	1.3450	1.3450	1.3450	1.3450
310	1.2150	1.2150	1.2150	1.2150	1.2150	1.2150	1.2150	1.2150
315	1.0750	1.0750	1.0750	1.0750	1.0750	1.0750	1.0750	1.0750
320	0.9200	0.9200	0.9200	0.9200	0.9200	0.9200	0.9200	0.9200

325	0.7450	0.7450	0.7450	0.7450	0.7450	0.7450	0.7450	0.7450
330	0.5700	0.5700	0.5700	0.5700	0.5700	0.5700	0.5700	0.5700
335	0.4050	0.4050	0.4050	0.4050	0.4050	0.4050	0.4050	0.4050
338	0.3290	0.3290	0.3290	0.3290	0.3290	0.3290	0.3290	0.3290
339	0.3055	0.3055	0.3055	0.3055	0.3055	0.3055	0.3055	0.3055
340	0.2820	0.2820	0.2820	0.2820	0.2820	0.2820	0.2820	0.2820
341	0.2600	0.2600	0.2600	0.2600	0.2600	0.2600	0.2600	0.1400
342	0.2380	0.2380	0.2380	0.2380	0.2380	0.2380	0.2380	0.0244
343	0.2170	0.2170	0.2170	0.2170	0.2170	0.1730	0.1200	0.0223
344	0.1960	0.1960	0.1960	0.1960	0.1960	0.1080	0.0240	0.0203
345	0.1770	0.1770	0.1770	0.1450	0.1020	0.0251	0.0218	0.0185
346	0.1580	0.1580	0.1580	0.0940	0.0245	0.0227	0.0197	0.0168
347	0.1405	0.1190	0.0770	0.0259	0.0223	0.0206	0.0179	0.0153
348	0.1230	0.0800	0.0288	0.0235	0.0202	0.0187	0.0163	0.0140
349	0.0925	0.0315	0.0262	0.0213	0.0183	0.0170	0.0148	0.0128
350	0.0620	0.0288	0.0238	0.0194	0.0166	0.0154	0.0134	0.0117
351	0.0327	0.0264	0.0217	0.0176	0.0150	0.0139	0.0122	0.0108
352	0.0303	0.0242	0.0198	0.0159	0.0136	0.0126	0.0111	0.0100
353	0.0282	0.0223	0.0181	0.0145	0.0123	0.0115	0.0101	0.0093
354	0.0263	0.0206	0.0166	0.0132	0.0112	0.0102	0.0093	0.0087
355	0.0247	0.0192	0.0153	0.0121	0.0102	0.0095	0.0087	0.0083
356	0.0235	0.0181	0.0144	0.0112	0.0096	0.0089	0.0084	0.0079
357	0.0225	0.0172	0.0137	0.0107	0.0091	0.0086	0.0080	0.0077
358	0.0219	0.0167	0.0131	0.0104	0.0088	0.0083	0.0078	0.0075
359	0.0215	0.0163	0.0129	0.0102	0.0087	0.0082	0.0077	0.0073

```
------------------------------------------------------------------------
AIRFOIL: NACA 0018
DATA: Pitching Moment Coefficients
------------------------------------------------------------------------
ORIGINAL SOURCE: Sheldahl, R. E. and Klimas, P. C., Aerodynamic
Characteristics of Seven Airfoil Sections Through
180 Degrees Angle of Attack for Use in Aerodynamic
Analysis of Vertical Axis Wind Turbines, SAND80-2114,
March 1981, Sandia National Laboratories, Albuquerque,
New Mexico.

NOTES: The data herein were synthesised from a combination of
experimental results and computer calculations.


The original report contains data for lower Reynolds numbers
than contained herein, but there are some anomalies, in
particular with CL at small angles of attack.


Data extended to 360 degrees of attack and glaring anomalies
corrected by L. Lazauskas. All deviations from the original
are due to L. Lazauskas.


Please refer to the original report for more details.



------------------------------------------------------------------------
Pitching Moment Coefficient
--------------------------------- REYNOLDS NUMBER ----------------------
ALPHA   360000  500000  680000
------------------------------------------------------------------------
0       0.0000  0.0000  0.0000
1       0.0000  0.0000  0.0000
2       0.0000  0.0000  0.0000
3       0.0000  0.0000  0.0000
4       0.0000  0.0000  0.0000
```

5	0.0000	0.0000	0.0000
6	0.0300	0.0000	0.0075
7	0.0300	0.0000	0.0150
8	0.0300	0.0150	0.0225
9	0.0300	0.0275	0.0275
10	0.0300	0.0400	0.0350
11	0.0300	0.0420	0.0380
12	0.0300	0.0440	0.0410
13	0.0320	0.0460	0.0435
14	0.0350	0.0480	0.0475
15	0.0400	0.0500	0.0500
16	0.0000	0.0000	0.0380
17	-0.0600	-0.0600	0.0220
18	-0.0600	-0.0600	0.0000
19	-0.0600	-0.0700	-0.0125
20	-0.0600	-0.0600	-0.0250
21	-0.0630	-0.0610	-0.0300
22	-0.0660	-0.0620	-0.0400
23	-0.0690	-0.0630	-0.0450
24	-0.0720	-0.0640	-0.0575
25	-0.0750	-0.0650	-0.0600
26	-0.0765	-0.0850	-0.0850
27	-0.0782	-0.0950	-0.1000
30	-0.0800	-0.1100	-0.1300
35	-0.0800	-0.1250	-0.1400
40	-0.1000	-0.2000	-0.1650
45	-0.2250	-0.1500	-0.1550
50	-0.3400	-0.2500	-0.2650
55	-0.3500	-0.2500	-0.0500
60	-0.4000	-0.2100	-0.2700
65	-0.4600	-0.3200	-0.1500
70	-0.1500	-0.1500	-0.4100
75	-0.4800	-0.4000	-0.3000
80	-0.2600	-0.4250	-0.2100
85	-0.4600	-0.2250	-0.3800
90	-0.5000	-0.3150	-0.4200
95	-0.2800	-0.2300	-0.4150
100	-0.4500	-0.3400	-0.4500
105	-0.2750	-0.4250	-0.4500

```
110     -0.4900 -0.5400 -0.1900
115     -0.5400 -0.3600 -0.3900
120     -0.5600 -0.5800 -0.5400
125     -0.4700 -0.4800 -0.4900
130     -0.4100 -0.4000 -0.4400
135     -0.4200 -0.4300 -0.5250
140     -0.4000 -0.4150 -0.4750
145     -0.5000 -0.4200 -0.3800
150     -0.3500 -0.4000 -0.3800
155     -0.3250 -0.3200 -0.3300
160     -0.2850 -0.3000 -0.3000
165     -0.2750 -0.2900 -0.3500
170     -0.4200 -0.4600 -0.4250
175     -0.2800 -0.2800 -0.3100
180     0.0250  0.0800  -0.0600
185     0.2800  0.2800  0.3100
190     0.4200  0.4600  0.4250
195     0.2750  0.2900  0.3500
200     0.2850  0.3000  0.3000
205     0.3250  0.3200  0.3300
210     0.3500  0.4000  0.3800
215     0.5000  0.4200  0.3800
220     0.4000  0.4150  0.4750
225     0.4200  0.4300  0.5250
230     0.4100  0.4000  0.4400
235     0.4700  0.4800  0.4900
240     0.5600  0.5800  0.5400
245     0.5400  0.3600  0.3900
250     0.4900  0.5400  0.1900
255     0.2750  0.4250  0.4500
260     0.4500  0.3400  0.4500
265     0.2800  0.2300  0.4150
270     0.5000  0.3150  0.4200
275     0.4600  0.2250  0.3800
280     0.2600  0.4250  0.2100
285     0.4800  0.4000  0.3000
290     0.1500  0.1500  0.4100
295     0.4600  0.3200  0.1500
300     0.4000  0.2100  0.2700
```

```
305     0.3500  0.2500  0.0500
310     0.3400  0.2500  0.2650
315     0.2250  0.1500  0.1550
320     0.1000  0.2000  0.1650
325     0.0800  0.1250  0.1400
330     0.0800  0.1100  0.1300
333     0.0782  0.0950  0.1000
334     0.0765  0.0850  0.0850
335     0.0750  0.0650  0.0600
336     0.0720  0.0640  0.0575
337     0.0690  0.0630  0.0450
338     0.0660  0.0620  0.0400
339     0.0630  0.0610  0.0300
340     0.0600  0.0600  0.0250
341     0.0600  0.0700  0.0125
342     0.0600  0.0600  0.0000
343     0.0600  0.0600  -0.0220
344     0.0000  0.0000  -0.0380
345     -0.0400 -0.0500 -0.0500
346     -0.0350 -0.0480 -0.0475
347     -0.0320 -0.0460 -0.0435
348     -0.0300 -0.0440 -0.0410
349     -0.0300 -0.0420 -0.0380
350     -0.0300 -0.0400 -0.0350
351     -0.0300 -0.0275 -0.0275
352     -0.0300 -0.0150 -0.0225
353     -0.0300 0.0000  -0.0150
354     -0.0300 0.0000  -0.0075
355     0.0000  0.0000  0.0000
356     0.0000  0.0000  0.0000
357     0.0000  0.0000  0.0000
358     0.0000  0.0000  0.0000
359     0.0000  0.0000  0.0000
-------------------------------------------------------------------------
```

The following lift and drag data was used for the mathematical modelling of the performance of the wind tunnel turbine. It has been synthesised using the experimental data measured for the test turbine blade (see Section 9.3.1) for angles of attack up to 50° and the data of Lazauskas (2002) for higher angles. Pitching moment data from Lazauskas (2002) was used for all angles.

The data is plotted in Figure D.2.

Lift coefficients

AoA	Reynolds Number		
	1600000	250000	360000
0	0	0	0
1	0.09	0.09	0.09
2	0.177	0.177	0.177
3	0.26	0.26	0.26
4	0.336	0.336	0.336
5	0.414	0.414	0.414
6	0.487	0.487	0.487
7	0.559	0.559	0.559
8	0.635	0.635	0.635
9	0.718	0.718	0.718
10	0.802	0.802	0.802
11	0.873	0.873	0.873
12	0.916	0.916	0.916
13	0.959	0.959	0.959
14	1.001	1.001	1.001
15	0.782	1.044	1.044
16	0.497	1.065	1.065
17	0.453	1.082	1.082
18	0.46	1.058	1.1
19	0.475	0.864	1.106
20	0.487	0.496	1.099
21	0.506	0.506	0.884
22	0.524	0.524	0.524
25	0.566	0.566	0.566
30	0.68	0.68	0.68
35	0.737	0.737	0.737
40	0.783	0.783	0.783
45	0.803	0.803	0.803
50	0.791	0.791	0.791

Drag coefficients

AoA	Reynolds Number		
	1600000	250000	360000
0	0.0272	0.0173	0.0173
1	0.0266	0.0185	0.0185
2	0.0272	0.0194	0.0194
3	0.0272	0.0208	0.0208
4	0.0295	0.0225	0.0225
5	0.0324	0.0246	0.0246
6	0.0364	0.0277	0.0277
7	0.0393	0.0315	0.0315
8	0.0428	0.0353	0.0353
9	0.048	0.04	0.04
10	0.0543	0.046	0.046
11	0.0613	0.0517	0.0517
12	0.0665	0.0575	0.0575
13	0.0711	0.0627	0.0627
14	0.078	0.0702	0.0702
15	0.1292	0.0774	0.0774
16	0.2211	0.084	0.084
17	0.2393	0.0936	0.0936
18	0.2532	0.108	0.102
19	0.2749	0.191	0.114
20	0.29	0.29	0.132
21	0.309	0.309	0.253
22	0.329	0.329	0.329
25	0.378	0.378	0.378
30	0.5	0.5	0.5
35	0.607	0.607	0.607
40	0.728	0.728	0.728
45	0.855	0.855	0.855
50	0.983	0.983	0.983

55	0.764	0.764	0.764	55	1.11	1.11	1.11
60	0.738	0.738	0.738	60	1.237	1.237	1.237
65	0.682	0.682	0.682	65	1.364	1.364	1.364
70	0.611	0.611	0.611	70	1.503	1.503	1.503
75	0.492	0.492	0.492	75	1.613	1.613	1.613
80	0.375	0.375	0.375	80	1.676	1.676	1.676
85	0.23	0.23	0.23	85	1.711	1.711	1.711
90	0.09	0.09	0.09	90	1.728	1.728	1.728
95	-0.05	-0.05	-0.05	95	1.734	1.734	1.734
100	-0.185	-0.185	-0.185	100	1.705	1.705	1.705
105	-0.32	-0.32	-0.32	105	1.676	1.676	1.676
110	-0.45	-0.45	-0.45	110	1.613	1.613	1.613
115	-0.575	-0.575	-0.575	115	1.555	1.555	1.555
120	-0.67	-0.67	-0.67	120	1.465	1.465	1.465
125	-0.76	-0.76	-0.76	125	1.35	1.35	1.35
130	-0.85	-0.85	-0.85	130	1.225	1.225	1.225
135	-0.93	-0.93	-0.93	135	1.085	1.085	1.085
140	-0.98	-0.98	-0.98	140	0.925	0.925	0.925
145	-0.9	-0.9	-0.9	145	0.755	0.755	0.755
150	-0.77	-0.77	-0.77	150	0.575	0.575	0.575
155	-0.67	-0.67	-0.67	155	0.42	0.42	0.42
160	-0.635	-0.635	-0.635	160	0.32	0.32	0.32
165	-0.68	-0.68	-0.68	165	0.23	0.23	0.23
170	-0.85	-0.85	-0.85	170	0.14	0.14	0.14
175	-0.66	-0.66	-0.66	175	0.055	0.055	0.055
180	0	0	0	180	0.025	0.025	0.025
185	0.66	0.66	0.66	185	0.055	0.055	0.055
190	0.85	0.85	0.85	190	0.14	0.14	0.14
195	0.68	0.68	0.68	195	0.23	0.23	0.23
200	0.635	0.635	0.635	200	0.32	0.32	0.32
205	0.67	0.67	0.67	205	0.42	0.42	0.42
210	0.77	0.77	0.77	210	0.575	0.575	0.575
215	0.9	0.9	0.9	215	0.755	0.755	0.755
220	0.98	0.98	0.98	220	0.925	0.925	0.925
225	0.93	0.93	0.93	225	1.085	1.085	1.085
230	0.85	0.85	0.85	230	1.225	1.225	1.225
235	0.76	0.76	0.76	235	1.35	1.35	1.35
240	0.67	0.67	0.67	240	1.465	1.465	1.465
245	0.575	0.575	0.575	245	1.555	1.555	1.555

250	0.45	0.45	0.45	250	1.613	1.613	1.613
255	0.32	0.32	0.32	255	1.676	1.676	1.676
260	0.185	0.185	0.185	260	1.705	1.705	1.705
265	0.05	0.05	0.05	265	1.734	1.734	1.734
270	-0.09	-0.09	-0.09	270	1.728	1.728	1.728
275	-0.23	-0.23	-0.23	275	1.711	1.711	1.711
280	-0.375	-0.375	-0.375	280	1.676	1.676	1.676
285	-0.492	-0.492	-0.492	285	1.613	1.613	1.613
290	-0.611	-0.611	-0.611	290	1.503	1.503	1.503
295	-0.682	-0.682	-0.682	295	1.364	1.364	1.364
300	-0.738	-0.738	-0.738	300	1.237	1.237	1.237
305	-0.764	-0.764	-0.764	305	1.11	1.11	1.11
310	-0.791	-0.791	-0.791	310	0.983	0.983	0.983
315	-0.803	-0.803	-0.803	315	0.855	0.855	0.855
320	-0.783	-0.783	-0.783	320	0.728	0.728	0.728
325	-0.737	-0.737	-0.737	325	0.607	0.607	0.607
330	-0.68	-0.68	-0.68	330	0.5	0.5	0.5
335	-0.566	-0.566	-0.566	335	0.378	0.378	0.378
338	-0.524	-0.524	-0.524	338	0.329	0.329	0.329
339	-0.506	-0.506	-0.884	339	0.309	0.309	0.253
340	-0.487	-0.496	-1.099	340	0.29	0.29	0.132
341	-0.475	-0.864	-1.106	341	0.2749	0.191	0.114
342	-0.46	-1.058	-1.1	342	0.2532	0.108	0.102
343	-0.453	-1.082	-1.082	343	0.2393	0.0936	0.0936
344	-0.497	-1.065	-1.065	344	0.2211	0.084	0.084
345	-0.782	-1.044	-1.044	345	0.1292	0.0774	0.0774
346	-1.001	-1.001	-1.001	346	0.078	0.0702	0.0702
347	-0.959	-0.959	-0.959	347	0.0711	0.0627	0.0627
348	-0.916	-0.916	-0.916	348	0.0665	0.0575	0.0575
349	-0.873	-0.873	-0.873	349	0.0613	0.0517	0.0517
350	-0.802	-0.802	-0.802	350	0.0543	0.046	0.046
351	-0.718	-0.718	-0.718	351	0.048	0.04	0.04
352	-0.635	-0.635	-0.635	352	0.0428	0.0353	0.0353
353	-0.559	-0.559	-0.559	353	0.0393	0.0315	0.0315
354	-0.487	-0.487	-0.487	354	0.0364	0.0277	0.0277
355	-0.414	-0.414	-0.414	355	0.0324	0.0246	0.0246
356	-0.336	-0.336	-0.336	356	0.0295	0.0225	0.0225
357	-0.26	-0.26	-0.26	357	0.0272	0.0208	0.0208
358	-0.177	-0.177	-0.177	358	0.0272	0.0194	0.0194

359	-0.09	-0.09	-0.09	359	0.0266	0.0185	0.0185
360	0	0	0	360	0.0272	0.0173	0.0173

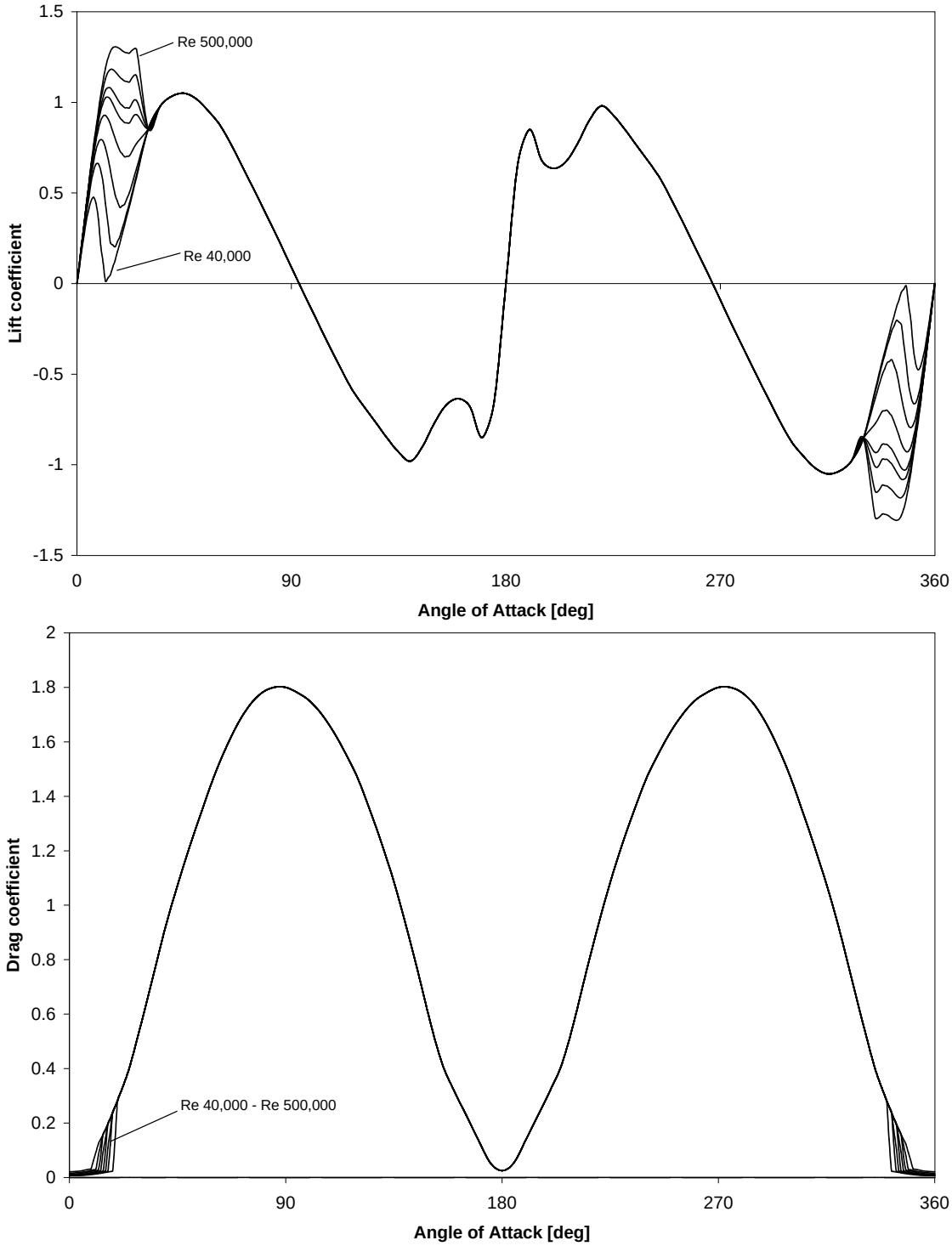

Figure D.1: Lift and drag coefficient data from Sheldahl and Klimas (1981) presented by Lazauskas (2002)

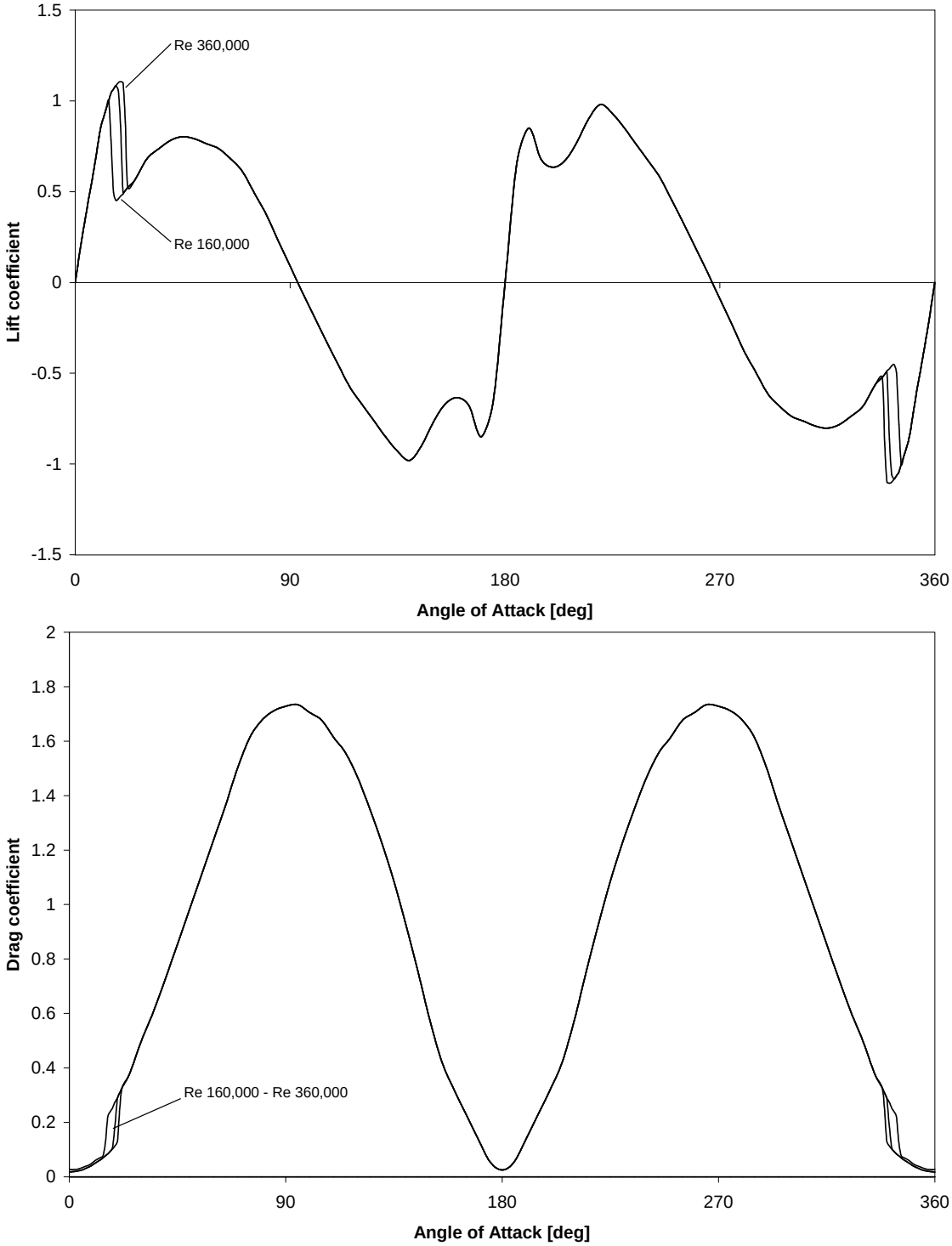

Figure D.2: Lift and drag coefficient data synthesised from experimental data for angles of attack below 50° and that of Sheldahl and Klimas (1981) presented by Lazauskas (2002) for higher angles.

Appendix E

Code listing

The momentum and vortex theory mathematical models described in Chapters 5 and 6 are embodied in a Windows 98/NT/XP application written using Visual C++ 5. The source code and a compiled executable file are included on a CD-ROM inside the back cover.

Note that there is a bug in the Release version of the executable that produces erroneous results from the momentum theory analysis. All results presented in this thesis were obtained by using the Debug version of the program.

Appendix F

Photographs of Test Rig

The completed turbine set up in the wind tunnel test section. The section is then rolled into place in the wind tunnel.

The completed turbine set up in the wind tunnel test section. The section is then rolled into place in the wind tunnel.

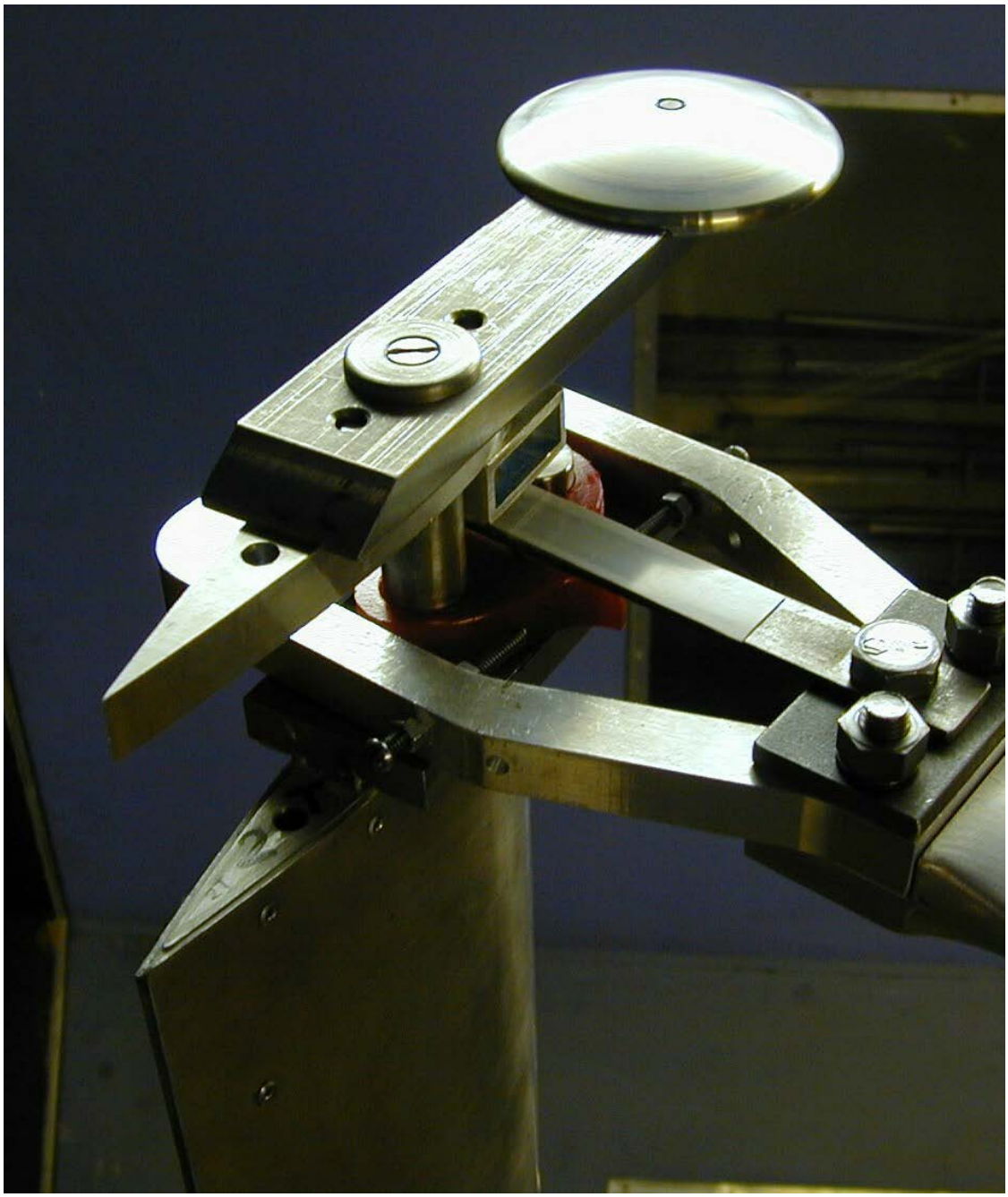

Detail of blade and arm housing.

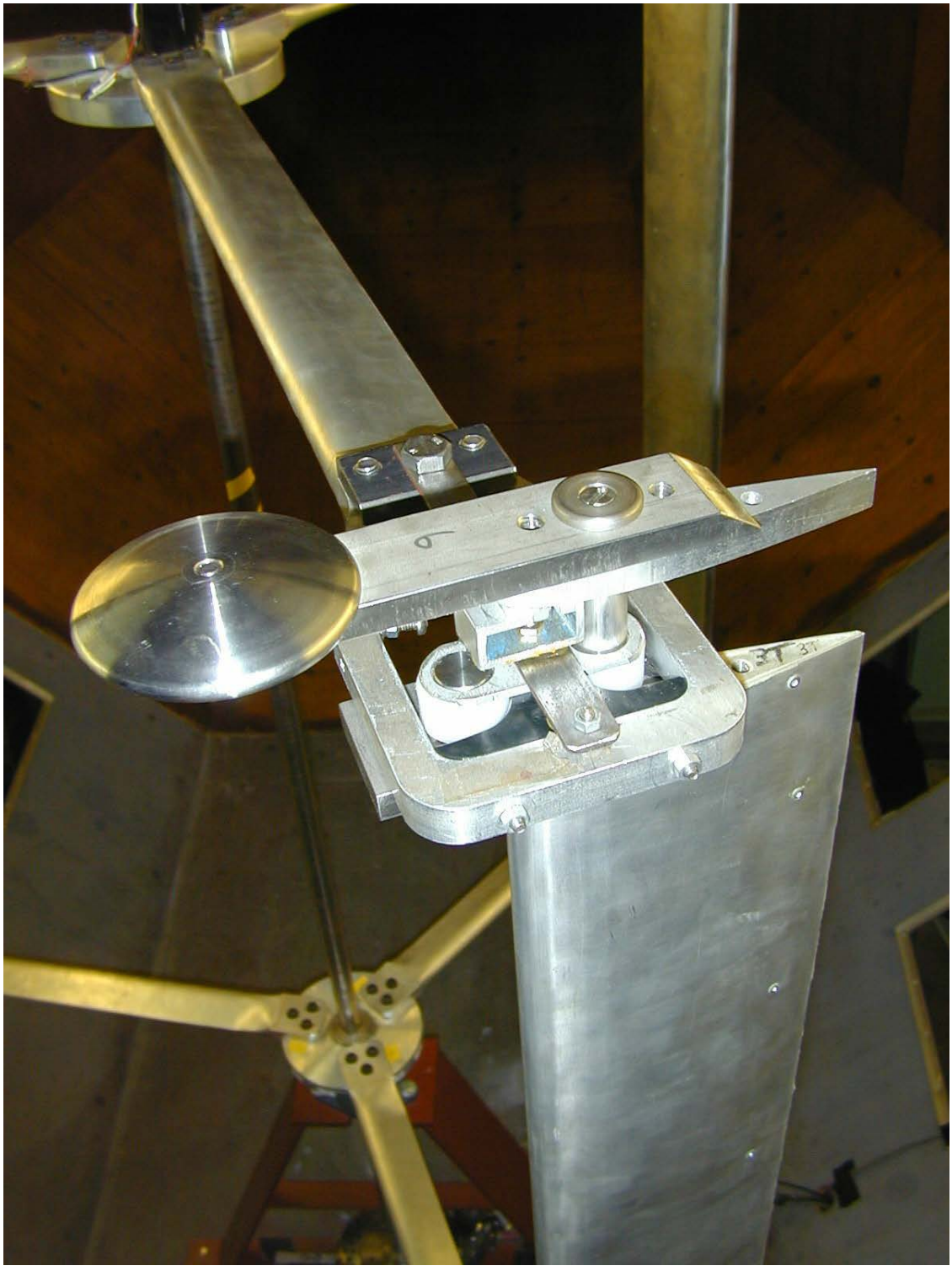

View from above showing blade with Type B High Density Polyethylene component.

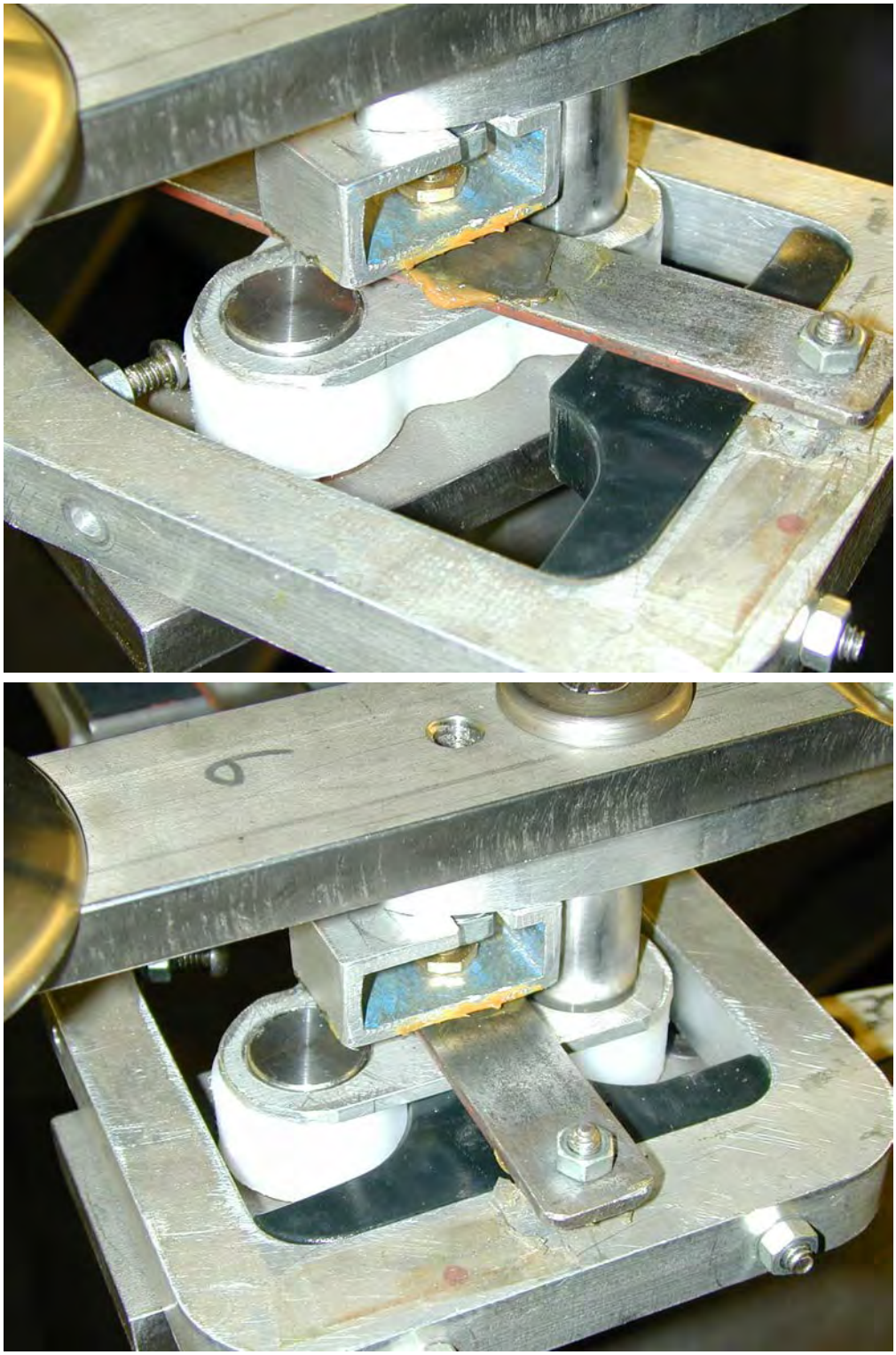

Close up of the High Density Polyethylene Type B component on one of the turbine blades.